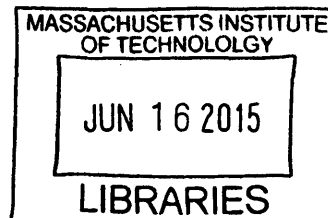


**DEVELOPMENT OF MICROREACTOR SETUPS FOR ARCHIVES  
MICROWAVE ORGANIC SYNTHESIS**

by

**Wen-Hsuan Lee**



Bachelor of Science, Chemical Engineering, National Taiwan University, 2008  
Master of Science, Chemical Engineering Practice, Massachusetts Institute of Technology, 2011

SUBMITTED TO THE DEPARTMENT OF CHEMICAL ENGINEERING  
IN PARTIAL FULFILLMENT OF THE REQUIREMENTS FOR THE DEGREE OF

DOCTOR OF PHILOSOPHY IN CHEMICAL ENGINEERING  
AT THE  
MASSACHUSETTS INSTITUTE OF TECHNOLOGY

FEBRUARY 2015

© 2015 Massachusetts Institute of Technology. All rights reserved.

**Signature redacted**

Author \_\_\_\_\_

Wen-Hsuan Lee

Department of Chemical Engineering

October 3, 2014

**Signature redacted**

Certified by \_\_\_\_\_

Klavs F. Jensen

Warren K. Lewis Professor of Chemical Engineering

Professor of Materials Science and Engineering

Thesis Supervisor

**Signature redacted**

Accepted by \_\_\_\_\_

Patrick S. Doyle

Professor of Chemical Engineering

Chairman, Committee for Graduate Students



# DEVELOPMENT OF MICROREACTOR SETUPS FOR MICROWAVE ORGANIC SYNTHESIS

by

Wen-Hsuan Lee

Submitted to the Department of Chemical Engineering  
on October 3, 2014 in partial fulfillment of the  
requirements for the degree of  
Doctor of Philosophy in Chemical Engineering

## ABSTRACT

---

The main contribution of this work is the understanding of microwave heating and the microreactor design challenges involved through both chemical experiments and computational models. The original goal of this research is to develop a microreactor system in order to carry the microwave organic synthesis in continuous flow format and to understand the basic phenomena of microwave heating through accurate kinetic studies.

Several heating issues were observed with the first microreactor setup, including an uneven temperature distribution across the microwave irradiated area and a temperature limitation that depends on the position of the reactor. To find the root of these problems, the electromagnetic field and the heat transfer scheme of the microwave system were modeled with COMSOL. The simulations show that there are three main causes to the heating issues: (1) the electric field has an inherent resonance structure and thus has an uneven magnitude within the microwave cavity, (2) the electric field changes with not only the material, but also the sizes and positions of the objects in the microwave cavity, (3) the air gaps in the microwave waveguide creates a large natural convection heat loss. The simulations gave us a deeper understanding of the microwave heating phenomena and were used to find the optimum design of the microreactor.

A second multiple-layered glass reactor was designed accordingly to overcome the heating limitation and minimized the temperature unevenness. However, the non-uniform heating rate cannot be eliminated since it is inherent in the resonance structure of microwaves. Both the experimental results and the simulations of the final reactor show that even though the reactor can reach the desired temperature, the temperature range across the reactor could be up to 20 °C. In addition, it was found that the flow rate of the reaction greatly affects the thermal equilibrium of the reaction volume. Accurate temperature control is therefore still a challenge for kinetic studies to be feasible with the current single-mode microwave system. The benefit of microwave heating is therefore still in the qualitative screening of chemical compounds, a feature which was demonstrated with a Fischer-Indole screening in the final setup.

**Thesis Supervisor:** Klavs F. Jensen

**Title:** Department Head, Chemical Engineering  
Warren K. Lewis Professor of Chemical Engineering  
Professor of Materials Science and Engineering



*To my parents,  
Cheing-Tung and I-Ling;  
and in Loving Memory of  
my Grandfather.*



## ACKNOWLEDGEMENTS

---

The pursuit of this degree has been a humbling journey that has bent and shaped me as both a scientist and a human being, hopefully into a better form in each respect. I am only able to travel to the end of this road because of the amazingly supportive family, friends, mentors, and colleagues that I have been fortunate enough to have known. They have all been an instrumental part of my growth throughout these years. During the completion of this thesis, I have longed to put down in words my gratitude for the overwhelming help and encouragement they have provided me.

I would like to start by thanking my advisor, Professor Klavs Jensen, without whom this thesis would not have been possible. I am deeply grateful for his years of guidance and support, be it technical, financial, or beyond. I am still at awe by not only his remarkable breadth and depth of knowledge, but also the substantial time and care he puts towards his students despite his busy schedule. I greatly appreciate his policy of keeping his doors open to his students at all times, and for his efforts in creating an encouraging lab environment. Thank you, Klavs, for believing in my work and my scientific abilities, especially at times when I lose sight of the prospects myself.

I would also like to thank Professor Bill Green and Professor Tim Jamison, my thesis committee members, for their feedbacks throughout the years. Both of them have provided crucial and inspiring suggestions that helped me focus on the contributions of this project to the research community and its applications. Thank you for lending your time to me and offering me your viewpoints from your expertise.

This work was funded by the National Science Foundation and Novartis AG. I deeply appreciate these institutions for helping me fulfill my goal to pursue scientific research in the States while putting a roof over my head. I also acknowledge CEM for generously lending us the microwave unit used for this study for the past six years. Furthermore, I would like to thank Professor Aaron Beeler and Professor John Porco for hatching the idea of this project.

Numerous people have helped me acquire technical skills and offered me scientific discussion throughout this thesis. I am grateful for the knowledge they have passed on to me. I would especially like to thank Dr. Will Grover, who took out generous amount of time to train me in glass microfabrication and lent me his photo exposure setup. Thanks to Lih Feng Cheow

for helping me use the CNC drill press in the Han Lab. I also owe many thanks to YiMing and ShaoLing in the Buchwald Lab, and Christina Dai in the Jamison Lab, for the useful suggestions on purifying the Indole products and for generously lending me their setups when our lab was under renovation. I gratefully appreciate everyone in the Jensen Lab, past and present, for keeping a friendly work environment and for kindly providing me with constructive suggestions as well as insightful discussions. In particular, I would like to thank Stephen Born, Stephen Newman, and Chris Smith, for helping me with my organic chemistry; Lei Gu, for the suggestions on COMSOL; and Jason, Patrick, Brandon, and Everett, for helping me on the numerous miscellaneous problems I run into every now and then. This has been a really enjoyable lab to work in.

The people in ChemE have enriched my graduate school experiences, and I deeply appreciate the staff and faculty that have helped me throughout the years: Professor William Deen and Professor Patrick Doyle, thank you for letting me TA your class. It was both a privilege and a delight working for you. Claude Lupis and Chris Marton, thank you for directing us at Practice School. It was a very valuable experience. To the staffs, you do the best job at keeping the department affairs efficiently in order while creating a warm and welcoming atmosphere for us all. Alina Haverty, Barbara Balkwill, Iris Chang, Christine Preston, Suzanne Maguire, Joel Dashnaw, and Beth Tuths, thank you for all the care and the friendly faces over the years.

The support of my friends here in Boston/Cambridge have carried me through the hardships of graduate school and have helped me find home in this foreign city. I am astounded by these friendships that I've been blessed with, and I treasure every profound discussion, every silly laugh, every happy drink, every delicious meal, and every heartfelt moment we've shared together. Many of these friendships have been forged in the Jensen lab: Chao Ling, thank you for rekindling my faith in research every time my visions are flickering. Vicki, thank you for being not only a wonderful TA and a knowledgeable mentor, but also an understanding friend who always sees the good in me and encourages me to treat myself kinder. Tanya and Maria, thank you for being my comrades that pump one another up at all times, in every aspect of life. Norbert, thank you for lamenting with me the ups and downs we've both experienced. Gino, thank you for making sure I still had an enjoyable life outside of work while I was making the final sprint this past year. To my friends at MIT: Kunle, thank you for taking me in as your mentee when I was a



first year and as your “other roommate” during your last few years in Ashdown. Kristin, you’re an awesome person to chill with at all occasions. I am very thankful that I got to know you better throughout the years and that you’ve held my hand through some of my worst moments. Jungmin and Vivian, thanks for all the food adventures and fashion exchanges. Ilia and Amy, thank you for all the epic hangouts and for being there whenever I need someone to talk to. Harry, Simon, Kevin, Bonnie, and Michael Hess, thanks for being there at battle with me since first year and helping me maintain my work-life balance from then on. I greatly appreciate all the friends I made through the Taiwanese ties both at MIT and in the greater Boston area: Yina, I am grateful to have you as a friend that I can always talk honestly to and share all sorts of ideas with. Andrew, thank you for your advice on all things, especially finance, in life. Chih-Chao, thank you for giving me care and support as the older brother I’ve never had. Joyce, I’m happy to have a friend who shares so many interests as me. Ingrid, Michelle, Sherry, and Lisa, thank you for treating me as a sister and always opening up your home to me. To my friends who I’ve had the fortune to nourish relationships with for more than a decade: Chih-Ying, thank you for commiserating and traveling with me throughout grad school. Yuan-Hsi, Chia-Chen, and You-yu, thank you for all the postcards throughout the years. I know that wherever I may go, you’ll be there for me anywhere you are. A very special group of friends in Ashdown House have been my Boston family. We’ve spent countless celebrations and consolations together ever since we all moved into Ashdown the first year it opened. I know we can always rely on one another to be there for the big moments. Kao Tsung, thanks for being there for me during all sorts of problems, from getting me started with electromagnetic simulation to talking with me through personal issues. Kay, thank you for guiding me through all stages of grad school and teaching me the ins and outs of MIT ChemE. Jackie, thank you for being a considerate roommate. Albert, Samuel, Vgod, thank you for all the fun talks and for driving me whenever I need a lift. Without naming names, I would also like to thank the people I have met at an MIT support group. The intelligence and resilience they’ve shown throughout experiences that resonate with mine have given me immense hope and comfort.

For the last year and a half, I have to thank Michael for his continuous love and support. Both his compassion and craziness have kept me grounded and motivated for life. Michael, thank you for appreciating me as who I am and inspiring me to be better. I am grateful to have you as my personalized Hoptimist. I am looking forward to all the delicious journeys we have ahead.

My deepest gratitude goes to my parents, whom I admire and respect more and more each day. If I can go through life with half the wit, grit, and kindness they have, I would consider myself a success. I am grateful that despite the hardships they've faced, they have always put raising my siblings and me with the right values as the utmost priority. I would not have been in MIT if they had not taught me the importance of learning and being independent. Dad, thank you for taking me to the library ever since I learned how to read, and for never putting a price on our education. Mom, thank you for encouraging me to never limit my interest or potential to the social expectation of the gender I was born in, and for teaching me the values of a curious mind and a kind heart over outer appearances. Most importantly, I would like to thank you both for giving me the three most wonderful siblings anyone can ask for: Judy, Michael, and Meimei, thank you for the years of companionship, entertainment, and, at times if not most, tolerance. It gives me strength to know that the three of you have always looked up to me not for what I did, but for who I am. Last but not least, I would like to thank the rest of my family for their encouragement, especially my Grandma and cousin Marian, who surprised me with care packages for the last six years, and my Grandpa, who took me to grade school every day and whose memories I will forever cherish.

# TABLE OF CONTENTS

---

ABSTRACT.....	3
ACKNOWLEDGEMENTS.....	7
TABLE OF CONTENTS.....	11
LIST OF FIGURES .....	15
LIST OF TABLES.....	23
LIST OF SCHEMES .....	25
CHAPTER 1. MOTIVATION AND BACKGROUND.....	27
1.1 Motivation .....	27
1.2 Microwave-assisted Organic synthesis.....	29
1.2.1 Microwave Heating Mechanism.....	29
1.2.2 Microwave Heating Effects and Applications.....	30
1.2.3 Microwave Units and Equipment.....	36
1.2.4 Microwave Synthesis in Continuous Flow.....	39
1.3 Glass Microreactor Fabrication .....	42
1.3.1 Glass Microreactor Fabrication .....	42
1.3.2 Packaging Techniques .....	45
1.4 Thesis Overview .....	47
CHAPTER 2. INITIAL SYSTEM DESIGN .....	49
2.1 Introduction .....	49
2.2 Discover Microwave Unit .....	49
2.3 Microreactor Setup and Fabrication Methods .....	50
2.4 Validation Reactions.....	54
2.5 Heating Issues.....	57
CHAPTER 3. MICROWAVE HEATING SIMULATIONS .....	61
3.1 Introduction .....	61
3.2 Theoretical Background .....	62
3.3 Initial Model without Air Convection .....	64

3.3.1 Model Geometry .....	64
3.3.2 Simulation Model Description.....	66
3.3.3 Simulation Results .....	68
3.3.4 Improving Reactor Design with Simulations .....	73
3.3.5 Model Deficiency .....	73
3.4 Air Convection Models .....	74
3.4.1 Thermal Conductivity Estimation Model .....	76
3.4.2 Single-Phase Flow Model.....	79
CHAPTER 4. SPIRAL REACTOR SETUP .....	87
4.1 Introduction .....	87
4.2 Reactor Design and Heating Testing.....	87
4.2.1 First Generation of Spiral Microreactor .....	87
4.2.2 Chemistry Testing and Mechanical Stability.....	88
4.2.3 Second Generation of Spiral Microreactor .....	91
4.3 Spiral Reactor Simulations .....	91
4.3.1 Spiral Reactor Simulations with Empty Channels .....	92
4.3.2 Spiral Reactor Simulations with Static Acetic Acid.....	94
CHAPTER 5. VERIFICATION EXPERIMENTS.....	105
5.1 Introduction .....	105
5.2 Condensation Reaction Kinetics.....	105
5.2.1 Direct Microwave Heating at Two Different Positions.....	105
5.2.2 Experiments with a Microwave-Shielding Glycerol Bath.....	108
5.3 Temperature Results of Reactor Models with Flow .....	110
5.3.1 Kinetic Mean Temperature Definition .....	110
5.3.2 Spiral Reactor Simulations with Flow.....	111
5.3.3 Simulation Parameter Sensitivity .....	115
5.4 Fischer Indole Screening .....	121
5.4.1 Experimental Procedures .....	123
5.4.2 Fischer Indole Synthesis Results .....	123
CHAPTER 6. CONCLUSIONS AND FUTURE PERSPECTIVES.....	127
6.1 Summary of Thesis Achievements and Findings .....	127

6.2 Future Perspectives.....	131
6.2.1 Redesigning a Microwave Unit.....	131
6.2.2 3D Temperature Sensor.....	132
6.2.3 Simulation for Accurate Temperature Prediction.....	132
REFERENCES .....	135
APPENDIX A. CHAPTER 2 SUPPORTING INFORMATION .....	141
A.1 Fabrication Details.....	141
A.2 Designs of Initial Glass Microreactor Holders .....	144
A.3 Mixing Quality.....	145
A.4 Experimental Procedure.....	146
APPENDIX B. CHAPTER 3 SUPPORTING INFORMATION .....	151
B.1 Nusselt Number Calculation Details and Matlab Code for Thermal Conductivity Estimation Model .....	151
B.2 Additional Temperature Plots for Each Simulation Models.....	153
APPENDIX C. CHAPTER 5 SUPPORTING INFORMATION .....	159
C.1 Condensation Reaction Experimental Procedure.....	159
C.2 Matlab Code for Reactor Mean Temperature Calculation.....	160
C.3 Fischer Indole Synthesis GC Chromatography, Mass Spectrum, and NMR.....	162



## LIST OF FIGURES

---

Figure 1.1: Microwave heating of ethanol under atmospheric pressure with 75W of irradiation power. <sup>4</sup> .....	31
Figure 1.2: Kinetic data collected from microwave heating (○) and conventional heating (●) for esterification reaction. <sup>4</sup> .....	31
Figure 1.3: Different shapes of waveguides in single-mode microwave units: (a) Circular waveguide in CEM Discover. (b) Rectangular waveguide in Biotage Initiator. <sup>5</sup> .....	38
Figure 1.4: CEM Voyager® continuous flow system and its different reactors. <sup>15, 47</sup> .....	38
Figure 1.5: (a) Microreactor, and (b) capillary reactor designed by the Haswell group for Suzuki cross-coupling reactions. <sup>48-49</sup> .....	40
Figure 1.6: (a) Single capillary reactor system and (b) parallel, capillary multireactor system for continuous flow microwave reaction designed by the Organ group. <sup>18-19</sup> .....	41
Figure 1.7: Schematics of the sand-filled flow cell designed by the Bagley group. <sup>51</sup> .....	42
Figure 1.8: Schematic of microfabrication in glass. ....	43
Figure 1.9: Glass-glass bonding with FEP Teflon film to create membrane valves. (a) The exploded and assembled illustration of the bonding pieces. (b) Cross-sectional schematic the operation of a single valve. <sup>62</sup> .....	44
Figure 1.10: (a) Schematic of three-dimensional channels in the pile-up reactors aligned for thermal bonding. (b) Photograph of the ten-layer, pile-up reactor. <sup>54</sup> .....	45
Figure 1.11: Compression packaging of glass reactors in the Kitamori group: (a) Cross-sectional schematic of the tube connection. (b) Photograph of the pile-up glass reactor with tube connections. <sup>54</sup> .....	46
Figure 1.12: Reactor setup for glass tube brazing procedure. <sup>68</sup> .....	47
Figure 2.1: CEM Discover® 1 unit used for this research: (a) Front view of the unit. (b) Schematic of internal microwave configuration view from the top. <sup>47</sup> .....	50
Figure 2.2: Side view of the microreactor fitting into the microwave unit. Red arrows depict the direction of microwave irradiation.....	51

Figure 2.3: 1 <sup>st</sup> generation of microreactor: (a) Microreactor without packaging. (b) Packaging of microreactor with PEEK assembly and Teflon holder for the fiber optic temperature probe. (c) Backside of assembly with PEEK screws.....	52
Figure 2.4: Microreactor setup for continuous-flow microwave synthesis. ....	53
Figure 2.5: Conversion profile for 2-methylbenzimidazole formation with first microreactor setup. ....	56
Figure 2.6: Arrhenius plot of $\ln k$ versus $1/T$ used to determine the activation energy and pre-exponential factor of the condensation reaction with the results from the initial microreactor for microwave.....	56
Figure 2.7: Comparison of the aromatic substitution results from microwave microreactor and conventional cartridge heater.....	57
Figure 2.8: Deposits in reaction channels after aromatic substitution reactions. ....	57
Figure 2.9: Schematic of the reactor temperature as measured by a thermal couple after heating the aromatic substitution solution to 260 °C.....	58
Figure 2.10: Temperature profile at different solvents inside the microreactor irradiated at the maximum microwave power. ....	59
Figure 2.11: Temperature profiles of empty reactor surface center under different microwave power irradiation at positions (a) parallel to microwave port, (b) perpendicular to microwave port. ....	59
Figure 3.1: Internal structure of the CEM Discover Unit: (a) top view of all components, (b) side view of waveguide and steel wall without the Teflon piece, and (c) picture of the Teflon component with a side hole.....	65
Figure 3.2: Isotropic view of simulation geometry schematics with reactor positioned (a) parallel to microwave port, and (b) perpendicular to microwave port. (Colored axes show the directions in the simulation geometry drawing.).....	66
Figure 3.3: Simulated reactor surface temperature of an empty reactor under 300 W microwave irradiation for 60 seconds at (a) parallel-to-port position, and (b) perpendicular-to-port position. (Inserts show the surface position and direction) .....	68
Figure 3.4: Simulated total power dissipation/heating rate in microwave cavity across reactor center plane under 300 W microwave irradiation for 60 seconds at (a) parallel-to-port position, and (b) perpendicular-to-port position.....	69



Figure 3.5: Simulated electric field strength in microwave cavity across reactor center plane of empty reactor under 300 W microwave irradiation for 60 seconds at (a) parallel-to-port position, and (b) perpendicular-to-port position. .... 70

Figure 3.6: Simulated electric field of empty reactor under 300 W microwave irradiation for 60 seconds: (a) Isometric view of parallel-to-port position. (b) Isometric view of perpendicular-to-port position. (c) Top view of parallel-to-port position. (d) Top view of perpendicular-to-port position. .... 71

Figure 3.7: Size view of the electric field resonance in the cavity and the start of the waveguide. .... 72

Figure 3.8: Electric field strengths and temperatures of reactor center with various reactor thicknesses under 60 seconds of 300 W microwave irradiation. .... 73

Figure 3.9: Temperature of reactor center in initial simulation models after 60 minutes of microwave irradiation. .... 74

Figure 3.10: (a) Domain in the simulation model that required natural convection model. (b) Schematics of the side view of the air gap in the cavity and waveguide. .... 75

Figure 3.11: Comparison between the experimental and simulated heating profiles with the k-estimation models of empty reactors under different power exposure at parallel-to-port position. .... 77

Figure 3.12: Comparison between the experimental and simulated heating profiles with the k-estimation models of empty reactors under different power exposure at perpendicular-to-port position. .... 78

Figure 3.13: Velocity field on cavity center plane viewed from the front of the unit in the single-phase flow simulation when reactor is parallel to port. (Color bar shows velocity magnitude, arrows indicate velocity direction projected onto the 2D plane.) .... 81

Figure 3.14: Velocity field on cavity and waveguide center plane viewed from the right side of the unit in the single-phase flow simulation when reactor is parallel to port. (Color bar shows velocity magnitude, arrows indicate velocity direction projected onto the 2D plane.)..... 82

Figure 3.15: Velocity field on cavity center plane viewed from the front of the unit in the single-phase flow simulation when reactor is perpendicular to port. (Color bar

shows velocity magnitude, arrows indicate velocity direction projected onto the 2D plane.) .....	82
Figure 3.16: Velocity field on cavity and waveguide center plane viewed from the right side of the unit in the single-phase flow simulation when reactor is perpendicular to port. (Color bar shows velocity magnitude, arrows indicate velocity direction projected onto the 2D plane.).....	83
Figure 3.17: Comparison of heating profiles between the two air-convection simulation models and experimental data for empty reactor under 300 W microwave irradiation at (a) parallel-to-port and (b) perpendicular-to-port position.....	84
Figure 4.1: 1 <sup>st</sup> spiral, multilayer microreactor design: (a) front view, (b) angled view, (c) side view schematics, and (d) picture of actual reactor.....	88
Figure 4.2: Comparison of the aromatic substitution results from microwave microreactor and conventional cartridge heater.....	89
Figure 4.3: 2 <sup>nd</sup> spiral, multilayer microreactor design: (a) picture of reactor, (b) front view picture with packaging, (c) angled view picture with packaging. ....	91
Figure 4.4: Isotropic view of (a) entire simulation geometry for spiral reactor positioned parallel to microwave port, and (b) close-up schematics of the reactor with reaction channels colored in blue. ....	92
Figure 4.5: Comparison between the experimental and simulated heating profiles with the k-estimation models of empty spiral reactors under different power exposure at parallel-to-port position. ....	93
Figure 4.6: Simulated temperature profile of spiral reactor filled with acetic acid under various power of microwave irradiation. (Insert shows the point of temperature measurement.).....	95
Figure 4.7: Electric field strength of different planes viewed from the front side of the unit for spiral reactor under 6 W irradiation.....	96
Figure 4.8: Power dissipation density of different planes viewed from the front side of the unit for spiral reactor under 6 W irradiation. ....	97
Figure 4.9: Temperature of reactor center plane viewed from the front side of the unit for spiral reactor under 6 W irradiation at different time points. ....	99

Figure 4.10: Temperature of different planes viewed from the front side of the unit for spiral reactor at t=60 minutes under 6 W irradiation.....	100
Figure 4.11: Temperature along the reaction volume in the spiral reactor at t=60 minutes under 6 W irradiation.....	101
Figure 4.12: Electric field strength of cavity and waveguide center plane viewed from the right side of the unit for spiral reactor at t=60 minutes under 6 W irradiation.....	102
Figure 4.13: Power dissipation density of cavity and waveguide center plane viewed from the right side of the unit for spiral reactor at t=60 minutes under 6 W irradiation.....	103
Figure 4.14: Temperature of cavity and waveguide center plane viewed from the right side of the unit for spiral reactor at t=60 minutes under 6 W irradiation.....	103
Figure 5.1: Conversion data of condensation reaction of <i>o</i> -phenylenediamine and acetic acid from spiral microreactor.....	106
Figure 5.2: Conversion data of condensation reaction of <i>o</i> -phenylenediamine and acetic acid from spiral microreactor.....	109
Figure 5.3: Temperature along the reaction volume in the spiral reactor under constant 6 W irradiation for continuous flow with different residence times.....	115
Figure 5.4: The input power dependencies of the average power dissipation density (●) and the total heating rate in the reaction volume (◆).....	116
Figure 5.5: The input power dependencies of the reactor kinetic mean temperature at various flow rates.....	117
Figure 5.6: The permittivity dependence of the total heating rate in the reaction volume.....	118
Figure 5.7: The permittivity dependence of the kinetic mean temperature of the reaction without flow.....	119
Figure 5.8: The dielectric constant dependencies of the kinetic mean temperature of the reaction without flow at various dielectric loss values.....	120
Figure 5.9: The dielectric loss dependencies of the kinetic mean temperature of the reaction without flow at various dielectric constant values.....	121
Figure A.1: Calibration curve of glass wet-etched with 49 % HF solution.....	141
Figure A.2: Microscope picture of furnace bonded glass reactor etched on single side. (Scale unit: 10 μm).....	143

Figure A.3: Microscope picture of furnace bonded glass reactor etched on both sides. (Scale unit: 10 $\mu\text{m}$ ) .....	143
Figure A.4: Drawing of PEEK holder for initial microreactor setup. (Unit: inch).....	144
Figure A.5: Drawing of Teflon holder for fiber optic probe. (Unit: mm) .....	144
Figure A.6: Simulation of mixing length for microreactor with 4.5 $\mu\text{l}/\text{min}$ flow rate at each inlet. ....	145
Figure A.7: Simulation of mixing length for microreactor with 750 $\mu\text{l}/\text{min}$ flow rate at each inlet. ....	146
Figure A.8: Arrhenius plot of $\ln k$ versus $1/T$ for Diels-Alder reaction using initial microreactor with microwave. ....	147
Figure A.9: Arrhenius plot of $\ln k$ versus $1/T$ for Diels-Alder reaction in batch experiments with microwave.....	148
Figure A.10: Arrhenius plot of $\ln k$ versus $1/T$ for the condensation reaction using the reported conversions in reference “ <i>Damm, M.; Glasnov, T. N.; Kappe, C. O., Translating High-Temperature Microwave Chemistry to Scalable Continuous Flow Processes. Org. Process Res. Dev. 2009, 14 (1), 215-224.</i> ” .....	149
Figure A.11: Arrhenius plot of $\ln k$ versus $1/T$ of the condensation reaction with the results from the cartridge-heated microreactor. The results from the red calibration line were used to determine the activation energy and pre-exponential factor. ....	150
Figure B.1: Temperature of cavity center plane viewed from the front side of the unit when reactor is parallel to port at $t=3000$ seconds under 300 W irradiation for initial model without air convection. ....	153
Figure B.2: Temperature of cavity and waveguide center plane viewed from the right side of the unit when reactor is parallel to port at $t=3000$ seconds under 300 W irradiation for initial model without air convection. ....	153
Figure B.3: Temperature of cavity center plane viewed from the front side of the unit when reactor is perpendicular to port at $t=3000$ seconds under 300 W irradiation for initial model without air convection. ....	154
Figure B.4: Temperature of cavity and waveguide center plane viewed from the right side of the unit when reactor is perpendicular to port at $t=3000$ seconds for under 300 W irradiation initial model without air convection. ....	154

Figure B.5: Temperature of cavity center plane viewed from the front side of the unit when reactor is parallel to port at t=3000 seconds under 300 W irradiation for k-estimation model.....	155
Figure B.6: Temperature of cavity and waveguide center plane viewed from the right side of the unit when reactor is parallel to port at t=3000 seconds under 300 W irradiation for k-estimation model.....	155
Figure B.7: Temperature of cavity center plane viewed from the front side of the unit when reactor is perpendicular to port at t=3000 seconds under 300 W irradiation for k-estimation model.....	156
Figure B.8: Temperature of cavity and waveguide center plane viewed from the right side of the unit when reactor is perpendicular to port at t=3000 seconds under 300 W irradiation for k-estimation model.....	156
Figure B.9: Temperature of cavity center plane viewed from the front side of the unit when reactor is parallel to port at t=1000 seconds under 300 W irradiation for laminar flow model.....	157
Figure B.10: Temperature of cavity and waveguide center plane viewed from the right side of the unit when reactor is parallel to port at t=1000 seconds under 300 W irradiation for laminar flow model.....	157
Figure B.11: Temperature of cavity center plane viewed from the front side of the unit when reactor is perpendicular to port at t=1000 seconds under 300 W irradiation for laminar flow model.....	158
Figure B.12: Temperature of cavity and waveguide center plane viewed from the right side of the unit when reactor is perpendicular to port at t=1000 seconds under 300 W irradiation for laminar flow model.....	158
Figure C.1: GC-FID chromatography for condensation reaction with glycerol jacket at 140 °C, 10 min residence time.....	160
Figure C.2: NMR spectrum of solvent deuterated chloroform.....	162
Figure C.3: NMR spectrum of internal standard 1,3,5-trimethoxybenzene.....	163
Figure C.4: GC-FID chromatography for Fischer indolization of c1 at 180 °C, 3 min residence time.....	164
Figure C.5: GC mass spectrum for c1.....	165

Figure C.6: NMR spectrum for crude collection of c1 at 180 °C, 3 min residence time. ....	165
Figure C.7: NMR spectrum for purified c1 at 180 °C, 3 min residence time.....	166
Figure C.8: GC-FID chromatography for Fischer indolization of c2 at 170 °C, 3 min residence time. ....	167
Figure C.9: GC mass spectrum for c2.....	168
Figure C.10: NMR spectrum for crude collection of c2 at 170 °C, 10 min residence time. ....	168
Figure C.11: NMR spectrum for purified c2 at 170 °C, 3 min residence time.....	169
Figure C.12: GC-FID chromatography for Fischer indolization of c3 at 180 °C, 15 min residence time. ....	170
Figure C.13: GC mass spectrum for c3.....	171
Figure C.14: NMR spectrum for crude collection of c3 at 180 °C, 20 min residence time. ....	171
Figure C.15: NMR spectrum for purified c3 at 180 °C, 30 min residence time.....	172
Figure C.16: GC-FID chromatography for Fischer indolization of c4 at 180 °C, 30 min residence time. ....	173
Figure C.17: GC mass spectrum for c4.....	174
Figure C.18: NMR spectrum for crude collection of c4 at 180 °C, 20 min residence time. ....	174
Figure C.19: NMR spectrum for purified c4 at 180 °C, 20 min residence time.....	175
Figure C.20: GC-FID chromatography for Fischer indolization of c5 at 180 °C, 10 min residence time. ....	176
Figure C.21: GC mass spectrum for c5.....	177
Figure C.22: NMR spectrum for crude collection of c5 at 180 °C, 3 min residence time. ....	177
Figure C.23: NMR spectrum for purified c5 at 180 °C, 3 min residence time.....	178

## LIST OF TABLES

---

Table 1.1: Loss tangent values of selected solvents at 2.45 GHz, 20 °C. <sup>5</sup> .....	29
Table 1.2: Sample scope of chemistries run under microwave irradiation. <sup>5, 32</sup> .....	35
Table 2.1: Diels-Alder results compared with literature data. ....	55
Table 3.1: Parameters used for microwave geometry in COMSOL.....	66
Table 3.2: Material electrical properties used in the simulation. <sup>1, 77</sup> .....	67
Table 3.3: Effective thermal conductivities, equivalent heat transfer coefficients, and Nusselt numbers for k-estimation models of parallel-to-port reactor. ( $Nu_{\text{rectangular}}$ calculated from reference <sup>87</sup> ).....	77
Table 3.4: Effective thermal conductivities, equivalent heat transfer coefficients, and Nusselt numbers for k-estimation models of perpendicular-to-port reactor. ( $Nu_{\text{rectangular}}$ calculated from reference <sup>87</sup> ).....	78
Table 3.5: Rayleigh numbers of the air gaps in the microwave unit at different reactor positions and different power settings. ....	80
Table 4.1: Condensation results and kinetic mean temperature calculations from 1 <sup>st</sup> spiral microreactor .....	90
Table 4.2: Microwave heating rate versus irradiation power for spiral reactor channels with acetic acid. ....	95
Table 5.1: Condensation results and kinetic mean temperature calculation from spiral microreactor at parallel-to-port position. ....	107
Table 5.2: Condensation results and kinetic mean temperature calculation from spiral microreactor at perpendicular-to-port position. ....	107
Table 5.3: Condensation results and kinetic mean temperature calculation from spiral microreactor heated with glycerol bath. ....	110
Table 5.4: Laminar flow and creeping flow simulation comparison.....	112
Table 5.5: Results from spiral reactor flow simulations with acetic acid as solvent and 6 W microwave irradiation. ....	114
Table 5.6: Optimization of phenylhydrazine and cyclohexanone indolization with microwave spiral reactor. ....	124

Table 5.7: Synthesis of indole derivatives with microwave spiral microreactor.....	125
Table A.1: Diels-Alder results in batch mode. ....	148



## LIST OF SCHEMES

---

Scheme 1.1: Friedel-Crafts benzylation of deuterated <i>p</i> -xylene with results reported by Dudley and Steigman. <sup>44</sup> .....	34
Scheme 1.2: Biginelli three-component reaction that generates DHPM library. Numbers stand for the potential number of compounds that can be used or generated. <sup>2, 10</sup> .....	35
Scheme 2.1: Diels-Alder reaction of isoprene and maleic anhydride.....	54
Scheme 2.2: Condensation reaction of <i>o</i> -phenyldiamine and acetic acid.....	54
Scheme 2.3: Aromatic substitution of 2-chloropyridine with piperidine. ....	54
Scheme 5.1: Fischer indole synthesis. ....	122
Scheme 5.2: Fischer indolization of phenylhydrazine and cyclohexanone to 1,2,3,4-tetrahydrocarbazole.....	122



# CHAPTER 1. MOTIVATION AND BACKGROUND

---

## 1.1 Motivation

The goal of the thesis research is to engineer microreactor setups that can perform microwave-assisted organic flow synthesis with rigorous experiments in order to obtain a better characterization of microwave heating and probe its benefits. In specific, the aims were to integrate the microreactor system with an automated platform for reaction screening, and perform kinetic studies of microwave reactions.

Microwave-assisted organic synthesis (MAOS) has become increasingly popular ever since microwave irradiation was first introduced to organic synthesis in 1986.<sup>1-2</sup> The rising interest in this field is due to the numerous advantages brought about by the unique mechanisms of microwave heating.<sup>3</sup> The main advantage of microwave heating is the dramatic increase in heating rate compared with conventional heating since molecules in the reaction mixtures can absorb the microwave energy directly within a microwave-transparent vessel. The reactions in microwave synthesis therefore result in less reaction time, higher yields, and cleaner profiles.<sup>3</sup> Other benefits include the abilities to superheat solvents under atmospheric pressure<sup>4</sup> and to heat certain components selectively.<sup>5</sup> Selectively heating different reaction components under microwave have led to reports of novel reaction pathways and product distributions that differ from conventional heating under the same temperatures.<sup>6-7</sup> The ability to collect data rapidly and the potential to expand chemical space make MAOS attractive to the fields of kinetic studies,<sup>8</sup> high-throughput synthesis, chemical/drug discovery and reaction optimization.<sup>2, 9-10</sup>

However, by the start of this thesis project, most of the work on microwave synthesis had been done in batch mode. The preparation and cleanup steps required in batch reactions are considerably time and labor intensive even when most microwave units come with a robotic handler for the vials. These problems were especially hindering when a large amount of data and experiments are required.<sup>11</sup> In addition, batch experiments often leads to inaccurate data collection, such as the vapor build up in headspace resulting in higher concentration measurement and residue heat from slow quenching resulting in longer actual residence time than intended.<sup>12</sup> This is especially important for microwave experiments since the reactions run at higher temperatures and inaccurate temperature measurements have been proven to be the

cause behind most extraordinary chemistry results that mislead scientists to believe microwave has non-thermal effects on chemistry.<sup>13</sup> Furthermore, the limitations of batch reactors create the main challenges in bringing microwave synthesis from laboratory scales to production scales.<sup>14-15</sup> Some of these scale-up issues include the restriction on the size of the reactors due to the penetration depth of microwave irradiations, the requirement of significantly higher power supply to heat up larger volumes, the need for complicated cooling systems, and the reduction of energy efficiency in turning electricity into microwave irradiation when going up to large volumes.<sup>14-16</sup> Therefore, there has been significant interest in performing microwave reactions in continuous flow conditions in order to address the above issues. There are only a few examples of continuous flow systems for microwave reactions, and none of them have been applied to kinetic modeling or high-throughput synthesis.<sup>17-21</sup>

Microreactor setups have the ability to operate microwave reactions in continuous flow format. This advantage allows us to prevent the previously mentioned data inaccuracy and scale-up issues and to perform large numbers of experiments faster, which is extremely advantageous for high-throughput screening.<sup>22</sup> In addition, continuous processes reduce material costs, improve process safety, and provide easier scaling.<sup>23-24</sup>

The small channel size of microreactors also provides numerous advantages. The small reaction volumes of microreactors greatly decrease chemical consumption in experiments, and thus reduce the cost for high-throughput testing. The reduced amount of toxic or hazardous materials in the microreactors at any time point also makes the processes safer for dangerous chemistries.<sup>25-26</sup> In addition, the large surface to volume ratios and small length scales of the channels allow fast mass and heat transfer in microreactors, therefore leading to faster and more uniform mixing of reactants and more uniform heating where isothermal conditions can easily be achieved.<sup>23</sup> The large surface to volume ratio is also beneficial for additional features, such as coating catalysts along the surfaces.

Furthermore, many of the advantages of microwave heating, such as less reaction time, higher yield, and purer products, are also found with microreactors without microwave heating.<sup>27</sup> Therefore, the comparisons of kinetic data of reactions in microreactors with conventional heating and with microwave heating gives insight into the basic phenomena of microwave effects and helps us evaluate the usefulness of microwave synthesis on reaction screening with microreactors.

## 1.2 Microwave-assisted Organic synthesis

### 1.2.1 Microwave Heating Mechanism

Microwaves are electromagnetic radiation that consists of oscillating electric fields and magnetic fields in between the frequency of 300 MHz to 300 GHz. Most microwave units in chemistry lab operate at 2.45 GHz. The energy of microwave photon at 2.45 GHz is only 0.0016 eV, much lower than molecular bond energies, and is therefore unable to start chemical reactions by cleaving molecular bonds. Instead, microwave induces heating by dipolar polarization and ionic conduction.<sup>5</sup> The dipoles and ions of the materials under microwave irradiation will continuously adjust their positions to align with the oscillating electric field. During the realignment, energy is turned into heat through dielectric loss and molecular friction, and the process is called dielectric heating.<sup>5, 28-29</sup> The ability of materials to absorb microwave energy and convert them into heat thus depends on their dielectric properties, which is expressed as the complex permittivity:<sup>30-31</sup>

$$\varepsilon = \varepsilon' - i\varepsilon'' \quad (1.1)$$

The real part of the permittivity is the lossless term and stands for how well the material absorbs and propagates the microwave energy, while the imaginary part of the permittivity is the energy loss term and stands for how well the material converts the microwave energy into heat.

The loss tangent is then defined as the ratio of the lossy portion in the electric field to the lossless reaction:<sup>30</sup>

$$\tan\delta = \frac{\varepsilon''}{\varepsilon'} \quad (1.2)$$

The permittivity, and therefore loss tangent, is dependent on the frequency and temperature that the material is under (Table 1.1). The larger the loss tangent of a material, the faster it heats up under microwave irradiation.<sup>3, 5, 29</sup>

**Table 1.1: Loss tangent values of selected solvents at 2.45 GHz, 20 °C.<sup>5</sup>**

Solvent / Material	$\tan\delta$	Solvent / Material	$\tan\delta$
ethylene glycol	1.350	1,2-dichloroethane	0.127
ethanol	0.941	water	0.123
DMSO	0.825	chlorobenzene	0.101
2-propanol	0.799	chloroform	0.091
formic acid	0.722	acetonitrile	0.062
methanol	0.659	ethyl acetate	0.059

Solvent / Material	$\tan\delta$	Solvent / Material	$\tan\delta$
nitrobenzene	0.589	acetone	0.054
1-butanol	0.571	tetrahydrofuran	0.047
2-butanol	0.447	dichloromethane	0.042
1,2-dichlorobenzene	0.280	toluene	0.040
NMP	0.275	hexane	0.020
acetic acid	0.174	Pyrex	0.010
DMF	0.161	Telfon	0.0015

### 1.2.2 Microwave Heating Effects and Applications

The fact that different materials couple with microwave radiation differently leads to many benefits and applications. The key advantage is volumetric heating, where reactants can be heated up directly when placed in a microwave transparent vessel ( $\tan\delta < 0.01$ ), such as Pyrex/glass or Telfon containers. The reactants can therefore be heated up faster to higher temperature regimes that cannot be easily achieved by conventional heating. This in turn leads to greatly reduced reaction times and higher conversions for many reactions.<sup>3, 32</sup>

In addition, studies have shown that microwave radiation can superheat organic solvents under atmospheric conditions (Figure 1.1).<sup>4, 33</sup> The extent of the super-heating temperature from a solvent's classic boiling point varies with different solvent and can be as high as 40 °C and is useful in expanding the range of data collection for kinetic studies, as demonstrated by Chemat *et al.* with the esterification reaction of benzoic acid in excess of methyl alcohol catalyzed by sulphuric acid (Figure 1.2).<sup>4</sup> However, this feature is not often employed since most microwave reactions are run under sealed vessel conditions, where pressures are allowed to rise above the atmospheric temperature.<sup>5</sup>

Other special techniques in microwave heating include putting small traces of strongly microwave absorbing materials into reaction solutions that are weaker in absorbing microwave energy in order to improve the heating effect, or to add thin metal catalyst inside the solutions to create small hot spots where the reactions take place.<sup>5, 9</sup> For example, the Kappe group added 1-butyl-3-methylimidazolium hexafluorophosphate (bmimPF<sub>6</sub>), a strongly microwave absorbing ionic liquid, to aid the intramolecular hetero-Diels–Alder reaction of alkenyl-tethered pyrazinone in 1,2-dichloroethane. The original reaction took an hour to complete while the reaction with the ionic liquid added was complete in 13 minutes since it was able to reach a higher temperature in a much small time range.<sup>9</sup>

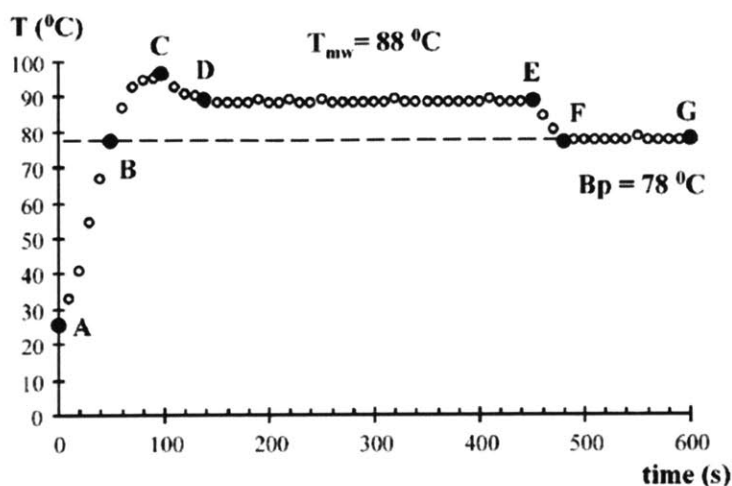


**Figure 1.1: Microwave heating of ethanol under atmospheric pressure with 75W of irradiation power.<sup>4</sup>**

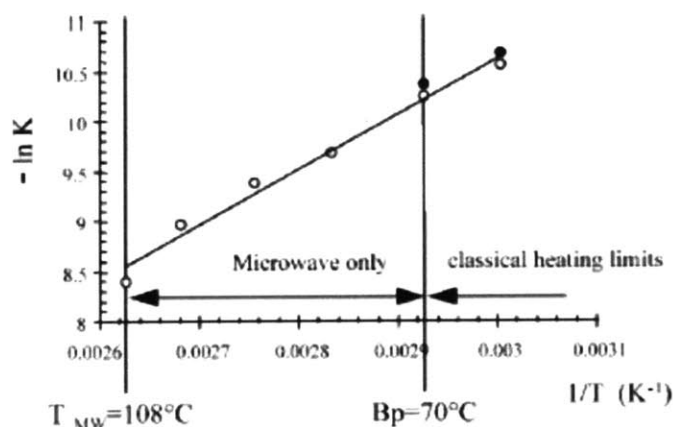


**Figure 1.2: Kinetic data collected from microwave heating (○) and conventional heating (●) for esterification reaction.<sup>4</sup>**

In addition to the benefits mentioned above, some people had suggested that microwave heating can also bring about “non-thermal effects.”<sup>5, 34</sup> This topic has been highly controversial. Microwave reactions with rate-accelerated results or special product distribution that cannot be replicated by conventional heating are often suggested to exhibit non-thermal effects.<sup>34-35</sup> In order to facilitate a clear discussion of how microwave can affect chemical reactions, C. Oliver Kappe proposed the following terms to describe the different attributes of microwave in organic reactions: (1) thermal effects, (2) specific microwave effects, and (3) non-thermal microwave

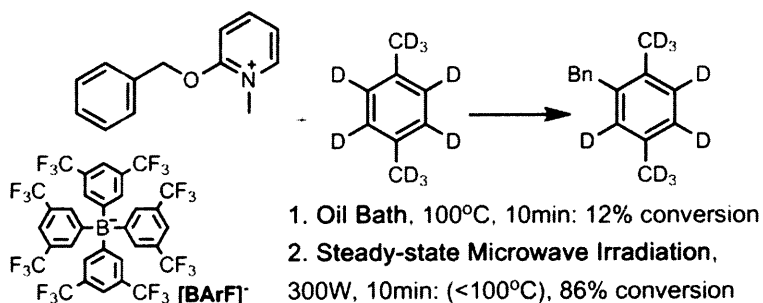
effects.<sup>5</sup> Microwave chemistry enhancement that results from rapid heating and the ability to reach a higher temperature regime is categorized as displaying thermal effects. The rate enhancement or cleaner profile obtained under microwave heating is purely due to thermal/kinetic effect that can be explained with the bulk reaction temperature by the same Arrhenius equation as the one of the same chemistry under conventional heating. Kappe defines specific microwave effects as *“accelerations of chemical transformations in a microwave field that can not be achieved or duplicated by conventional heating, but essentially are still thermal effects.”*<sup>5</sup> These include the aforementioned microwave heating applications, such as superheating solvents and selectively heating strong microwave-absorbing materials, and the elimination of wall effects that can result from conventional heating. For selectively-heated reactions that display specific microwave effect, not only are the reaction conditions hard to replicate without microwave, but the exact experimental temperatures are also hard to determine since the localized “hot spots” in the reaction is not the same as the bulk temperature. Non-thermal microwave effects include all other reaction accelerations that cannot be explained by thermal effect or specific microwave effect. It has been postulated that non-thermal effects result from the direct interaction of microwave electric field with specific reaction molecules.<sup>34</sup> For instance, if the reaction transition state is more polar than ground state, then the electric field can stabilize process of the reactants going to the transition state. This results in a lower activation energy that leads to increase in reactivity. It is also hypothesized that the rotation of the molecules may sometimes result in a higher pre-exponential factor in the Arrhenius equation. These effects are stated to be stronger in solvent-free reactions or in low microwave-absorbing solvents because the microwave can interact directly with the reactants instead of being “blocked” by polar solvents.<sup>29, 34, 36-37</sup> However, many author argues that differences in microwave heating and conventional heating in these examples are due to inaccurate temperature readings in microwave units or other poor control of the reaction conditions.<sup>35, 38</sup> Many reactions that have been claimed to display non-thermal effect were found to produce the same results as conventional heating after careful reconstruction of the reactions in identical temperature settings.<sup>39-40</sup> Kappe’s group have been prominent in debunking many non-thermal microwave effect claims in the past decade by recreating reactions in microwave units with fiber-optic temperature setups that provide more accurate temperature measurements than the built-in IR sensors in typical microwave units (section 1.2.3 Microwave Units and Equipment).<sup>39</sup> A



representative example is the Diel-Alder cycloaddition of phenylacetylene to methyl 2-oxo-2H-pyran-3-carboxylate reported by Loupy *et al.* in 2004. After reinvestigating the reaction with a fiber-optic temperature sensor, Kappe's group found that higher yield in Loupy's study under microwave irradiation compared to oil bath heating was due to the underestimation of the bulk microwave reaction temperature by the IR sensors.<sup>36, 39</sup> Kappe's group has also assessed the existence of non-thermal effect by investigating chemical transformations in a silicon carbide vial.<sup>40-41</sup> Silicon carbide is a chemically inert material with high microwave absorbance and high thermal conductivity. Therefore, under microwave irradiations, the SiC vial converts the microwave field into heat and conducts the heat to the reaction such as in conventional heating settings, while a Pyrex vial will allow the reaction to be exposed to the microwave field. The chemistry results from a Pyrex vial and the SiC vial turn out to be the same under the same temperature setting, and therefore Kappe concluded that the microwave field does not affect the reactions.<sup>40</sup>

Due to the extensive effort placed in the reinvestigation of microwave reactions, most scientists today agree that non-thermal microwave effect does not exist. However, disputes are still taking place over which reactions or reaction conditions qualify as displaying "specific microwave effects" and whether these reactions are significant enough for chemistry application. One of these examples was the arguments Gregory B. Dudley and Albert E. Stiegman had with C. Oliver Kappe over the Friedel-Crafts benzylation of both deuterated *p*-xylene and toluene that Dudley and Stiegman reported in 2012 (Scheme 1.1).<sup>13, 42-44</sup> The xylene and toluene in the reaction act as both reactants and microwave transparent solvents. Dudley and Stiegman proposed that the polar solute, 2-Benzyloxy-1-methylpyridinium BArF, is selectively heated up in the homogeneous solution, and therefore the solute reactivity is not only temperature dependent but will also be affected by the power of the microwave irradiation. They suggested the solute create local hot spots and collide more frequently on a molecular level, and thus increasing the pre-exponential factor in the Arrhenius equation and leads to a reactivity enhancement cannot be captured by the bulk temperature of the solution.<sup>44</sup> This is an analogy to heterogeneous microwave reaction where solid catalysts are selectively heated amidst solvent with lower microwave absorbance. While they ran the xylene reactions under open vessel conditions, they ran a second series of toluene benzylation under reflux condition to ensure the reaction temperature is the same between the microwave irradiated and the oil bath experiments, and the

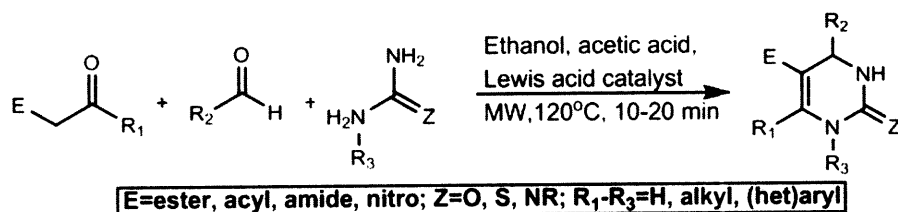
conversion rates were also higher under microwave irradiation.<sup>44</sup> Kappe's group recreated the experiments with a fiber optic probe and reported the same conversions between the two heating methods, and therefore concluded that Dudley and Stiegman's observation is due to inaccurate temperature measurement and also superheating affects under atmospheric temperature.<sup>13</sup> They believe the reaction enhancement Dudley and Steigman reported was due to the increase of the bulk solvent temperature instead of solute hot spots. Dudley and Stiegman, however, refuted this argument since they claim Kappe did not accurately replicate their experiments: for the xylene microwave experiment, Kappe's group used a constant temperature setting at 100 °C with a lower microwave power irradiation; while for the toluene microwave experiment, Kappe's group added boiling chips to the solution. Dudley and Stiegman argue that the lower power settings diminished the high power steady-state microwave irradiation effect that they intentionally aimed for in their design, and that Kappe's group reported the same increased conversions as Dudley and Stiegman's original paper when boiling chips were not added in the toluene experiments.<sup>42</sup> Dudley and Steigman also ruled out superheating as the cause of increased reactivity since they added stir bars to all their experiments and also demonstrated the stirred toluene has the same temperature with and without boiling chips.<sup>42</sup> In summary, Kappe believes the results Dudley and Stiegman observed can be explained by the bulk solution temperature, and the rate enhancement can be achieved by simply increasing the bulk reaction temperature.<sup>13,</sup><sup>43</sup> However, Dudley and Stiegman believe this is a case of selective heating of a homogeneous solution, and with strategic experimental designs, reactions with polar solute in microwave transparent solvents can benefit from constant high power microwave irradiation; they encourage chemists to further explore this area.<sup>42</sup>



**Scheme 1.1: Friedel-Crafts benzylation of deuterated *p*-xylene with results reported by Dudley and Steigman.<sup>44</sup>**

Aside from the dispute on the nature and application of microwave effects, the potential of microwave heating to speed up the rate of synthesis for high-throughput synthesis and kinetic studies have also been anticipated and exploited.<sup>2, 8, 22, 45</sup> An example of library synthesis by microwave is the generation of a dihydropyrimidine (DHPM) library by Biginelli multicomponent reactions (Scheme 1.2).<sup>2, 10</sup> Reactions were carried out in an automatic sequential format with sealed-vessel vials irradiated batch-wise. The microwave irradiation significantly increased the reaction rate and was able to screen 48 compounds in 12 hours. This is a great improvement compared to the traditional synthetic procedure of Biginelli reactions, which took some time between 2 to 12 hours to run one single reaction.<sup>10</sup>

An example of microwave heating used in kinetic studies is the reevaluation of the Newman-Kwart Rearrangement by Gilday et al.<sup>8</sup> The reaction they chose was one on which no specific or non-thermal microwave effect was reported. After demonstrating that microwave heating produced the same conversion as conventional heating, they collected a larger range of data with microwave synthesis. The analysis showed that the reaction order for the rearrangement changes with the reactant concentration as opposed to exhibiting a constant first order kinetic profile. The study demonstrates how data can be rapidly collected by microwave heating.<sup>8</sup>



**Scheme 1.2: Biginelli three-component reaction that generates DHPM library. Numbers stand for the potential number of compounds that can be used or generated.<sup>2, 10</sup>**

As a summary, many types of organic reactions have been successfully conducted through microwave heating, and several examples are shown in Table 1.2. Detailed reviews can be found in reference 5.

**Table 1.2: Sample scope of chemistries run under microwave irradiation.<sup>5, 32</sup>**

Reaction Type	Example
Heck Reactions	

Reaction Type	Example
Suzuki–Miyaura Reactions	
Buchwald-Hartwig Reactions	
Diels-Alder Reaction	
Nucleophilic Aromatic Substitution	
Multicomponent Synthesis	

### 1.2.3 Microwave Units and Equipment

When the field of microwave organic synthesis started to emerge, most reactions were performed in domestic microwave ovens modified by the researchers. However, due to the increasing trend of microwave synthesis studies, dedicated microwave units have been developed which features better control and measurements of temperature, power, pressure, and ensures safety.<sup>5, 46</sup> A microwave reactor is composed of a magnetron which generates the microwave, a waveguide that transmit the microwave, and a cavity in which the microwave is resonated and energy is coupled.<sup>31</sup> Different modes can be generated depending on how the energy is coupled inside the cavity. Microwave reactors can in turn be classified into two general types. The multimode reactors are like kitchen microwave ovens and can generate power up to 1000 to 1600 watts, but require rotation of the cavity because of the highly inhomogeneous energy field they generate. The low power density also prevents small-scale synthesis (< 3 mL) inside multimode reactors. Therefore, most of the lab scale processes right now are performed in single-mode reactors, where the energy field is relatively homogeneous and high in density.<sup>5</sup>

Single-mode microwaves generally have a more accurately designed waveguide that directs the irradiation waves to a confined cavity at a fixed position in which the reaction sample is loaded. Several companies provide single-mode microwave reactor units for lab-scale organic synthesis.<sup>5, 15</sup> The waveguides of the models come in different shapes that direct the irradiation into the cavity through different geometries (Figure 1.3). Different units also include different features of control and different formats to process the reactions. In general, single-mode microwave units can provide power output up to 300 to 400W and can operate either under constant power output, or use the power output to regulate the temperature or pressure of the reaction with the help of temperature sensors, pressure sensors, and a control program. The reaction vials are placed in the cavities and are usually irradiated one at a time. The volume of the vials can range anywhere between 0.2 mL to 80 mL. Although some units allow the reactions to run under open-vessel conditions, most units use vials designed with a sealed cap that allows the reaction pressure to go up to around 20 bar. In order to increase the speed of this type of batch-wise experiment, several companies offer integration of an automated system, where a robotic gripper can be used to handle a set of vials. The only commercial single-mode microwave units that can run reactions in flow are the CEM Voyager® systems. These microwave units come with reactors made out of glass or Teflon coils, and can be run in continuous flow or stop flow mode (Figure 1.4). The reactors come in volumes of 10 or 80 mL and can allow flow rates up to 20 mL/min. The operation limit is 250 °C and 17 bar.<sup>5</sup> In addition to the above features, microwave units often come with a compressed-air cooling application that can be used to cool the sample after the reaction or to achieve simultaneous cooling of the reaction vessel while the samples are being heated up by microwave irradiation.

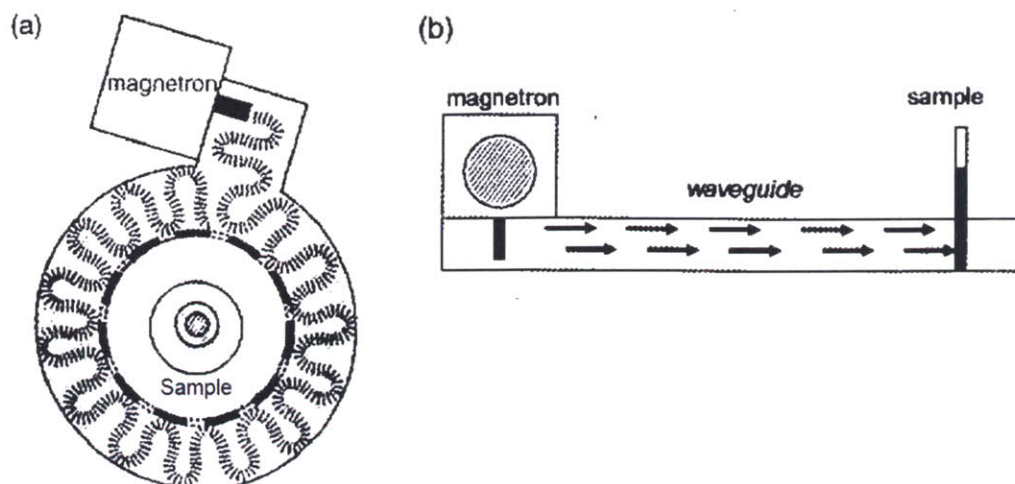


**Figure 1.3: Different shapes of waveguides in single-mode microwave units: (a) Circular waveguide in CEM Discover. (b) Rectangular waveguide in Biotage Initiator.<sup>5</sup>**

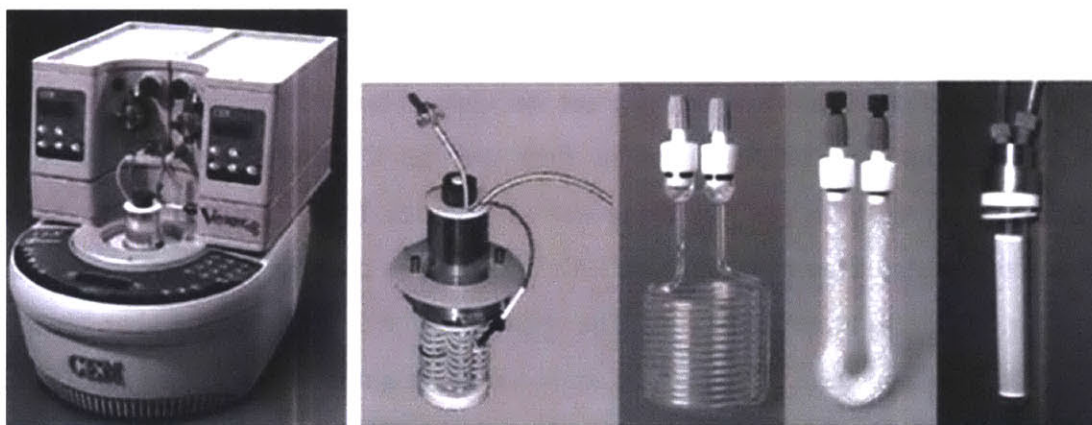


**Figure 1.4: CEM Voyager® continuous flow system and its different reactors.<sup>15, 47</sup>**

Accurate temperature measurement is a crucial task in conducting microwave reactions and has been a challenging issue in the design of a microwave unit. Traditional temperature sensors such as thermometers and thermocouples cannot be used as they will couple with the electromagnetic field. Most microwave units include a built-in IR sensor to detect the temperature of the reaction from a fixed distance. The sensors are mounted at different positions for different models, for example, the sensors in the CEM Discover® units are positioned at the bottom of the cavity while the ones in the Biotage Initiator® units are placed in the cavity wall. The main disadvantage of the IR sensor is that it reads the temperature of the outer wall of the reaction vessel instead of the actual reaction mixture. Because the reactor vessel is usually

microwave-transparent and the solution heats up directly under microwave heating schemes, the IR reading will often be lower than the actual reaction temperature. The results obtained by the inaccurate temperature readings thus need to be treated carefully especially when compared with the data from conventional heating schemes.<sup>39</sup> Another common alternative to IR sensor is a fiber-optic sensor which can detect the internal temperature of a reaction. The CEM Discover® model has a fiber-optic temperature measuring option. The fiber-optic can provide a more accurate temperature measurement even though its range of detection is smaller and is sensitive to mechanical stress.<sup>39</sup> Still, because of the inhomogeneous heating field inside a microwave reactor, several studies have tried to use thermo-vision cameras to monitor the whole temperature scheme inside a microwave reactor.<sup>28</sup>

#### **1.2.4 Microwave Synthesis in Continuous Flow**

Most microwave reactions in current studies are run in batch mode. However, because of the scale-up issues involved with batch reactions and the interest in increasing the speed for high-throughput synthesis and reaction screening, several studies have been made on performing microwave reactions in continuous flow.<sup>14, 16</sup> Most of these studies used microwave-transparent tubes in different configurations to conduct the continuous flow.<sup>18-21</sup> For the interest of this thesis, examples of continuous flow in microfluidic scales (channel diameter < 1mm) are summarized below.

The Haswell group designed a microfluidic glass block composed of two pieces of glass: a glass piece with three inlet/outlet holes connected with a bottom piece that has a channel that was 1.5mm wide, 50 or 80µm deep, and 15mm long (Figure 1.5). The channel was coated with heterogeneous Pd-supported catalyst to perform Suzuki cross-coupling reactions. Reactants were pumped into the reservoirs by a syringe pump connected through peek tubing. The whole block was placed inside a single-mode microwave cavity with an IR sensor at the bottom.<sup>48-49</sup> Another design from the same group is a U-shaped capillary glass tube (Figure Figure 1.5) with an inner diameter of 800µm. The bottom of the tube was filled with catalyst particles held into place by two glass rods. Suzuki cross-coupling reactions were also successfully carried out.<sup>20</sup>

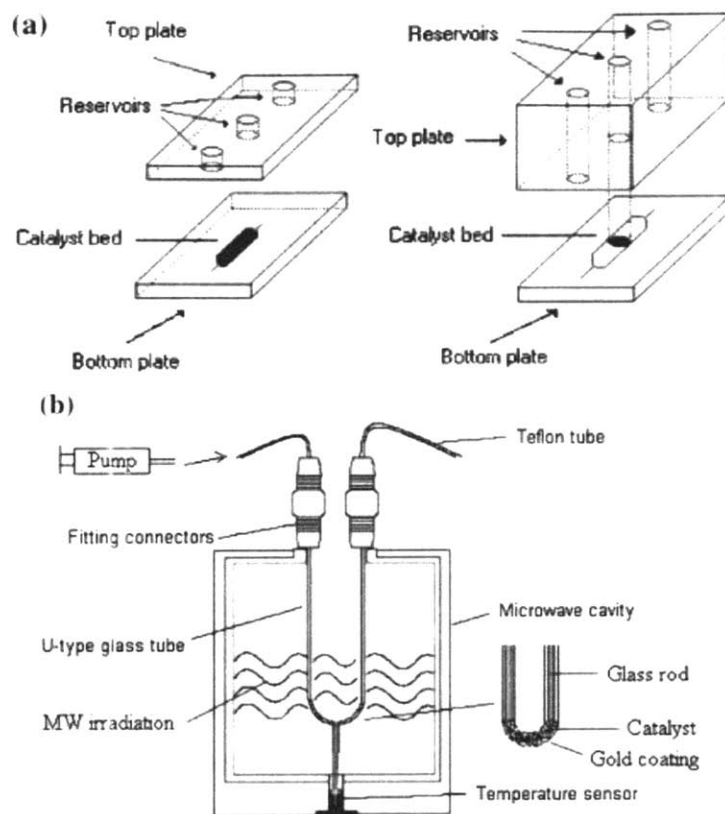


**Figure 1.5: (a) Microreactor, and (b) capillary reactor designed by the Haswell group for Suzuki cross-coupling reactions.**<sup>48-49</sup>

Michael Organ and co-workers assembled a capillary flow system where three inlet tubes merged to a single capillary glass tube that went through a single-mode microwave cavity and delivered the outlet to collection (Figure 1.6).<sup>19</sup> The capillary tube could be changed for an inner diameter between 200 to 1150 $\mu\text{m}$ . The reaction temperatures were detected by an IR sensor mounted on the walls of the cavity. Many homogeneous reactions had been successfully demonstrated with the design, including Suzuki-Miyaura Couplings, ring-closing metathesis reaction, nucleophilic aromatic substitution, and Wittig reactions. To increase the throughput of reactions, a parallel capillary system was modified from the first design (Figure 1.6). The assembly consisted of four parallel capillaries in to microwave chamber which each had two inlets feeding reactants to it. The system could perform combinatorial synthesis for a small compound library. A 2 $\times$ 2 array of nucleophilic aromatic substitution products was created in a single run with the parallel set up; and a 2 $\times$ 4 array was produced in two sequential runs.<sup>18</sup> The same group also developed methods to deposit thin Pd films on the interior wall of the capillary



tubes. The application was successfully used to conduct and study Suzuki, Heck, and Diels-Alder cycloaddition reactions.<sup>6-7</sup>

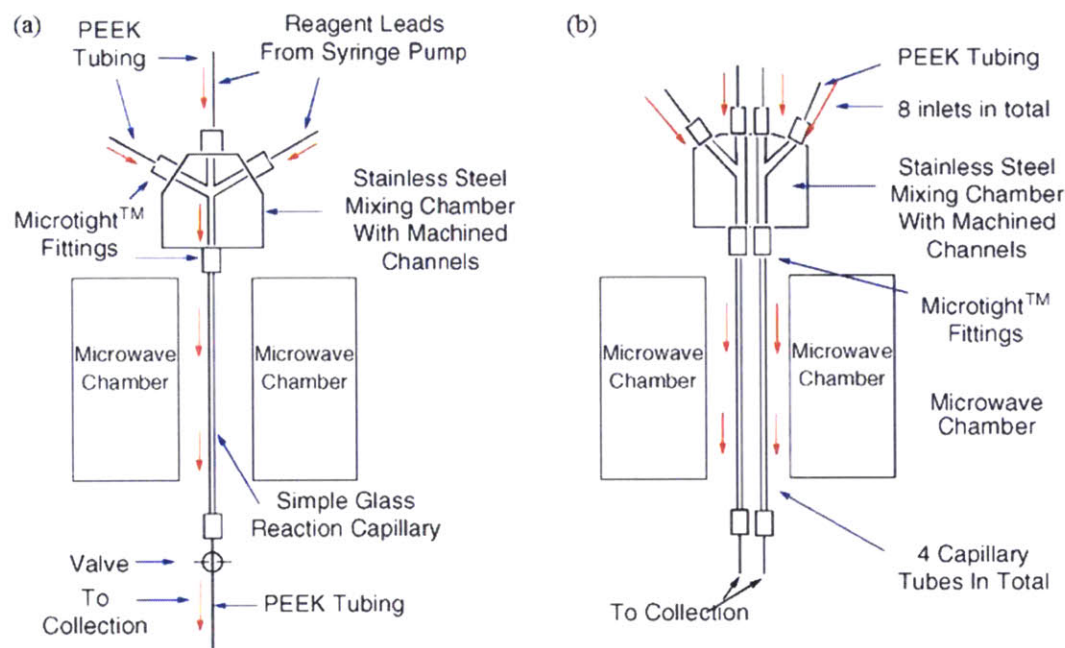


**Figure 1.6: (a) Single capillary reactor system and (b) parallel, capillary multireactor system for continuous flow microwave reaction designed by the Organ group.<sup>18-19</sup>**

The Bagley group designed a simple flow reactor by filling a standard 10 mL glass tube with sand that is held between two drilled porous frits (Figure 1.7).<sup>50-51</sup> The reaction mixture is pumped to the bottom of the tube and passes through the void in the sand that is effectively a network of microchannels. The hydrolysis of 4-(chloromethyl)thiazole and a Fischer indole synthesis of phenylhydrazine and cyclohexanone were used to test the reactor. In addition, a Bohlmann-Rahtz pyridine synthesis was carried out to compare the energy efficiency of the reactor with batch processing and a commercial Teflon coil reactor for continuous flow (Figure 1.4), and Bagley's reactor demonstrated the best heating efficiency.<sup>51</sup> A similar flow cell was used in the Kappe group where 2 mm glass beads were used to pack the Pyrex tube instead of sand.<sup>52</sup>

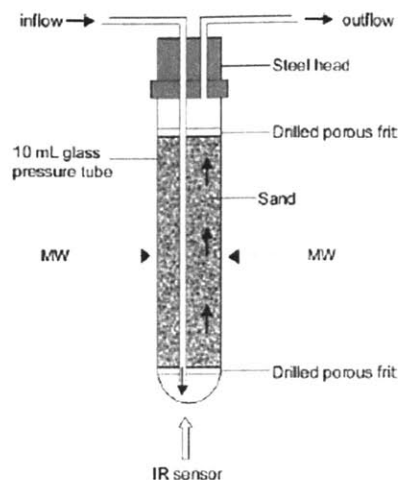


**Figure 1.7: Schematics of the sand-filled flow cell designed by the Bagley group.<sup>51</sup>**

## 1.3 Glass Microreactor Fabrication

### 1.3.1 Glass Microreactor Fabrication

Borosilicate glass, commonly known as Pyrex, is the standard material for glassware used in chemical synthesis. Many microreactor systems have been fabricated from this material because of its high chemical inertness and optical transparency.<sup>53-56</sup> Depending on the source of the glass substrate, borosilicate glass contains different components of impurity in addition to the main SiO<sub>2</sub> component.<sup>57-58</sup> Therefore, standard deep reactive ion etching (DRIE) techniques used on silicon cannot be used on glass.<sup>58</sup> Although several studies have been made on the development of special dry etch techniques to create deep, vertical channels in glass,<sup>57, 59-60</sup> the standard process of glass fabrication is still using photolithographic wet etching method.<sup>53-54, 61</sup>

The general procedure of wet etching glass is shown in Figure Figure 1.8. A glass substrate is first cleaned and polished. A layer of gold or chrome is then deposited onto the substrate. This layer act as an adhesive to ensure good contact with the photoresist that is later coated on. The channel features are then exposed on the photoresist using an UV lamp and photomask containing the channel patterns. The exposed photoresist is then developed, followed by etching of the exposed metal layer. The glass substrate is then wet etched by a HF solution. After the glass is etched to the desired depth, the photoresist and metal layers are stripped off. The glass substrates can then be bonded to another glass plate through various bonding techniques. Inlet and outlet holes to the channels can be drilled on either piece of the glass.

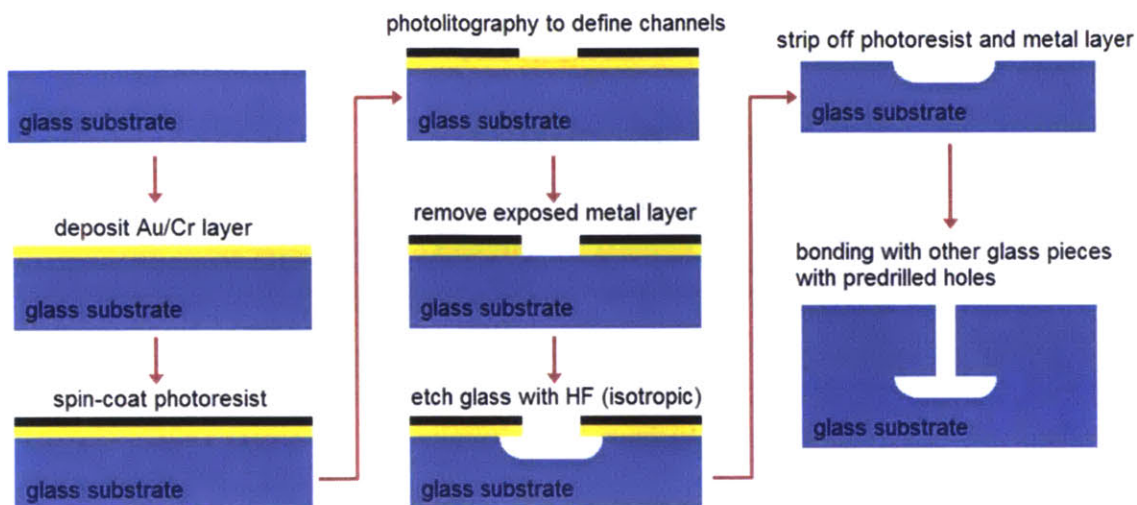


**Figure 1.8: Schematic of microfabrication in glass.**

The etching of glass with HF is isotropic; therefore the etched depth to width ratio is usually 1:2 to 1:3. Dimensions of the channels can be adjusted by the width of the channels on the photomask, but the resulting channels all have a longer width compared to their depth. This limits the feature density that can be inserted into glass substrates.<sup>56</sup> The etching rate of the HF depends on the concentration and composition of the solution and the source of substrate used; reported etching rates vary between  $0.063\mu\text{m}/\text{min}$  to  $13\mu\text{m}/\text{min}$ .<sup>62-64</sup>

The inlet and outlet holes to the reactor channels can be drilled by various methods. Diamond-tipped drill bits can be used with a manual mill or a CNC mill to drill the holes.<sup>62</sup> Ultrasonic sandblasting is also another option where up to hundreds of holes can be drilled at the same time and holes as small as  $10\mu\text{m}$  can be achieved. For CNC drilling, W. H. Grover has written a software that can read in a DXF file containing the desired hole locations and create language codes like G-code for a programmed mill.<sup>65</sup>

Numerous glass-glass bonding techniques have been developed. Several of these include bonding glass pieces at room temperature or relatively low temperature using high pressure and various adhesives, such as sodium silicate, UV-curable glue, and epoxy glue, between the bonding pieces.<sup>64, 66-67</sup> Grove *et al.* employed a DuPont C-20 FEP Teflon film into a bonding process.<sup>62</sup> The film is able to form adhesive once heated up but does not lose the chemical inertness of the Teflon material. The Teflon film was placed in between the two bonding glass plates and a pressure around 7MPa was applied to the assembly. The assembly was then heated up in an oven at  $90\text{ }^\circ\text{C}$ . This type of bonding with a piece of film allowed the authors to etch

different features on both pieces of glass and use them as microfluidic membrane valves and pumps (Figure 1.9).<sup>62</sup>

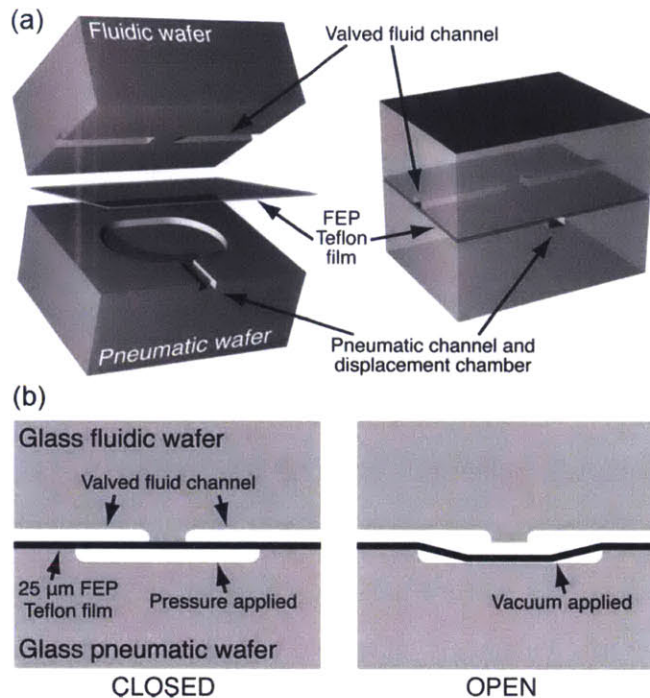


**Figure 1.9: Glass-glass bonding with FEP Teflon film to create membrane valves. (a) The exploded and assembled illustration of the bonding pieces. (b) Cross-sectional schematic the operation of a single valve.**<sup>62</sup>

However, low temperature bonding often results in weaker bonding strengths and the adhesives or glues may clog channels that are especially shallow.<sup>67</sup> An alternative is thermal bonding at high temperatures above 550 °C, which is around the glass transition temperature for Pyrex. In general, the procedure in this method is to clean the two pieces of bonding glass with Piranha solution (a mixture of 3:1 concentrated sulfuric acid to 30% hydrogen peroxide solution), sandwich the pieces in between two flat blocks made of material that can withstand the furnace temperature and not bond with the glass pieces, and heat the assembly up in a furnace. Once a bonding succeeds in this process, the glass pieces will become as one whole piece of glass block. The success of thermal bonding highly depends on several factors: the cleanness and flatness of the glass substrates, the bonding temperature, the heating time, the rate of cooling down, and the material and weight of the blocks. Therefore, different recipes have been developed.<sup>54, 61, 63-64</sup> The Han group has developed a method in which the glass surfaces can be chemically activated by ammonium hydroxide and form a temporary bond before placed in the furnace.<sup>64</sup> The bonding

succeeded without any blocks placed on top of the glass pieces. Therefore, the channels will not distort as much when the glass material is softened under high temperature, making this process extremely attractive for nano-scale channels (depth < 10  $\mu\text{m}$ ). The Kitamori group was able to thermally bond 11 pieces of glass together under 650  $^{\circ}\text{C}$  for 5 hours while using alumina plates as sandwich blocks (Figure 1.11).<sup>54</sup> They reported that the bonding procedure for 11 pieces of glass were just the same as for two. The pile-up reactor, which contained ten layers of channel features, was tested with an amide formation reaction and resulted in favorable yields. The maximum flow rate that can be achieved was ten times higher than that of a single layer glass reactor, demonstrating a higher throughput.

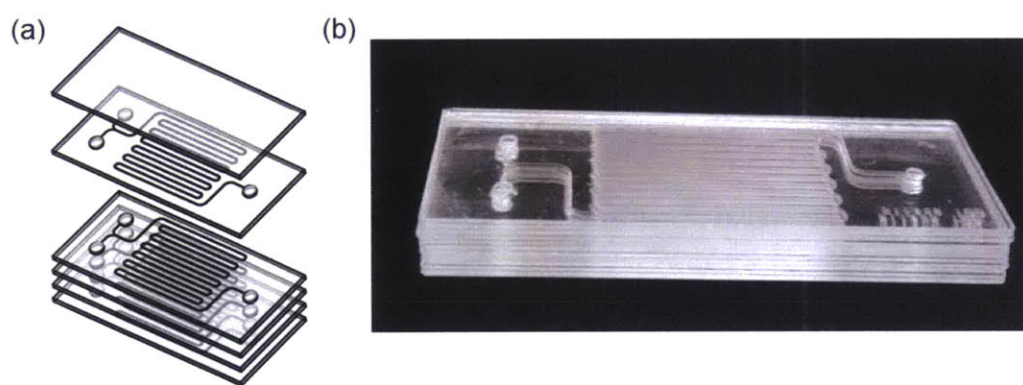


**Figure 1.10: (a) Schematic of three-dimensional channels in the pile-up reactors aligned for thermal bonding. (b) Photograph of the ten-layer, pile-up reactor.**<sup>54</sup>

### 1.3.2 Packaging Techniques

Several packaging schemes used for glass reactors are available. Compression packaging is one option. The Kitamori group used a plastic holder to sandwich their reactors with screws.<sup>54, 61, 63</sup> The holder had threaded hole for inlet and outlet tubing. The tubes were glued to Teflon screws and screwed down the threaded holes of the holder. O-rings were placed in between the glass piece and the screws to ensure sealing (Figure 1.11).

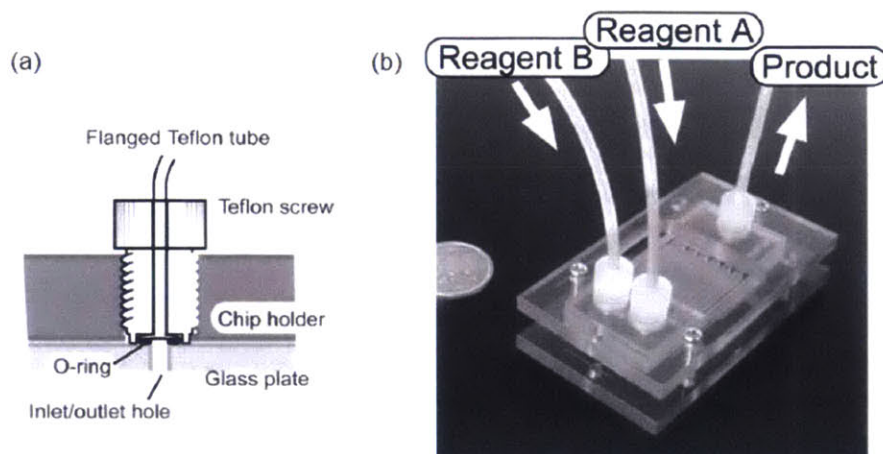


**Figure 1.11: Compression packaging of glass reactors in the Kitamori group: (a) Cross-sectional schematic of the tube connection. (b) Photograph of the pile-up glass reactor with tube connections.<sup>54</sup>**

Tubes can also be sealed directly with inlets and outlets of reactors. Our lab has developed glass brazing techniques to connect capillary glass tubes with reactors (Figure 1.12).<sup>68</sup> The silicone reactors had inlet and outlet holes on the side, and the capillary glass tubes were connected by heating up a sealant glass powder at the interface of the connection. The powder sealed the tubes to the reactor once it melted, and the capillary tubes were able to connect with other tubes, such as FEP or PEEK tubing. This technique allows the tubing to be connected to the side of the reactors. The key requirement in this process is that the thermal expansion coefficients of the reactor, tubes, and brazing powder have to be similar in order to minimize thermal expansion stresses.

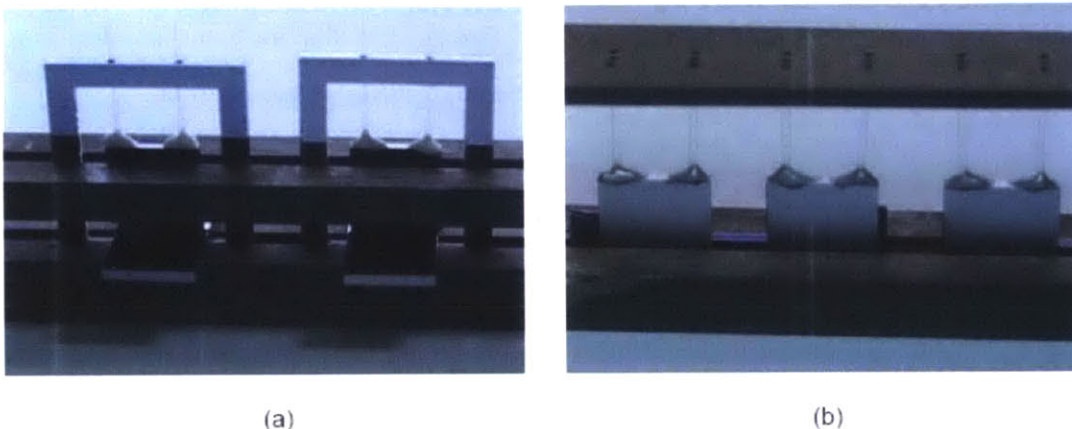


**Figure 1.12: Reactor setup for glass tube brazing procedure.<sup>68</sup>**

## 1.4 Thesis Overview

The goal of thesis research is to engineer microreactors that can perform microwave reactions with rigorous experiments in order to obtain a better characterization of microwave effects and to harness the benefits of microwave heating. The following summary provides the roadmap to both this research and the thesis:

Chapter 2 describes the design of the first microreactor setup. This chapter includes the selection of microwave unit, the choice of material and fabrication method, and the details of the geometry configuration. The chapter also includes the validation chemistries and kinetic analysis done with the microreactor, from which heating issues were discovered.

Chapter 3 provides the background, procedure, and results of the microwave simulations. Due to the heating issues described in Chapter 2, microwave computational models were set up for a better understanding of the microwave heating pattern. The computational models combine electromagnetic radiation, heat transfer, and fluid dynamics mechanisms to simulation the microwave heating pattern. The simulation results provide explanations to the heating challenges and were used to design a second microreactor setup.

Chapter 4 includes the design and simulation of the improved microreactor. The changes in design will be explained from the understandings obtained in Chapter 3. This chapter also includes the simulation results of the final reactor design in order to confirm the microwave heating outcome and to establish temperature estimations of chemistry reactions that will be describe in Chapter 5.

Chapter 5 details the chemistries performed with the final reactor design. A kinetic analysis and a screening reaction are demonstrated. The chapter also includes a simulation model of the spiral reactor with flow to reflect the experimental finding in this chapter.

Chapter 6 concludes the main results and important findings from this thesis research. Future directions of studies in microwave chemistry with microreactors are also suggested.



## CHAPTER 2. INITIAL SYSTEM DESIGN

---

### 2.1 Introduction

The first stage of this project was to design a microreactor system that can perform microwave reactions in continuous flow. This included creating a microreactor, integrating it into a microwave unit, and achieving precise temperature, pressure, and power control. Validation chemistries were ran with the initial system to test the reactor performance in terms of pressure limitations, mechanical stabilities, and accuracies in temperature measurements. The chemistry results revealed heating issues with the initial design, including uneven temperature distribution across the reactor, unexpectedly low heating rates that led to temperature limits, and changes in the heating pattern when the reactor position was altered.

### 2.2 Discover Microwave Unit

The Discover® 1 unit from CEM Corporations was chosen for our studies (Figure 2.1).<sup>69</sup> The unit has an opening at the top designed for open-vessel reaction and a metal attenuator is used to prevent microwave leakage. This opening allows tubing connecting into the microwave chamber for a continuous flow setup.

The microwave module is a single-mode unit with a circular waveguide, in which the microwave radiation enters the chamber/cavity from the side walls (Figure 2.1(b)). The magnetron generates the microwave at a variable power setting at the end of the waveguide. The magnetron is angled at a position such that the electric field would be perpendicular to the waveguide wall. The cross-section of the waveguide at the point of microwave entry is the microwave port.<sup>70</sup> The cavity is about 90 mm deep and 70 mm in diameter, the waveguide is about 20 mm wide, and the attenuator is about 80 mm long and 40 mm in diameter. The cavity is where the samples are held and heated up, and the samples are usually put into a glass tube and placed into the cavity from the top of the attenuator. The unit is connected to a computer where the Synergy™ software developed by the company can be used to program the unit and monitor the reaction parameters, including the temperature, pressure, operation time length, and power output. There are two settings to operate the microwave unit: the first is the constant power

setting, in which a fixed power will be generated from the magnetron during the operation; the second is the constant temperature setting, in which the microwave software will adjust the power outputs to reach and maintain the measured temperature at a value set by the operator. The maximum power the unit can provide is 300 W, and the temperature detection range is 0 - 300 °C.

The unit comes with two temperature sensing devices: a built-in IR sensor at the bottom of the microwave chamber (Figure 2.2) and an external fiber optic temperature sensor (Figure 2.4). The IR sensor is a non-contact detection method, while the fiber optic sensor reads the temperature of the material it is in contact with. The fiber optic temperature sensor consists of a control box and a long blue probe about 1.5 mm in diameter. The probe is sheathed in inert plastic and has two polished mirrors at its tip that are separated by an air gap about 1-inch long. Light is passes though the mirrors at the tip of the fiber optic probe and reflected back to the sensor's control box. When the tip is heated up, the length of the air gap will change and shift the phase of the return light. The differences in light signal correspond to different temperature readings and are calibrated for temperature measurement in the microwave unit's software.<sup>71</sup>

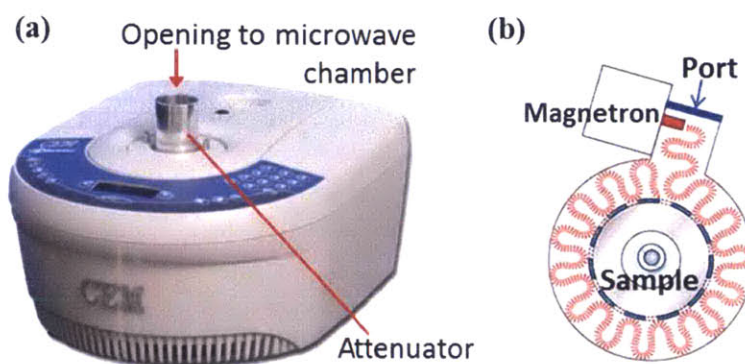


**Figure 2.1: CEM Discover® 1 unit used for this research: (a) Front view of the unit. (b) Schematic of internal microwave configuration view from the top.<sup>47</sup>**

### 2.3 Microreactor Setup and Fabrication Methods

Due to the configuration of the microwave unit, the microreactor was designed to enter the cavity vertically downwards from the top opening to receive the irradiation from the side of the walls (Figure 2.2). In this arrangement, the IR temperature sensor at the bottom cannot detect the temperature on the glass surface, and therefore, the fiber optic probe was used for the setup. In order to minimize the amount of irradiation on the packaging material and to increase the area

of the channels that is irradiated, the microreactor was designed into a thin, long shape: the top part of the microreactor with the packaging would be in the attenuator, while only the reactor channels would be in the microwave cavity (Figure 2.2).

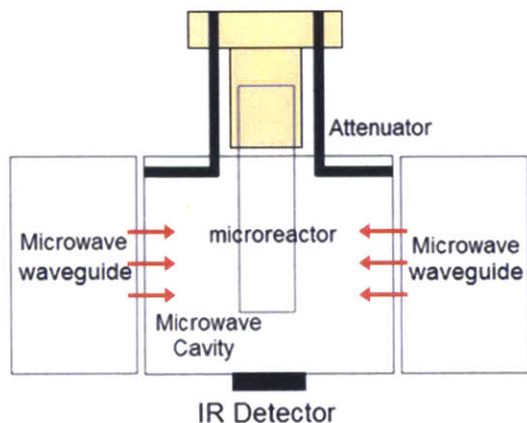


**Figure 2.2: Side view of the microreactor fitting into the microwave unit. Red arrows depict the direction of microwave irradiation.**

The material of the microreactor had to be chemically inert and microwave transparent. Although standard silicon microreactors in our lab demonstrated many advantages for microfluidic organic synthesis,<sup>56, 72</sup> preliminary testing of heating these reactors in a microwave unit showed that the silicon material is strongly microwave absorbent, reaching 187 °C in 5 minute with a low power microwave irradiation of 5 W. Therefore, glass was chosen as the reactor material.

The reactor was made from a commercially available 6-inch square, 0.7-mm thick borosilicate glass wafer that was pre-coated with a 120 nm chrome layer and a 500 nm photoresist layer.<sup>69</sup> The wafers were wet etched with 49 % HF solution to produce reaction channels that are about 400  $\mu\text{m}$  in width and 160  $\mu\text{m}$  in depth. The inlet and outlet holes were drilled with a 0.039-inch diamond drill bit and a CNC mill. The finished glass pieces were cleaned with Piranha solution and thermally bonded together by compression under 650 °C in a furnace. This method fused the two pieces of glass together into a single glass block that could withstand at least 250 psi of pressure. Details of the fabrication procedures and recipes are recorded in Appendix A.1.

The reactor is 30 mm wide, 101 mm long, and 1.4 mm thick (Figure 2.3). The inlet and outlet holes are 1 mm wide in diameter. There are two inlets that merge together and pass

through a short serpentine-shaped mixing zone and then enter the long U-shaped reaction channels at the bottom half of the reactor. The reaction volume is 280  $\mu\text{l}$ , and the mixing zone is 20  $\mu\text{l}$ .

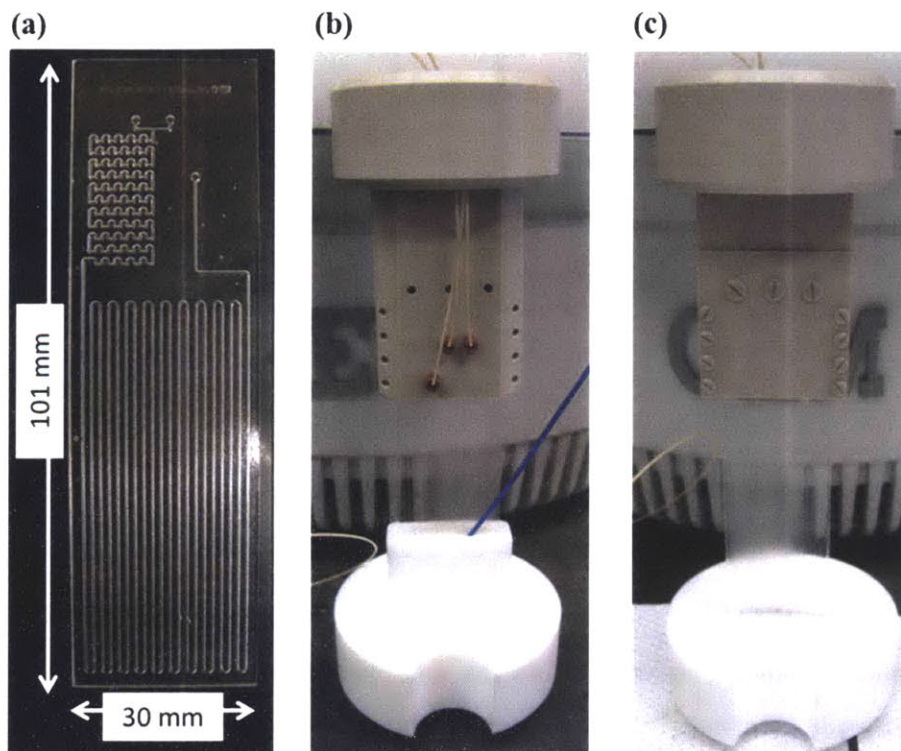


**Figure 2.3: 1<sup>st</sup> generation of microreactor: (a) Microreactor without packaging. (b) Packaging of microreactor with PEEK assembly and Teflon holder for the fiber optic temperature probe. (c) Backside of assembly with PEEK screws.**

The packaging assembly connects the reactor to the inlet and outlet tubing for continuous-flow reactions. The packaging is located in the microwave attenuator and is subjected to certain degrees of microwave irradiation. Therefore, the packaging needs to exhibit both high chemical compatibility and microwave transparency, withstand the operation temperature and pressure, and ensure sealed connection of the reactor with the tubing. Polyether ether ketone (PEEK) was thus chosen as the material for a compressed packaging configuration: a PEEK block was machine with a sitting for the reactor and three standard 6-32 ports for Upchurch Scientific® MicroTight® fittings for the tubing connection; another PEEK sheet was drilled with screw holes, and the reactor was sandwiched between the two PEEK pieces with PEEK screws (Figure 2.3 (b)(c)). The assembly was then screwed onto a disc-shaped PEEK block that was machined to fit on top of the attenuator, hanging the microreactor into the microwave cavity

from the microwave unit opening. The microreactor is therefore set at a fixed height, but the PEEK disc can rotate on the attenuator and change the direction of the microreactor surface within the cavity. The red MicroTight® headless fittings connect the reactor to Upchurch Scientific® PEEK™ Tubings, which have a 1/32 inch outer diameter and 0.015 inch inner diameter.

A Teflon® holder was machined to hold the fiber optic probe firmly onto the reactor for temperature measurement (Figure 2.3 (b)). The holder is about 36 mm wide, 20 mm long, and 14.5 mm thick. A 30 mm wide and 1.4 mm thick hole is cut through the holder for the reactor to pass through, and a 1.5 mm round slit was made to fit the fiber optic probe (Figure A.5). During future reactions, the holder and the tip of the fiber optic probe were positioned around the center of the microreactor.

Figure 2.4 shows the layout of the entire microreactor setup for microwave continuous flow synthesis: Harvard Apparatus syringe pumps are used to inject the reaction solutions into the microreactor, which is positioned in the microwave chamber by hanging onto the microwave attenuator. An Upchurch Scientific® back pressure regulator with the required pressure rating is connected to the outlet. The microwave operations are monitored by the fiber optic sensor and the Synergy™ software.

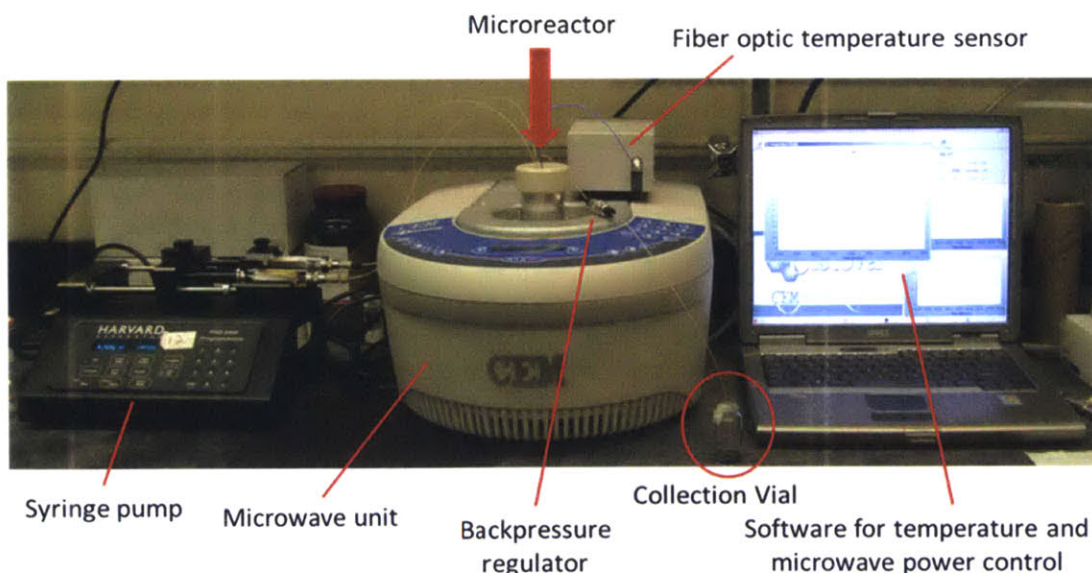
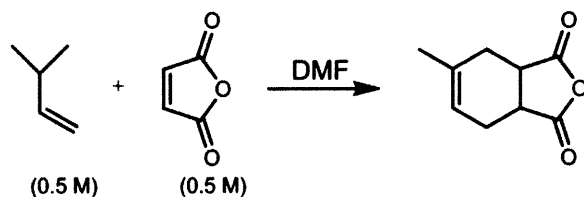


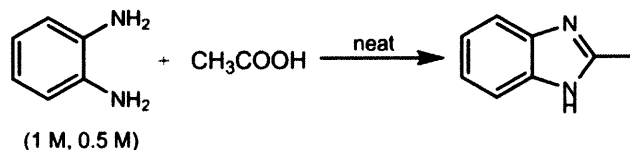
**Figure 2.4: Microreactor setup for continuous-flow microwave synthesis.**

## 2.4 Validation Reactions

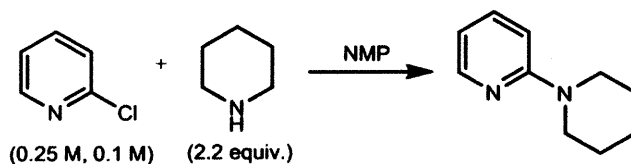
The new setup was tested with three reactions found in literatures: a Diels-Alder reaction between isoprene and maleic anhydride in dimethylformamide (Scheme 2.1), a condensation reaction of *o*-phenyldiamine and acetic acid (Scheme 2.2), and an aromatic substitution of 2-chloropyridine with piperidine in N-Methyl-2-pyrrolidone (Scheme 2.3). These reactions were chosen to assess the microreactor because they are straightforward and no side reactions have been observed in previous studies.<sup>73-76</sup> The kinetics of the first two reactions has also been reported in the literature and provides a basis for the temperature and expected conversion calculations.<sup>73, 75</sup> The latter two reactions were also run with a microreactor heated by a cartridge heater to compare the results between microwave heating and conventional heating.



**Scheme 2.1: Diels-Alder reaction of isoprene and maleic anhydride.**



**Scheme 2.2: Condensation reaction of *o*-phenyldiamine and acetic acid.**



**Scheme 2.3: Aromatic substitution of 2-chloropyridine with piperidine.**

All reactions were run under set temperature mode, in which the microwave software was allowed to automatically adjust the radiation power to reach the target temperature. The syringes were set to flow at the lowest flow rate (longest residence time) at the same time the microwave was turned on until the reactor reached steady-state at the target temperature (temperature oscillation maintained within  $\pm 5$  °C of the set temperature.) Then the pump flow rate was adjusted for different residence time for data collection. Each data point was collected after

purging at least 2 times the reactor volume through the outlet. Further experimental details are listed in Appendix A.4.

The Diels-Alder reaction was run at 80 °C, 90 °C, 100 °C with residence times of 3, 5, and 10 minutes. The results show a conversion that is around 17 % to 30 % lower than the expected conversion calculated with the reported kinetic data,<sup>75</sup> which also indicates that the liquid temperature was around 10 °C to 20 °C lower than the set temperature (Table 2.1). The experiments were also highly unrepeatable in both continuous flow or batch synthesis and an accurate kinetic data could not be obtained to compare with the literature values (Appendix A.4.1). It is most likely that the volatile isoprene (b.p. 34.07 °C) evaporates too fast and accurate data for this reaction could not be obtained without an inline analysis setup.<sup>75</sup>

**Table 2.1: Diels-Alder results compared with literature data.**

<b>Reaction Condition</b>	<b>Microreactor MW Conversion (%)</b>	<b>Expected conversion from literature data <sup>75</sup> (%)</b>	<b>Actual temperature calculated from reported kinetic data <sup>75</sup> (°C)</b>
80 °C, 3 min	29.5	47.1	67
80 °C, 5 min	29.1	59.7	63
90 °C, 3 min	49.9	60.1	74
90 °C, 5 min	43.7	71.5	68
100 °C, 3 min	57.9	71.3	88
100 °C, 5 min	63.6	80.6	83
100 °C, 10 min	72.6	89.2	78

The condensation reaction was run under 100 psi back pressure at 130 °C, 150 °C, 160 °C, and 180 °C with residence times of 1, 3, and 5 minutes for kinetic analysis. The Kappe group had reported this reaction to follow a first order rate law with respect to the *o*-phenyldiamine.<sup>73</sup> The conversions from the microwave microreactor are within 6 % difference from the conversions calculated from the literature data, and the results match a first order rate law with a pre-exponential factor of  $(5.61 \pm 1.86) \times 10^5 \text{ s}^{-1}$  and an activation energy of  $66.7 \pm 1.44 \text{ kJ/mol}$ . These kinetic data are lower than the reported values of a  $3.1 \times 10^8 \text{ s}^{-1}$  pre-exponential factor and a 73.43 kJ/mol activation energy.<sup>73</sup> However, the microwave results fall within the same range of the results from the cartridge-heated microreactor, which give a  $(9.83 \pm 8.65) \times 10^5 \text{ s}^{-1}$  pre-exponential factor and a  $67.9 \pm 7.43 \text{ kJ/mol}$  activation energy (see Appendix A.4.2). It therefore seems as if that the glass microreactor could be used to obtain accurate kinetic data.

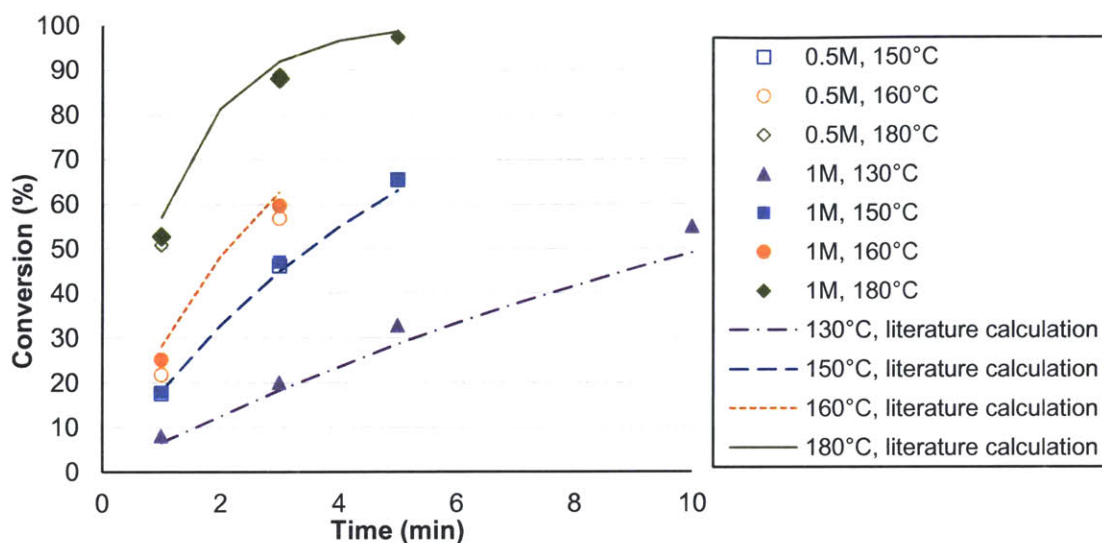


**Figure 2.5: Conversion profile for 2-methylbenzimidazole formation with first microreactor setup.**

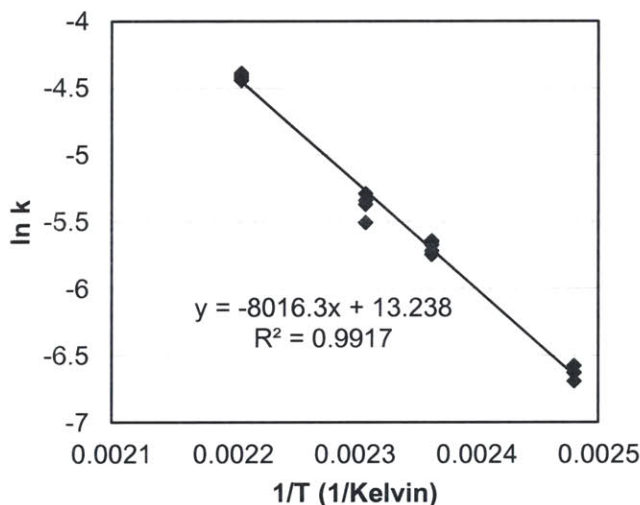


**Figure 2.6: Arrhenius plot of ln k versus 1/T used to determine the activation energy and pre-exponential factor of the condensation reaction with the results from the initial microreactor for microwave.**

However, the conversions of the aromatic substitution reaction are not as high as expected. This reaction have been reported with a 40 % yield when irradiated by microwave at 120 °C for 20 minutes under solvent free conditions,<sup>76</sup> and also a 100 % conversion when run in a steel coil reactor heated by a hot plate at 260 °C for 20 minutes in flow.<sup>74</sup> We ran the reaction under 100 psi back pressure at 260 °C and 280 °C with residence times of 1, 5, and 10 minutes.



The conversion data obtained in the microwave microreactor setup are more than a half lower than the conversions of the reaction in the cartridge-heated microreactor under the same reaction conditions (Figure 2.7). In addition, dark deposits were observed in the glass reactor channels at the area where the holder is placed (Figure 2.8). The results suggest that the fiber optic temperature sensor was not accurately measuring the temperatures of the reactions.

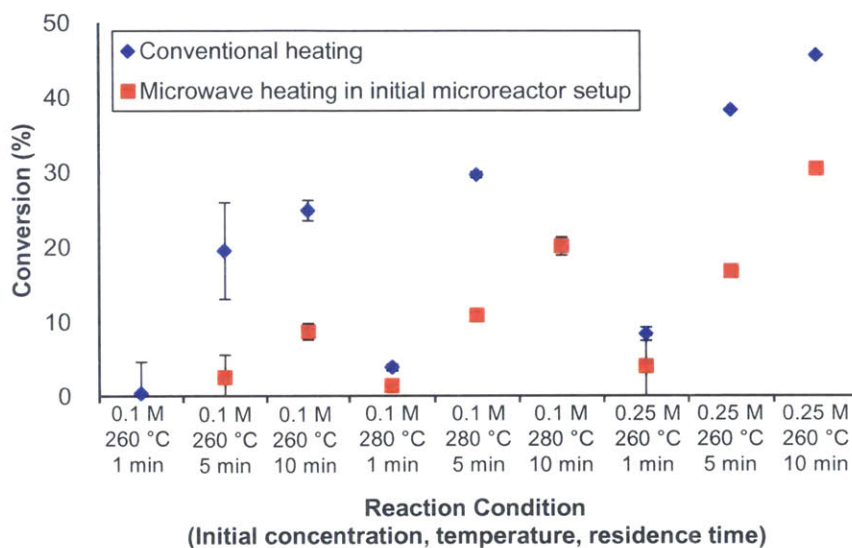


**Figure 2.7: Comparison of the aromatic substitution results from microwave microreactor and conventional cartridge heater.**



**Figure 2.8: Deposits in reaction channels after aromatic substitution reactions.**

## 2.5 Heating Issues

It was suspected that the microwave setup had lower conversions because the reaction temperatures were actually lower than the fiber optic measurements. Therefore, an external thermal couple was used to measure the reactor temperature immediately after microwaving the

reactor to the previous reaction temperatures. The thermal couple measurements show that the reactor was not heated up uniformly: in every heating experiment, the area covered by the fiber optic holder had the highest temperature while the rest of the reactor displayed a lower temperature. Figure 2.9 illustrates the temperature measurements across the reactor after heating NMP to 260 °C in the microwave: the highest temperature was at the tip of the fiber optic probe, which already cooled down drastically from 260 °C to 250 °C within seconds of removal from the microwave.

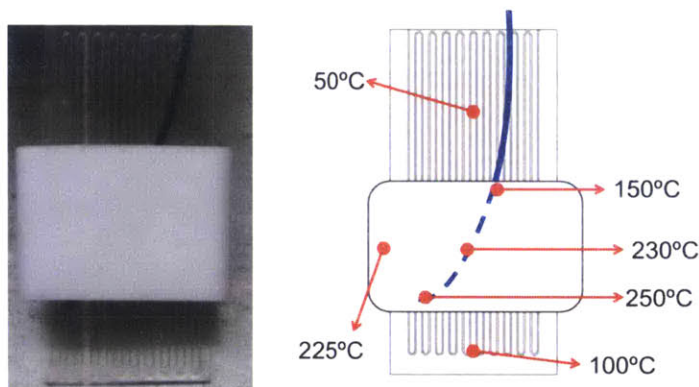


**Figure 2.9: Schematic of the reactor temperature as measured by a thermal couple after heating the aromatic substitution solution to 260 °C.**

Since the area with the Teflon holder was heating up to a higher temperature, it was postulated that the Teflon holder was absorbing more irradiation power because it had a larger size than the reactor. This issue was investigated by heating the reactor up without the Teflon holder. The fiber optic probe was taped to the reactor with Teflon tape in these heating experiments. The results showed that without the Teflon holder, the reactor did indeed heat up slower. However, even without the holder, there was the same pattern of uneven temperature distribution across the reactor: the highest temperature was always at the position about 1/4 to 1/3 of the channel length from the bottom of the reactor.

Another interesting observation of the heating experiments without the Teflon holder was that under a constant microwave power input, the reactor will reach a steady-state temperature limit. This occurred even when the liquid inside the channels were not flowing and the power was set at the equipment maximum of 300 W. The maximum temperature changes according to the input power, the types of solvents in the channel (Figure 2.10), and the angular position of the reactor (Figure 2.11). Under the same microwave power, the steady-state temperature is the highest when the reactor is parallel to the microwave port (Figure 2.1 (b), Figure 2.11 (a)). When

the reactor is rotated 90 degrees to the perpendicular-to-port position, the temperature limit is the lowest (Figure 2.11 (b)). The results in Figure 2.11 were heating experiments done with empty reactors. Even though there are no strong microwave absorbing solvents in the channel, Pyrex does has a low dielectric loss ( $\epsilon''$ , the imaginary part of the permittivity) and can still heat up under microwave irradiation.

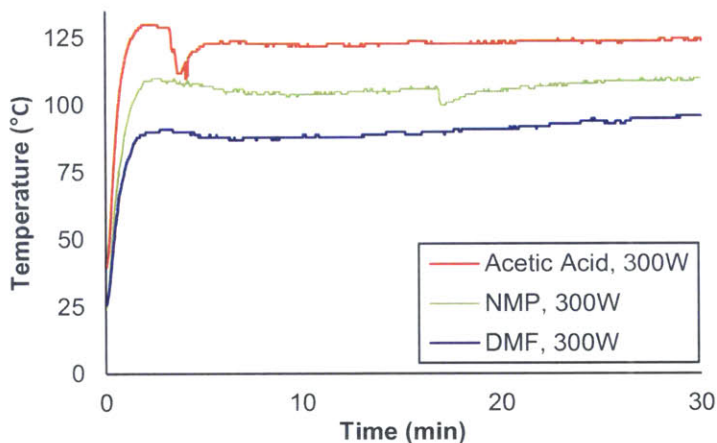


**Figure 2.10: Temperature profile at different solvents inside the microreactor irradiated at the maximum microwave power.**

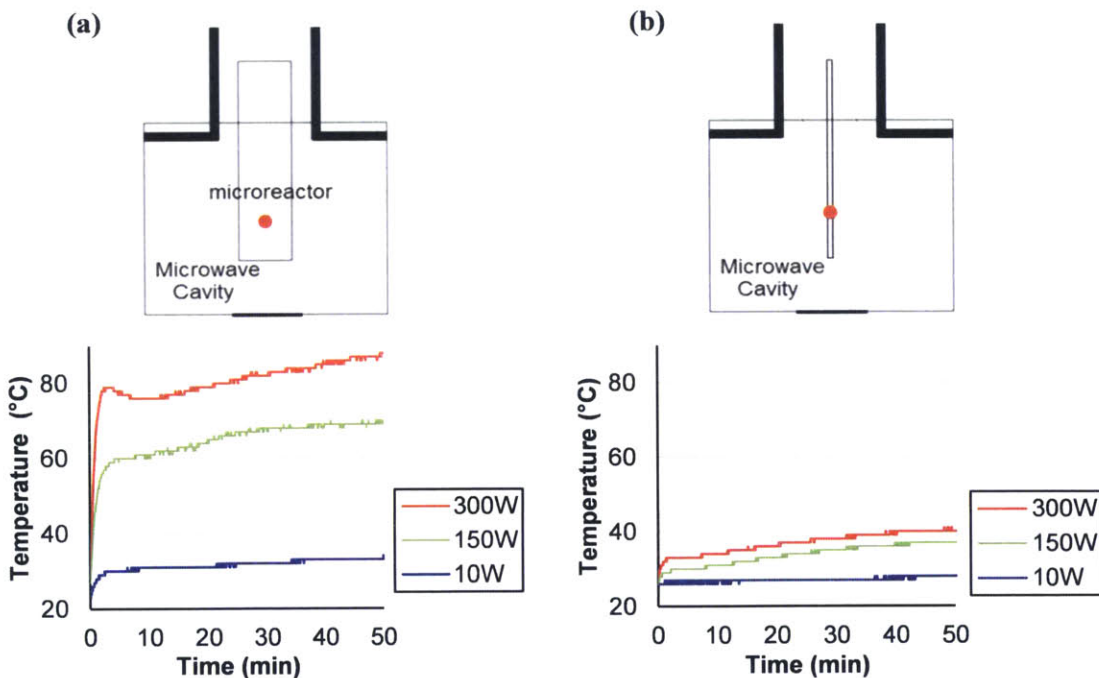


**Figure 2.11: Temperature profiles of empty reactor surface center under different microwave power irradiation at positions (a) parallel to microwave port, (b) perpendicular to microwave port.**

From these heating experiments, it can be concluded that the lower conversions occurred because a larger portion of the reaction volume did not reach the set temperature. While the point of the fiber optic probe reached the desired temperature, the uneven temperature distribution shows that only the area covered by the Teflon holder was around the temperature we aimed for, while the rest of the reactor was more than 50 °C cooler. The temperature unevenness also indicates that the center of the reactor had a higher temperature than the measured value, which might be the causing materials to burn onto the reactor and form dark deposits at the center (Figure 2.8).

In addition, the reactor temperature changes when the reactor is rotated to a different position. The unrepeatable experiments that arose during experiments were most likely due to small changes in the angular position of the reactor.

Another problem with the reactor was the temperature limit. The maximum temperatures the solvents could reach were lower or barely above the temperatures set for the validation reactions (Figure 2.10). The device needed to be altered to achieve a higher reaction temperature that is uniform across the entire reaction volume, and a deeper understanding on how microwave works was required to reach this goal.

## CHAPTER 3. MICROWAVE HEATING SIMULATIONS

---

### 3.1 Introduction

In order to tackle with the heating issues with the first microreactor, a fundamental understanding of physical principles behind the microwave irradiation and heating was required. Therefore, we simulated the microwave heating patterns inside the system with COMSOL Multiphysics®<sup>1</sup> to find the cause of the problems. The COMSOL software uses finite element methods to solve the Maxwell equations that govern the electromagnetic field and then takes the calculated heating rate to simulate the heat transfer scheme of the materials.

Several microwave simulation studies of the CEM Discover Unit have been done with COMSOL in the past few years. At the time we started our modeling, Robinson *et al.* had published a modeling study of a quartz tube and a Pyrex tube each loaded with different solvents inside the Discover microwave unit.<sup>77</sup> The study showed the temperature gradients inside the microwaved vials, demonstrating that the measured temperature changes according to the position of the temperature device. After we modeled our system and discovered the cause of the uneven temperature distribution in the system, Sturm *et al.* published a study that has the same finding as our results:<sup>78</sup> the heating non-uniformity is caused by the resonance structure inherent in microwave radiation. In Sturm's study, solvent-filled glass vials in the Discover unit were also simulated with COMSOL such as the Robinson study, but with two additional features: a magnetron model that accounts for the complex reflection scheme between the magnetron and the microwave circuit, and a fluid dynamic model to account for the convection of the solvent in the vials. The same group later published a study on the sensitivity of the heating rate on the vial's geometric parameters.<sup>79</sup> Although these studies employed the same method as us and reported similar findings, the simulations were all done on standardized glass tubes and do not fully address the unexpectedly low heating rates we encountered with the microreactor; furthermore, the simulations in the publications were all done with 2 seconds to 5 minutes of constant microwave irradiation and do not reflect the steady-state temperature limit observed in our experiments.

In our computational studies, we first performed 3D modeling on an empty reactor placed at different positions in the cavity with a steady-state electric field. The results were used to find

the cause of the low heating rate and to discover how the heating rate can be increased by the parameters in the systems. The results also explained the uneven temperature distribution and how the non-uniformity can be minimized. Later on, refined models that account for the air convection in the microwave unit were built to explain the temperature limits.

### 3.2 Theoretical Background

Electromagnetic fields are governed by the Maxwell equations, which in the time-varying, differential form are written as:<sup>31</sup>

$$\nabla \times \mathbf{E} = -\frac{\partial \mathbf{B}}{\partial t} \quad (3.1)$$

$$\nabla \times \mathbf{H} = \mathbf{J} + \frac{\partial \mathbf{D}}{\partial t} \quad (3.2)$$

$$\nabla \cdot \mathbf{D} = \rho_e \quad (3.3)$$

$$\nabla \times \mathbf{B} = 0 \quad (3.4)$$

where  $\mathbf{E}$  is the electric field,  $\mathbf{H}$  is the magnetic field,  $\mathbf{D}$  is the electric flux density,  $\mathbf{B}$  is the magnetic flux density,  $\mathbf{J}$  is the current density, and  $\rho_e$  is the electric charge density.

In the Radio Frequency Module in COMSOL, all the electromagnetic waves are solved from the Maxwell equation in the time-harmonic form, assuming a sinusoidal excitation and linear media (the polarization in the materials is directly proportional to the electric field). When the system's relative magnetic permeability is 1, the equation is written as:<sup>80</sup>

$$\nabla \times (\nabla \times \mathbf{E}) - \left(\frac{\omega}{c_0}\right)^2 \varepsilon_r \mathbf{E} = \mathbf{0} \quad (3.5)$$

where  $c_0$  is the speed of light,  $\omega$  is the angular frequency of the microwave, and  $\varepsilon_r$  is the relative permittivity of the material, and

$$\varepsilon = \varepsilon_r \varepsilon_0 \quad (3.6)$$

where  $\varepsilon_0 \cong 8.85 \times 10^{-12}$  [F/m] is the electric permittivity of vacuum, and  $\varepsilon$  is the permittivity defined in Chapter. 1 (Equation (1.1)).

The equation shows that the electric and magnetic fields strongly depends on the electrical properties of the materials under irradiation as well as the geometry of the microwave unit. The materials also determine the boundary conditions in the system. The general boundary

conditions of the electric and magnetic field inside is as follow, assuming there is no surface current in the system.<sup>80</sup>

$$\mathbf{n} \times (\mathbf{E}_1 - \mathbf{E}_2) = \mathbf{0} \quad (3.7)$$

$$\mathbf{n} \times (\mathbf{H}_1 - \mathbf{H}_2) = \mathbf{0} \quad (3.8)$$

the subscript 1 refers to the exterior of the sample, the subscript 2 stands for the interior of the sample, and  $\mathbf{n}$  stands for the outward unit normal vector from interior to exterior.

The source of the microwave radiation can be directly defined as a Port boundary condition in the Radio Frequency Module. In this boundary condition, the power of the wave excitation and the propagation mode of the waveguide are entered as the microwave source. Propagation modes are the configurations of how the microwave can travel through the waveguide, and the modes depend on the operating wavelength and polarization and the shape and size of the guide. Each mode corresponds to a cutoff frequency below which the wave cannot exist in the guide. The CEM Discover has a hollow waveguide that has a rectangular cross-section and operates at the transverse electric mode, TE mode, meaning that the electric field is perpendicular to the direction of propagation; and the size of the waveguide is designed such that it operates at the lowest cut-off frequency of 2.45 GHz, where only one mode can exist, the TE<sub>10</sub> mode.<sup>70, 81</sup>

The energy conservation inside an electromagnetic system is governed by the Poynting Theorem.<sup>31</sup> From the theorem, the equation for dielectric heating rate of all materials inside any electromagnetic system can be derived as:<sup>28</sup>

$$Q = \frac{1}{2} \omega \epsilon_0 \epsilon_r'' \mathbf{E} \cdot \mathbf{E}^* \quad (3.9)$$

where  $Q$  is the volumetric heating rate termed total power dissipation density in electromagnetic studies,  $\omega$  is the frequency of the electromagnetic radiation,  $\epsilon_r''$  is the imaginary part of the material's relative permittivity and depends on the radiation frequency, and  $\mathbf{E}^*$  is the complex conjugate of the electric field. This function for the electromagnetic heat source is already built in the Microwave Heating Interface underneath the COMSOL Radio Frequency Module. In our experiments and simulations, the only electromagnetic radiation that causes dielectric heating is the microwave input at 2.45 GHz. Furthermore, the radiative heat transfer caused by electromagnetic radiation is not considered in our simulations.

The heat transfer in the system is solved by the conservation of energy equation:<sup>81-82</sup>

$$\rho C_p \left( \frac{\partial T}{\partial t} + \mathbf{v} \cdot \nabla T \right) = \nabla \cdot (k \nabla T) + Q \quad (3.10)$$

where  $\rho$  is the material density,  $C_p$  is the specific heat capacity at constant pressure,  $T$  is the temperature,  $t$  is time,  $k$  is the thermal conductivity,  $Q$  is the volumetric heat source that is defined by Equation (3.9), and  $\mathbf{v}$  is the flow velocity vector which is zero for heat transfer in solid materials. The boundary condition for the heat transfer across the interfaces of different domains follows the energy balance, where the heat flux normal to the interfaces in the first domain must be equal to the normal heat flux in the second domain when there is no energy generation at the interface. The convective heat transfer boundary equation should apply on the interface between a solid and a fluid. The details of the heat transfer boundary conditions used will be discuss in the model descriptions in Chapter 3.3.2, Chapter 3.4.1, and Chapter 3.4.2.

Solving for a microwave heating scheme is a fully-coupled problem since the temperature is dependent on the microwave heat generation, which is dependent on the material permittivity and the electric field strength. The electric field strength also depends on the material permittivity, which is temperature dependent for most solvents.<sup>77</sup>

### 3.3 Initial Model without Air Convection

#### 3.3.1 Model Geometry

The CEM Discover Unit was taken apart for dimension measurements and internal structure configuration.

Figure 3.1 shows the magnetron connected to the end of the waveguide at the back of the unit. The waveguide circles around the cavity, forming a closed loop. The cylindrical cavity has an IR sensor at the bottom and a hole that can connect to a tube of cooling air. A Teflon ring is placed inside the cavity and has a circumference smaller than the metal wall such that there is about a 2 mm air gap in between the waveguide wall and the Teflon ring. The Teflon ring can be removed to show the structure of the waveguide wall (Figure 3.1(b)). The wall of the waveguide is made of structural steel, and the side of the wall forming the cavity has six slots opened at unevenly-distributed angles. The slots allow the microwave to travel between the waveguide and the cavity.<sup>70</sup> Both the Teflon ring and the waveguide have a hole that is about 1 cm in diameter



cut through their left side. These holes were made to allow access for external temperature sensors into the cavity if required.

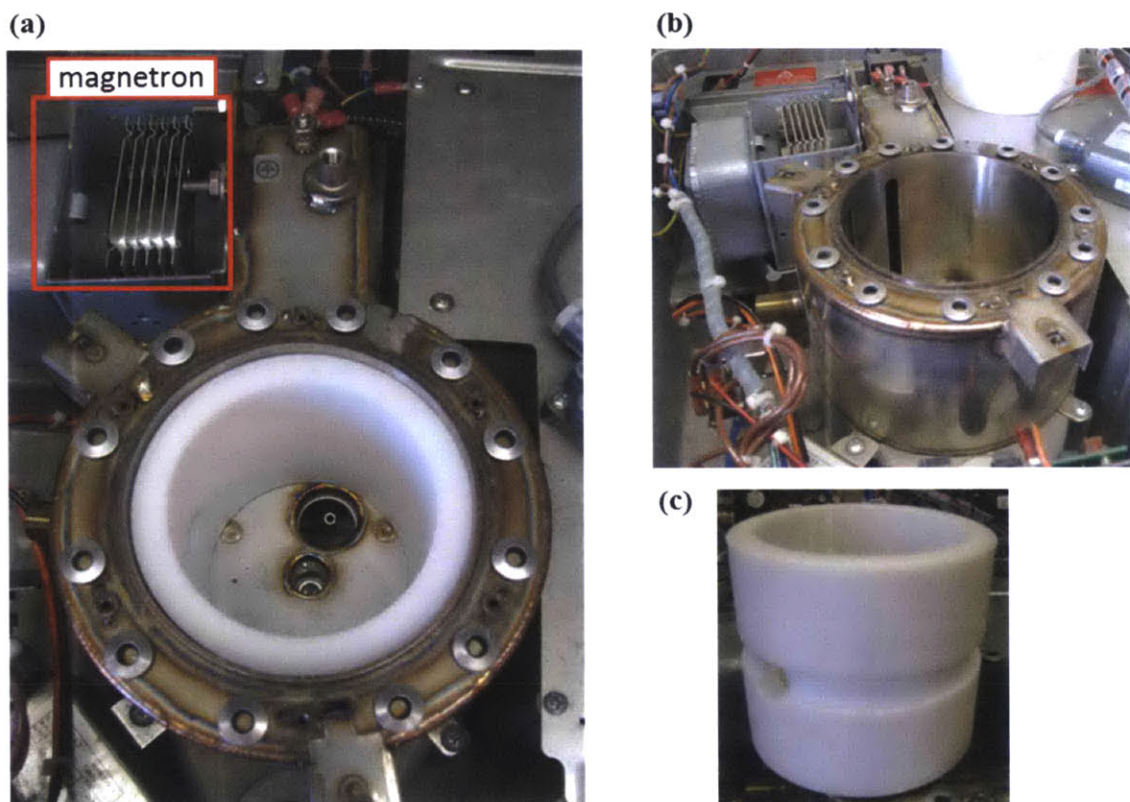


**Figure 3.1: Internal structure of the CEM Discover Unit: (a) top view of all components, (b) side view of waveguide and steel wall without the Teflon piece, and (c) picture of the Teflon component with a side hole.**

The microwave geometry was drawn directly in COMSOL Multiphysics® 4.2 with the dimensions listed in Table 3.1. The microreactor was also drawn in COMSOL with the dimensions and channel sizes described in Ch. 2. The height of the microreactor exposed in the cavity was found by measuring the reactor length from the bottom of the attenuator, which is positioned as the top wall of the cavity. The angular positions of the reactor were made by rotating the reactor at the center of the cavity (Figure 3.2). The different positions of the microreactor will be referred to by the direction of its surface to the plane of the microwave port. The microwave port is the rectangular surface at the very end of the waveguide. The magnetron, the attenuator, and the fiber optic probe were not included in the simulations.

**Table 3.1: Parameters used for microwave geometry in COMSOL.**

<b>Parameter Description</b>	<b>Value (mm)</b>
Width of waveguide	78
Height of waveguide	86
Depth of waveguide	44
Outer radius of waveguide	67
Inner radius of waveguide	48.25
Thickness of the wall	2
Outer radius of Teflon block	47.75
Radius of the cavity	37.475
Slot length of the metal wall	67
Slot diameter of the metal wall	6.5
Radius of the side hole	5.5
Height of the side hole	36
Height of reactor in cavity	58

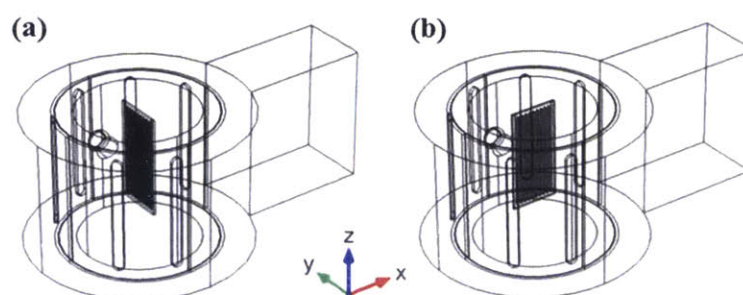


**Figure 3.2: Isotropic view of simulation geometry schematics with reactor positioned (a) parallel to microwave port, and (b) perpendicular to microwave port. (Colored axes show the directions in the simulation geometry drawing.)**

### 3.3.2 Simulation Model Description

The simulations were done with the Microwave Heating Interface in COMSOL Multiphysics® 4.2 and were all run as 3D models. The initial models were all done with empty reactors. This simplifies the computation by eliminating the need to include fluid flow inside the reactor channels and need to include the temperature-dependent permittivity of most solvents.

The exterior wall of the waveguide was built as boundary conditions with metal properties, while the interior wall connecting to the cavity was built as a three dimensional domain. The air in the cavity and the waveguide were connected to each other by the side hole, and the two areas are combined as a single domain in the model. The built-in material properties of stainless steel were used for the waveguide wall, and that of air were used for the space inside

the waveguide and the cavity. The material properties and simulation domain are listed in Table 3.2.<sup>1,77</sup>

**Table 3.2: Material electrical properties used in the simulation.**<sup>1,77</sup>

Domain Description	Material	Relative Permittivity	Electrical Conductivity (S/m)
Cavity and waveguide, reactor channels	Air	$1 - 0i$	0
Interior metal wall of waveguide	Structural Steel	$1 - 0i$	$4.032 \times 10^6$
Teflon ring	Teflon	$2.1 - 0.00315i$	0.25
Reactor	Pyrex glass	$2.5 - 0.025i$	1.1

The port boundary conditions were set for TE<sub>10</sub> at various power settings, the simulations were run at the frequency-transient setting with the frequency of 2.45 GHz, and time duration of 60 seconds with time steps of 1 s. The boundary condition of the metal walls of the microwave waveguide were set as perfect electric conductors, where the tangential component of the electric field is zero due to the metal material. The initial temperature for the whole system is set at 25 °C. The exterior surface of the entire geometry is set with natural convection boundary condition with the heat transfer coefficient set at 25 W/m<sup>2</sup>K, the upper limit of natural air convection.<sup>83</sup>

In each of the final simulations, the finite element mesh was set to the COMSOL mesh level of “fine” for the reactor and the reactor channels, and the rest of the geometry was set at the “normal” level. The domains with the “fine” element settings had a total of 69332 tetrahedral elements with an average element size of 0.039 mm<sup>3</sup>, an average element quality of 0.617, and an element volume ratio of  $8.20 \times 10^{-4}$ . The remaining domains with the “normal” element settings had a total of 232485 tetrahedral elements with an average element size of 6.792 mm<sup>3</sup>, an average element quality of 0.699, and an element volume ratio of  $8.33 \times 10^{-6}$ . The entire geometry had a total of 301817 elements. The element quality is a value that ranges between 0 and 1 that measures the geometric anisotropy and is preferably higher for faster and more robust convergence.<sup>84-85</sup> The element volume ratio is the ratio between the minimum element volume and the maximum element volume and shows the scale of the elements across the chosen domain.<sup>84</sup>

### 3.3.3 Simulation Results

The 2D plots of the reactor surface temperature at the two different angular positions are shown in Figure 3.3. The results match the observed uneven temperature distribution observed in all heating experiments: the center of the reactor surface had the highest temperature, and the temperature decreases radially from the reactor surface center.

The results also show different temperature ranges for the two angular positions, reflecting the experimental observations (Figure 2.11). The surface temperature of the reactor ranges from 29.5 °C to 78.1 °C at the parallel position, and from 26.8 °C to 37.8 °C at the perpendicular position. After 60 seconds of 300 W microwave irradiation, the maximum temperatures for both cases are approximately equal to the experimental temperature limit measured by the fiber optic probe (Figure 2.11).

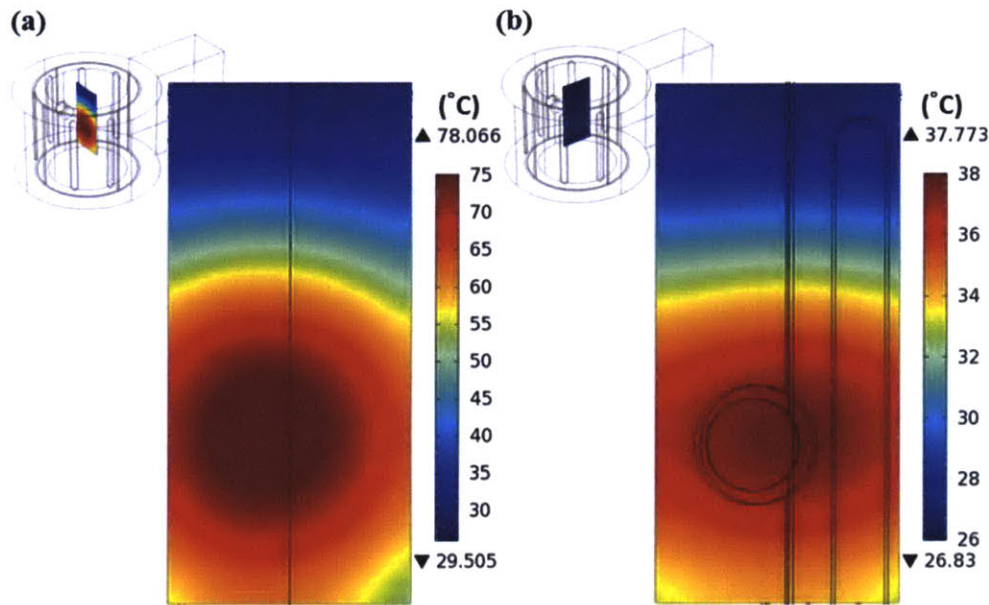


**Figure 3.3: Simulated reactor surface temperature of an empty reactor under 300 W microwave irradiation for 60 seconds at (a) parallel-to-port position, and (b) perpendicular-to-port position. (Inserts show the surface position and direction)**

Since the reactors were empty in the simulations, the microwave heat could only be generated by the Pyrex reactor and the Teflon ring. The plots of the microwave power dissipation density (Figure 3.4) show that the heat mostly came from the reactor, while the Teflon barely heated up at all. The plots are the cross-section view of the cavity along the plane of the reactor center for each reactor position, and the color bars for the heating rate are adjusted to be of the same range for both plots for ease of comparison. In both cases, the heating rates of the reactor

are highest at the cavity center and radially decrease outwards from the center of the cavity. The overall heating rate is higher when the reactor is placed at the parallel-to-port position, ranging from 0 to  $1.65 \times 10^6 \text{ W/m}^3$ , while at the perpendicular-to-port position, the heating rate ranges from 0 to  $5.66 \times 10^5 \text{ W/m}^3$ . In the two scenarios, the  $90^\circ$  angular difference causes about a three-fold difference in the reactor heating rate.

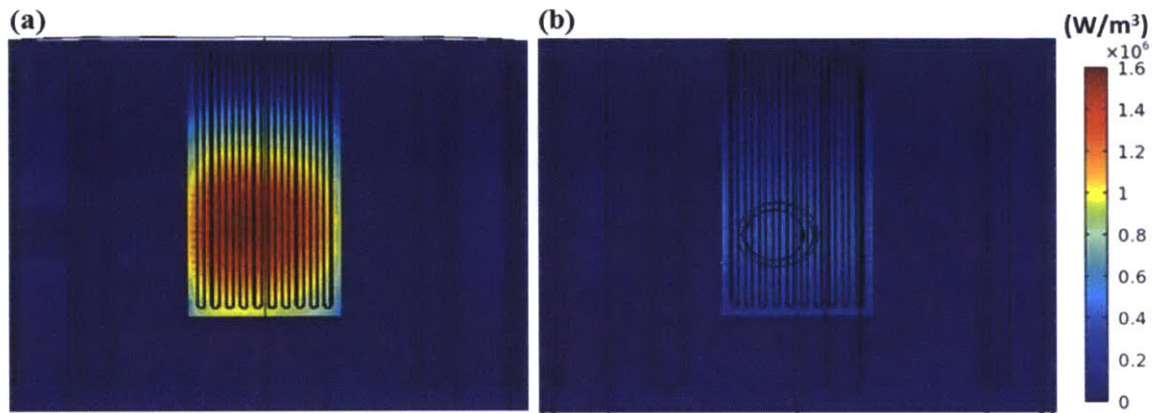


**Figure 3.4: Simulated total power dissipation/heating rate in microwave cavity across reactor center plane under 300 W microwave irradiation for 60 seconds at (a) parallel-to-port position, and (b) perpendicular-to-port position.**

Since we know from Equation (3.9) that the heating rate only depends on the material permittivity and the electric field, the electric field magnitude/strength was inspected. The results showed that the temperature distributions are indeed caused by uneven distributions of the electric field (Figure 3.5). Even though the angular position of the reactor is different in both cases, the electric field strength is always strongest at the cavity center, and therefore the heating rate and temperature of the reactor is the highest at the cavity center. The results show that in both cases, the electric field resonates at the center of the cavity as a whole, but is distorted locally by the objects in the cavity. Since the plots are made on two different planes, a direct comparison cannot be made on the electric field differences across the entire cavity. A three-dimensional inspection of the entire electric field provides a better understanding of the differences between the two cases.

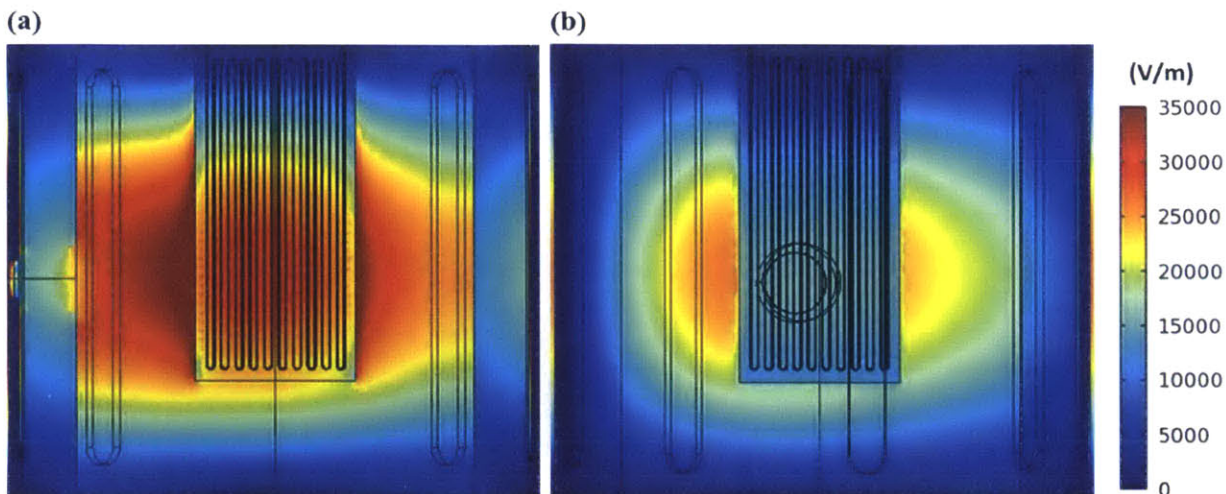


**Figure 3.5: Simulated electric field strength in microwave cavity across reactor center plane of empty reactor under 300 W microwave irradiation for 60 seconds at (a) parallel-to-port position, and (b) perpendicular-to-port position.**

Figure 3.6 shows the electric field distribution in a 3D perspective. The tip of the cone shows the directions and the electric field vector, and the color bar indicates the strength of the electric field. The top two pictures show the electric field for the two reactor positions in isotropic view, and the bottom two pictures show the top view. The plots confirm that the entire 3D distribution of the electric field changes with the reactor position. When the reactor position is rotated  $90^\circ$ , not only the magnitude, but also the direction of the electric field varies when the electromagnetic wave passes through the cavity. When the reactor is placed at different angles, it perturbs the electric field from different directions and results in different field strengths. Since the electric field depends on material dielectric properties, the combined effect of all the materials and their positions in the cavity will result in a different “net permittivity” that affects the electric field distribution differently.

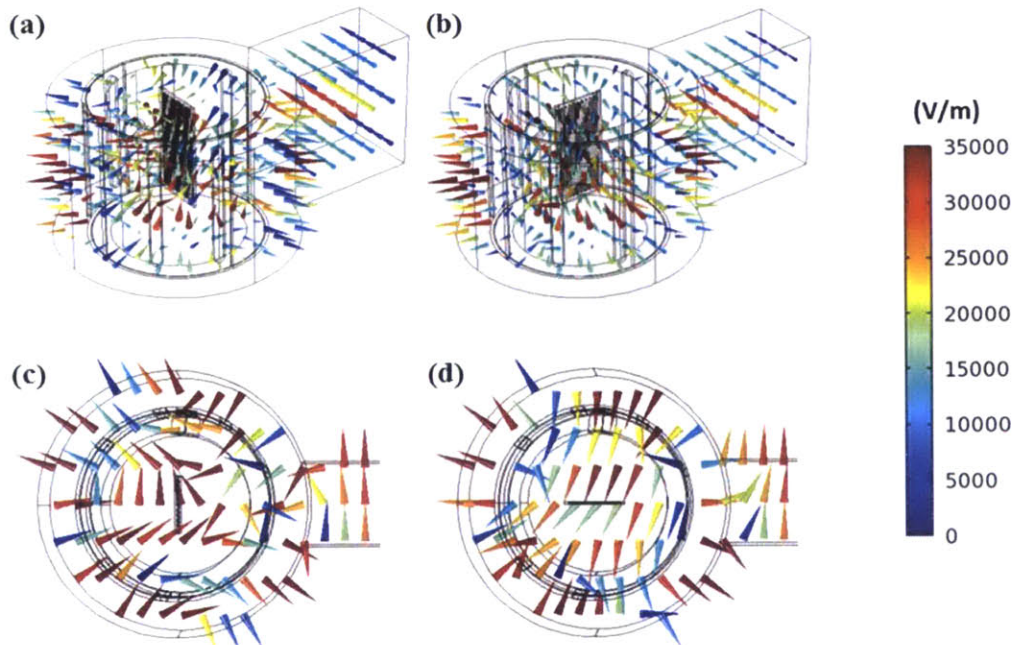


**Figure 3.6: Simulated electric field of empty reactor under 300 W microwave irradiation for 60 seconds: (a) Isometric view of parallel-to-port position. (b) Isometric view of perpendicular-to-port position. (c) Top view of parallel-to-port position. (d) Top view of perpendicular-to-port position.**

This phenomenon can be understood by treating the microwave unit as an analogy to a circuit. The materials inside the microwave cavity can be thought of as the resistant load that changes the electric field, similar to how a resistor changes the current passing through a circuit under the same voltage. The resistivity of the microwave load will change with its size and dielectric properties, just as a resistor will change with its size and electrical resistivity. Therefore, changing the direction of the reactor is essentially changing the resistivity of the microwave load and in turn changes the electric field. In other words, the electric field distribution and its strength are not only dependent on the material properties, but also extremely sensitive to the size and position of the objects placed in the microwave cavity.

The uneven electric field strength on the radial direction from the cavity center is the cause of the heating and temperature non-uniformity. The simulations show that the microwave unit is designed for the electric field to act as a single standing wave in the cavity (Figure 3.7). Figure 3.7 is a picture frame collection of a video showing the oscillating electric field in the empty microwave cavity and waveguide from the right side view of the microwave unit. The color bar shows the magnitude and direction of the electric field: the positive and negative sign

indicates the y-component direction of the oscillation, and the absolute value of the color bar is the electric field strength in unit V/m. The resonance structure is inherent in microwave propagation. Due to the standing wave, the non-uniform electric field strength will always be present in the cavity and will unavoidably lead to uneven heating across the reactor.

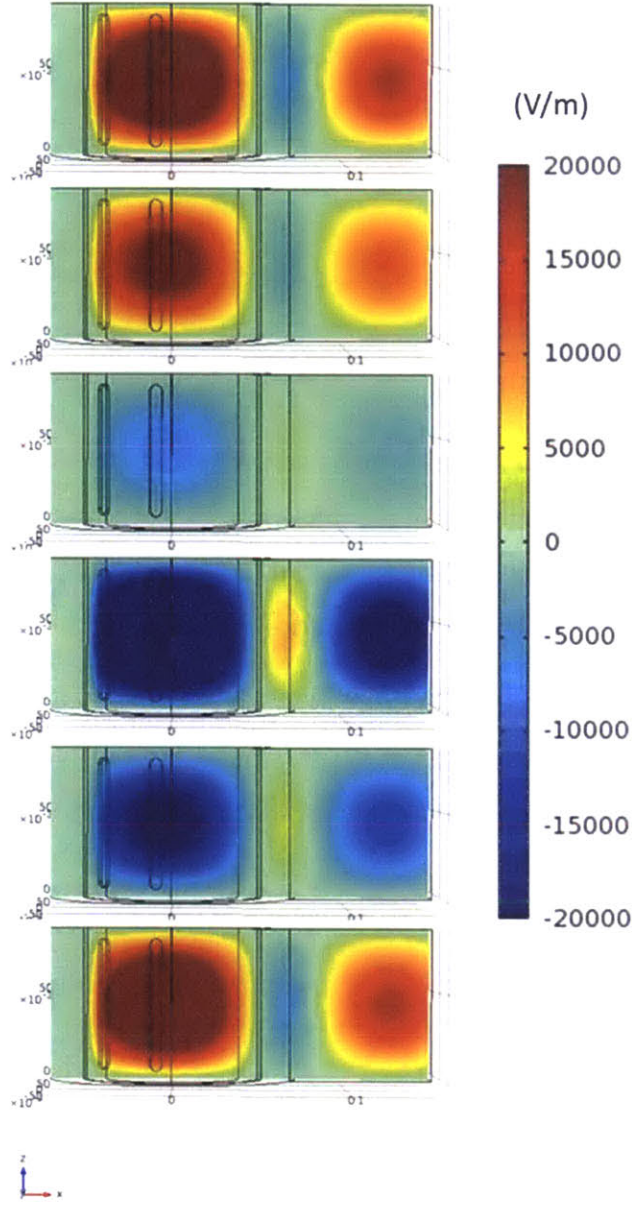


**Figure 3.7: Size view of the electric field resonance in the cavity and the start of the waveguide.**



### 3.3.4 Improving Reactor Design with Simulations

Since the electric field depends on the load inside the cavity, the size of the reactor can be modified to induce a higher electric field that will result in higher microwave power dissipation. Using the simulation, we varied the thickness of the microreactor to search for the optimum dimension that creates the highest electric field strength. The reactor was kept at the parallel-to-port position since the original reactor showed the highest electric field strength at that angle, and the power was kept at the maximum 300 W. The results show that the optimum thickness of the reactor is between 6 mm to 8 mm (Figure 3.8). Both the electric field strength and the temperature after 60 seconds of irradiation are the highest in between this region. The results were used to redesign the microreactor that will be shown in Chapter 4.

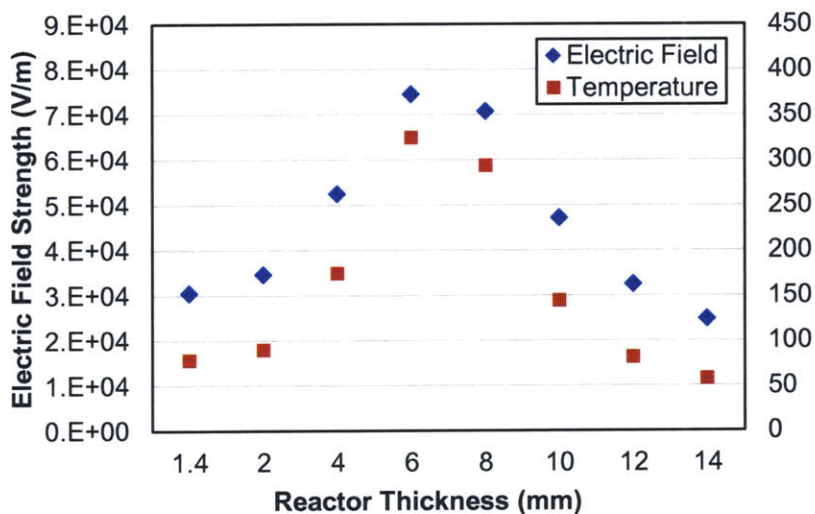


**Figure 3.8: Electric field strengths and temperatures of reactor center with various reactor thicknesses under 60 seconds of 300 W microwave irradiation.**

### 3.3.5 Model Deficiency

Although the computational models explained the cause of the temperature non-uniformity and reactor position difference, the temperature limitations are not shown in the simulations for longer heating periods (Figure 3.9). Figure 3.9 shows the temperature measurement at the center of the reactor surface versus the time under microwave heating. The modeling results for 60 minutes of microwave heating shows that the empty reactor can be heated up to 300 °C using the maximum power of the microwave unit. Even at 150 W, the reactor in the model can heat up to the range of 130 °C to 160 °C for the condensation reaction. The steady-state temperatures of the simulations do not match the experimental temperature

limits, which is around 90 °C for 300 W, 70 °C for 150 W, and 35 °C for 10 W of microwave irradiation (Figure 2.11). The initial models therefore does not account for all the heat loss in the microwave unit. Since the heat transfer to the environment outside of the microwave guide is already approximated with the maximum natural air convection, the additional heat loss that is missing in the models is most likely the natural convection of the air inside the cavity and waveguide. The air gaps in the models were originally treated as solids and only the heat conduction in air was considered. Models that included the air convection were then developed to better reflect the experimental observation.

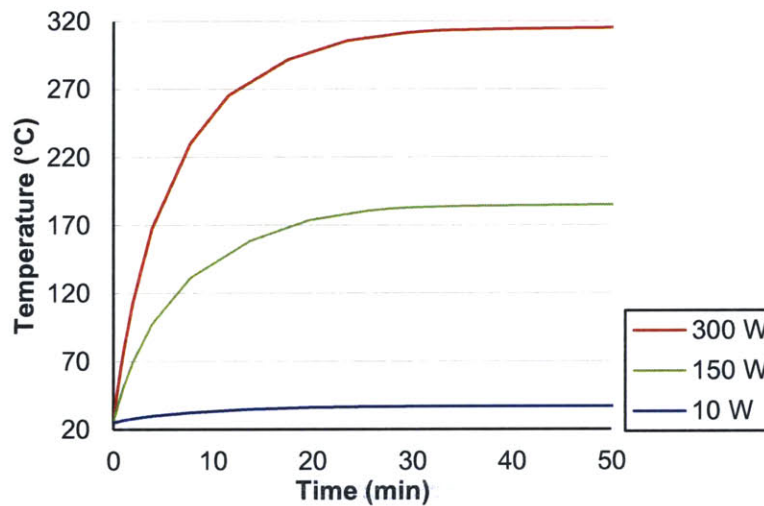


**Figure 3.9: Temperature of reactor center in initial simulation models after 60 minutes of microwave irradiation.**

### 3.4 Air Convection Models

In order to fully explain the temperature limit, we approximated the air convections inside the microwave unit (Figure 3.10) by two models: the first one is by approximating the heat conductivities of the air material properties within the cavity gaps; the second one is adding a laminar-flow model onto the domain modeled for air in COMSOL.

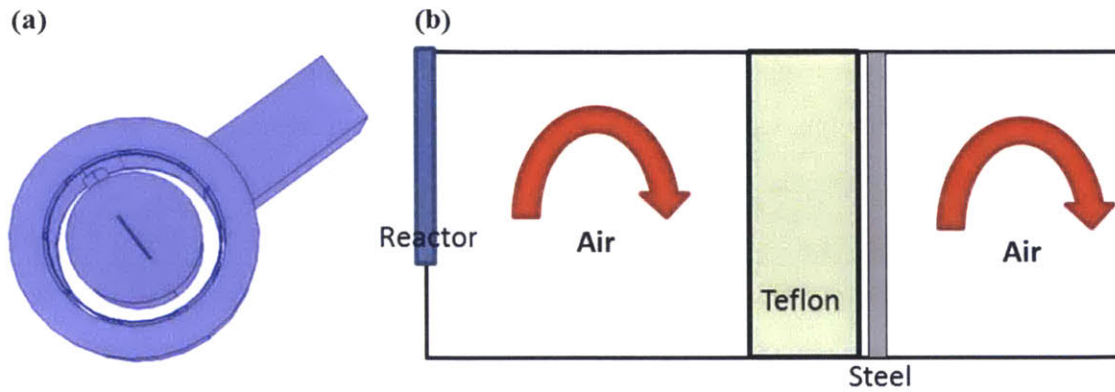


**Figure 3.10: (a) Domain in the simulation model that required natural convection model. (b) Schematics of the side view of the air gap in the cavity and waveguide.**

Natural convection, or buoyance-driven flow, is caused by the density difference in the fluid body due to temperature change.<sup>82</sup> To accurately account for the air convection, the fluid mechanics have to be included and solved along with the heat transfer models.

Many studies have been published on the natural air convection in enclosures, and the relationship between the convective and conductive heat transfer effect have been analyzed for various geometries.<sup>86-89</sup> The ratio of the convective and conductive heat transfer across the fluid boundary is defined as the dimensionless Nusselt number,  $Nu$ :

$$Nu = \frac{hL}{k} \quad (3.11)$$

where  $h$  is the heat transfer coefficient,  $k$  is the thermal conductivity, and  $L$  is the characteristic length of the convection boundary layer. The empirical functions of the Nusselt number are available for various geometries. If the Nusselt number is known for a particular geometry, then the heat transfer coefficient can be found by Equation (3.11) and used to calculate the natural convection effect. Unfortunately, no studies of the Nusselt number for our geometry (a ring connecting to a column with the same center, Figure 3.10) were found, and we needed to build our own convection models.

Note that the additional air convection models will not change the electric field and power dissipation density simulated from the initial models since the materials' size, position, and dielectric properties do not change in the cavity.

### 3.4.1 Thermal Conductivity Estimation Model

In order to simplify our model problem and exclude the additional fluid dynamics variables that need to be solve, we first developed a model that approximate the fluid convective heat flux by an “effective thermal conductivity”,  $k_{eff}$ .

The air is modeled as a solid domain with a higher thermal conductivity due to the added effect of convection heat transfer. The convection heat transfer in fluids is usually expressed as the heat transfer coefficient times the difference between the bulk fluid temperature ( $T_{bulk}$ ) and the fluid temperature at the boundary surface ( $T$ ). In our model, this convection heat transfer term is approximated into a normal heat conduction term shown as Equation (3.12).

$$h \cdot (T_{bulk} - T) = -\mathbf{n} \cdot (-k_{eff} \nabla T) \quad (3.12)$$

This idea behind the approximation is similar to the concept from a convection boundary condition between a solid phase and a liquid phase,<sup>82</sup> where the normal heat transfer is assumed to be purely by conduction and the heat flux. The difference, however, is that the terms on both side of the equation is for the same domain, which is the air gap in our model.

The effective thermal conductivity can also be thought of as the heat transfer coefficient times the characteristic length:

$$k_{eff} \cong hL \quad (3.13)$$

Since the waveguide in our system is about 18.75 mm wide, and the cavity radius is about 37.75 mm (Table 3.1), the characteristic length in our system is taken as the average 28.25 mm.

Therefore, the previous simulation models were rerun with various thermal conductivity values for the air domain to see if the temperature results will reflect the experimental heating profile of the reactors.

The final results matches well with the observed temperature profile for empty reactors under different power settings (Figure 3.11). The effective thermal conductivities found for each case of power irradiation are listed in Table 3.3. The simulated heating profiles not only match the steady-state temperature range, but also have the effect of the temperature drops around 8 minutes of heating in the cases of high power settings.

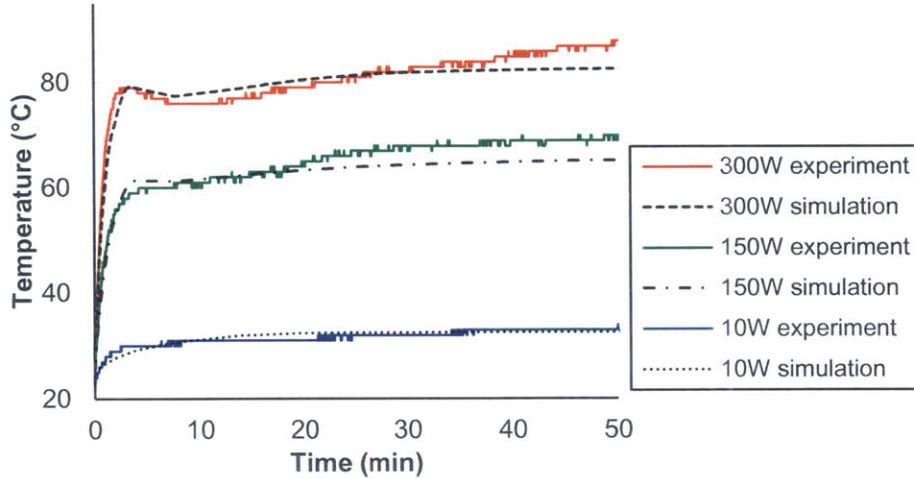


**Figure 3.11: Comparison between the experimental and simulated heating profiles with the k-estimation models of empty reactors under different power exposure at parallel-to-port position.**

The equivalent heat transfer coefficient for each case was calculated with Equation (3.13), using 28.25 mm as the characteristic convection length (Table 3.3). The results all fall within the range of 2 – 25 ( $\text{W}/\text{m}^2\text{K}$ ), the range of heat transfer coefficients for natural air convection.<sup>83</sup> The Nusselt numbers with the subscript “simulation” are the ratio of the effective thermal conductivity over 0.03 ( $\text{W}/\text{mK}$ ), the approximate thermal conductivity of air between the range 25 °C to 100 °C under atmospheric pressure.<sup>90</sup> These values are compared against the Nusselt numbers of natural convection in an enclosed rectangular box,  $Nu_{rectangular}$ , which are calculated by assuming the air is in a box of the same height and width as the average width of the microwave waveguide and cavity (Appendix B.1).<sup>87</sup> The Nusselt numbers for our simulation and for an enclosed rectangular space are of the same order of magnitude. The temperature profile and the calculations confirm that the heating limitations are due to the air convections in the gaps within the microwave unit itself and that the thermal conductivity can provide a good estimation for the convective heat transfer effect.

**Table 3.3: Effective thermal conductivities, equivalent heat transfer coefficients, and Nusselt numbers for k-estimation models of parallel-to-port reactor. ( $Nu_{rectangular}$  calculated from reference<sup>87</sup>)**

Power	$k_{eff} \left(\frac{\text{W}}{\text{mK}}\right)$	$h \left(\frac{\text{W}}{\text{m}^2\text{K}}\right)$	$Nu_{simulation}$	$Nu_{rectangular}$
300 W	0.3	10.6	10.0	4.1

Power	$k_{eff} \left(\frac{W}{mK}\right)$	$h \left(\frac{W}{m^2K}\right)$	$Nu_{simulation}$	$Nu_{rectangular}$
150 W	0.2	7.1	6.7	3.8
10 W	0.05	1.8	1.7	2.5

The simulation was also repeated for the models of the reactor at the perpendicular-to-port positions, and similar results were found (Figure 3.12, Table 3.4). Although the temperature profiles do not seem to completely match the experimental data, the differences between each case are within 3 °C. The simulations still follow the general trend of the experimental data, and have greatly decreased the temperature from the initial simulation models without air convection consideration within the microwave cavity and waveguide.

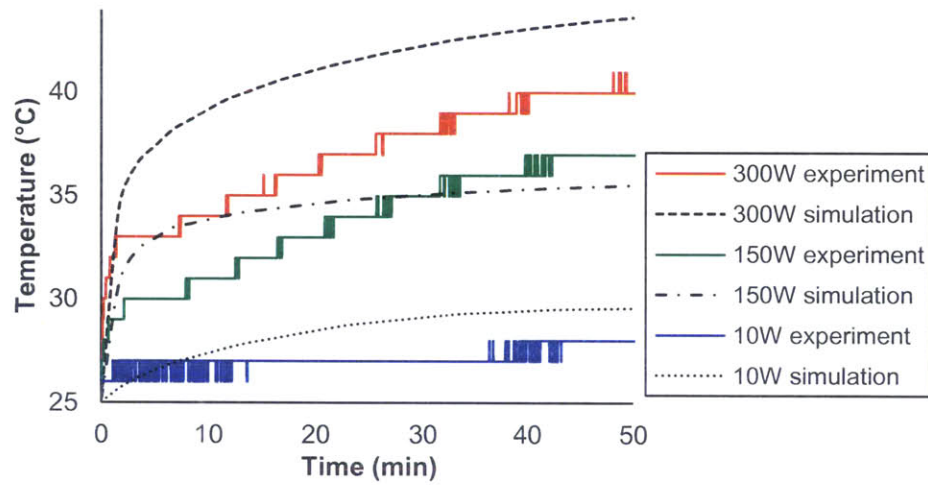


**Figure 3.12: Comparison between the experimental and simulated heating profiles with the k-estimation models of empty reactors under different power exposure at perpendicular-to-port position.**

**Table 3.4: Effective thermal conductivities, equivalent heat transfer coefficients, and Nusselt numbers for k-estimation models of perpendicular-to-port reactor. ( $Nu_{rectangular}$  calculated from reference<sup>87</sup>)**

Power	$k_{eff} \left(\frac{W}{mK}\right)$	$h \left(\frac{W}{m^2K}\right)$	$Nu_{simulation}$	$Nu_{rectangular}$
300 W	0.3	10.6	10.0	2.8
150 W	0.2	7.1	6.7	2.6
10 W	0.01	0.35	0.33	1.8

### 3.4.2 Single-Phase Flow Model

After confirming that the heat loss is due to natural air convection, we set up a more rigorous simulation model that incorporates the single-flow module, which solves for the Cauchy's form of conservation of momentum with the continuity equation:<sup>82</sup>

$$\rho \left[ \frac{\partial \mathbf{v}}{\partial t} + \mathbf{v} \cdot \nabla \mathbf{v} \right] = \mathbf{F} - \nabla P + \nabla \cdot \boldsymbol{\tau} \quad (3.14)$$

$$\nabla \cdot \mathbf{v} = 0 \quad (3.15)$$

$\rho$  is the density of air at the initial pressure and temperature,  $\mathbf{F}$  is the sum of all body force exerted on the air per unit volume,  $P$  is the pressure of air, and  $\boldsymbol{\tau}$  is the viscous stress tensor. Equation (3.15) can be used for air as long as the fluid velocity is much smaller than the speed of sound, and it is an excellent approximation in natural convection even though the fluid density is not constant.<sup>82</sup>

The only body force in the convective system is force of gravity caused by the variation in air density, which in turn depends on the fluid temperature:

$$\mathbf{F} = \rho \mathbf{g} = -9.8 \times \frac{PM_w}{RT} \mathbf{e}_z \quad (3.16)$$

where  $\mathbf{g} = -9.8 \text{ m/s}^2 \mathbf{e}_z$  is the gravitational acceleration that only goes in the downwards direction of the  $\mathbf{z}$  axis (Figure 3.2), and the air density,  $\rho$ , is found by the ideal gas law:  $M_w$  is the average air molecular weight,  $R$  is the universal gas constant,  $P$  is the pressure of air, and  $T$  is the air temperature.

Equation (3.16) is substituted into Equation (3.14) for the force term, and the velocity field of the air domain,  $\mathbf{v}$ , can be solved by Equation (3.14) and (3.15). The velocity field is then used in the energy equation, Equation (3.10), to solve for the temperature with the same electromagnetic and heat transfer model as before. Note that the temperature is an input to Equation (3.16), and therefore the fluid mechanics are coupled with the heat transfer model in both directions.

The convection in the microwave unit is all within the laminar flow regime since the Rayleigh number is all smaller than  $10^9$  (Table 3.5).<sup>83</sup> Rayleigh number is defined as:

$$Ra = \frac{g\beta(T_1 - T_2)L^3}{\nu\alpha} \quad (3.17)$$

where  $\nu$  is the kinetic viscosity of air,  $\alpha$  is the thermal diffusivity of air,  $\beta$  is the coefficient of thermal expansion,  $T_1$  and  $T_2$  are the temperatures of the two wall, and  $L$  is the characteristic length of the confined region (Appendix B.1).

**Table 3.5: Rayleigh numbers of the air gaps in the microwave unit at different reactor positions and different power settings.**

<b>Power</b>	<b><i>Ra</i> at parallel-to-port position</b>	<b><i>Ra</i> at perpendicular-to-port position</b>
300 W	1.21E+05	3.03E+04
150 W	8.67E+04	2.44E+04
10 W	2.04E+04	6.18E+03

The above equations were built into COMSOL by adding a Laminar Flow Interface in the Fluid Flow Module onto the existing model described in Chapter 3.3.2. Only the air domain (Figure 3.10 (a)) was added to the Laminar Flow Interface. Since the Microwave Heating Interface sets all heat transfer as a solid domain by default, the “Heat Transfer in Fluids” node had to be added to the original model. The air domain is selected for the “Heat Transfer in Fluids” node plus the “Wave Equation” node, while the remaining geometry is modeled in the “Microwave Heating” node. In the Laminar Flow Interface, the temperature of air is set as an input from the Heat Transfer in Fluids node, while the velocity field is set as an output to the Heat Transfer in Fluid node. There is no microwave heat source in the air domain since the dielectric loss of air is zero. The density of air in all of these models is set to the COMSOL default material property for air, in which the air density is dependent on pressure and temperature through the ideal gas law (Equation (3.16)). Therefore, the air density is variable in all three interfaces (Equation (3.10), Equation (3.14), and Equation (3.16))

In the final simulations, the finite element mesh was set to the COMSOL mesh level of the entire geometry was set to the “normal” level. The domains had a total of 306495 tetrahedral elements with an average element size of 5.15 mm<sup>3</sup>, an average element quality of 0.676, and an element volume ratio of 1.36×10<sup>-7</sup>. The models were only simulated for the cases of microwave irradiation at 300 W. The simulations were run at the frequency-transient setting with the



frequency of 2.45 GHz, and time duration of 1000 seconds with time steps of 100 s. The total degree of freedom to solve was 2537836.

The air convections were successfully simulated in the single-phase flow model. Figure 3.13 - Figure 3.16 display the simulated velocity projected onto 2D planes crossing the center of the cavities. The velocity field shown are all at the last simulated time point, 1000 seconds. The inserts next to the figures indicated the direction of view for each figure. The color bars show the velocity magnitude, and the range are all adjusted to 0 – 0.1 m/s. The black arrows show the velocity direction projected onto each of the 2D planes with the tails of the arrows indicating the start of the air circulation. In both cases, the convection is stronger where the air is in contact with the larger side of the reactor surface rather than the width of the reactor: for the parallel-to-port position, Figure 3.14 show a faster velocity field from the side view than Figure 3.13 from the front view; for the perpendicular-to-port position, the speed in Figure 3.15 is higher than in Figure 3.16. Furthermore, when the reactor is parallel to the port, the convection is stronger than when the reactor is perpendicular to the port. This result matches the expectation since the higher heating rate and temperature rate in the former position will led to a larger air density difference and result in a stronger buoyancy-driven flow.

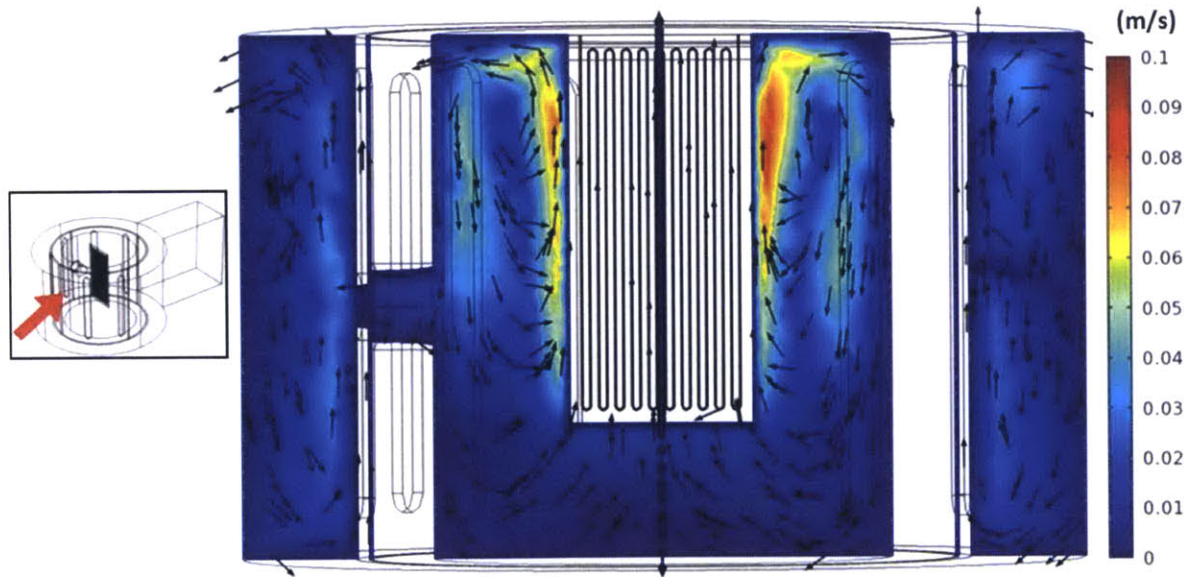


**Figure 3.13: Velocity field on cavity center plane viewed from the front of the unit in the single-phase flow simulation when reactor is parallel to port. (Color bar shows velocity magnitude, arrows indicate velocity direction projected onto the 2D plane.)**

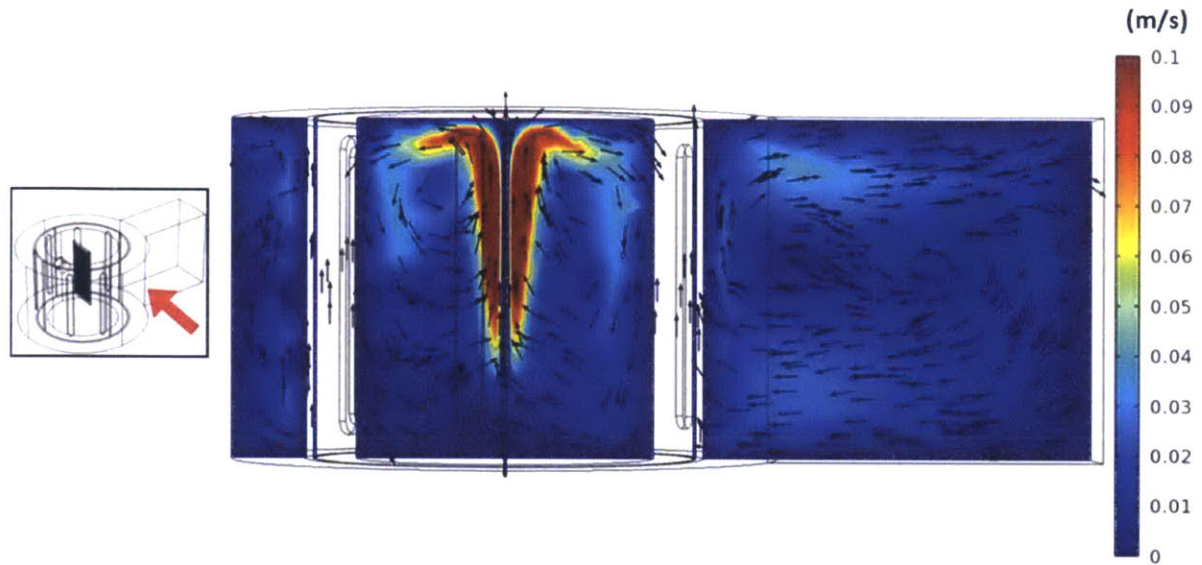


Figure 3.14: Velocity field on cavity and waveguide center plane viewed from the right side of the unit in the single-phase flow simulation when reactor is parallel to port. (Color bar shows velocity magnitude, arrows indicate velocity direction projected onto the 2D plane.)

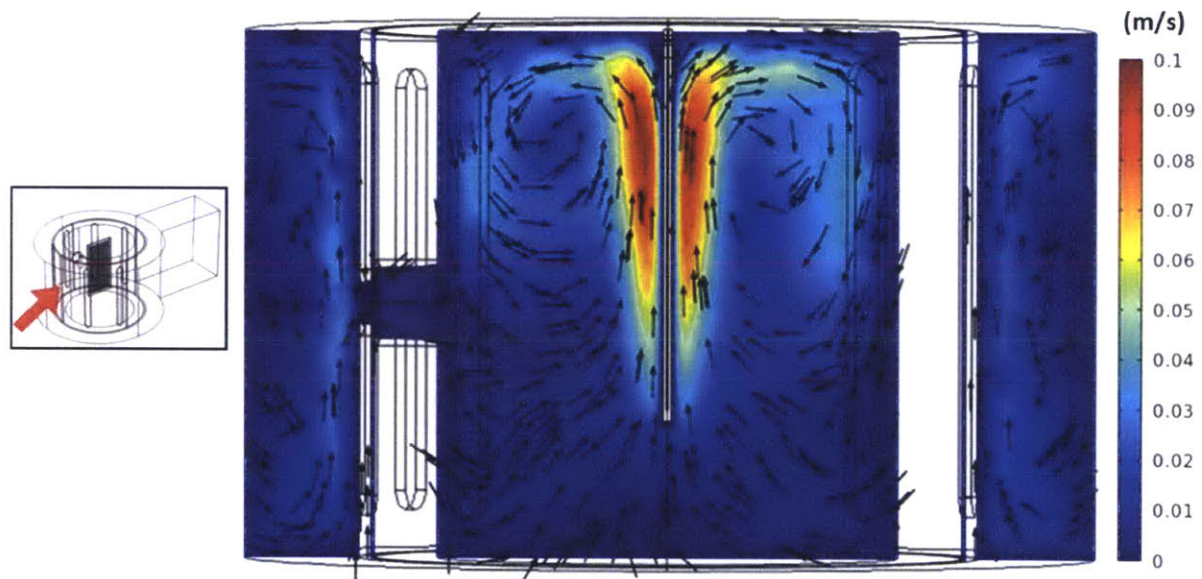
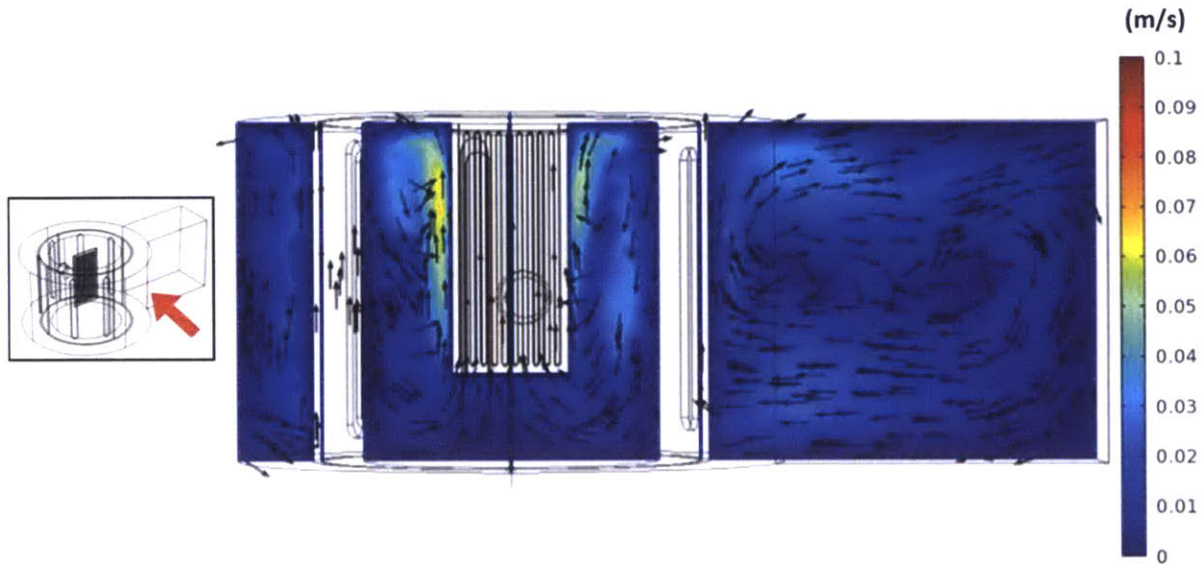
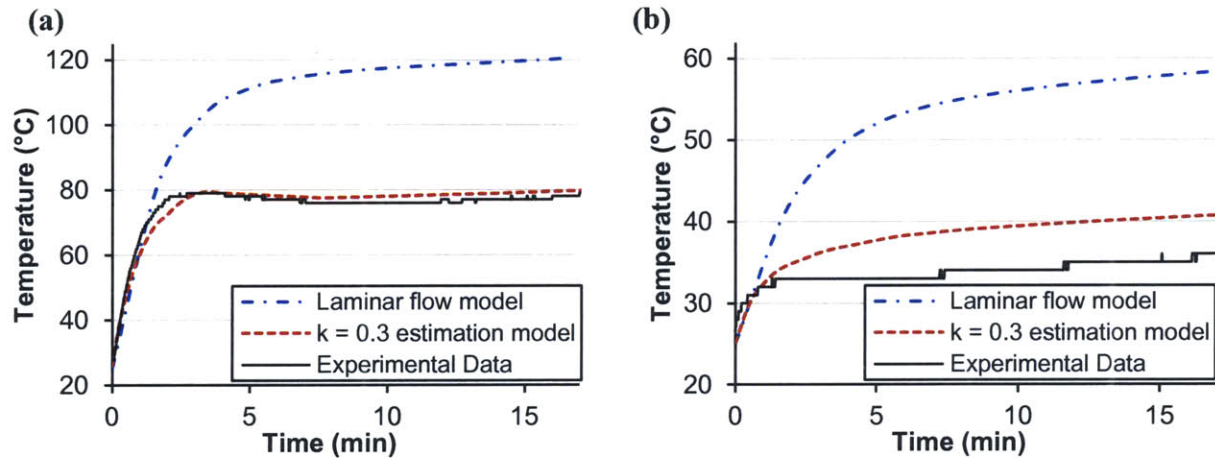


Figure 3.15: Velocity field on cavity center plane viewed from the front of the unit in the single-phase flow simulation when reactor is perpendicular to port. (Color bar shows velocity magnitude, arrows indicate velocity direction projected onto the 2D plane.)



**Figure 3.16: Velocity field on cavity and waveguide center plane viewed from the right side of the unit in the single-phase flow simulation when reactor is perpendicular to port. (Color bar shows velocity magnitude, arrows indicate velocity direction projected onto the 2D plane.)**

The reactor temperatures at the surface center from this model is much closer to the experimental data than the initial model (Figure 3.17). The overall heating rate is greatly reduced after the heat loss was accounted for by the air gap in the cavity. However, the results did not match the experimental data as closely as the thermal conductivity estimation (k-estimation) model. The remaining difference between the profiles might be accounted for by refining the meshes and decreasing the time steps of the simulations. The velocity fields in Figure 3.13 - Figure 3.16 also shows that the mesh is not fine enough. Sharp edges between different speeds can be seen in the figures, indicating that these areas have rather coarse meshes that can be improved upon.



**Figure 3.17: Comparison of heating profiles between the two air-convection simulation models and experimental data for empty reactor under 300 W microwave irradiation at (a) parallel-to-port and (b) perpendicular-to-port position.**

The mesh refinements were not completed because the computational cost of adding the flow module is much higher than the k-estimation model: the natural convection model takes about 9 days to converge on the same problem size that takes the k-estimation model 10 hours to converge. We refined the meshes of the models to the “fine” level of 505534 elements, and the model solution progress was only 40 % after 4 weeks.

Another reason why the single-phase flow model gave a poorer prediction of the heating profile than the k-estimation model is that there are other heat losses not captured in the microwave model or an over-estimation of the microwave power. The heat loss to the environment outside of the cavity was modeled as the a convective boundary condition in all three models, while in reality the waveguide is enclosed in the microwave unit casing and surrounded by wirings (Figure 3.1) and might have a higher heat loss. The heat loss to the metal attenuator and the PEEK packaging were also not considered. The input of the microwave was also simplified as a port boundary condition, where as in reality, the magnetron of each microwave unit decays with time and might not be providing the nominal power output.<sup>70, 78</sup> The simplified port microwave input also does not take into account the reflective interaction of the specific type of magnetron used in the Discover unit. In a microwave unit, part of the energy generated by the magnetron is absorbed by the cavity while part of it is reflected back to the magnetron, and the reflected energy is partly absorbed by the magnetron and partly reflected back to the cavity. The reflective coefficient that results from this complex interaction varies for

different types of magnetron and also the differences in the angle it is placed in the microwave unit.<sup>78</sup> Therefore, the actual power input is different than the set power input during the experiments. The port boundary condition only accounts for the reflection as a simplified equivalent circuit, and the power input in the simulation was set as the nominal value used in the experimental setting.

The advantage of the k-estimation model is that the other possible heat losses are all lumped into the effective thermal conductivity, and therefore the heating profiles can be adjusted to better match the experimental observations without having to consider the complex interaction of the magnetron and the microwave load. The k-estimation model can provide a fairly accurate prediction of the heat distribution inside a microwave cavity with a shorter computational time.

In conclusion, using the computational models, we found that the heating challenges were caused by three issues (1) the weak electric field strength, (2) the heat loss due to the natural air convection, and (3) the uneven heating rate across the cavity. The first two issues can be resolved by changing the size of the reactor to induce a higher heating rate from the microwave. However, the uneven heating rate will always be present because it is caused by the inherent nature of electromagnetic wave radiation. The results were used to redesign the microreactor, which is presented in Chapter 4.



## CHAPTER 4. SPIRAL REACTOR SETUP

---

### 4.1 Introduction

Based on the simulation results, a new design was proposed to overcome the heating issues of the original reactor, including how to induce higher microwave heating rate and to minimize the temperature distribution difference. Mechanical issues were encountered for the design, and the issues were solved or minimized by changing the packaging design as well as the reaction operating conditions. Simulations of the final design were made to both confirm the heating pattern of the new reactor and to demonstrate the temperature variation for the validation chemistry, the latter of which will be discussed in Chapter 5.

### 4.2 Reactor Design and Heating Testing

#### 4.2.1 First Generation of Spiral Microreactor

From the simulations of difference reactor thicknesses, the electric field was found to be the highest when the reactor is between 6 to 8 mm, and results in the highest heating rate (Figure 3.8). The new microreactor was therefore designed as 6.5 mm thick to overcome the heating limits of the original reactor (Figure 4.1). In addition, the reaction zone of the new design was spiral-shaped and positioned at the center of the cavity in order to reduce the range of temperature variation across the reaction channels.

The reactor consisted of five layers of glass, four of which had spiral reaction channels, and one with two slots to hold the temperature sensor. The two center pieces were 30 mm wide, 105 mm long, and 1 mm thick: one of the pieces had the inlet and outlet channels as well as the spiral channels drilled in it, while the other piece only had a mirrored version of the spiral channel drilled in and acted as a seal for the inlet and outlet channels. Two of the side pieces also only contain spiral channels that mirrored each other; these two pieces were each 30 mm times 30 mm wide and 1 mm thick (Figure 4.1(b)). The spiral channels were all 0.5 mm deep by 0.5 mm wide. The spiral channels between the different layers were connected through clearance holes at the positions where the spiral channels connect to the inlet and outlet channels. The combined reaction zone was 285  $\mu$ l. On the other side of the reactor was a 2.5 mm thick glass

piece acting as a fiber optic probe holder: the slots for the optical fiber were 2 mm deep, 2 mm wide, and 27 mm long. The optical fiber could be positioned at either slot during microwave experiments. The position of each slot is about half way through the spiral channels.

The reactors were made by the company Little Thing Factory GmbH,<sup>91</sup> a supplier for microfluidics technology. They sandblasted the reactor channels and fusion bonded the multiple layers of glasses together. Sandblasting is an abrasive etching technique that creates channel features in the glass by physically chipping the glass with a slurry solution of sand or microparticles under high speed and high impact. Compared with the HF wet-etching method, sandblasting is able to produce deeper, narrower channels and sharper-angled corners. The channels for the spiral reactor are therefore closer to rectangles. The PEEK holder for the first microreactor with the long U-shaped channel was also used for this spiral reactor (Appendix A.2).

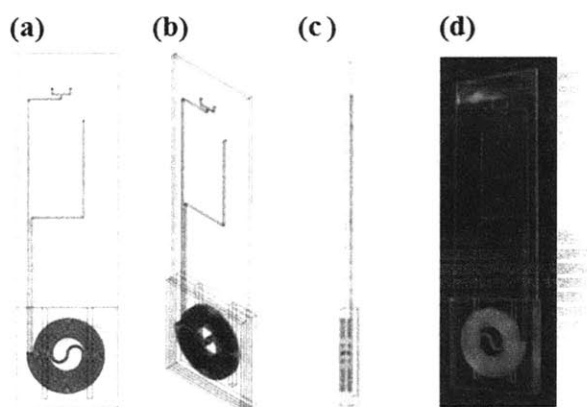


**Figure 4.1: 1<sup>st</sup> spiral, multilayer microreactor design: (a) front view, (b) angled view, (c) side view schematics, and (d) picture of actual reactor.**

#### **4.2.2 Chemistry Testing and Mechanical Stability**

The reaction solvents could be microwaved to the desired reaction temperatures with the new reactor design, and the previous condensation reaction and aromatic substitution reactions were used to test the new setup. Both reactions resulted in higher conversions than conventional heating (Figure 4.2, Table 4.1).



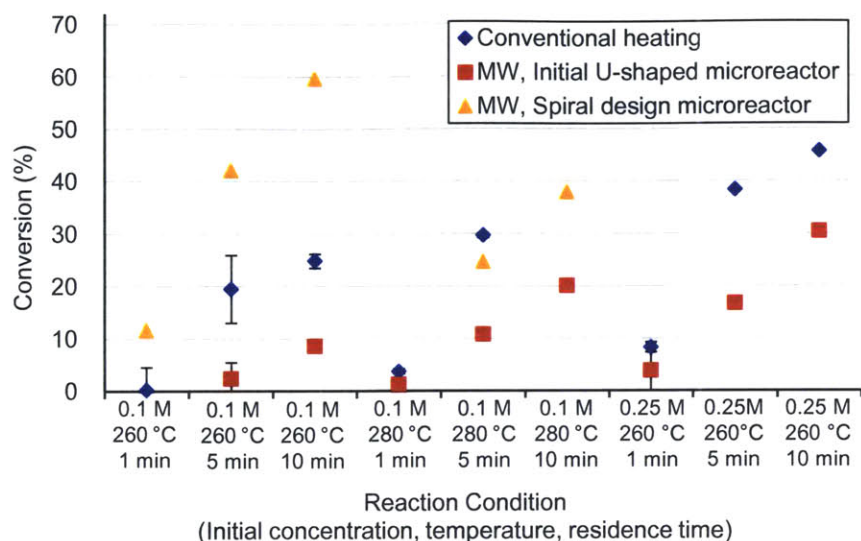


**Figure 4.2: Comparison of the aromatic substitution results from microwave microreactor and conventional cartridge heater.**

The conversion data and the kinetic data of the condensation reaction were used to calculate the actual mean temperatures of the reaction during each experimental setting. The actual mean temperatures calculated through this method will be termed the kinetic mean temperature in this thesis. The activation energy used for the calculation was determined from the literature as 76.7 kJ/mol;<sup>73</sup> and the pre-exponential factor  $1.03 \times 10^7 \text{ s}^{-1}$  was calculated from our cartridge-heated microreactor conversion data using the 76.7 kJ/mol activation energy (Appendix A.4.2). The results showed that the actual liquid temperature is about 20 °C to 25 °C higher than the measured temperature with the optical fiber (Table 4.1). This showed that the temperature measured at a single point of the reactor surface is not accurate enough to represent the entire temperature distribution along the reactor channels. For accurate data collection, a temperature sensor that measures the solvent temperature in the entire three-dimensional space is required. As an alternative, we attempted to use the kinetic data, the data on microwave power irradiation, and the simulation results to establish correlations between the measured temperature and the kinetic mean temperature of specific solvents in the microwave (Chapter 5.3).

**Table 4.1: Condensation results and kinetic mean temperature calculations from 1<sup>st</sup> spiral microreactor**

Set/Measured temperature (°C)	Residence time (min)	Conversion (%)	Temperature calculated from conversion (°C)	Temperature Difference (°C)
130	1	18.5	151	21
	2	36.5	153	23
	3	47.9	152	22
	5	65.4	151	21
	10	87.0	151	21
140	1	29.7	163	23
	2	52.6	164	24
	3	65.6	163	23
	5	83.7	164	24
	10	94.8	159	19
150	1	40.3	172	22
	2	70.6	177	27
	3	82.9	176	26
	5	91.4	171	21

The reactors all broke during the heating process for further chemistry testing after only one set of experiment was performed for each of the two validation reactions. The reactors were design to withstand 15 bar of pressure, 400 °C of temperature, and a shock temperature of 175 °C. Since the reactions conditions were all kept within these specifications, the reactors most likely broke because the mechanical stress imposed on the glass during sandblasting was not entirely relieved during the bonding process.

Another possible reason for the reactor breaking was the rapid heating rate. The reactions were all ran under fixed temperature mode. During the fixed temperature setting, the microwave radiation always starts at the maximum 300 W and slowing decrease in power when the temperature reaches the target value. The instantaneous microwave irradiation at 300 W during the reaction might have caused the temperature to rise too fast and the solvents vaporized before the spring in the back pressure regulator could respond. In order to increase the reactor stability and decrease the stress placed on the reactor, a modified version of the microreactor and packaging was designed, and the maximum microwave power was set at 100 W for future experiments.

### 4.2.3 Second Generation of Spiral Microreactor

In the modified reactor design, all the glass layers have the same width and height (Figure 4.3). The same dimension allowed the internal stress to be better relieved during the annealing process. Since the size of the packaged reactor is confined inside the microwave attenuator (4 cm in diameter) and the new reactor design is thicker, a new packaging device that takes up less space was constructed.

The reactor length was increased and two grooves were cut across the top of the finished reactor (Figure 4.1 (a)). To assembly the packaging, the reactor is slid into a PEEK holder that fits the grooves and holds the reactor from the top. The tubing is connected by screwing flat-bottom fittings against the reactor at the inlets and outlet holes. Additional metal clamps are added to the final assembly to create a tighter seal (Figure 4.1 (b) and (c)). The modified reactor and new holder were both made by Little Things Factory. The sealing and reactor strength were tested with different backpressure and can stand up to 250 psi.

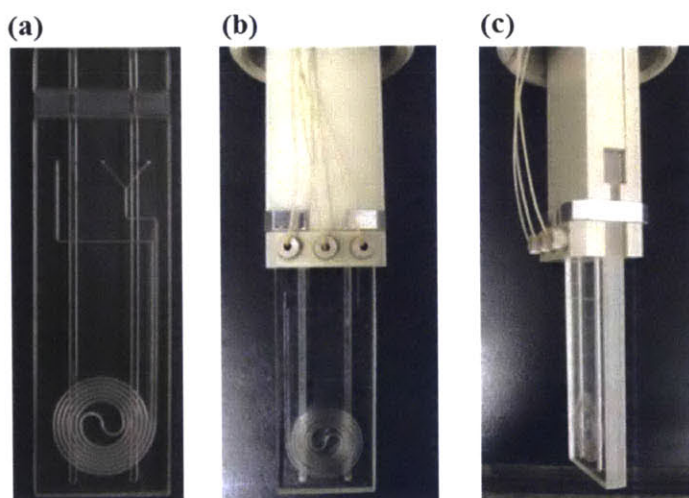


**Figure 4.3: 2<sup>nd</sup> spiral, multilayer microreactor design: (a) picture of reactor, (b) front view picture with packaging, (c) angled view picture with packaging.**

### 4.3 Spiral Reactor Simulations

The final design was simulated with the thermal conductivity estimation model. The reactor is drawn in COMSOL by importing the 2D AutoCAD® files of the spiral channels into the COMSOL geometry. The reactor was drawn parallel to the microwave port with the fiber

optic holders closer to the front of the microwave unit (Figure 4.4), reflecting the position it was placed in during the chemical experiments (Chapter 5.)

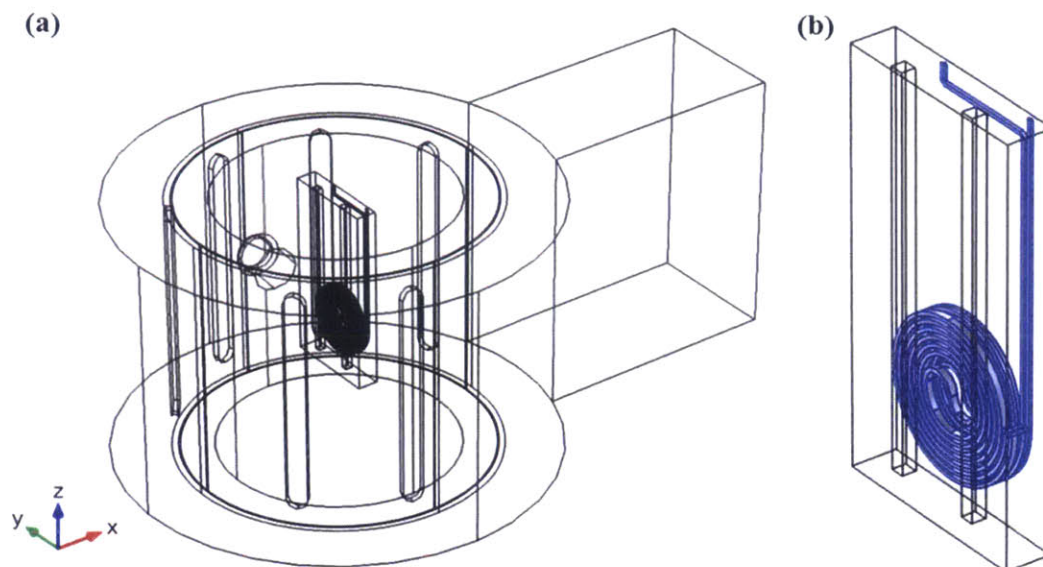


**Figure 4.4: Isotropic view of (a) entire simulation geometry for spiral reactor positioned parallel to microwave port, and (b) close-up schematics of the reactor with reaction channels colored in blue.**

The mesh was set at the “normal” level in COMSOL to generate the mesh automatically. The final mesh had a total of 213807 tetrahedral elements with an average element size of  $7.18 \text{ mm}^3$ , an average element quality of 0.662, and an element volume ratio of  $6.29 \times 10^{-7}$ . The reactor channels had the smallest average mesh size of  $0.055 \text{ mm}^3$  over 6650 tetrahedral element, with an average element quality of 0.484, and an element volume ratio of  $3.08 \times 10^{-3}$ . The meshes of the reactor channels are relatively fine compared with its volume of  $285 \text{ mm}^3$ . The mesh were not further refined due to both the difficulties in generating smaller meshes and the large computational cost involved to store the solution of a finer mesh.

#### **4.3.1 Spiral Reactor Simulations with Empty Channels**

The reactor was first simulated with empty channels and compared with the experimental heating results (Figure 4.5). The estimated thermal coefficients listed in Table 3.3 were used for the computational models. The simulated temperatures were taken at the reactor center. The experimental reactor temperatures were measured at the reactor surface center since the PEEK

holder was not properly machined at the time and the fiber optic probe had to be held with a Teflon tape to the reactor surface.

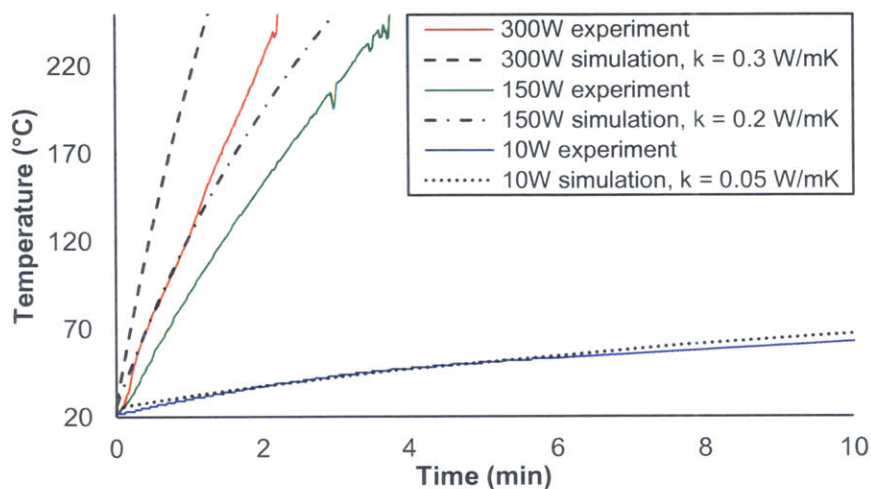


**Figure 4.5: Comparison between the experimental and simulated heating profiles with the k-estimation models of empty spiral reactors under different power exposure at parallel-to-port position.**

The temperature profiles show that the estimated thermal conductivities for the initial microreactor at 300 W and 150 W did not work as well for the spiral reactor, while the estimated thermal conductivity at 10 W predicted the experimental heating rate quite nicely. This could be caused by the difference in temperature measurement position since the fiber optic probe was held together with a Teflon tape instead of in the reactor slot. Besides the experimental error, the discrepancy is most likely due to the faster heating rate of the spiral reactors. Under the same microwave irradiation, the spiral reactor induces a larger electric field than the initial model, and the reactor therefore heats up faster. The sudden increase of temperature will cause the air convection to rise faster, and therefore the effective thermal conductivities of the spiral reactor should be higher. The results of 300 W and 150 W show the over-estimation of temperature due to underestimating the air convection effect. This underestimation did not occur for the 10 W heating profile since the air convection is not as strong when the power is low. This can be seen by comparing Figure 3.9 and Figure 3.11: for the 10 W experiment, the air convection model did not make a large difference on the temperature profile.

### 4.3.2 Spiral Reactor Simulations with Static Acetic Acid

Since the condensation reaction uses acetic acid as the solvent, the simulations were ran with acetic acid as the reactor channel material. The relative permittivity of the solvent was set to  $6.2-1.0788i$ : the real part was taken from reference 92, and the imaginary part was calculated from the loss tangent value taken from reference 5, where acetic acid was listed with  $\tan \delta = 0.174$ . The permittivity is assumed to be independent of temperature to simplify the computation model. During the condensation experiments at 130 °C, the microwave power input fluctuated between 4 W to 6 W during steady-state. In order to simplify the computation, the model was simulated with constant power inputs of 4 W, 6 W, and 10 W; the last power setting was added to compare with the empty channel models. The estimated conductivity model was used with  $k = 0.05 \text{ W/m}^2\text{K}$ . The simulations were first performed with no flow in the reactors.

The results show that the temperature starts to plateau at after 60 minutes of irradiation at a constant power (Figure 4.6). The temperature measurement was taken at the tip of the slot the fiber optic probe was placed in; this position is shown as a red spot on the inserted picture in Figure 4.6. The final steady-state temperature for the three power settings 10 W, 6 W, 4 W are 225 °C, 139 °C, and 100 °C, respectively.

The experimental temperature measurement of 130 °C is within the range of the steady-state temperature for 4 W and 6 W, demonstrating that the simulation provides a good estimation for the microwave-heated acetic acid. The temperature profile at 10 W increased greatly with acetic acid added to the channel: the temperature reached 130 °C after 10 minutes of heating, while the temperature of the empty reactor slowly rose to 70 °C after the same time frame (Figure 4.5), showing the effect of microwave heating where a dielectric material such as acetic acid heats up much faster than the microwave transparent borosilicate reactor.

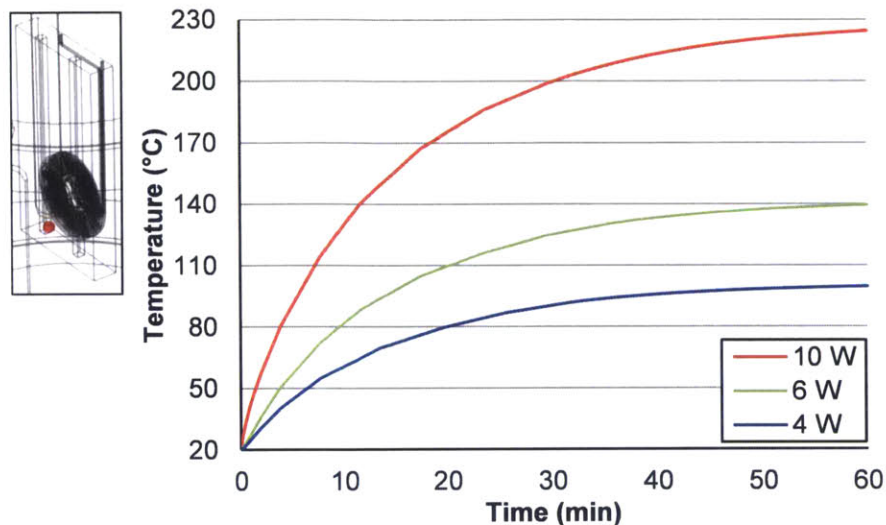


**Figure 4.6: Simulated temperature profile of spiral reactor filled with acetic acid under various power of microwave irradiation. (Insert shows the point of temperature measurement.)**

The average heating rate of the acetic acid was calculated for each power setting, and the results show that the heating rate is directly proportional to the microwave input power (Table 4.2). This linearity can be used to calculate the heating rate of the system at different input power as long as the objects inside the microwave cavity do not change in material or position.

**Table 4.2: Microwave heating rate versus irradiation power for spiral reactor channels with acetic acid.**

Irradiation power (W)	10	6	4
Average heating rate ( $\text{W}/\text{m}^3$ )	5.42E+06	3.25E+06	2.17E+06
Heating rate per input power ( $(\text{W}/\text{m}^3)/\text{W}$ )	5.42E+05	5.42E+05	5.42E+05

The details of the microwave interaction with the spiral reactor are inspected using the 6 W simulation as an example: The electric field resonates at the center of the cavity as a standing wave as expected, and is locally distorted by the reactor and reactor channels (Figure 4.7). An interesting observation is the diffraction pattern of the electric field along the reactor channels. The small, closely-spaced spiral channels scatter the electric field and leads to a wide range of electric field strength variation across the reaction volume. This phenomenon was not seen in the initial microreactor model and was not anticipated during design for the spiral reactor. The reaction channels are visibly parted into four different portions, with two portions having a much

weaker electric field than the other half of the channels. The electric field magnitude in the entire reaction volume ranges from 2832 V/m to 9125 V/m. The maximum value is more than three time larger than the minimum electric field strength.

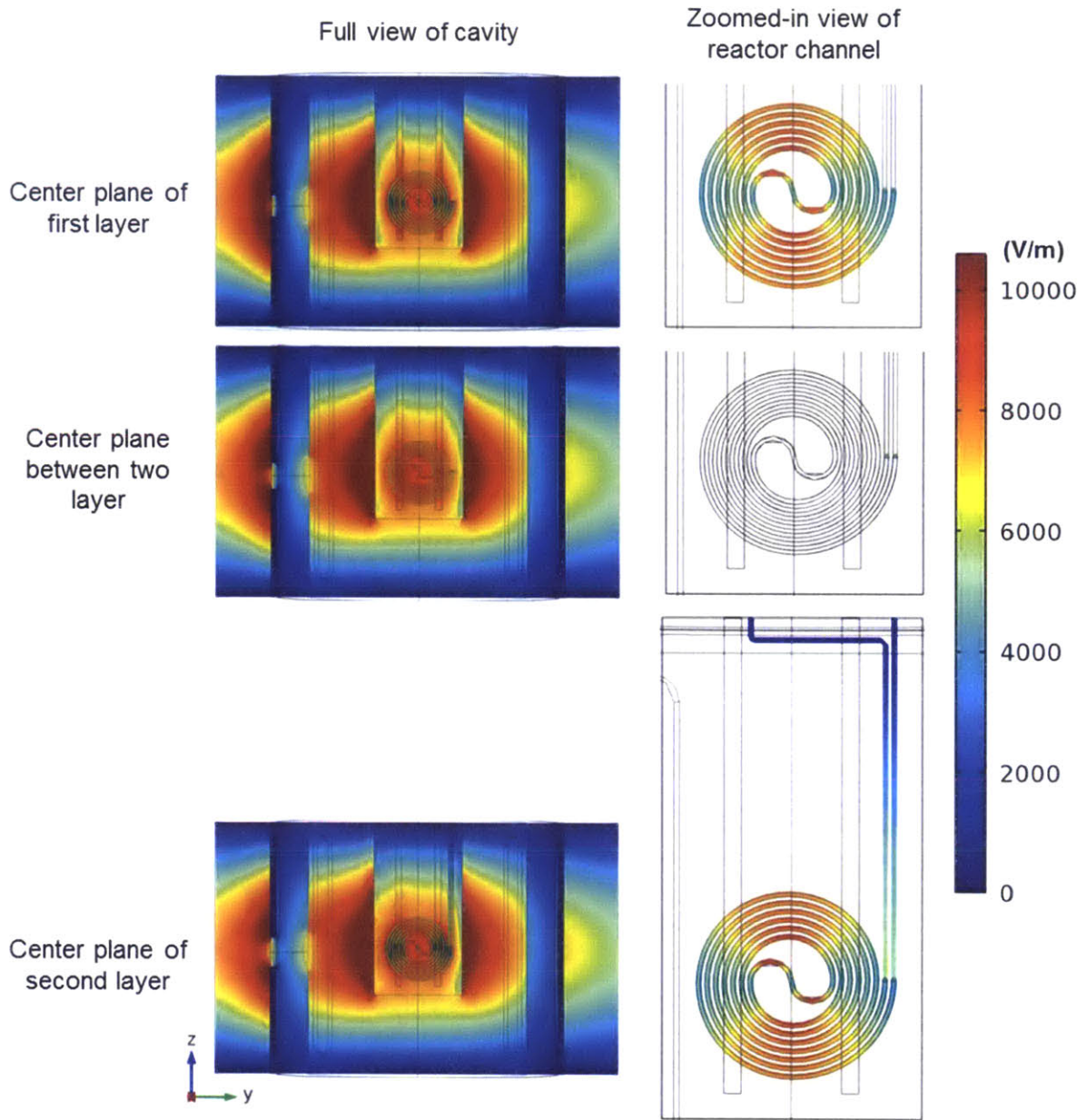


**Figure 4.7: Electric field strength of different planes viewed from the front side of the unit for spiral reactor under 6 W irradiation.**

The electric field diffraction results in an uneven heating rate across the channels, where half of the reaction volume is heated up ten times faster than the other half, ranging from  $5.9 \times 10^5 \text{ W/m}^3$  to  $6.1 \times 10^6 \text{ W/m}^3$  (Figure 4.8). An interesting observation is that the region of the



reaction channels with a lower heating rate heats up only as fast as the inlet and outlet channels of the reactor even though the entire reaction volume (the spiral portion) is sitting in the cavity center. This was an unexpected result since in the computational results from the initial reactor, the reactor heating rate of the center of the cavity (Figure 3.4) was the highest in the entire cavity and did not show diffractions that led to two zones of different heating rate.

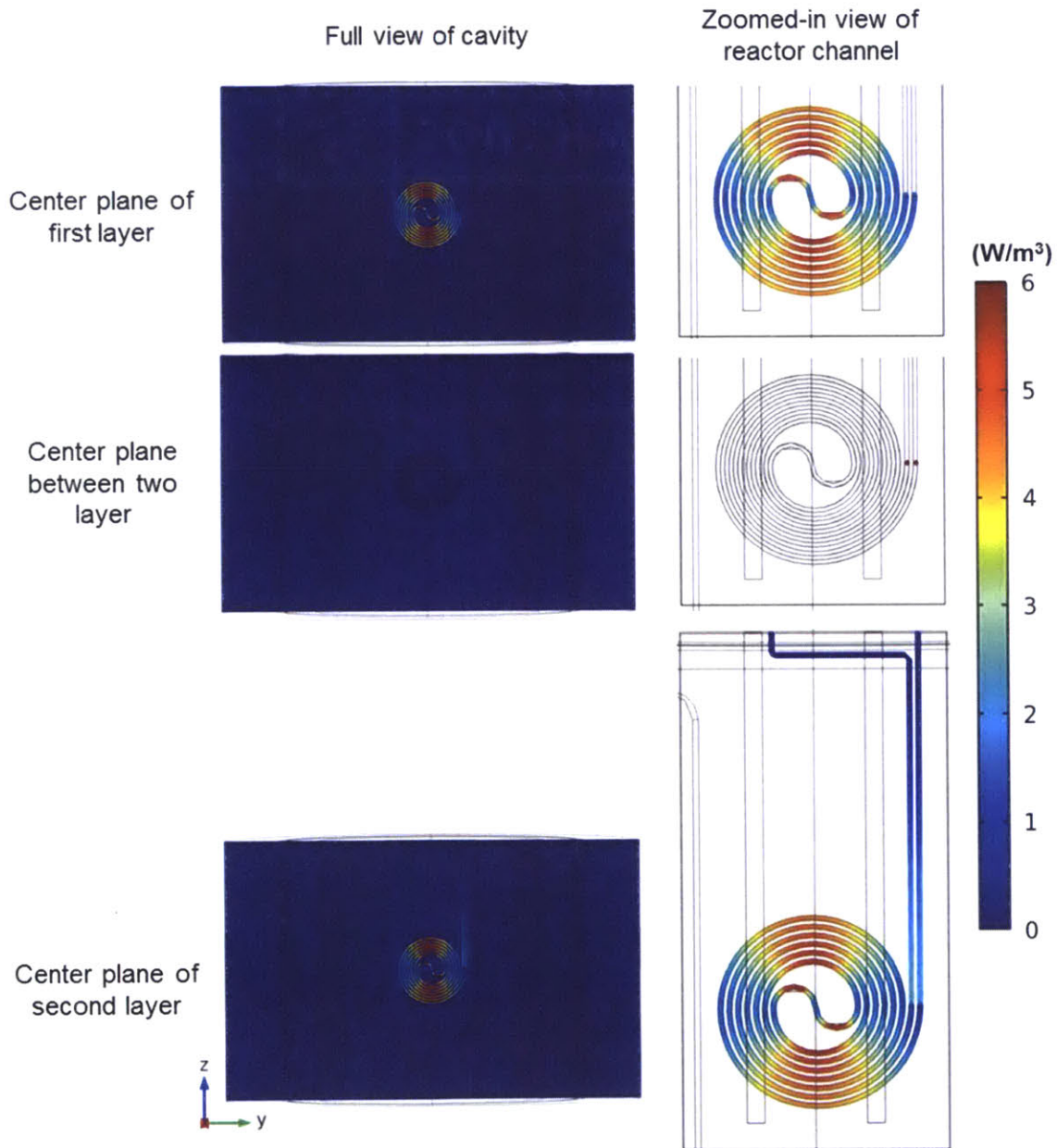


**Figure 4.8: Power dissipation density of different planes viewed from the front side of the unit for spiral reactor under 6 W irradiation.**

Aside from the microwave heating of the solvent, the reactor itself also absorbs a little bit of microwave energy. However, the heating rate of the borosilicate material is much lower than the lowest heating rate of the acetic acid in the reaction volume. The maximum heating rate of the reactor is about  $3 \times 10^5 \text{ W/m}^3$ , which is only around half as much as the lowest heating rate of the solvent. This demonstrates the inverse heating scheme in microwave heating as oppose to conventional heating: the volumetric heating of the dielectric solvents is the main heat source in the system, and the heat transfers from the solvent to the vessel instead of in the opposite direction.

Although the heating rate changes drastically along the reaction channels, the temperature of the reactor is eventually evened out by the conduction of the reactor and the air convection during the heating process (Figure 4.9). The reactors channels initially have higher temperature at the top and the bottom, but the temperature gradually rises up at the regions with lower heating rate. By 5 minutes of microwave heating, the temperature in the reaction channels is higher than the rest of the microreactor and the microwave cavity. The progress of the heating simulation shows that during the scale of seconds, the reactor channels have two separate zones of hot and cool area due to the diffraction heating pattern; however, when the heating time progresses to the scale of minutes, the reactor conduction and air convection take over, and the spiral portion of the channels are all within the same temperature range that is higher than the rest of the cavity.

The results after 60 minutes of heating show that the temperature of the reactor still decreases radially from a position near the cavity center due to the single-mode microwave resonance structure (Figure 4.10). The spiral design allows the entire reaction volume to be within the center region that is close to the set temperature for the experiments. However, some portion of the channels surpass the set temperature, and the temperature variation in the channels is fairly large. The temperature ranges from 134 °C to 155 °C in the reaction volume (from dark orange to dark red on the color bar of Figure 4.10), while the temeperature at the fiber optic point of measurement is 139 °C.

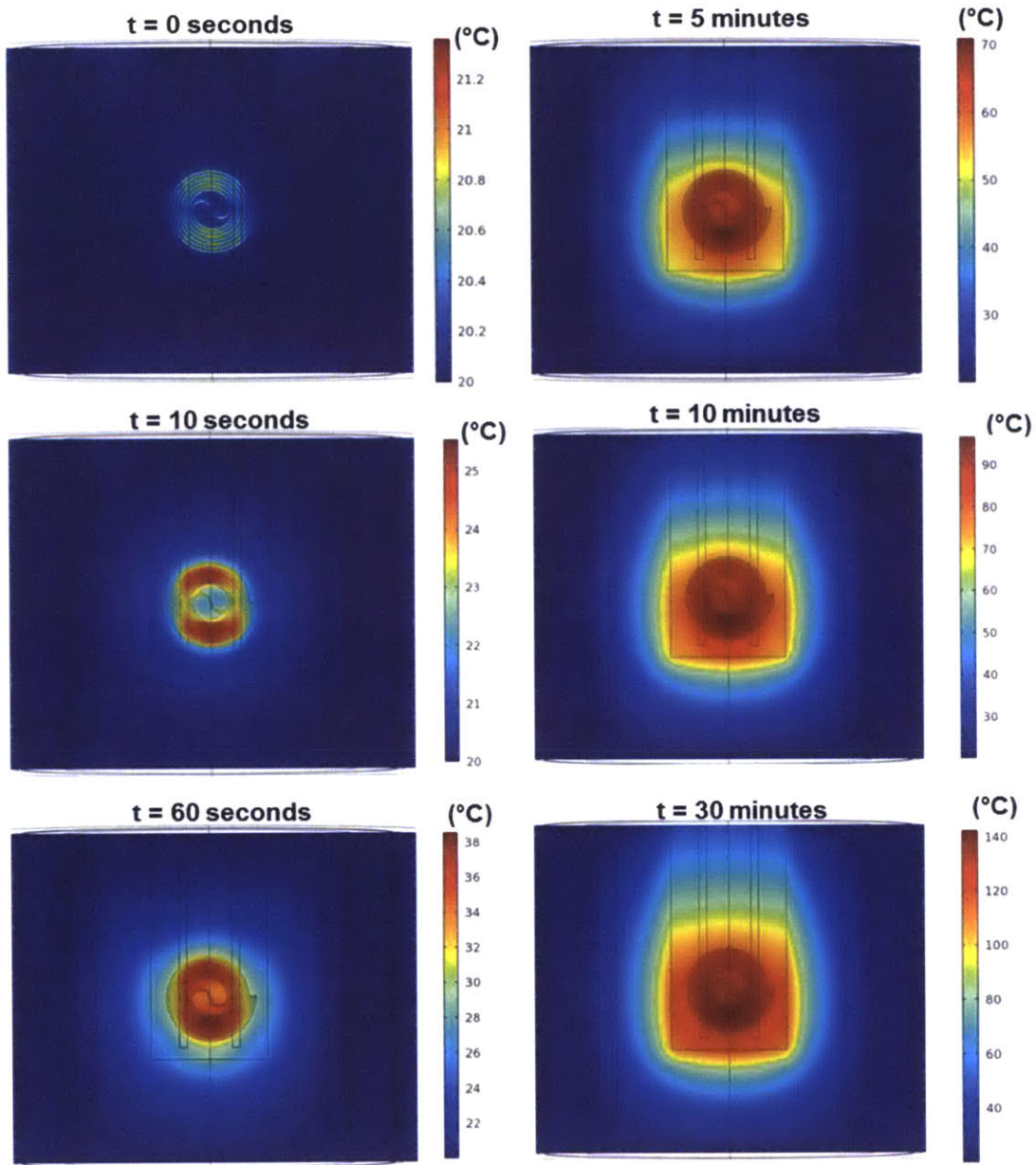
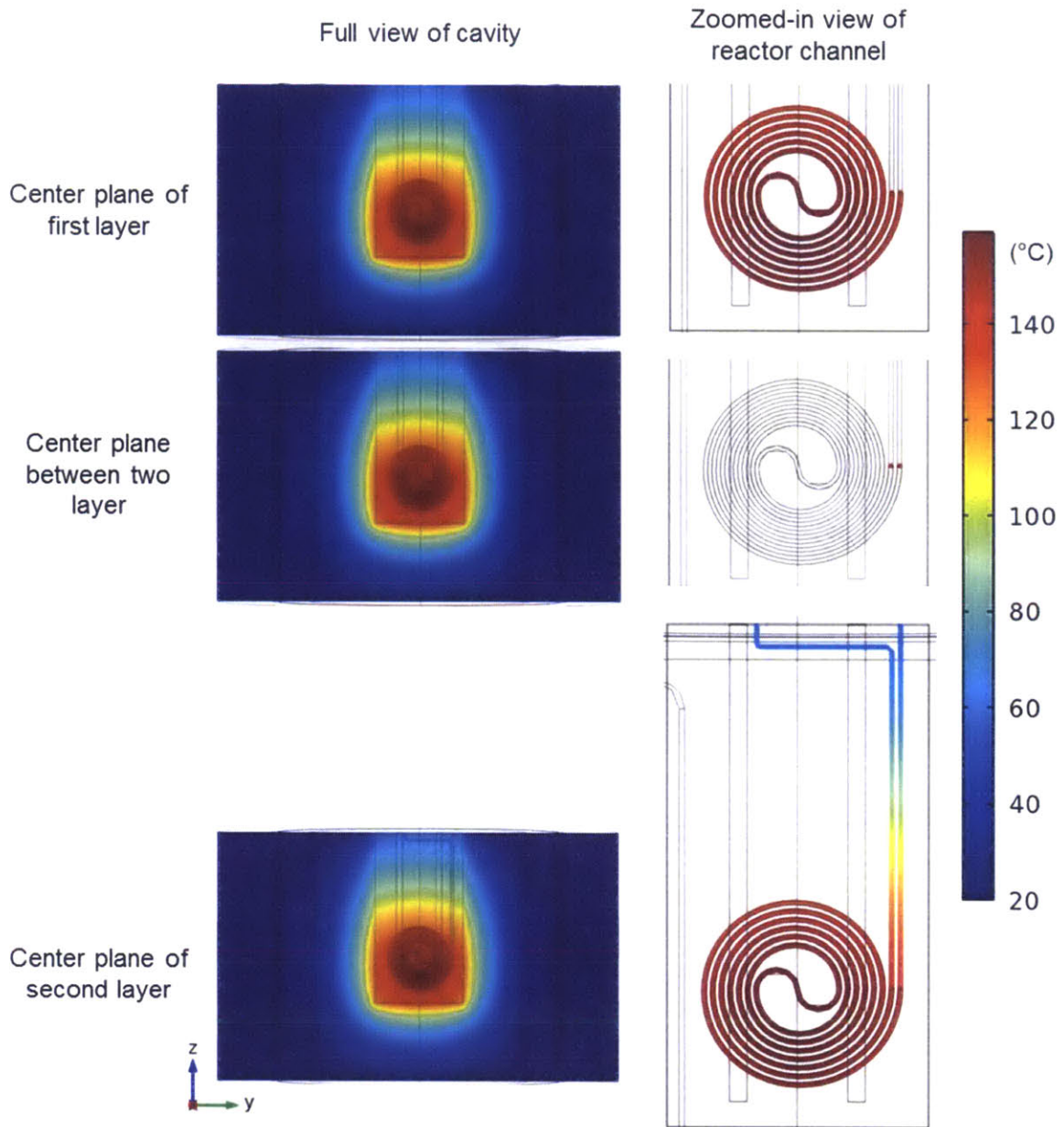


Figure 4.9: Temperature of reactor center plane viewed from the front side of the unit for spiral reactor under 6 W irradiation at different time points.



**Figure 4.10: Temperature of different planes viewed from the front side of the unit for spiral reactor at  $t=60$  minutes under 6 W irradiation.**

From the point of view of the flow according to the 2D plot (Figure 4.10), it enters the highest temperature zone once it reaches the inlet to the spiral channels and goes through a concave temperature change in the reaction zone: as the flow moves along the spiral channels, its temperature gradually rises until it reaches the position around the reactor center, and then the temperature decreases as it flows away from the reactor center. However, the 1D plot of the

temperature along the reactor channel shows that the temperature variation is slightly more complicated than a simple concave function (Figure 4.11).

The temperature measurement of the reaction volume is taken as the direction of the flow starting at the position where the flow enters the spiral portion and ending at the position where the flow leaves the spiral channels (insert of Figure 4.11). The temperature is taken from the spiral layer that is closer to the fiber optic probes. The temperature profile shows that the warmest part in the reaction volume is actually the bottom of the spiral channels, around a 90 degrees turn from the position of the channel entrance; and the coolest part is the top of the spiral channels, around a 270 degrees angle from the from the position of the channel entrance. For each full turn of the spiral channel, the fluid temperature rises to a local maximum at the bottom portion of the channels and decreases to a local minimum at the top of the spirals. The oscillation magnitude between the local maximum and minimum of each full turn decreases as the channels get small and closer to the spiral center, and then increases again as it flows out from the spiral center. The overall effect is that the flow temperature is roughly a concave profile that peaks at the center of the reaction volume; and within this concave profile, the temperature changes as a local concave curve for each full spiral turn. The hottest point in the entire reactor volume is at the most inner channel at the bottom of the spirals, while the point with the lowest temperature is at the most outer channel at the top of the spiral channels.

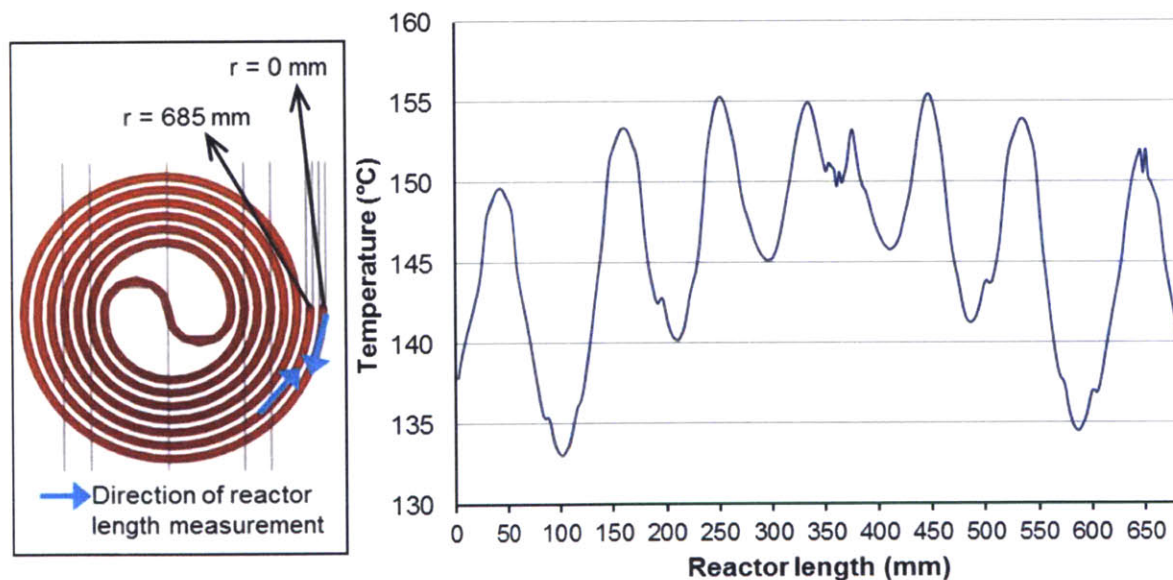


**Figure 4.11: Temperature along the reaction volume in the spiral reactor at t=60 minutes under 6 W irradiation.**

The temperature change that the fluid goes through in the reactor is very drastic. The temperature variation in the entire reaction volume is more than 20 °C and the change in each spiral turn ranges from 5 °C to 15 °C. The results demonstrate that a uniform temperature distribution in the reaction volume still cannot be achieved with the new reactor design. Without a good control of the temperature, kinetic studies of microwave chemistry is still not feasible.

The variation of the electric field along the depth of the reactor is not as large as the variation across the width of the reactors (Figure 4.12). This is partly because of the direction of the electric field coupling, and partly because there is not that many number of closely-spaced channels to diffract the electric field. Since the electric field does not change a lot in this direction, the heating rate is also fairly uniform across the reactor depth (Figure 4.13). Therefore, the temperature variation in the channels across the depth of the reactor is not as significant as the variation across the radial direction of the spiral (Figure 4.14). The temperature differences across the two layers are less than 1 °C for the same position along the flow direction (same y, z position on the plot).

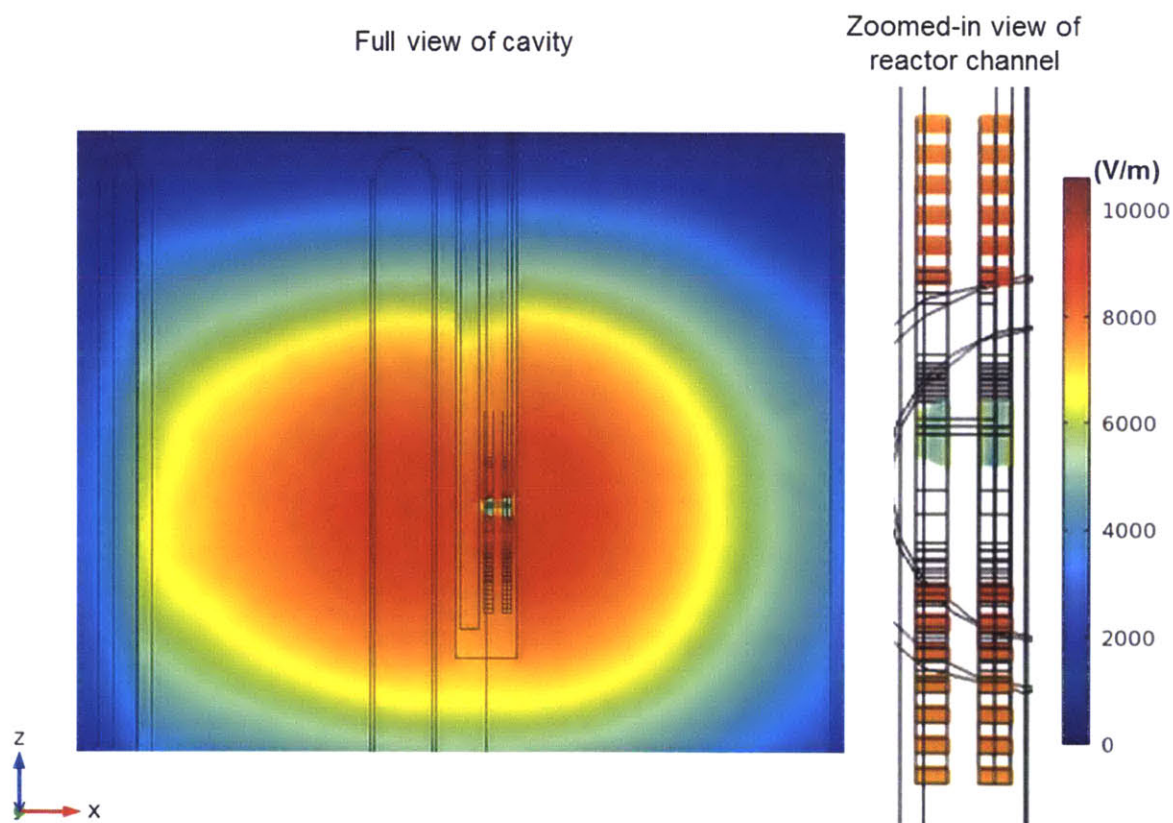


**Figure 4.12: Electric field strength of cavity and waveguide center plane viewed from the right side of the unit for spiral reactor at t=60 minutes under 6 W irradiation.**

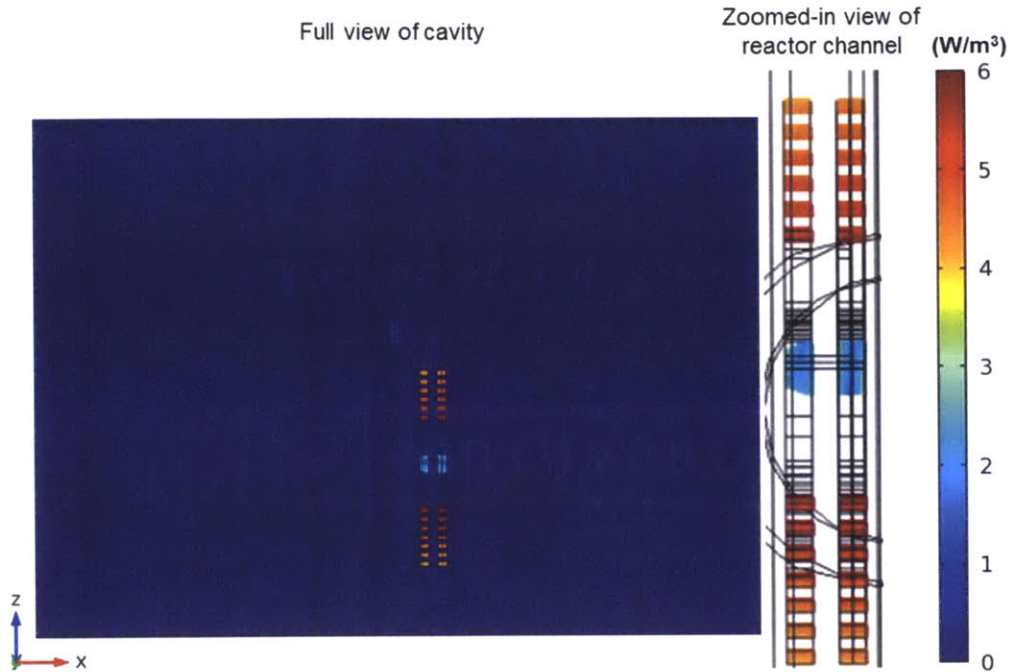


Figure 4.13: Power dissipation density of cavity and waveguide center plane viewed from the right side of the unit for spiral reactor at  $t=60$  minutes under 6 W irradiation.

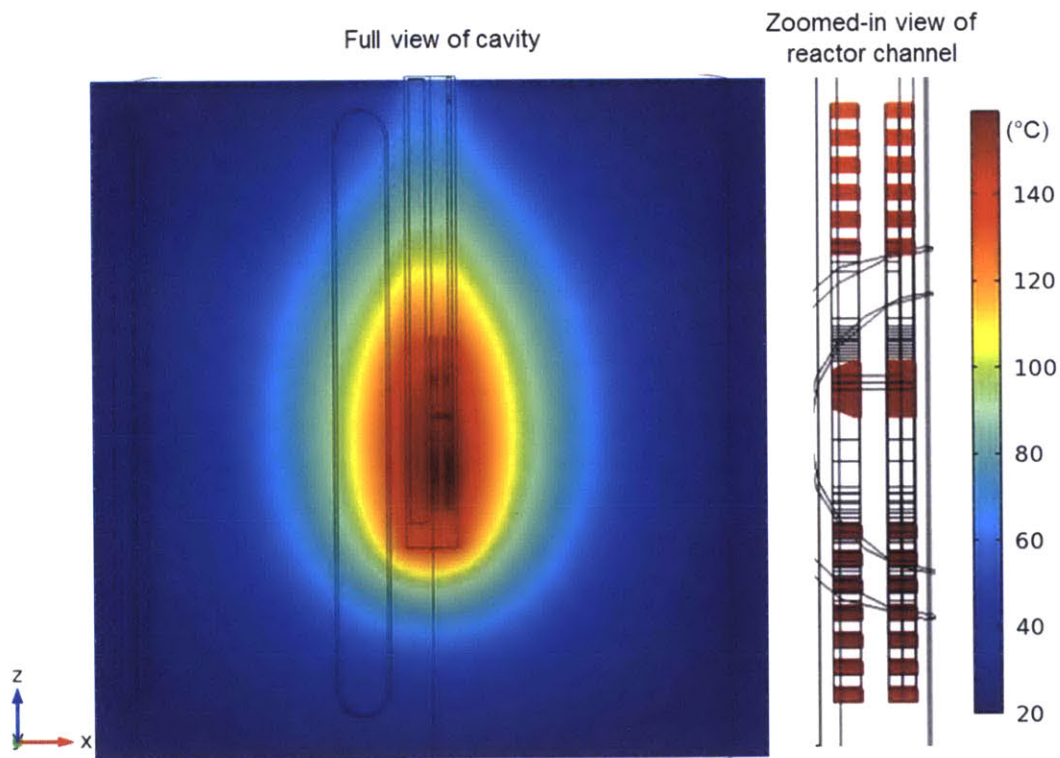


Figure 4.14: Temperature of cavity and waveguide center plane viewed from the right side of the unit for spiral reactor at  $t=60$  minutes under 6 W irradiation.





## CHAPTER 5. VERIFICATION EXPERIMENTS

---

### 5.1 Introduction

In this chapter, the chemistries performed with the final setup are presented along with a temperature estimation model derived from the condensation calculation and the simulation results from Chapter 4. The new spiral reactor was tested with the same condensation reaction and produced repeatable results. The conversion data were used to calculate the actual mean temperature of the reaction volume for each experimental setting. The results were used with the simulated temperature profiles to demonstrate that that reactor is at the thermal entrance region of the microwave heated system. The temperature calculations also provided an understanding on how the actual temperature in the system can be estimated with the computational models along with the known microwave power at steady-state. Finally, a set of Fischer indole reactions was run to demonstrate the application of the setup in reaction screening.

### 5.2 Condensation Reaction Kinetics

#### 5.2.1 Direct Microwave Heating at Two Different Positions

The condensation reaction of *o*-phenylenediamine and acetic acid (Scheme 2.2) was tested on the new spiral microreactor. To avoid the reactor breaking due to rapid heating, the maximum microwave power was set to a 100 W during all experiments. The reactor was capable of reaching the set temperatures even at the perpendicular-to-port position where the heating rate is the lowest.

The experimental data are repeatable in the new reactor as long as the position of the reactor is set at the same angle: Figure 5.1 shows that the standard deviations of the conversion results are within 5 % except for the last three residence times at 130 °C at the parallel position; all the experiments were repeated at least three times. The conversion results are all higher than expected from the kinetic data, and the results at different position even at the same reaction setting are not the same. The conversions are on average 6.6 % lower when the reactor is positioned perpendicular, instead of parallel, to the microwave port.

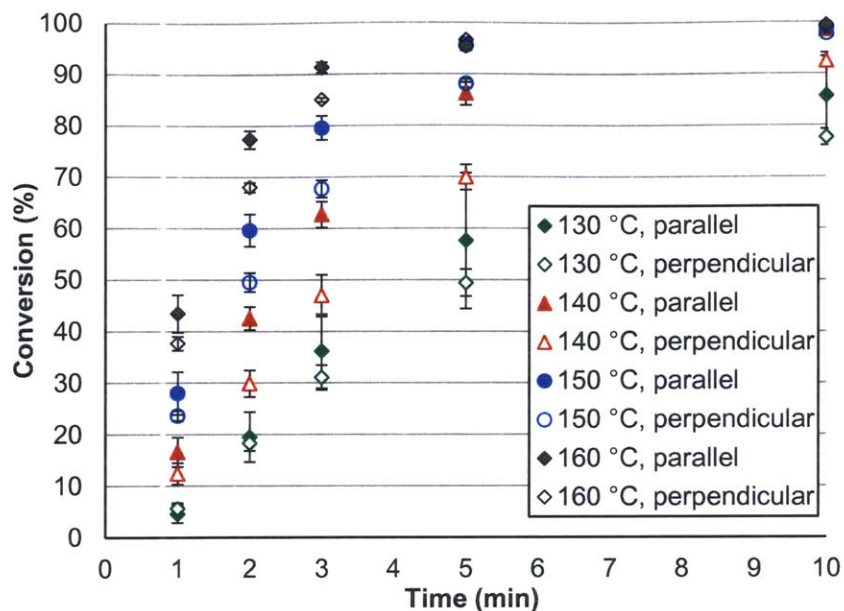


**Figure 5.1: Conversion data of condensation reaction of *o*-phenylenediamine and acetic acid from spiral microreactor.**

The reaction conversion has a first order reaction rate in respect to the diamine concentration. With the kinetic parameters calculated from the literature<sup>73</sup> and from our cartridge-heated experiments, we used the conversion data to calculate the average mean temperature of the reaction in our microwave-heated microreactor for each reaction condition, which includes the set temperature, residence time, and reactor position in the cavity (Table 5.1, Table 5.2).

The results show that the difference between the mean temperature and the set temperature rises as the residence time increases. The only exceptions are when the reaction is nearly complete (conversion > 97 %). This shows that the temperature distribution of the reaction changes with different residence time at the same temperature settings as measured by the fiber optic probe: the longer the residence time, the higher the temperature ranges for the reaction. This is consistent with the mechanism of microwave heating where the liquid is heated up directly under irradiation. If the heating rate is the same for the solvent at all time in the system, the longer the solvent stays in the microwave cavity, the higher its temperature gets, and thus resulting in an overall higher temperature distribution for higher residence time. The effect is demonstrated by simulating the heat transfer phenomenon in COMSOL and will be discussed in Chapter 5.3.

The lower conversions for the reactor at the perpendicular-to-port position also indicated the reaction actual mean temperatures are lower at this position. This is again consistent with the microwave heating results shown in Chapter 3: when the reactor is placed at the perpendicular position, the microwave heating rate is lower due to a weaker electric field.

**Table 5.1: Condensation results and kinetic mean temperature calculation from spiral microreactor at parallel-to-port position.**

Residence time (min)	Set/Measured temperature (°C)	Conversion (%)	Temperature calculated from conversion (°C)	Difference (°C)
1	130	4.6 ± 1.7	123 ± 6	-7
2	130	19.5 ± 4.8	138 ± 4	8
3	130	36.1 ± 7.2	144 ± 4	14
5	130	57.6 ± 13.2	146 ± 6	16
10	130	85.7 ± 8.3	149 ± 5	19
1	140	16.6 ± 2.9	147 ± 3	7
2	140	42.5 ± 2.2	156 ± 1	16
3	140	62.7 ± 2.5	159 ± 1	19
5	140	86.2 ± 2.3	163 ± 1	23
10	140	98.5 ± 0.9	164 ± 3	24
1	150	28.0 ± 4.1	159 ± 3	9
2	150	59.6 ± 3.1	166 ± 1	16
3	150	79.6 ± 2.3	169 ± 1	19
5	150	95.6 ± 1.0	172 ± 1	22
10	150	99.0 ± 0.5	166 ± 2	16
1	160	43.4 ± 3.7	170 ± 2	10
2	160	77.4 ± 1.7	176 ± 1	16
3	160	91.3 ± 1.1	178 ± 1	18
5	160	95.4 ± 0.7	172 ± 1	12
10	160	99.2 ± 0.2	167 ± 1	7

**Table 5.2: Condensation results and kinetic mean temperature calculation from spiral microreactor at perpendicular-to-port position.**

Residence time (min)	Set/Measured temperature (°C)	Conversion (%)	Temperature calculated from conversion (°C)	Difference (°C)
1	130	5.6 ± 1.1	127 ± 3	-3
2	130	18.3 ± 1.5	136 ± 1	6
3	130	31.1 ± 2.4	140 ± 1	10
5	130	49.4 ± 2.6	142 ± 1	12
10	130	77.7 ± 1.6	144 ± 1	14
1	140	12.4 ± 2.1	141 ± 3	1

Residence time (min)	Set/Measured temperature (°C)	Conversion (%)	Temperature calculated from conversion (°C)	Difference (°C)
2	140	29.9 ± 2.6	147 ± 2	7
3	140	46.9 ± 4.0	150 ± 2	10
5	140	69.9 ± 2.4	153 ± 1	13
10	140	92.4 ± 1.0	154 ± 1	14
1	150	23.6 ± 1.0	155 ± 1	5
2	150	49.5 ± 1.8	160 ± 1	10
3	150	67.7 ± 1.7	162 ± 1	12
5	150	88.2 ± 0.8	164 ± 1	14
10	150	97.9 ± 0.6	162 ± 1	12
1	160	37.6 ± 1.3	166 ± 1	6
2	160	68.0 ± 1.0	170 ± 0.4	10
3	160	85.1 ± 0.4	173 ± 0.2	13
5	160	96.6 ± 0.5	174 ± 1	14
10	160	99.4 ± 0.4	168 ± 2	8

### 5.2.2 Experiments with a Microwave-Shielding Glycerol Bath

In order to demonstrate that the enhanced temperature difference in the above experiments is due to the large heating rate of the solvents under direct volumetric heating, the same microwave reaction was repeated with the reactor immersed in a glycerol bath. A 100 mL beaker filled with 80 mL glycerol was placed into the microwave cavity before the microreactor in put onto the microwave attenuator. The level of the glycerol is high enough that the glycerol completely covers the spiral channel portion of the microreactor. This setup was designed to mimic a conventionally heated setup: since glycerol absorbs microwave faster than acetic acid, which is the reaction solvent, the reactor is heated up mostly by heat conduction from the glycerol jacket. Setups with this concept have been used by both Oliver C. Kappe and the Albert E. Stiegman and Gregory B. Dudley team to study microwave effects. The Kappe group has used strong microwave-absorbing silicon carbide vials to shield reactions from microwave irradiation and comparing the results to reactions in Pyrex vials.<sup>40-41</sup> In Albert E. Stiegman and Gregory B. Dudley report on the Friedel-Crafts benzylation of deuterated *p*-xylene, they used the strong microwave-absorbing propylene glycol as a heating jacket to demonstrate the effect of microwave on the benzylation.<sup>44</sup>

Although our reaction is not reported with any special microwave heating effect, immersing the reactor in glycerol lowered the extremely high volumetric heating the acetic acid

receives from the microwave since the microwave power was mostly absorbed by the glycerol solution. The glycerol also acted as a heating jacket that ensured a uniform heating across the surface of the reactor as oppose to the heating distribution observed in previous experiments and simulations. Due to safety concerns, glycerol was chosen since it was the only solvent with a highly loss tangent than acetic acid that has a flash point (160 °C) higher than the experimental temperature range. Only the experiments at 130 °C and 140 °C were repeated with the reactor kept at the parallel-to-port position.

Figure 5.2 and Table 5.3 show that the conversions obtain from the glycerol bath are lower than the directly microwaved spiral reactor and match the expected values from the kinetic data. The average temperature calculated from the conversion data is all within 3 °C difference of the temperature measured from the fiber optic probe. The glycerol bath successfully acted as a heating jacket and recreated a conventional heating setup. These results therefore demonstrate that under direct microwave irradiation, the solvent temperature in the reaction channel still has a wide range of distribution that cannot be properly interpreted by a single point fiber optic temperature measurement.

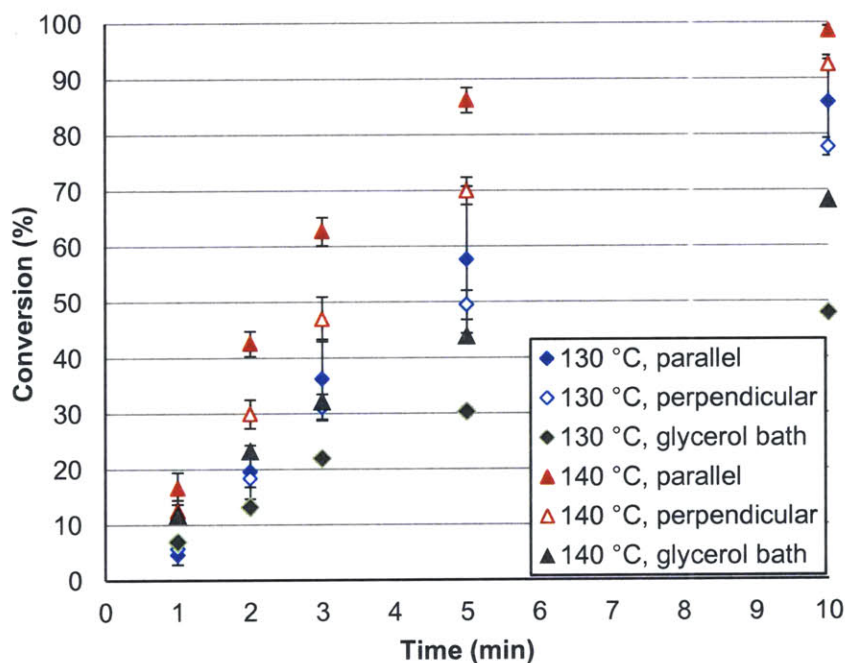


**Figure 5.2: Conversion data of condensation reaction of *o*-phenylenediamine and acetic acid from spiral microreactor.**

**Table 5.3: Condensation results and kinetic mean temperature calculation from spiral microreactor heated with glycerol bath.**

<b>Residence time (min)</b>	<b>Set/Measured temperature (°C)</b>	<b>Conversion (%)</b>	<b>Temperature calculated from conversion (°C)</b>	<b>Difference (°C)</b>
1	130	6.9	130	0
2	130	13.1	130	0
3	130	21.9	133	3
5	130	30.3	130	0
10	130	47.9	129	-1
1	140	11.8	140	0
2	140	23.3	141	1
3	140	32.2	141	1
5	140	43.9	139	-1
10	140	68.2	139	-1

## 5.3 Temperature Results of Reactor Models with Flow

### 5.3.1 Kinetic Mean Temperature Definition

The condensation reaction in Chapter 5.2.1 gave higher conversions than the expected values calculated from the kinetic parameters. The calculations from the conversion data show that not only are the mean temperatures in the reaction channels actually higher than the fiber optic measurement, the mean temperature increases with higher residence time.

The simulation results of the irradiated spiral channels confirm that the measurement inaccuracy is due to the uneven heating (Figure 4.10). The electric field oscillates around the center of the microwave cavity, causing heating rates of the liquid in the microchannels to change at different positions, leading to different temperatures throughout the reaction channels. The temperature of the spiral reactor gradually increases along the direction of the flow and reaches the highest temperature at the reactor center; then the temperature decreases as it flows away from the reactor center. In the case where the reaction solvent is not flowing and is subjected to 6 W of microwave irradiation, the temperature of the reaction channel ranged from 134 °C to 155 °C while the fiber optic measurement was 139 °C. The actual mean temperature calculated from the conversions in Chapter 5.2.1 is therefore an average of the temperature that is integrated over the Arrhenius equation with respect to the residence time:

$$-\frac{dC_1}{dt} = kC_1 = Ae^{-\frac{E_a}{RT(t)}} \times C_1 \quad (5.1)$$

$$\frac{1}{A} \times \int -\frac{dC_1}{C_1} = \int_0^{t_{res}} e^{-\frac{E_a}{RT(t)}} dt = e^{-\frac{E_a}{RT_{avg}}} \times t_{res} \quad (5.2)$$

$$T_{avg} = -\frac{E_a}{R} \times \left[ \ln \left( \int_0^{t_{res}} e^{-\frac{E_a}{RT(t)}} dt \right) - \ln(t_{res}) \right]^{-1} \quad (5.3)$$

where  $E_a$  is the reaction activation energy,  $R$  is the universal gas constant,  $t_{res}$  is the total residence time,  $T(t)$  is the function of the temperature with respect to the time in the reactor, and  $T_{avg}$  is the actual mean temperature. It is important to note that the actual mean temperature calculated with the integral over the Arrhenius equation is not the same as the volume average temperature of the reaction channel. In order to distinguish between the two average temperatures, the actual mean temperatures calculated with the Arrhenius equation will be termed the “kinetic mean temperature” in this thesis. The kinetic mean temperature is the same for all residence time if the temperature distribution in the reactor is the same. These calculations are confirmed by integrating the Equation (5.3) over different  $T(t)$  in Matlab (Appendix C.2).

Since the kinetic mean temperature does not vary with residence time for the same temperature distribution, the variation of the kinetic mean temperature in Table 5.2 and Table 5.3 for the same temperature settings indicates that the reaction temperature distribution also changes with residence time. This means the flow rate affects the steady-state heat transfer results, and the spiral reactor simulation was updated accordingly to include the effect of flow in the channels.

### 5.3.2 Spiral Reactor Simulations with Flow

The spiral reactor model in Chapter 4.3.2 was simulated with static acetic acid in the reactor channels. To incorporate solvent flow into the model, the Laminar Flow Interface was added for the reaction channels. The flow rates for the residence time used in the experiments all fall within the laminar flow regime, with the highest Reynolds number being 3.7 at the largest flow rate (Table 5.5). The Reynolds numbers were calculated using the hydraulic diameter of the channels by approximating the channel cross sections as 0.5 mm by 1 mm rectangles. Because of the large ratio of the channel length to channel width, the flow was assumed to be unidirectional and fully developed. For a cylindrical tube with a diameter equivalent to our reactor’s hydraulic

diameter, the entrance length required to reach fully developed flow is about 1.06 mm for the largest flow rate.<sup>82</sup> Given that our reactor channel lengths are a couple of hundred millimeters, the fully developed flow is a valid assumption.

In order to further simplify the computation, the COMSOL interface was set to the Creeping Flow option, where the program ignores the inertial term ( $\mathbf{v} \cdot \nabla \mathbf{v}$  in Equation (3.14)). Creeping flow assumptions can be made when the Reynolds number is close to zero.<sup>82</sup> To verify if the Creeping Flow option was valid assumption for our simulations, a simple simulation was run to solve the fluid dynamics and heat transfer of the reactor geometry solely without the microwave unit. The heating rate of the fluid was set as the volumetric average heating rate calculated from the 6 W microwave simulation (Table 4.2). Although the Reynolds numbers were not all smaller than 1 for the flow rates inspected, the average velocity calculated with and without the creeping flow assumption were within 5 % difference (Table 5.4). Furthermore, the kinetic mean temperatures and average temperatures calculated with the creeping flow assumption differ less than 1 °C from the temperatures calculated without the creeping flow assumption (Table 5.4). The creeping flow option was therefore implemented in the full simulation with the microwave heating to reduce computational cost.

**Table 5.4: Laminar flow and creeping flow simulation comparison.**

Residence time (min)	Average velocity magnitude (m/s)		Reynolds number		Kinetic mean temperature (°C)		Volumetric average temperature (°C)	
	Laminar flow	Creeping flow	Laminar flow	Creeping flow	Laminar flow	Creeping flow	Laminar flow	Creeping flow
1	7.10E-03	6.80E-03	4.1	3.9	136.8	137.2	135.8	136.2
2	3.50E-03	3.40E-03	2.0	1.9	140.6	140.8	139.3	139.5
3	2.40E-03	2.30E-03	1.4	1.3	141.9	142.0	140.5	140.6
5	1.40E-03	1.40E-03	0.8	0.8	142.8	142.8	141.3	141.3
10	7.08E-04	6.77E-04	0.4	0.4	143.4	143.3	141.8	141.7

The reaction channels were also selected for the “Heat Transfer in Fluids” node plus the “Wave Equation” node that was added to the original model, while the remaining geometry is modeled in the “Microwave Heating” node. In the velocity field of the reaction channels in the Heat Transfer in Fluids node was linked as an output from the Laminar Flow Interface. The residence time was set as a changeable parameter in the model. The inlet boundary of the reaction channels was set at a flow rate of the reaction volume over the residence time, and the



model was run by sweeping through the five different residence times used in the condensation chemistry. The simulation was set to model the results for the 130 °C experiments with the reactor parallel-to-port. Since the power input oscillated around 6 W during the experiments at 130 °C, the simulation was set at a constant 6 W power input and the models was solved for the steady-state results.

The reactor mean temperatures of the simulated results were calculated with Equation (5.3). The simulation follow the trend of the kinetic mean temperature calculated by the experimental results, showing a different temperature distribution for different residence times with the kinetic mean temperature increasing for the longer residence times (Table 5.5). However, the experimental kinetic mean temperature variations among different residence times are about two to three times larger than that of the computational calculation. The kinetic mean temperatures calculated from the simulations are between 1 °C to 16 °C lower than the experimental values. One of the main sources of the discrepancy is that the experiments were not run under constant power settings. During the experiment, the microwave was set to a target temperature, and the power is automatically adjusted by the CEM software to maintain the temperature at the set point. The power varies every couple of second between 4 W and 8 W during the experiments, and the oscillation pattern is not exactly the same for each repeated experiment. The constant power assumption in the simulation does not fully capture the experimental settings. Another cause of the discrepancy between the simulated and experimental mean temperatures is that the actual permittivity of the reaction is unknown and could not be implemented in the simulation. The permittivity used in the simulation was that of the pure solvent, acetic acid, at 20 °C, whereas the actual permittivity of the reaction is different due to the presence of reactants and products and also due to the varying temperature. The effects of the input power and permittivity will be discussed in Chapter 5.3.3. Other oversights of the model may include the lack of the flow model of the air gaps to properly account for the natural convection, and the rough approximation of the heat loss to the environment outside of the waveguide.

Although the temperatures are not an exact match, the results qualitative demonstrate the large temperature variations and the effect of flow rate in the reactor. Both results show a large decrease in temperature from the 2-minute residence time to the 1-minute residence time setting. The kinetic mean temperature difference between the 1-minute residence time setting and the 2-

minutes residence time setting is even higher than the kinetic mean temperature difference between the 2-minute residence time setting and the 10-minute residence time setting.

**Table 5.5: Results from spiral reactor flow simulations with acetic acid as solvent and 6 W microwave irradiation.**

<b>Residence time (min)</b>	<b>Average velocity magnitude (m/s)</b>	<b>Reynolds number</b>	<b>Kinetic mean temperature from simulations (°C)</b>	<b>Experimental kinetic mean temperature (°C)</b>
1	6.40E-03	3.7	121	123 ± 6
2	3.20E-03	1.8	129	138 ± 4
3	2.10E-03	1.2	131	144 ± 4
5	1.30E-03	0.7	132	146 ± 6
10	6.44E-04	0.4	133	149 ± 5

Similar to the temperature variation saw in Figure 4.11 along the reactor length, the temperature in the reaction volume for each flow rate follows the rough concave profile with oscillations in every full turn along the spiral pathway (Figure 5.3). The temperature of the acetic acid with no flow is also included as reference. The temperature profile when there is no flow is the maximum limit the reactor could reach under 6 W irradiation. The temperature of the entire reactor decreases with increasing flow rate (smaller residence time). The huge gap between the temperature at 1-minute residence time and that of the other residence times is also shown in then simulation.

The large uneven temperature distribution still exists at every flow rate. The overall temperature differences are about 20 °C for all flow rates. However, the magnitude of the temperature oscillation in each spiral turn decreases with increasing flow rate, and the temperature profile is slightly closer to a single concave curve. The drastic change of the temperature along the reaction channel is a challenge for exact temperature measurements and control for kinetic studies. Furthermore, the simulation can only provide guidance and rough estimations of the heating patterns, and an exact prediction of the temperatures is difficult to make without a more complicated model.

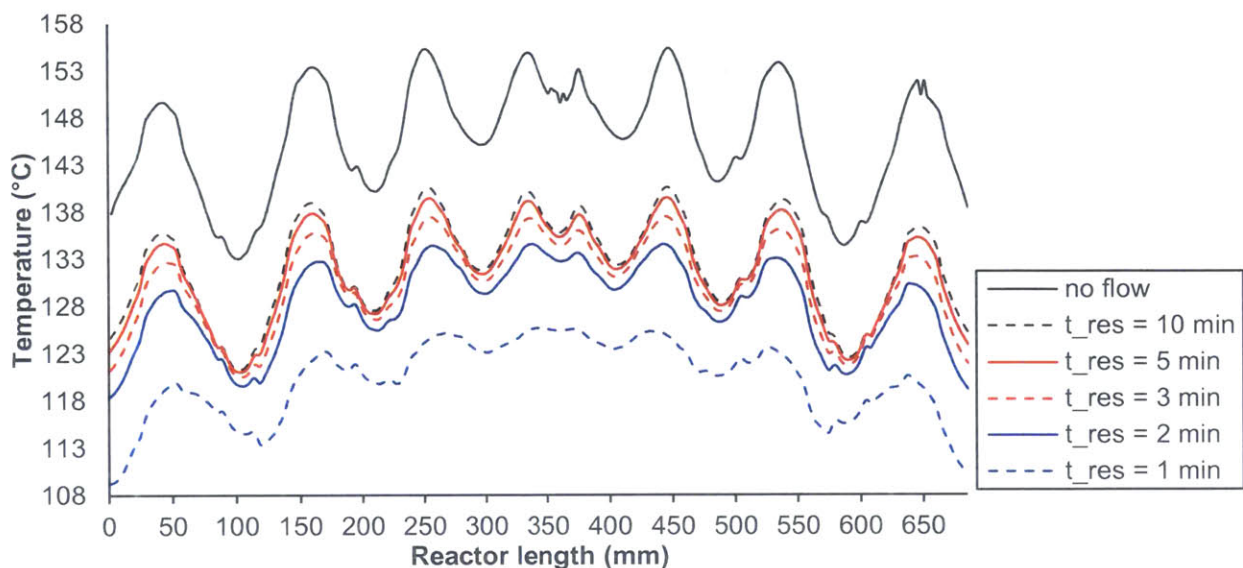


**Figure 5.3: Temperature along the reaction volume in the spiral reactor under constant 6 W irradiation for continuous flow with different residence times.**

### 5.3.3 Simulation Parameter Sensitivity

The simulated kinetic mean temperature is about 1 to 16 °C lower than the experimental values (Table 5.5). The two main causes of the discrepancy are the assumption of a constant power input at 6 W and the assumption of a constant permittivity of the reaction solution. Additional simulations were run with different values of the input power and reaction permittivity to understand the effect of these two parameters on the simulated kinetic mean temperature.

In the original simulation for the kinetic mean temperature calculation, the steady-state result was obtained assuming a constant input power of 6 W. While during the experiments, the power automatically varies every couple of second between 4 W and 8 W to maintain the desire temperature of 130 °C, and the power oscillation pattern is not exactly the same for each repeated experiment. The actually power input is therefore hard to recreate in the simulations. A model with a varying power input would also be a larger computational problem since it has to be solved as a transient problem and the steady-state solution cannot be directly solved for. Furthermore, the power input shown in the experiments was the nominal power input of microwave unit, the actual power irradiated by the magnetron varies for each specific microwave unit.<sup>43, 93</sup> The 6 W power input is therefore the ideal average value observed from the experiments. For the parameter sensitivity study, the input power was changed from 2 W to 10

W with a 1 W increment, the minimum input power variation the microwave unit works at. The simulations solved for the steady-state power and temperature distribution.

Both the power dissipation and kinetic mean temperature of the reaction volume vary linearly with the input power (Figure 5.4, Figure 5.5). Every 1 W of input power variation leads to a 0.2 W change in the total reaction heating rate (Figure 5.4, linear regression slope = 0.1996). The kinetic mean temperature sensitivity towards the input power varies slightly with the reaction flow rate, ranging between 16.84 °C/W to 21.92 °C/W (Figure 5.5) with an average of 18.87 °C. The parameter sensitivity shows that even a 1 W error in the power estimation can result in about a 19 °C inaccuracy in the simulated temperature result. The 19 °C temperature variation is larger than the 1 to 16 °C differences between the simulation and experiments. Therefore, the sensitivity demonstrates that the power input is indeed one of the main causes of the temperature underestimation of the simulation.

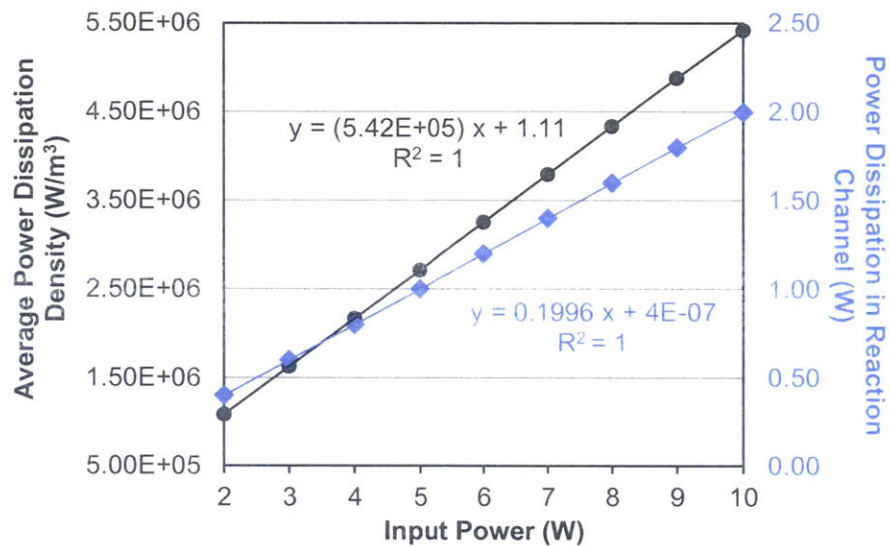


**Figure 5.4: The input power dependencies of the average power dissipation density (●) and the total heating rate in the reaction volume (◆).**

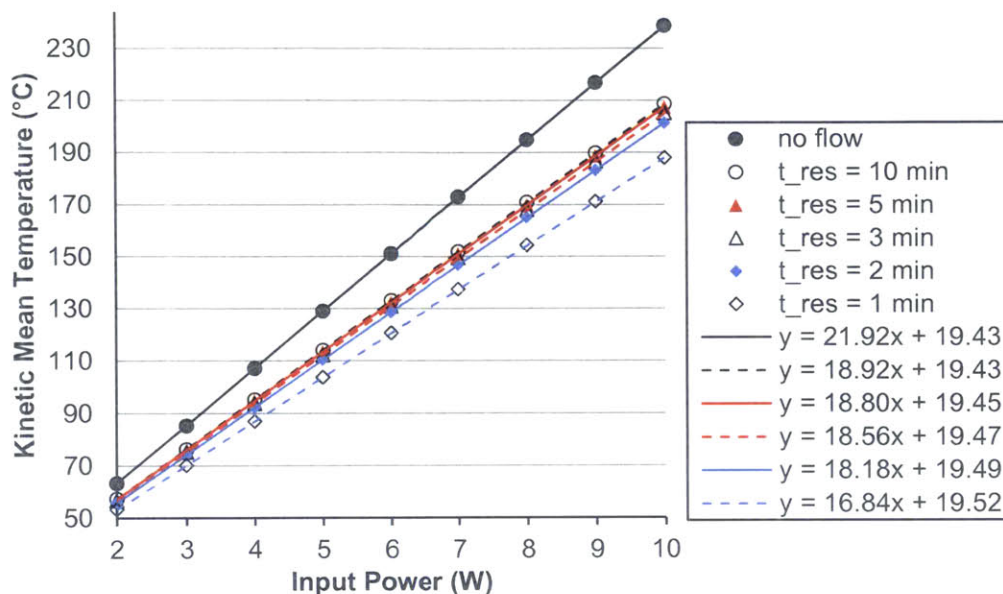


**Figure 5.5: The input power dependencies of the reactor kinetic mean temperature at various flow rates.**

Since the actual permittivity of the reaction is unknown, the relative permittivity of pure acetic acid at 20 °C was used in the original simulation, where  $\epsilon' - i\epsilon'' = 6.2 - 1.0788i$ , and thus the loss tangent value,  $\tan \delta = 0.174$ . In reality, the reaction should have a different permittivity since the solutes changes the permittivity from the pure solvent. The permittivity should also be temperature dependent although it was set as constant in the simulations. The effect of the permittivity was studied by varying the real and imaginary parts of the permittivity, the dielectric constant and the dielectric loss, respectively, to 10, 2, 1, 0.5, and 0.1 times the values originally used ( $\epsilon' = 62, 12.4, 6.2, 3.1, 0.62$ ;  $\epsilon'' = 10.788, 2.1576, 1.0788, 0.5394, 0.10788$ ). Therefore, a total of 25 permittivity combinations were simulated for the steady-state microwave heating results of the reaction without flow for this sensitivity study. All simulations were ran with a 6 W power input.

The total reaction heating rate depends on both the dielectric constant and the dielectric loss in the expected trends (Figure 5.6). Materials with a higher dielectric constant are better at aligning with the electromagnetic wave and allowing the wave to pass through, and thus have lower power dissipations (heating rates). Materials with a higher dielectric loss are better at converting the electromagnetic energy into heat, and thus have higher heating rates. Therefore, the reaction absorbs the most microwave energy, about 5.05 W, when the permittivity has the

lowest dielectric constant and highest dielectric loss ( $\epsilon' - i\epsilon'' = 0.62-10.788i$ ); and the reaction heating rate is lowest, at about 0.01 W, when the permittivity has the highest dielectric constant and lowest dielectric loss ( $\epsilon' - i\epsilon'' = 62-0.10788i$ ). An interesting observation is that the permittivity values that have the same  $\tan\delta$  (the same  $\epsilon''$  to  $\epsilon'$  ratio) do not result in the same heating rate. In Figure 5.6, the permittivity combinations that have the same loss tangent value as the pure acetic acid permittivity are marked in green: the heating rates of these five simulations range from 1.20 W to 0.51 W even though they all have the same loss tangent. The loss tangent is therefore only a rough indicator of a material's ability to be heated up by microwave and cannot be used to predict the exact heating rate of the material.

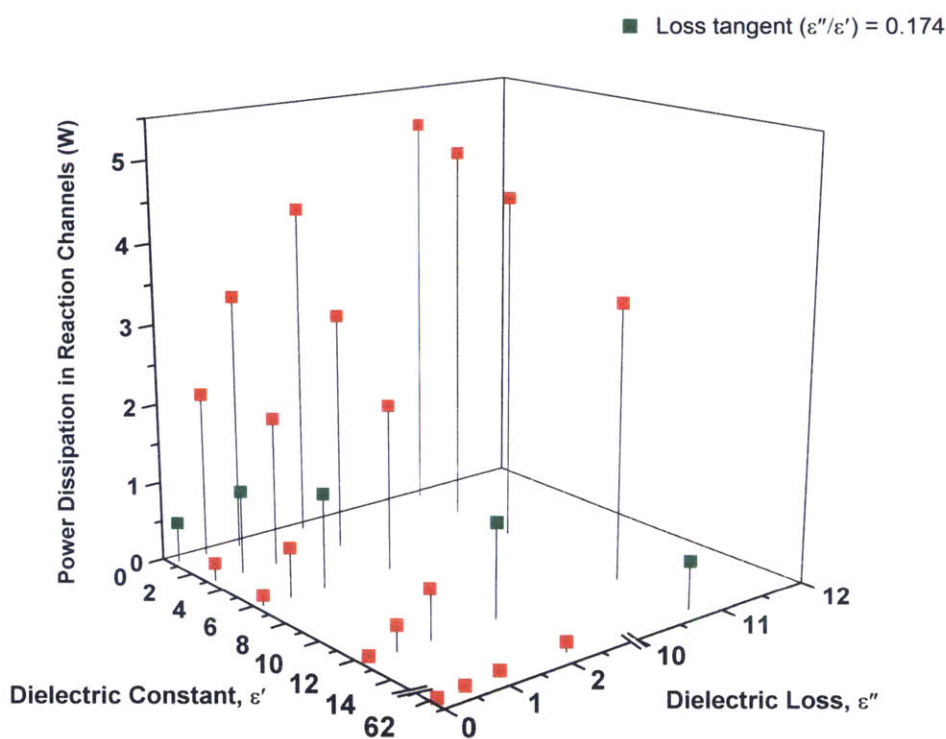


**Figure 5.6: The permittivity dependence of the total heating rate in the reaction volume.**

The kinetic mean temperature also depends on the permittivity in the same trends as the heating rate (Figure 5.7). For the ranges of dielectric constant and dielectric loss used in the sensitivity study, the temperature varies between 29.1 °C to 404 °C. The lowest temperature corresponds to the permittivity with the highest dielectric constant and lowest dielectric loss ( $\epsilon' - i\epsilon'' = 62-0.10788i$ ), while the highest temperature corresponds to the permittivity with the lowest dielectric constant and highest dielectric loss ( $\epsilon' - i\epsilon'' = 0.62-10.788i$ ).

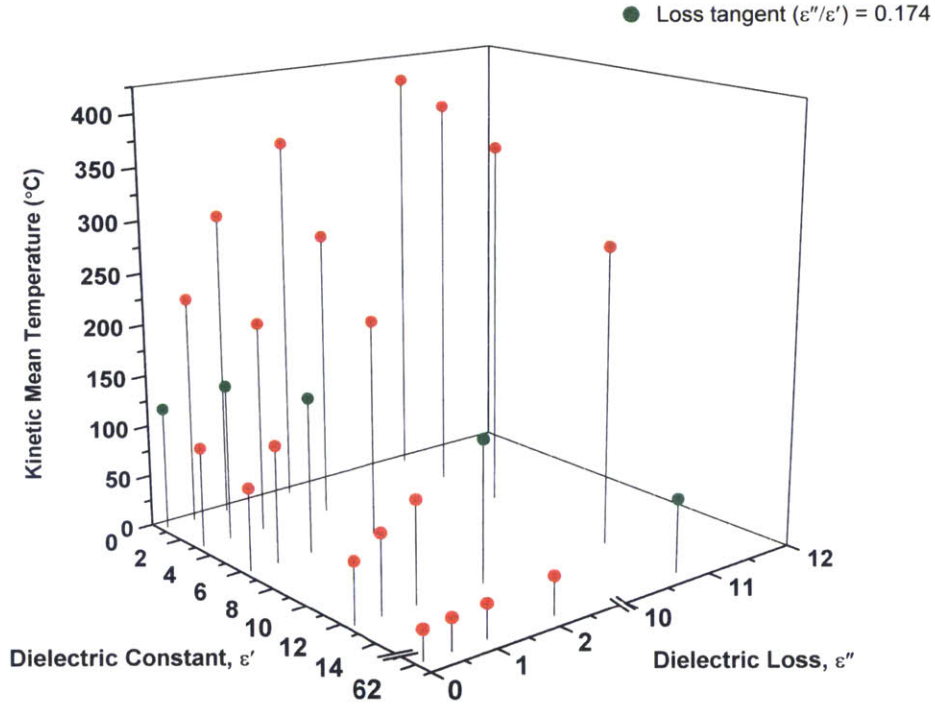


**Figure 5.7: The permittivity dependence of the kinetic mean temperature of the reaction without flow.**

The dependencies of the kinetic mean temperature on each part of the permittivity are easier to visualize in the projected 2D scatter plots (Figure 5.8, Figure 5.9). The function of the kinetic mean temperature variation with the dielectric constant is different for every fixed dielectric loss value (Figure 5.8). In order to find the local sensitivity of kinetic mean temperature to the permittivity of the original simulations ( $\epsilon' = 6.2$  and  $\epsilon'' = 1.0788$ ), we fitted the temperatures versus dielectric constant data at  $\epsilon'' = 1.0788$ . The best fitted curve is the logarithmic function:

$$T_{avg}(\epsilon'' = 1.0788) = -58.81 \ln(\epsilon') + 264.17 \quad (5.4)$$

which results in a local sensitivity of  $-9.48 \text{ }^\circ\text{C}/[-]$  towards the dielectric constant:

$$\frac{\partial T_{avg}}{\partial \epsilon'}(\epsilon' = 6.2, \epsilon'' = 1.0788) = -\frac{58.81}{\epsilon'} = -9.48 \frac{^\circ\text{C}}{[-]} \quad (5.5)$$

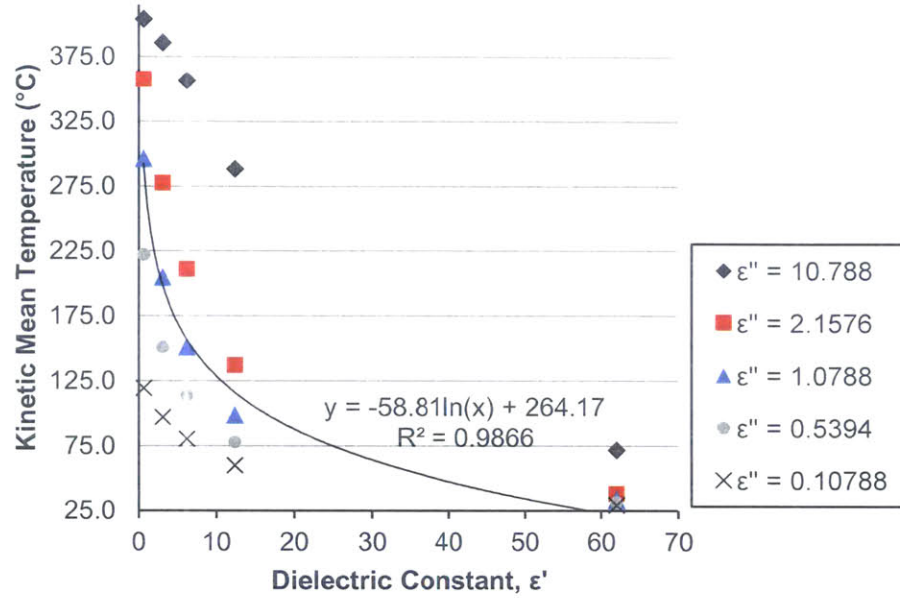


**Figure 5.8: The dielectric constant dependencies of the kinetic mean temperature of the reaction without flow at various dielectric loss values.**

Similarly, the function of the kinetic mean temperature variation with the dielectric loss is different for every fixed dielectric constant value (Figure 5.9). Using the same method, we fitted the temperatures versus dielectric loss data at  $\epsilon' = 6.2$ . The best fitted curve is the quadratic function:

$$T_{avg}(\epsilon' = 6.2) = -4.3806(\epsilon'')^2 + 73.378\epsilon'' + 74.367 \quad (5.6)$$

which results in a local sensitivity of  $63.9 \text{ }^\circ\text{C}/[-]$  towards the dielectric loss:

$$\frac{\partial T_{avg}}{\partial \epsilon''}(\epsilon' = 6.2, \epsilon'' = 1.0788) = -4.3806 \times 2\epsilon'' + 73.378 = 63.9 \frac{^\circ\text{C}}{[-]} \quad (5.7)$$



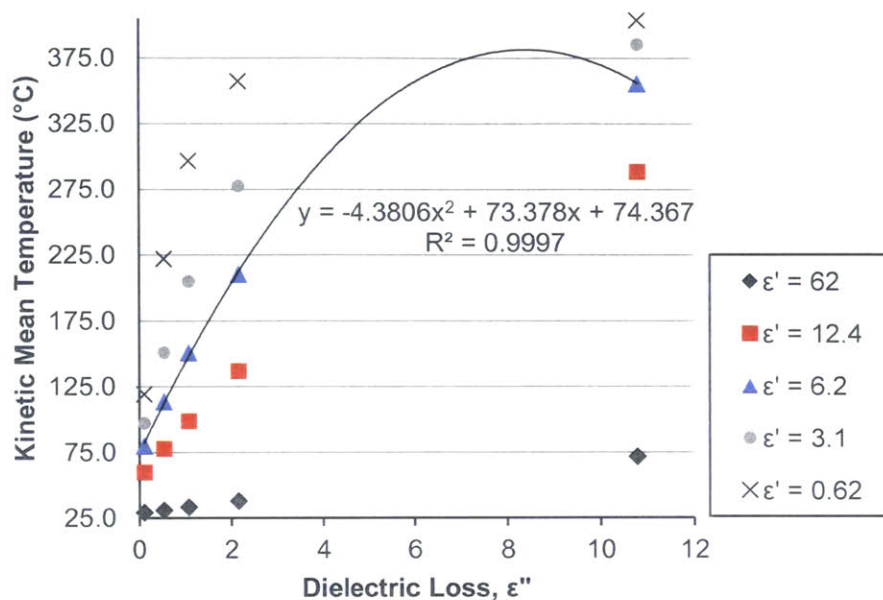


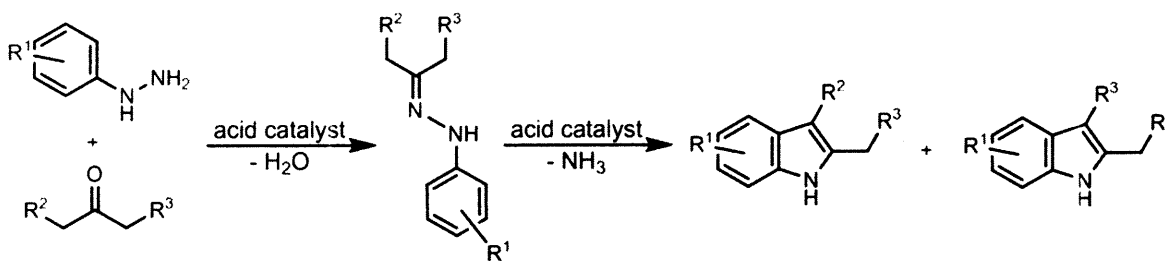
**Figure 5.9: The dielectric loss dependencies of the kinetic mean temperature of the reaction without flow at various dielectric constant values.**

The local sensitivities show that at  $\epsilon' = 6.2$  and  $\epsilon'' = 1.0788$ , every unit of dielectric constant error results in a  $-9.48$  °C kinetic mean temperature inaccuracy, and every unit of dielectric loss inaccuracy leads to a  $63.9$  °C kinetic mean temperature misestimation. Furthermore, doubling or halving the original values for either the dielectric constant or the dielectric loss all results in roughly a  $50$  °C change in the kinetic mean temperature. The simulated temperature is therefore highly susceptible to the material permittivity. The sensitivity analyses show that the simulation results are strongly dependent to the input power and both the real and imaginary parts of the material permittivity. The original simulation in Chapter 5.3.2 provides a fairly good estimation of the kinetic mean temperatures in comparison to the inaccuracies that can arise from a bad input power or permittivity assumption. The high sensitivities also demonstrate that precise input power and material permittivity is required to accurately predict the final temperature of a microwave heating scheme.

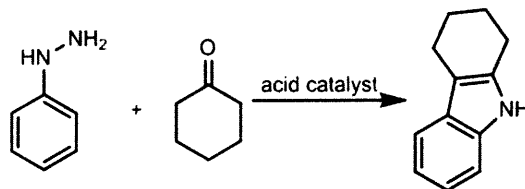
## 5.4 Fischer Indole Screening

The final step of the project is to demonstrate the application of the setup in reaction screening by completing a series of Fischer indolization between various ketones and arylhydrazines. Indoles are one of the essential structures in many biologically active

compounds,<sup>94</sup> and the Fischer indole synthesis is one of the most popular methods to prepare substituted indoles.<sup>95-96</sup> In this method, the starting reagent arylhydrazine and ketone or aldehyde first form an arylhydrazone, and then the arylhydrazone is heated in the presence of a protic or a Lewis acid to form the desired indole (Scheme 5.1).<sup>96</sup> The Fischer indole reaction between phenylhydrazine and cyclohexanone (Scheme 5.2) has been used as a validation chemistry in a couple of papers on continuous flow setups for microwave heating.<sup>51, 97</sup> Bagley *et al.* used their sand-filled flow cell (Chapter 1.2.4) to run the reaction under microwave in acetic acid at 150 °C for 4 minutes and reported a 91 % conversion.<sup>51</sup> The Larhed group used the same reaction to evaluate the setup they developed: a non-resonant microwave applicator with a borosilicate tube as the continuous-flow reactor.<sup>97</sup> They ran the reaction in a 3:1 acetic acid to isopropanol mixture and optimized the reaction to obtain 98 % conversion and 90 % isolated yield at 230 °C and 20 seconds residence time. The reaction has not been reported with any special effects or conversion enhancement under microwave heating, but it was chosen because it is faster to heat up the reaction with a microwave setup to the high temperature range desired for this synthesis. The idea of screening various hydrazines and ketones came from a publication from Desroses *et al.*: they presented a method of adding propylphosphonic acid cyclic anhydride as a catalyst to the Fischer indole synthesis and screen through the reactions for a total of 21 indole derivatives.<sup>95</sup> The catalyst allow them to lower the reaction temperature and drive the phenylhydrazine and cyclohexanone indolization to completion at 100 °C in 5 minutes.



**Scheme 5.1: Fischer indole synthesis.**



**Scheme 5.2: Fischer indolization of phenylhydrazine and cyclohexanone to 1,2,3,4-tetrahydrocarbazole.**

### 5.4.1 Experimental Procedures

The model reaction of phenylhydrazine and cyclohexanone was first optimized for our system, and then another 4 reactions were screened. Two stock solutions were prepared with a 3:1 mixture of acetic acid and isopropanol: one with 1.5 M (7.5 mmol) of arylhydrazine, and the other with 1.0 M (5 mmol) of ketone and a 0.1 equivalent of 1,3,5-trimethoxybenzene as the internal standard. The solutions were each loaded on to a 8 mL Harvard stainless steel syringe and fed into the system with a Harvard syringe pump. The conversions were obtained by both GC and  $^1\text{H}$  NMR, the yields were analyzed with  $^1\text{H}$  NMR, and the products were identified by both GC-MS and  $^1\text{H}$  NMR (Appendix C.3).

Because the products have low solubility in the solvent and kept crashing out after the exiting the reactor, a dilution stream was added to the reaction outlet with an Upchurch mixing tee. The dilution stream was pure acetic acid ran at the same flow rate as the reaction outlet, and the combined stream was fed into a 250 psi backpressure regulator. The fixed temperature mode was used for the microwave, while the maximum microwave power was set at 100 W. Under the 250 psi backpressure, the reaction could only stay as liquid until the point where the fiber optic temperature measurements were 180 °C; at any higher temperature settings, bubbles started forming in the reactor. The bubble point temperature of the solvent mixture is predicted to be 217 °C under 250 backpressure using the Peng-Robinson equation of state.<sup>98</sup> It is therefore estimated that the temperature within the system ranges between 180 °C to 217 °C. Since we do not have the permittivity of the reaction, the data reported are based on the measurements from the fiber optic probe and not the simulated temperature distribution in the reactor.

### 5.4.2 Fischer Indole Synthesis Results

The model reaction was run at 170 °C and 180 °C for 0.5 min, 1 min, 2 min, and 3 min residence time (Table 5.6). The screening of the all the reaction conditions took less than 90 minutes: including a 10 to 15 minute heating time to reach steady-state for each of the two desire temperature, and a 29.5 minute purging and collection time for all five residence times at each temperature. (Each data point had a 400  $\mu\text{l}$  collection after a 400  $\mu\text{l}$  purge.)

The conversions were all higher for the 180 °C set points. The reaction almost reached full completion at 99 % conversion and GC yield at the 180 °C set point with 4 minutes residence time. The result of 3 minutes residence time at 180 °C was not much lower than that of the 4 minutes: the 1 % difference in conversion is within the errors of the GC methods, while the

residence time decreased by a quarter. Therefore, the 180 °C, 3 minutes reaction condition was used for product purification and resulted in a 99 % isolated yield identified by NMR (Appendix C.3). A total of 254 mg (1.48 mmol) of 1,2,3,4-tetrahydrocarbazole (Scheme 5.2) was collected after 22 minutes.

**Table 5.6: Optimization of phenylhydrazine and cyclohexanone indolization with microwave spiral reactor.**

Set temperature (°C)	Residence time (min)	Conversion (%)	Yield (%)
170	0.5	79	78
170	1	87	87
170	2	94	94
170	3	96	96
170	4	98	98
180	0.5	92	88
180	1	94	91
180	2	96	93
180	3	98	98
180	4	99	99

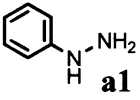
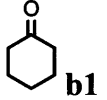
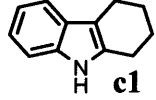
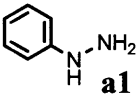
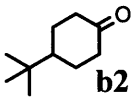
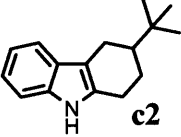
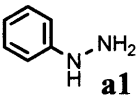
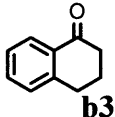
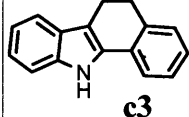
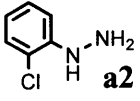
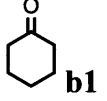
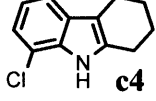
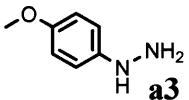
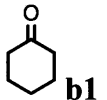
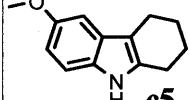
The phenylhydrazine and cyclohexanone were each screened with two other ketones and substituted phenylhydrazines, respectively (Table 5.7). The phenylhydrazine reaction with 4-*tert*-butylcyclohexanone (**b2**) had a faster conversion rate and reached full conversion and yield at 170 °C with 3 minutes residence time (entry 2). The product **c2** had a lower solubility and came out as partly solid in the collection even after the dilution. The flow rate of the dilution stream was therefore increased to 1.5 times the reaction flow rate in order to prevent clogging.

Although reaction with  $\alpha$ -tetralone (**c3**) successfully cyclized into the multi-ring structure, the reaction proceeded slower than the previous reactions, reaching only 62 % conversion after 3 minutes at 180 °C. Since the system was limited to 250 psi and the 180 °C set point, higher conversion could only be achieved by increasing the residence time. The longest residence time implemented was 30 minutes, resulting in a 74 % conversion and 70 % NMR yield (entry 3).

The cyclohexanone reaction with 2-chlorophenylhydrazine also had a slower reaction, perhaps due to the steric hindrance at the *ortho*-position. The reaction reached 98 % conversion and NMR yield at 180 °C after 20 minutes residence time (entry 4). This condition was used for product purification, and a total of 20.0 mg (0.097 mmol) of 8-chloro-2,3,4,9-tetrahydrocarbazole (**c4**) was collected after 14 minutes (98 %).

The 4-methoxyphenylhydrazine gave 100 % conversion and 100 % NMR yield after 10 minutes at 180 °C (entry 5).

**Table 5.7: Synthesis of indole derivatives with microwave spiral microreactor.**

Entry	Hydrazine	Ketone	Product	Temperature (°C)	Residence time (min)	Conversion (%)	Yield (%)
1	 <b>a1</b>	 <b>b1</b>	 <b>c1</b>	180	3	98	98 99 <sup>a</sup>
2	 <b>a1</b>	 <b>b2</b>	 <b>c2</b>	170	3	100	100 93 <sup>a</sup>
3	 <b>a1</b>	 <b>b3</b>	 <b>c3</b>	180	30	70	70 63 <sup>a</sup>
4	 <b>a2</b>	 <b>b1</b>	 <b>c4</b>	180	20	98	98 98 <sup>a</sup>
5	 <b>a3</b>	 <b>b1</b>	 <b>c5</b>	180	10	100	100 95 <sup>a</sup>

<sup>a</sup> Isolated yield

The screening of the last four reactions for the optimized reaction conditions took a total of 13.5 hours for 26 data points. Although this is about three folds the time that it would take in a batch reactor, the loss of time is compensated by both the extra heating time required in between each batch reactions and the small amount of material that is necessary for the continuous flow screening. Only 400 µl (~0.2 mmol of expected product) of solution was collected for each data point after purging the system with 400 µl of solution. Therefore, a mere total of 5 mmol of ketone and 6.5 mmol of hydrazine were used for each reaction. The ramp up time for heating to each temperature setting is only about 10 to 15 minutes. This screening experiment therefore demonstrates the system's advantages of fast heating with microwave and the reduction of material cost with continuous flow in microreactors.



## CHAPTER 6. CONCLUSIONS AND FUTURE PERSPECTIVES

---

### 6.1 Summary of Thesis Achievements and Findings

The main contribution of this thesis is the understanding of the different factors in microwave heating and the discovery of difficulties in designing a microreactor for the commercially available microwave units used in most chemical lab. In summary, we developed two glass microreactor setups that fits into the CEM single-mode microwave unit for microwave chemistry and tested the reactor performances with known chemistries and kinetic analysis. Throughout the design of the reactor, we constructed 3D microwave heating computational models that incorporate electromagnetic radiation, heat transfer, and fluid dynamics mechanisms to studying the microwave heating patterns. The findings from both the experiments and simulations shed light to several heating issues in the microwave unit and help us realize the limitations of microwave heating with glass microreactors.

We fabricated the initial microreactor through photolithographic wet etching and furnace bonding. One of the main challenges in the design was the limited space for tubing connections in the microwave attenuator. The reactor featured the first microchip design for microwave chemistry that used a fiber optic temperature probe. The validation chemistries showed lower conversions and were at times hard to replicate with this microreactor. These chemistry issues were caused by the uneven temperature across the reaction channels and the sensitivity of the reactor temperature to the angular position of the reactor. The thermal problems included: First, the reactor temperature was highest at the position close to the cavity center and decreases radially away from the hottest position. The temperature variation in the reaction channels was as high as 50 °C. Second, without the Teflon optical fiber holder, the reactor temperature has a maximum limit that was too low for our chemistry application. The temperature limit depends on the material in the reactor and was only 125 °C for the most microwave-absorbent solvent used in our chemistry. Last, the reactor temperature changes as the reactor rotates along the cavity axis. Even small changes in the angular position could lead to observable difference in the temperature and chemistry results.

We therefore built microwave heating models in COMSOL to find the roots of the heating problems. Although COMSOL microwave heating results have been published before,

our models were the first to incorporate the air convection in the system, geometries with small dimensions less than 1 mm wide, and the continuous flow of solvent in the microwaved reactor. The models were also the first to show the transient microwave heating period leading to the steady state equilibrium and to demonstrate how the reactor position changes the electromagnetic field.

The models showed that the electric field in the microwave cavity is always a single standing wave due to the geometry design for a single-mode microwave unit. However, the electric field strength and the local electric field pattern changes with the reactor size, reactor position, and material of the load. Since the heating rate is proportional to the square of the electric field strength, the low temperature limit was caused by the weak electric field strength induced by the reactor. For the two reactor positions that we studied, the electric field were different for each position both in magnitude in direction of the field vector. When the reactor is perpendicular to the microwave port, it prompted an even weaker electric field than when it is parallel to the port, resulting in an even lower temperature limit. The sensitivity of the electric field to the reactor positions also explained why the temperature changes when the reactor rotates. Consistent chemistry data can only be achieved if the reactor is set at a fixed position. In addition, the uneven temperature distribution was caused by the resonance structure of the electric field. The peak of the electric field oscillation is at the cavity center while the cavity walls are the nodes of the standing wave. The electric field strength is therefore stronger at the center and diminishes radially. This resonance pattern leads to uneven heating and creates a non-uniform temperature distribution across the reactor.

The simulation also shows that a significant amount of heat is lost to the natural air convection in the microwave cavity and in the microwave waveguide. The air convection was accounted for with two different models: In the first one, the estimated thermal conductivity model, the air domain was treated as a solid and was assigned higher thermal conductivities. In effect, the convective heat transfer portion was lumped into the conductive terms using this method. In the second model, the single-flow model, the air domain was treated as a fluid and the momentum conservative equations were solved along with the energy equations for flow. The k-estimation model matched the experimental results closely while the single-flow model overestimated the temperature of the reactors, showing that the microwave model was over simplified. The actual model might have underestimated the heat loss to the environment outside



of the waveguide, or overestimated the actual power input given from the microwave magnetron. The k-estimation model was able to adjust for the model simplification since any additional heat loss was accounted for by the air conductivity.

The simulation findings were used to redesign the reactor. In short, we found that the heating challenges were caused by three issues: first, the weak electric field strength; second, the heat loss due to the natural air convection; and third, the uneven heating rate across the cavity. The first two issues were resolved by changing the thickness of the reactor to induce a higher heating rate from the microwave. The third issue was minimized by changing the design to a spiral channel that is placed in the center of the microwave cavity, which is the center of the resonance with the highest electric field strength. However, the uneven heating rate will always be present because it is caused by the inherent nature of electromagnetic wave radiation. The unevenness was demonstrated in the simulation of the spiral reactor. The electric field was diffracted by the spiral channels and created two heating zones with different heating rates; the maximum heating rate was an order of magnitude higher than the minimum heating rate. When the microwave heating reached steady-state, the entire reactor volume of the spiral reactor lied in the warmest zone in the microwave cavity, although the temperature variations in the channels was up to 20 °C. The bottom portion of the spirals had the highest temperature while the top portion had the lowest. The temperature along the reactor follows an overall concave pattern with oscillations along each full turn of the spiral. The temperature oscillation of each turn was between 5 °C to 15 °C. Even though the reaction temperature variation was as much as 20 °C, it was already much smaller than the 50 °C variation of the initial reactor.

Through chemistry experiments, we demonstrated that the fiber optic temperature measurement could not accurately represent the large temperature span in the reaction volume. We tested the spiral reactor with the condensation reaction and calculated the average mean temperature of the reaction channels with the reaction conversions and established kinetic parameters. The spiral reactor overcame the temperature limit as expected and the experiments were repeatable as long as the reactor position was fixed. The calculated mean temperatures differed greatly (-7 °C to 24 °C) from the experimental temperature measurement at a single point. We demonstrated that this huge temperature difference was due to the uneven volumetric heating of the reaction solvent by comparing the results to the condensation reaction heated with a glycerol bath. The glycerol acted as a heating jacket to mimic a conventionally heated setup

where the acetic acid will not be directly heating by microwave. The mean temperatures calculated from the glycerol bath experiments were close matches to the measured temperature, with only 0 °C to 3 °C difference, showing that the reaction only has a large temperature variation when it is directly absorbing the microwave energy.

In addition, the actual mean temperature data suggested that the temperature distribution not only varied for the two different reactor positions but also changed for different reaction flow rates/residence times. The temperature increases with longer residence times. Knowing that the uneven temperature measurement cannot be obtained experimentally without an accurate 3D temperature sensor, we attempted to build a temperature prediction model from the microwave simulations by adding a flow module to the reactor channels and use the average microwave power observed during the experiments as the simulated power input. In the flow simulation, the reaction was simulated as a fully-developed, unidirectional stream of acetic acid. The results qualitatively match the trend of the temperature fluctuation with flow rates, displaying a lower temperature profile with increasing flow rate/decreasing residence time. However, the mean temperatures calculated from the simulation were about 2 °C to 10 °C lower than the experimental data. A parameter sensitivity study showed that this error is smaller than the mean temperature sensitivities towards the radiation power input and the reaction permittivity. Therefore, the simulations provided good insight to the different factors that affect the temperature distribution, but they could not be used to determine the exact temperatures of future chemistries.

In the end, we used the Fischer Indolization to demonstrate that the best application of microwave heating in chemistry is likely still in discovery chemistry where fast, qualitative results can be obtained. The screening condition was limited to maximum 250 psi back pressure the glass reactor can withstand. Even though microwave heating gives the promise of reaching higher temperature ranges, this benefit could not be taken into practice without a reactor with a higher pressure rating. The reaction temperature can only be as high as the reactant's bubble point at 250 psi; and because of the uneven heating, only a small portion of the reaction can reach this temperature limit, while the rest of the area can be 20 °C lower. The highest nominal temperature range we could reach was 180 °C as measured by the optical probe. This pitfall was compensated by increased residence time. Ultimately, five reactions were successfully screened

for the predicted product. The optimization of all the reaction took a total of about 15 hours, using up at most 6.5 mmol (less than one gram) of starting material for each reaction.

## 6.2 Future Perspectives

In order to harness the benefits of microwave heating for kinetic studies or chemistry characterization, accurate process control must be achieved. The main body of this thesis focused on the difficulties of maintaining or monitoring the reaction temperature. Even though we demonstrated the reaction screening ability of our final system, the results are hardly transferable to a different system because of the lack of actual temperature measurement. The single-mode microwave units currently seen in chemistry lab are designed for a single standing wave in the microwave cavity, and therefore an uneven heating rate and temperature distribution over any reactor is an inherent problem in microwave heating. There are three possible directions to take to proceed with designing a micro-scale continuous flow system for microwave heating: (1) Redesigning a microwave unit that has uniform electric field strength and uniform heating, (2) Implementing a 3D temperature sensor for the microwave, (3) Building a computational microwave heating model that accurately predicts the microwave temperature.

### 6.2.1 Redesigning a Microwave Unit

Knowing that the temperature variation results from the resonance structure of the microwave unit, designing a microwave waveguide to diminish the non-uniform electric field is the most direct solution to the root of the problem. In the recent year or two, efforts have been made toward this direction.<sup>97, 99-100</sup> Because of the inherent wave structure of electromagnetic fields, the task of reaching an even electric field is rather challenging. The same issues we had with the single-mode cavity have been observed also with different the microwave waveguide designs, including the multimode cavities often use in industries and kitchen microwave ovens.<sup>100</sup> G.S.J. Sturm *et al.* designed a rectangular microwave waveguide for a coiled continuous flow reactor,<sup>99</sup> and Öhrngren *et al.* designed a microwave applicator with a helical antenna surrounding a tube reactor suppress the standing wave caused by the microwave and eliminate cold and hot spots;<sup>97</sup> however, the temperature variation within their reactors still range anywhere from 5 °C to 20 °C or beyond. The most promising design is the coaxial traveling microwave reactor (TMR) concept proposed by G.S.J. Sturm *et al.* earlier this year.<sup>100</sup> By using

COMSOL simulations and Matlab calculations, they designed a system where the microchannels for the reaction travel in the tube-shaped waveguide along with the direction of the microwave, which is propagating in the transverse electromagnetic (TEM) mode. The deviation of the heating rate in their optimized design was only 4.6 % from the average heating rate of the reaction fluid.<sup>100</sup> Although the design has not been realized in practice, it shows promise that uniform heating can be achieved in theory. Furthermore, it demonstrates that microwave simulation is a useful tool to understand the heating distribution of a microwave system for the purpose of reactor design, which is a major learning in this thesis.

### **6.2.2 3D Temperature Sensor**

In the event that uneven temperature cannot be eliminated, 3D temperature monitoring will be an alternative for accurate temperature characterization. This is a huge challenge as the temperature sensor has to be microwave transparent and there needs to be a window in the cavity wall wide enough to capture the entire view of the reactor volume. The most promising idea we encountered in the literature is fluorescent thermal imaging.<sup>28</sup> This alternative temperature sensing technique was not implemented because of technical challenge with our system and also the impracticality of the additional benefits. There is only a 10 mm optical access to the microwave cavity. The size of this window is not large enough to create a 2D mapping of the entire spiral channel, and a 1D point measurement will not be sufficient to capture the uneven temperature distribution. The multiple layers of the reactor also make it difficult for the camera to focus on a single point or plane to obtain an accurate image while minimizing the surrounding noise. There is also a lack of data on fluorescent dyes work beyond 100 °C and reports of using the fluorescent dye during chemical reactions.<sup>28</sup> If the above challenges can be solved, kinetic studies can potentially be implemented by using the mean temperature calculations presented in Chapter 5.3 (Equation (5.3)).

### **6.2.3 Simulation for Accurate Temperature Prediction**

Aside from directly monitoring the 3D temperature, we also attempted to predict the exact temperature distribution in the system with simulations. If we could have established a correlation between the mean reaction temperature and the set temperature, then we could have used the relationship to estimate the actual mean temperature of other solvents heated up at the same conditions in the future. Also, had the simulation temperature match the experimental

temperature, kinetic studies could have been implemented with Equation (5.3). Although our simulations proved to be over simplified, the computational models could be updated with other considerations to better reflect the microwave heating in practice. These include, but not limited to, adding a magnetron model to account for the actual power used in the experiments, adding the temperature dependency of the solution's permittivity instead of using the pure solvent's permittivity at 20 °C as approximation, adding the heat loss to the enclosing around the microwave guide instead of approximating it with convection cooling, and modeling the power variation of the microwave instead of assuming the power input as the average experimental power.

The above three directions are all challenging in its own aspect and could each be a separate thesis project to tackle with the temperature issues in the microwave system.

Aside from the heating challenges faced in this thesis, the mechanical strength of the microreactor has been the second largest limitation. Glass microreactors are not only difficult and expensive for fabrication, but also its pressure ratings (< 250 psi) limited us from fully exploring the high temperature benefits of microwave heating. For future development of microstructural systems in microwave, materials that have a higher mechanical strength and ease of fabrication should be considered.



## REFERENCES

---

1. Gedye, R.; Smith, F.; Westaway, K.; Ali, H.; Baldisera, L.; Laberge, L.; Rousell, J., The use of microwave-ovens for rapid organic-synthesis. *Tetrahedron Lett.* **1986**, *27* (3), 279-282.
2. Kappe, C. O.; Dallinger, D., The impact of microwave synthesis on drug discovery. *Nat. Rev. Drug Discov.* **2006**, *5* (1), 51-63.
3. Kappe, C. O., Controlled microwave heating in modern organic synthesis. *Angew. Chem.-Int. Edit.* **2004**, *43* (46), 6250-6284.
4. Chemat, F.; Esveld, E., Microwave super-heated boiling of organic liquids: Origin, effect and application. *Chem. Eng. Technol.* **2001**, *24* (7), 735-744.
5. Kappe, C. O.; Dallinger, D.; Murphree, S. S., *Practical microwave synthesis for organic chemists : strategies, instruments, and protocols / C. Oliver Kappe, Doris Dallinger, and S. Shaun Murphree.* Weinheim : Wiley-VCH, c2009.: 2009.
6. Shore, G.; Morin, S.; Organ, M. G., Catalysis in capillaries by Pd thin films using microwave-assisted continuous-flow organic synthesis (MACOS). *Angew. Chem.-Int. Edit.* **2006**, *45* (17), 2761-2766.
7. Shore, G.; Organ, M. G., Diels-Alder cycloadditions by microwave-assisted, continuous flow organic synthesis (MACOS): the role of metal films in the flow tube. *Chem. Commun.* **2008**, (7), 838-840.
8. Gilday, J. P.; Lenden, P.; Moseley, J. D.; Cox, B. G., The Newman-Kwart rearrangement: A microwave kinetic study. *J. Org. Chem.* **2008**, *73* (8), 3130-3134.
9. Kappe, C. O., Microwave dielectric heating in synthetic organic chemistry. *Chem. Soc. Rev.* **2008**, *37* (6), 1127-1139.
10. Kappe, C. O.; Stadler, A., Building dihydropyrimidine libraries via microwave-assisted Biginelli multicomponent reactions. In *Combinatorial Chemistry, Pt B*, Academic Press Inc: San Diego, 2003; Vol. 369, pp 197-223.
11. Damm, M.; Kappe, C. O., High-throughput experimentation platform: parallel microwave chemistry in HPLC/GC vials. *J. Comb. Chem.* **2009**, *11* (3), 460-468.
12. Bedore, M. W.; Zaborenko, N.; Jensen, K. F.; Jamison, T. F., Aminolysis of epoxides in a microreactor system: a continuous flow approach to  $\beta$ -amino alcohols. *Organic Process Research & Development* **2010**, *14* (2), 432-440.
13. Kappe, C. O.; Pieber, B.; Dallinger, D., Microwave Effects in Organic Synthesis: Myth or Reality? *Angew. Chem.-Int. Edit.* **2013**, *52* (4), 1088-1094.
14. Glasnov, T. N.; Kappe, C. O., Microwave-assisted synthesis under continuous-flow conditions. *Macromol. Rapid Commun.* **2007**, *28* (4), 395-410.
15. Kreamsner, J. M.; Stadler, A.; Kappe, C. O., The scale-up of microwave-assisted organic synthesis. In *Microwave Methods in Organic Synthesis*, Springer-Verlag Berlin: Berlin, 2006; Vol. 266, pp 233-278.
16. Baxendale, I. R.; Hayward, J. J.; Ley, S. V., Microwave reactions under continuous flow conditions. *Comb. Chem. High Throughput Screen* **2007**, *10* (10), 802-836.
17. Bremner, W. S.; Organ, M. G., Multicomponent reactions to form heterocycles by microwave-assisted continuous flow organic synthesis. *J. Comb. Chem.* **2007**, *9* (1), 14-16.
18. Comer, E.; Organ, M. G., A microcapillary system for simultaneous, parallel microwave-assisted synthesis. *Chem.-Eur. J.* **2005**, *11* (24), 7223-7227.

19. Comer, E.; Organ, M. G., A microreactor for microwave-assisted capillary (continuous flow) organic synthesis. *J. Am. Chem. Soc.* **2005**, *127* (22), 8160-8167.
20. Ping, H.; Haswell, S. J.; Fletcher, P. D. I., Microwave-assisted Suzuki reactions in a continuous flow capillary reactor. *Appl. Catal. A-Gen.* **2004**, *274* (1-2), 111-114.
21. Wilson, N. S.; Sarko, C. R.; Roth, G. P., Development and applications of a practical continuous flow microwave cell. *Org. Process Res. Dev.* **2004**, *8* (3), 535-538.
22. Kirschning, A.; Solodenko, W.; Mennecke, K. In *Combining enabling techniques in organic synthesis: Continuous flow processes with heterogenized catalysts*, Budapest, Hungary, Aug 27-31; Wiley-VCH Verlag GmbH: Budapest, Hungary, 2006; pp 5972-5990.
23. Jensen, K. F. In *Microreaction engineering - is small better?*, Krakow, Poland, Sep 10-13; Pergamon-Elsevier Science Ltd: Krakow, Poland, 2000; pp 293-303.
24. Muller, G.; Gaupp, T.; Wahl, F.; Wille, G., Continuous chemistry in microreaction systems for practical use. *Chimia* **2006**, *60* (9), 618-622.
25. de Mas, N.; Gunther, A.; Schmidt, M. A.; Jensen, K. F., Microfabricated multiphase reactors for the selective direct fluorination of aromatics. *Ind. Eng. Chem. Res.* **2003**, *42* (4), 698-710.
26. Zaborenko, N.; Murphy, E. R.; Kralj, J. G.; Jensen, K. F., Synthesis and kinetics of highly energetic intermediates by micromixers: direct multistep synthesis of sodium nitrotetrazolate. *Ind. Eng. Chem. Res.* **2010**, *49* (9), 4132-4139.
27. Watts, P.; Wiles, C., Micro reactors: a new tool for the synthetic chemist. *Org. Biomol. Chem.* **2007**, *5* (5), 727-732.
28. Finegan, T.; Laibinis, P. E.; Hatton, T. A., In-situ measurements of temperature distributions in a microwave-heated cavity. *Aiche J.* **2006**, *52* (8), 2727-2735.
29. Loupy, A., *Microwaves in organic synthesis*. Wiley-VCH: Weinheim, 2006.
30. Finegan, T. M. Remote three-dimensional temperature sensing using planar laser induced fluorescence : development and applications to microwave heated liquids. Massachusetts Institute of Technology, Massachusetts Institute of Technology, 2004.
31. Haus, H. A., Melcher, James R. , *Electromagnetic fields and energy*. Prentice Hall 1989; p 742.
32. Kappe, C. O.; Dallinger, D., Controlled microwave heating in modern organic synthesis: highlights from the 2004-2008 literature. *Mol. Divers.* **2009**, *13* (2), 71-193.
33. Baghurst, D. R.; Mingos, D. M. P., Superheating effects associated with microwave dielectric heating. *J. Chem. Soc.-Chem. Commun.* **1992**, (9), 674-677.
34. Perreux, L.; Loupy, A., A tentative rationalization of microwave effects in organic synthesis according to the reaction medium, and mechanistic considerations. *Tetrahedron* **2001**, *57* (45), 9199-9223.
35. Kuhnert, N., Microwave-assisted reactions in organic synthesis - Are there any nonthermal microwave effects? *Angew. Chem.-Int. Edit.* **2002**, *41* (11), 1863-6.
36. de la Hoz, A.; Diaz-Ortiz, A.; Moreno, A., Microwaves in organic synthesis. Thermal and non-thermal microwave effects. *Chem. Soc. Rev.* **2005**, *34* (2), 164-178.
37. Loupy, A.; Maurel, F.; Sabatie-Gogova, A., Improvements in Diels-Alder cycloadditions with some acetylenic compounds under solvent-free microwave-assisted conditions: experimental results and theoretical approaches. *Tetrahedron* **2004**, *60* (7), 1683-1691.
38. Strauss, C. R., Microwave-assisted reactions in organic synthesis - Are there any nonthermal microwave effects? Response. *Angew. Chem.-Int. Edit.* **2002**, *41* (19), 3589-3590.



39. Herrero, M. A.; Kremsner, J. M.; Kappe, C. O., Nonthermal microwave effects revisited: On the importance of internal temperature monitoring and agitation in microwave chemistry. *J. Org. Chem.* **2008**, *73* (1), 36-47.
40. Obermayer, D. G., B.; Kappe, C. O., Microwave chemistry in silicon carbide reaction vials: separating thermal from nonthermal effects. *Angew. Chem.-Int. Edit.* **2009**, *48* (44), 8321-4.
41. Razzaq, T.; Kremsner, J. M.; Kappe, C. O., Investigating the existence of nonthermal/specific microwave effects using silicon carbide heating elements as power modulators. *J. Org. Chem.* **2008**, *73* (16), 6321-6329.
42. Dudley, G. B.; Stiegman, A. E.; Rosana, M. R., Correspondence on Microwave Effects in Organic Synthesis. *Angew. Chem.-Int. Edit.* **2013**, *52* (31), 7918-7923.
43. Kappe, C. O., Reply to the correspondence on microwave effects in organic synthesis. *Angew. Chem.-Int. Edit.* **2013**, *52* (31), 7924-7928.
44. Rosana, M. R.; Tao, Y. C.; Stiegman, A. E.; Dudley, G. B., On the rational design of microwave-actuated organic reactions. *Chemical Science* **2012**, *3* (4), 1240-1244.
45. Schmink, J. R.; Holcomb, J. L.; Leadbeater, N. E., Use of Raman spectroscopy as an in-situ tool to obtain kinetic data for organic transformations. *Chem.-Eur. J.* **2008**, *14* (32), 9943-9950.
46. Adam, D., Microwave chemistry: Out of the kitchen. *Nature* **2003**, *421* (6923), 571-572.
47. CEM Corporation Home Page. <http://www.cem.com/> (accessed July 26, 2014).
48. He, P.; Haswell, S. J.; Fletcher, P. D. I., Microwave heating of heterogeneously catalysed Suzuki reactions in a micro reactor. *Lab Chip* **2004**, *4* (1), 38-41.
49. He, P.; Haswell, S. J.; Fletcher, P. D. I., Efficiency, monitoring and control of microwave heating within a continuous flow capillary reactor. *Sens. Actuator B-Chem.* **2005**, *105* (2), 516-520.
50. Bagley, M. C.; Fusillo, V.; Jenkins, R. L.; Lubinu, M. C.; Mason, C., One-step synthesis of pyridines and dihydropyridines in a continuous flow microwave reactor. *Beilstein J. Org. Chem.* **2013**, *9*, 1957-1968.
51. Bagley, M. C.; Jenkins, R. L.; Lubinu, M. C.; Mason, C.; Wood, R., A simple continuous flow microwave reactor. *J. Org. Chem.* **2005**, *70* (17), 7003-7006.
52. Glasnov, T. N.; Vugts, D. J.; Koningstein, M. M.; Desai, B.; Fabian, W. M. F.; Orru, R. V. A.; Kappe, C. O., Microwave-assisted Dimroth rearrangement of thiazines to dihydropyrimidinethiones: synthetic and mechanistic aspects. *QSAR & Combinatorial Science* **2006**, *25* (5-6), 509-518.
53. Grover, W. H.; Skelley, A. M.; Liu, C. N.; Lagally, E. T.; Mathies, R. A., Monolithic membrane valves and diaphragm pumps for practical large-scale integration into glass microfluidic devices. *Sens. Actuator B-Chem.* **2003**, *89* (3), 315-323.
54. Kikutani, Y.; Hibara, A.; Uchiyama, K.; Hisamoto, H.; Tokeshi, M.; Kitamori, T., Pile-up glass microreactor. *Lab Chip* **2002**, *2* (4), 193-196.
55. Fletcher, P. D. I.; Haswell, S. J.; Pombo-Villar, E.; Warrington, B. H.; Watts, P.; Wong, S. Y. F.; Zhang, X. L., Micro reactors: principles and applications in organic synthesis. *Tetrahedron* **2002**, *58* (24), 4735-4757.
56. Hartman, R. L.; Jensen, K. F., Microchemical systems for continuous-flow synthesis. *Lab Chip* **2009**, *9* (17), 2495-507.
57. Baram, A.; Naftali, M., Dry etching of deep cavities in Pyrex for MEMS applications using standard lithography. *J. Micromech. Microeng.* **2006**, *16* (11), 2287-2291.

58. Zhu, H. X.; Holl, M.; Ray, T.; Bhushan, S.; Meldrum, D. R., Characterization of deep wet etching of fused silica glass for single cell and optical sensor deposition. *J. Micromech. Microeng.* **2009**, *19* (6), 8.
59. Akashi, T.; Yoshimura, Y.; Higashiyama, S.; Ieee In *Deep reactive ion etching of Pyrex glass using a bonded silicon wafer as an etching mask*, Miami Beach, FL, Jan 30-Feb 03; Ieee: Miami Beach, FL, 2005; pp 520-523.
60. Park, J. H.; Lee, N. E.; Lee, J.; Park, J. S.; Park, H. D., Deep dry etching of borosilicate glass using SF<sub>6</sub> and SF<sub>6</sub>/Ar inductively coupled plasmas. *Microelectron. Eng.* **2005**, *82* (2), 119-128.
61. Kikutani, Y.; Horiuchi, T.; Uchiyama, K.; Hisamoto, H.; Tokeshi, M.; Kitamori, T., Glass microchip with three-dimensional microchannel network for 2 x 2 parallel synthesis. *Lab Chip* **2002**, *2* (4), 188-192.
62. Grover, W. H.; von Muhlen, M. G.; Manalis, S. R., Teflon films for chemically-inert microfluidic valves and pumps. *Lab Chip* **2008**, *8* (6), 913-918.
63. Hibara, A.; Tokeshi, M.; Uchiyama, K.; Hisamoto, H.; Kitamori, T., Integrated multilayer flow system on a microchip. *Anal. Sci.* **2001**, *17* (1), 89-93.
64. Mao, P. Fabrication and characterization of nanofluidic channels for studying molecular dynamics in confined environments Master thesis, Massachusetts Institute of Technology, Cambridge, 2005.
65. Grover, W. H., Modrilla: software for drilling holes in glass wafers using a CNC mill, <http://openwetware.org/wiki/Modrilla>. 2008.
66. Jia, Z. J.; Fang, Q.; Fang, Z. L., Bonding of glass microfluidic chips at room temperatures. *Anal. Chem.* **2004**, *76* (18), 5597-5602.
67. Mao, P.; Han, J. Y., Fabrication and characterization of 20 nm planar nanofluidic channels by glass-glass and glass-silicon bonding. *Lab Chip* **2005**, *5* (8), 837-844.
68. Blackwell, B. S. Design, fabrication, and characterization of a micro fuel processor. Ph. D., Massachusetts Institute of Technology, 2007.
69. Telic Company Home Page. [www.TelicCompany.com](http://www.TelicCompany.com) (accessed July 26, 2014).
70. Meredith, R. J., *Engineers' handbook of industrial microwave heating / Roger Meredith*. London : Institution of Electrical Engineers, c1998.: 1998.
71. Lambert, J., CEM Corperation. 2009; p Personal Communication.
72. Jensen, K. F., Silicon-based microchemical systems: Characteristics and applications. *MRS Bull.* **2006**, *31* (2), 101-107.
73. Damm, M.; Glasnov, T. N.; Kappe, C. O., Translating high-temperature microwave chemistry to scalable continuous flow processes. *Org. Process Res. Dev.* **2009**, *14* (1), 215-224.
74. Hamper, B. C.; Tesfu, E., Direct uncatalyzed amination of 2-chloropyridine using a flow reactor. *Synlett* **2007**, (14), 2257-2261.
75. McMullen, J. P.; Jensen, K. F., Rapid determination of reaction kinetics with an automated microfluidic system. *Org. Process Res. Dev.* **2011**, *15* (2), 398-407.
76. Narayan, S.; Seelhammer, T.; Gawley, R. E., Microwave assisted solvent free amination of halo-(pyridine or pyrimidine) without transition metal catalyst. *Tetrahedron Lett.* **2004**, *45* (4), 757-759.
77. Robinson, J.; Kingman, S.; Irvine, D.; Licence, P.; Smith, A.; Dimitrakis, G.; Obermayer, D.; Kappe, C. O., Understanding microwave heating effects in single mode type cavities-theory and experiment. *Phys. Chem. Chem. Phys.* **2010**, *12* (18), 4750-4758.

78. Sturm, G. S. J.; Verweij, M. D.; van Gerven, T.; Stankiewicz, A. I.; Stefanidis, G. D., On the effect of resonant microwave fields on temperature distribution in time and space. *Int. J. Heat Mass Transf.* **2012**, *55* (13-14), 3800-3811.
79. Sturm, G. S. J.; Verweij, M. D.; van Gerven, T.; Stankiewicz, A. I.; Stefanidis, G. D., On the parametric sensitivity of heat generation by resonant microwave fields in process fluids. *Int. J. Heat Mass Transf.* **2013**, *57* (1), 375-388.
80. COMSOL RF Module User's Guide, Version 4.2. COMSOL AB Stockholm: 2011; p 165.
81. Hayes, B. L., *Microwave synthesis: chemistry at the speed of light*. CEM Publishing: Matthews, NC, 2002.
82. Deen, W. M., *Analysis of transport phenomena*. New York : Oxford University Press, 1998.: 1998.
83. Incropera, F. P. D., David P., *Fundamentals of heat and mass transfer*. New York : Wiley, c2002.5th ed.: 2002.
84. Burke, B.; Diamond, S., Asymmetric three-dimensional finite element analysis of a magnetically shielded room with access ports. In *17th International Conference on Biomagnetism Advances in Biomagnetism – Biomag2010*, Supek, S.; Sušac, A., Eds. Springer Berlin Heidelberg: 2010; Vol. 28, pp 54-57.
85. COMSOL Multiphysics Reference Guide, Version 4.3. COMSOL AB Stockholm: 2012; p 702.
86. Arshad, M.; Inayat, M. H.; Chughtai, I. R., Experimental study of natural convection heat transfer from an enclosed assembly of thin vertical cylinders. *Appl. Therm. Eng.* **2011**, *31* (1), 20-27.
87. Caton, I. In *Natural convection in enclosures*, Proceedings of the 6th International Heat Transfer Conference, Toronto, Canada., Washington : Hemisphere Pub. Corp.: Toronto, Canada., 1978; pp 13-43.
88. Fotiadis, D. I.; Kieda, S.; Jensen, K. F., Transport phenomena in vertical reactors for metalorganic vapor-phase epitaxy. 1. Effects of heat-transfer characteristics, reactor geometry, and operating-conditions. *J. Cryst. Growth* **1990**, *102* (3), 441-470.
89. Selver, R.; Kamotani, Y.; Ostrach, S., Natural convection of a liquid metal in vertical circular cylinders heated locally from the side. *J. Heat Transf.-Trans. ASME* **1998**, *120* (1), 108-114.
90. Stephan, K.; Laesecke, A., The thermal-conductivity of fluid air. *J. Phys. Chem. Ref. Data* **1985**, *14* (1), 227-234.
91. Little Things Factory Home Page. [http://www.ltf-gmbh.com/home\\_de.html](http://www.ltf-gmbh.com/home_de.html) (accessed July 26, 2014).
92. Riniker, S.; Horta, B. A. C.; Thijssen, B.; Gupta, S.; van Gunsteren, W. F.; Huenenberger, P. H., Temperature dependence of the dielectric permittivity of acetic acid, propionic acid and their methyl esters: a molecular dynamics simulation study. *Chemphyschem* **2012**, *13* (5), 1182-1190.
93. Sturm, G. S. J.; Verweij, M. D.; van Gerven, T.; Stankiewicz, A. I.; Stefanidis, G. D., On the effect of resonant microwave fields on temperature distribution in time and space. *International Journal of Heat and Mass Transfer* **2012**, *55* (13-14), 3800-3811.
94. Sharma, V.; Kumar, P.; Pathak, D., Biological importance of the indole nucleus in recent years: a comprehensive review. *J. Heterocycl. Chem.* **2010**, *47* (3), 491-502.

95. Desroses, M.; Wieckowski, K.; Stevens, M.; Odell, L. R., A microwave-assisted, propylphosphonic anhydride (T3P®) mediated one-pot Fischer indole synthesis. *Tetrahedron Lett.* **2011**, *52* (34), 4417-4420.
96. Kürti, L.; Czakó, B., *Strategic applications of named reactions in organic synthesis : background and detailed mechanisms / by László Kürti and Barbara Czakó.* Amsterdam ; Boston : Elsevier, c2005: 2005.
97. Öhrngren, P. F., A.; Russo, F.; Schanche, J.-S.; Fagrell, M.; Larhed, M., Evaluation of a nonresonant microwave applicator for continuous-flow chemistry applications. *Org. Process Res. Dev.* **2012**, *16* (5), 1053-1063.
98. CANARY by Quest, Bubble Points and Dew Points Estimation. <http://www2.questconsult.com/thermo/dewbub.html> (accessed July 26, 2014).
99. Sturm, G. S. J.; Houckgeest, A. Q. V.; Verweij, M. D.; Van Gerven, T.; Stankiewicz, A. I.; Stefanidis, G. D., Exploration of rectangular waveguides as a basis for microwave enhanced continuous flow chemistries. *Chem. Eng. Sci.* **2013**, *89*, 196-205.
100. Sturm, G. S. J.; Verweij, M. D.; Stankiewicz, A. I.; Stefanidis, G. D., Microwaves and microreactors: Design challenges and remedies. *Chem. Eng. J.* **2014**, *243*, 147-158.

## APPENDIX A. CHAPTER 2 SUPPORTING INFORMATION

### A.1 Fabrication Details

The borosilicate wafers were purchased from Telic Company. Each piece of wafer is 6 inches by 6 inches, 0.7 mm thick, and pre-coated with a 120 nm chrome layer and a 500 nm photoresist layer. The microchannel drawings were sent to CAD/Art Services, Inc. (<http://www.outputcity.com/>), where they were processed into negative print photo masks.

The wafer first went through photolithography in Prof. Scott Manalis's lab at MIT, and then was processed in Exploratory Materials Laboratory (EML), one of the facilities in the Microsystem Technology Laboratories (MTL) at MIT. During the photolithography, each wafer was covered with a photomask and exposed under a UV light source in a dark room to define the microchannels. The exposed layer of chrome was removed by soaking the wafer in the chrome-strip solution provided by the EML. The wafer was then soaked in a 49 % HF solution to etch the exposed glass layer. The etch rate was calibrated to be around 4.15  $\mu\text{m}/\text{min}$  for depth and produced an isotropic etch where the depth to width ratio is around 0.51 (Figure A.1). After the wet etch process, the wafer was rinsed with water and washed with acetone to dissolve the remaining photoresist. The wafer was then again soaked in chrome-strip solution to remove the remaining chrome layer.

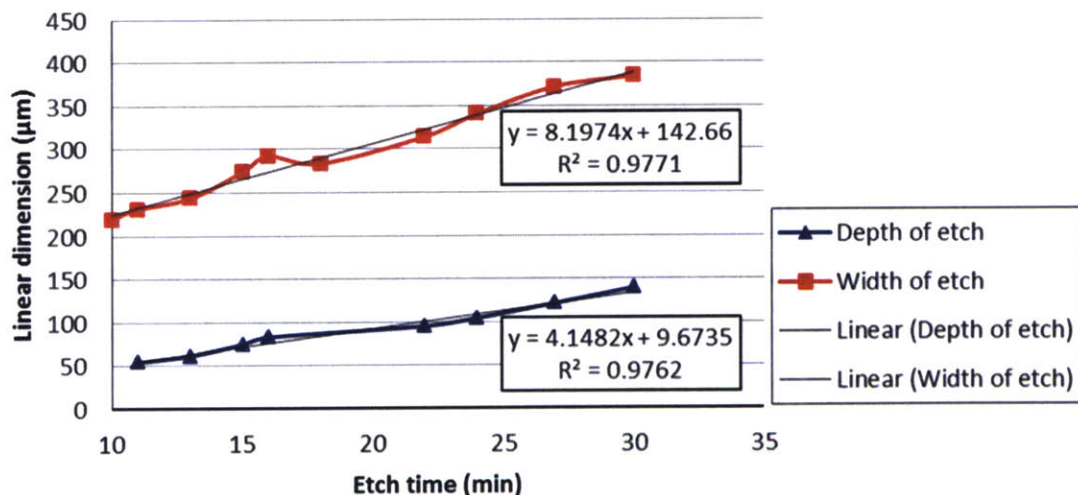


Figure A.1: Calibration curve of glass wet-etched with 49 % HF solution.

The wafer was then brought out of the EML to a lab with a CNC machine to drill the inlet and outlet holes. The wafer was first glued with resin onto a thicker (larger than 3 mm) glass substrate that acts as a mechanical support to prevent the wafer from shattering during the drilling. The holes were then drilled with a 0.039-inch round diamond drill bit bought from McMaster-Carr (<http://www.mcmaster.com/>). The positions of the holes were drawn as a DXF CAD file and read into the CNC machine by Modrilla, a Java software written by Dr. Will Grover. (Code for Modrilla: <http://wgrover.com/code/2010/01/01/modrilla.html>). Afterwards, the wafer is taken off the glass substrate by heating the binding pieces on a hot plate to melt off the resin. The wafer is gently slid off the glass substrate and rinsed with acetone to wash off the resin residue.

After the drilling process, the wafer was brought back to the MTL and cut into the desired reactor dimension with a diesaw cutting machine. The 101mm by 30 mm glass pieces were then brought back to the EML room for furnace bonding.

Each piece of glass that need to be bond was soaked in a Piranha solution (a mixture of 3:1 concentrated sulfuric acid to 30% hydrogen peroxide solution) for 10 minutes to clean the surfaces and ensure tight bonding for the next step. After 10 minutes, the glass pieces are moved into a water bath. Each piece of glass was then rinsed with water and dried with a nitrogen hose. Two pieces of glass for each reactor were manually aligned and pressed together immediately after the cleaning process. The glass assembly was then sandwich between two Glass-Mica ceramic blocks purchased from McMaster-Carr. The ceramic blocks acted as flat surfaced to maintain the shape of the reactor during high-temperature bonding. The size of the ceramic blocks was slightly larger than the reactor dimension, and the surfaces of the ceramic blocks were first roughened with sandpaper to prevent bonding with the glass surface in the furnace. The glass reactor and ceramic assembly was then placed in the furnace, and a 1 kg steel block was placed on top of the assembly to compress the reactor during bonding. The furnace was heated from room temperature to 650 °C in 7 hrs, held at 650 °C for 5 hrs, and then slowly cooled down to room temperature in 8 hrs.

Figure A.2 shows the cross-section view of a reactor with only one side etched with channels, and Figure A.3 shows a reactor etch on both side. There is no visible line separating the two glass pieces, showing that the high-temperature bonding procedure had melted the pieces into a single block of glass.

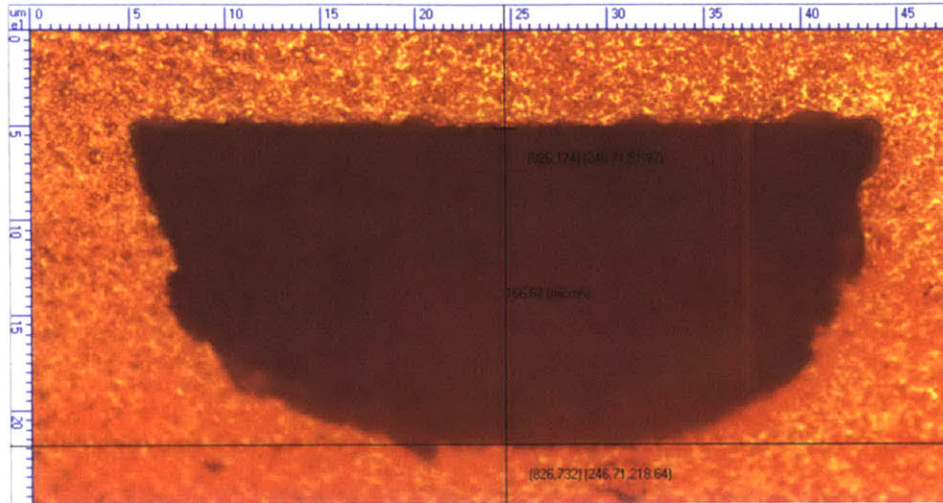


Figure A.2: Microscope picture of furnace bonded glass reactor etched on single side.  
(Scale unit: 10  $\mu\text{m}$ )

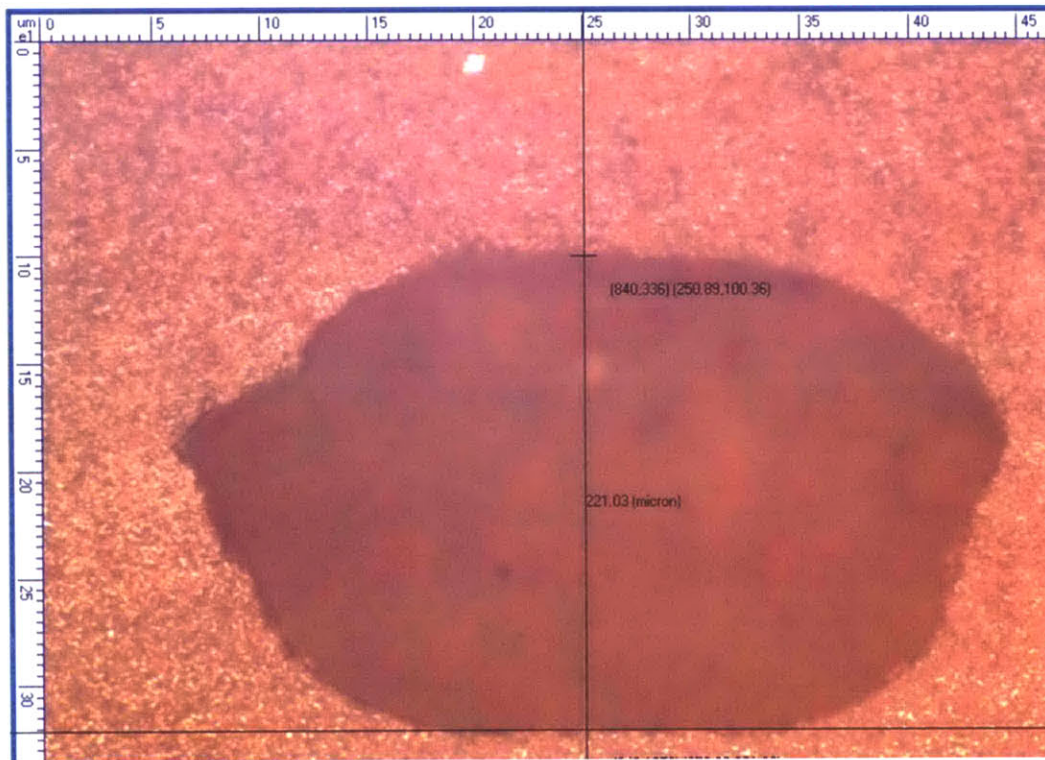
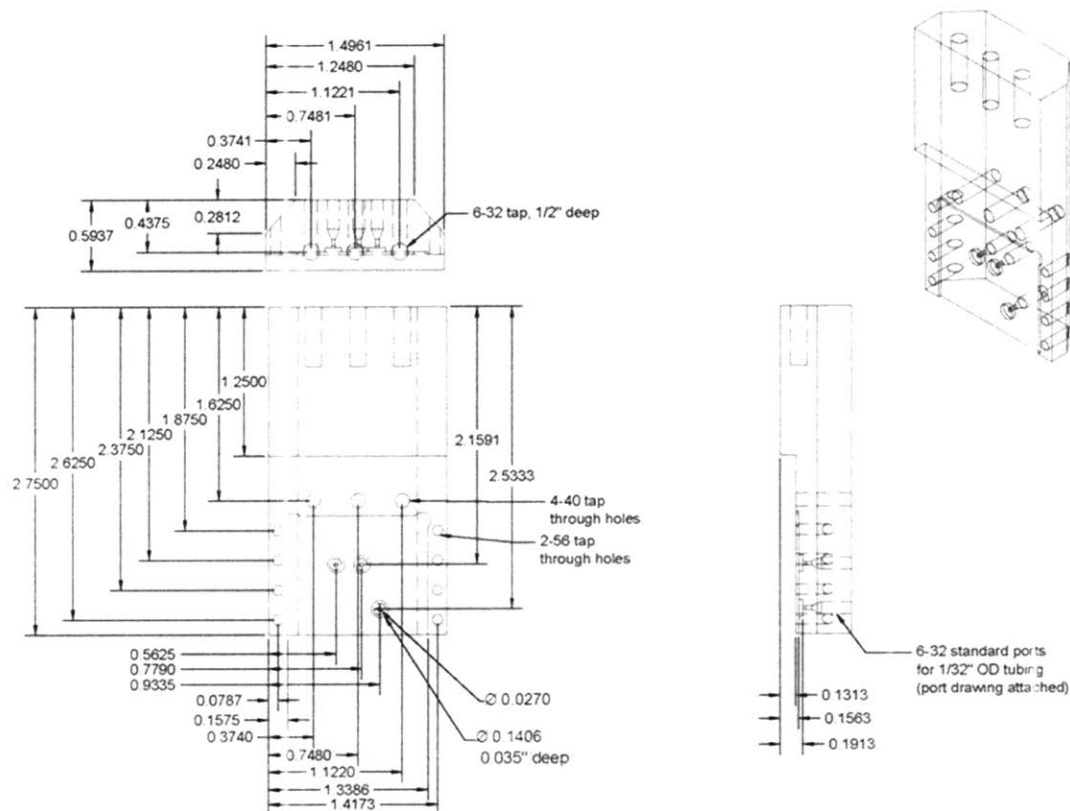


Figure A.3: Microscope picture of furnace bonded glass reactor etched on both sides. (Scale unit: 10  $\mu\text{m}$ )

## A.2 Designs of Initial Glass Microreactor Holders

Below are the drawings for the microreactor tubing packaging and the Teflon® fiber optic holder. The finish pieces were made by the MIT Central Machine Shop.



**Figure A.4: Drawing of PEEK holder for initial microreactor setup. (Unit: inch)**

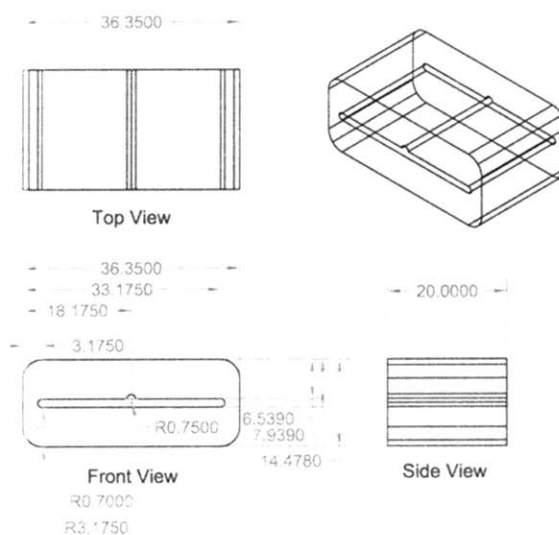


**Figure A.5: Drawing of Teflon holder for fiber optic probe. (Unit: mm)**



### A.3 Mixing Quality

The mixing effect was simulated with COMSOL to ensure that the reactor design allows for uniform mixing. The 2D channel design was imported as the simulation geometry. The inlets were to various flow rates. The results are show for the slowest and the fastest flow rates simulated. For the slowest flow rate, both inlets were set at 4.5  $\mu\text{l}/\text{min}$ , the lowest flow rate used in our chemistries. For the highest flow rate, both inlets were set at 750  $\mu\text{l}/\text{min}$ , which is 3 times faster than the flow rates used for our experiments. The concentration of one stream is set at 1000  $\text{mol}/\text{m}^3$ , equivalent to the maximum concentration used in all our experiments, while the other inlet stream was set at 0  $\text{mol}/\text{m}^3$ . The diffusion coefficient was set at  $1 \times 10^{-9} \text{ m}^2/\text{s}$ , the order of magnitude for the diffusion coefficient of most liquids.

The faster the flow rate, the longer the mixing length is required for fully mixed solutions. At 4.5  $\mu\text{l}/\text{min}$ , the mixing length is about 8 turns in the serpentine channel, which means it takes less than one row of the channel to reach full mixing (Figure A.6). At 750  $\mu\text{l}/\text{min}$ , a longer mixing length is required, and the streams are fully mixed at about the middle of the second row of the serpentine channel (Figure A.7). The results show that although the mixing zone is effective, having 11 rows of serpentine channel is redundant for the mixing purpose and adds technical challenges during fabrication. The mixing zone was therefore eliminated for reactor design later on.

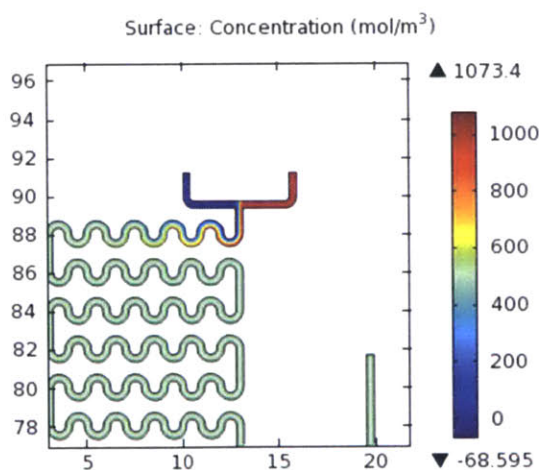


**Figure A.6: Simulation of mixing length for microreactor with 4.5  $\mu\text{l}/\text{min}$  flow rate at each inlet.**

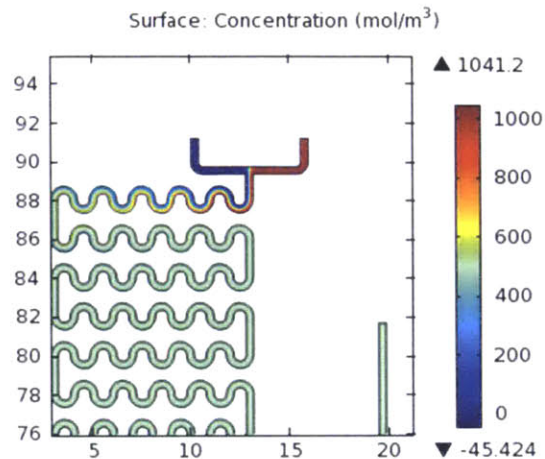


**Figure A.7: Simulation of mixing length for microreactor with 750  $\mu\text{L}/\text{min}$  flow rate at each inlet.**

## A.4 Experimental Procedure

The reaction solvents were all loaded into two 8 mL Harvard Apparatus stainless steel syringes connected to the two microreactor inlets and pumped through the system using Harvard Apparatus syringe pumps.

For each temperature, the microwave was turned on at the same time the pump was started. While waiting for reaction to reach the desired temperature, the pump was set at the lowest flow rate (the longest residence time) of the desired experimental conditions. Once the temperature monitor showed that the temperature oscillation is within 5 °C of the set temperature, the flow was purged for at least two times the reactor volume, and then the first sample was collected. If multiple collection of the same experimental condition were required for repeatability test, the flow was purged for one minute, and the next sample was collected. After all the samples for the first residence time were collected, the pump flow rate was adjusted to the next lowest flow rate, and the samples were collected after purging at least two times the reactor volume. The same steps were repeated until samples of all the residence time points were collected.

The microwave was then turned off until the unit reaches room temperature, and then turned on again for another temperature setting. The same steps as above were repeated for the sample collection of the new experiment temperature.

#### A.4.1 Diels-Alder Reaction

For each experiment, two stock solutions were prepared: one with 0.5 M of isoprene (purchased from Sigma-Aldrich) in DMF and a 0.5 equivalent of naphthalene as the internal standard; the other with a 0.5 M of maleic anhydride in DMF. The solutions are loaded into two different syringes and mixed in the reactor.

The concentration of isoprene were analyzed by adding 10  $\mu\text{L}$  of collection with 990  $\mu\text{L}$  DCM and run through an isocratic UPLC method using a 1:1 ratio of water with 0.1 % formic acid and acetonitrile at the eluent for 15 minutes. The absorbance was recorded at 220 nm.

The kinetics used for the Diels-Alder reaction was taken from the reference “*McMullen, J. P.; Jensen, K. F., Rapid Determination of Reaction Kinetics with an Automated Microfluidic System. Org. Process Res. Dev. 2011, 15 (2), 398-407.*” The reaction has a second order rate expression, where the reaction order with respect to each reactant is one:

$$r_1 = -kC_1C_2$$

$r_1$  is the rate of isoprene consumption,  $C_1$  and  $C_2$  are respectively the concentrations of isoprene and maleic anhydride, and  $k$  is the rate constant for which the pre-exponential value,  $A = (2.1 \pm 1.3) \times 10^6 \text{ M}^{-1} \text{ s}^{-1}$  and the activation energy,  $E_a = 56.3 \pm 1.9 \text{ kJ/mol}$ .

The repeatability of the experimental results were really poor and could not be used to establish a valid function for the rate constant (Figure A.8).

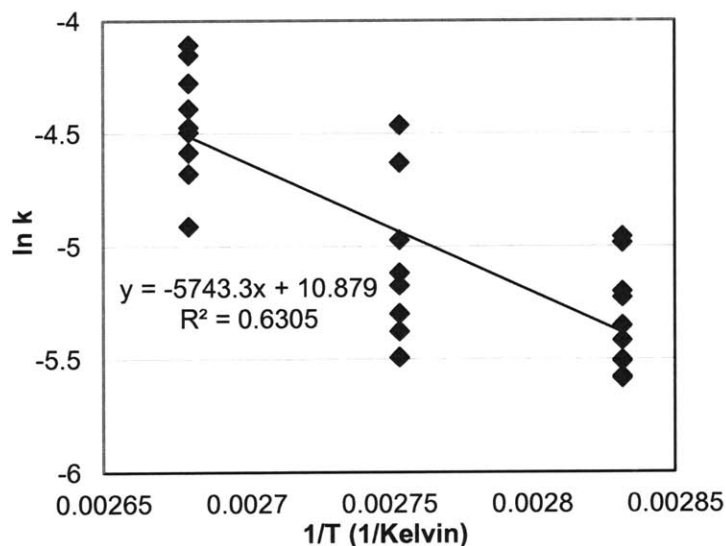


**Figure A.8: Arrhenius plot of ln k versus 1/T for Diels-Alder reaction using initial microreactor with microwave.**

The experiments were repeated in batch mode in the microwave to verify if the problem lied in the microreactor or this particular reaction. In the batch experiments, the reactants and internal standard were all prepared in one solution with the same initial concentration as before. The reactions were run in a 10 mL CEM glass vial and the temperature was recorded with the IR sensor of the microwave unit. The results display ill repeatability with a large deviation between results of the same conditions (Table A.1) and was also not able to provide a valid base for the rate constant calculation (Figure A.9). The average variance for the batch reaction was 13.27 %. This reaction was therefore not included in any future work to assess the microreactor.

**Table A.1: Diels-Alder results in batch mode.**

Conditions	# of experiments	Average (%)	Standard Deviation (%)
80 °C, 1 min	2.00	32.40	8.81
70 °C, 3 min	4.00	34.90	22.70
80 °C, 3 min	7.00	35.60	16.80
80 °C, 5 min	7.00	42.80	13.30
90 °C, 3 min	3.00	29.70	10.90

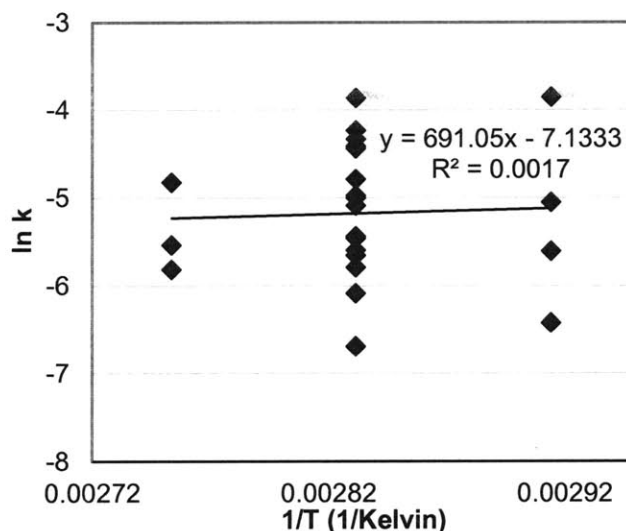


**Figure A.9: Arrhenius plot of ln k versus 1/T for Diels-Alder reaction in batch experiments with microwave.**

#### A.4.2 Condensation Reaction

For each experiment, a 0.5 M or 1 M solution of *o*-phenyldiamine (purchased from Sigma-Aldrich) was prepared with pure acetic acid, and a 0.5 equivalent of naphthalene was added as the internal standard. The conversions and yields were calculated from the GC-FID

chromatography. The GC oven was set to hold at 70 °C for a minute, increase to 300 °C with a 25 °C/min ramp and hold for a minute at the final temperature. The calibration curve for the product was made with 2-methylbenzimidazole purchased from Sigma-Aldrich. The naphthalene peak is at 3.03 minute, *o*-phenyldiamine at 3.25 minute, and 2-methylbenzimidazole at 4.90 minute.

The kinetics of the condensation reaction was previously reported in “Damm, M.; Glasnov, T. N.; Kappe, C. O., *Translating High-Temperature Microwave Chemistry to Scalable Continuous Flow Processes. Org. Process Res. Dev.* **2009**, *14* (1), 215-224.” The reaction has a first order rate expression with respect to the diamine:

$$r_1 = -kC_1$$

$r_1$  is the rate of diamine consumption,  $C_1$  is the concentrations of the diamine, and  $k$  is the rate constant for which the paper reported the pre-exponential value,  $A = 3.1 \times 10^8 \text{ s}^{-1}$  and the activation energy,  $E_a = 73.43 \text{ kJ/mol}$ .

However, this result differs from the conversions we obtained from both the microwave-heated and the cartridge-heated microreactor experiments. We therefore recalculated the expression of the rate constant from the conversion values listed in the supporting information of the paper. The results are different from the report, with  $A = 9.82 \times 10^6 \text{ s}^{-1}$  and  $E_a = 76.74 \text{ kJ/mol}$  (Figure A.10).

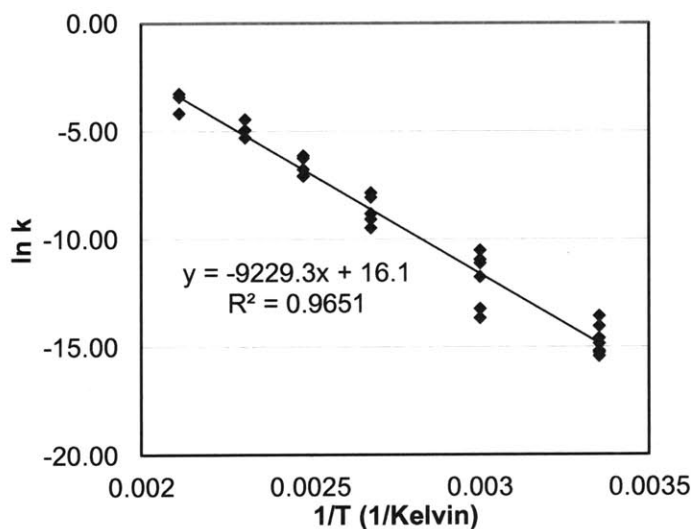


**Figure A.10:** Arrhenius plot of  $\ln k$  versus  $1/T$  for the condensation reaction using the reported conversions in reference “Damm, M.; Glasnov, T. N.; Kappe, C. O., *Translating*

*High-Temperature Microwave Chemistry to Scalable Continuous Flow Processes. Org. Process Res. Dev. 2009, 14 (1), 215-224.”*

The rate constant parameters we obtained from the cartridge-heated reactor were  $A = (9.83 \pm 8.65) \times 10^5 \text{ s}^{-1}$  and  $E_a = 67.9 \pm 7.43 \text{ kJ/mol}$  (Figure A.11). A regression line was made with the fixed activation energy from the calculation of the literature conversions,  $E_a = 76.74 \text{ kJ/mol}$ , and the resulting pre-exponential factor is  $A = 1.03 \times 10^7 \text{ s}^{-1}$  (red line in Figure A.11). The last set of parameters was used for all future calculations to validate the reactors with the condensation reactions.

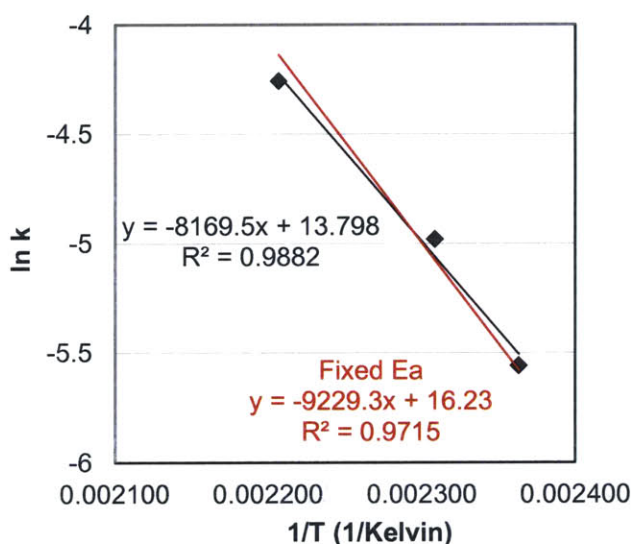


**Figure A.11: Arrhenius plot of  $\ln k$  versus  $1/T$  of the condensation reaction with the results from the cartridge-heated microreactor. The results from the red calibration line were used to determine the activation energy and pre-exponential factor.**

#### **A.4.3 Aromatic Substitution**

When the reaction was run with 0.5 M of starting material, the salt formation clogged the channels and broke the reactor. The concentration was therefore lowered to 0.1 M and 0.25 M. For each experiment, two stock solutions were prepared: one with a 0.1 M or 0.25 M 2-chloropyridine dissolved in NMP and a 0.5 equivalent added as the internal standard; and the other with a 2.2 equivalent (0.22 M or 0.55 M) of piperidine in NMP. The solutions are loaded into two different syringes and mixed in the reactor. The conversions and yields were calculated from the GC-FID chromatography. The GC oven was set to hold at 70 °C for a minute, increase to 300 °C with a 25 °C/min ramp and hold for a minute at the final temperature.

## APPENDIX B. CHAPTER 3 SUPPORTING INFORMATION

---

### B.1 Nusselt Number Calculation Details and Matlab Code for Thermal Conductivity Estimation Model

The Nusselt numbers in an equivalent rectangular enclosure,  $Nu_{rectangular}$ , are calculated from the reference “Caton, I. *In Natural convection in enclosures, Proceedings of the 6th International Heat Transfer Conference, Toronto, Canada., Washington : Hemisphere Pub. Corp.: Toronto, Canada., 1978; pp 13-43.*” For a rectangular area between two vertical walls of fixed temperature, the Nusselt number can be found as:

$$Nu_{rec} = 0.22 \left( \frac{Pr}{0.2 + Pr} Ra \right)^{0.28} \left( \frac{H}{L} \right)^{-0.25}$$

$$\text{when } 2 < \frac{H}{L} < 10, Pr < 10^5, \text{ and } Ra < 10^{10}$$

$$Nu_{rec} = 0.18 \left( \frac{Pr}{0.2 + Pr} Ra \right)^{0.29}$$

$$\text{when } 1 < \frac{H}{L} < 2, 10^{-3} < Pr < 10^5, \text{ and } 10^3 < \frac{RaPr}{0.2+Pr}$$

where L is the length of the gap between the two walls, H is the height of the wall, Pr is the Prandtl number, Ra is the Rayleigh number each defined as:

$$Pr = \frac{\nu}{\alpha}$$

$$Ra = \frac{g\beta(T_1 - T_2)L^3}{\nu\alpha}$$

where  $\nu$  is the kinetic viscosity of air,  $\alpha$  is the thermal diffusivity of air,  $\beta$  is the coefficient of thermal expansion,  $T_1$  and  $T_2$  are the temperatures of the two wall.

The numbers we used for our calculations were:

$$\nu = 1.59 \times 10^{-5} \frac{m^2}{s}, \alpha = 2.25 \times 10^{-5} \frac{m^2}{s}$$

$H = 0.086 \text{ m}$ , the height of the microwave cavity.

$L = 0.02825 \text{ m}$ , the average of cavity radius and the waveguide width.

$T_1$  is set as the steady-state temperature of the reactor: in the parallel-to-port situation, 363.15 K for the 300 W microwave irradiation, 343.15 K for 150 W microwave irradiation, and 308.15 K for 10 W microwave irradiation.

$T_2$  is set at room temperature, 298.15 K.

$\beta = \frac{1}{(T_1+T_2)/2}$ , using the ideal gas law, the coefficient of volume expansion is approximated as the inverse of the average temperature between the two walls.

The following Matlab code was written for the calculation:

```
function [Nu,Pr,Ra] =
NusseltNumber_Convection_RectangleEnclosure(T1,T2,v,alpha,H,L)
clc;
g = 9.8; % gravity [m/s^2]

Tair = (T1+T2)/2; % temperature of film, where air properties are evaluated
at
Pr = v/alpha; % Prandlt number
beta = 1/Tair; % coefficient of volume expansion, expression is for ideal gas
A = H/L; % aspect ratio of the enclosure
Ra = g*beta*(T1-T2)*L^3/(alpha*v); % Rayleigh number

if (A <= 10) && (A >= 2) && (Pr<=10^5) && (Ra<=10^10) && (Ra>=10^3)
    Nu = 0.22*(Pr/(0.2+Pr)*Ra)^0.28*(A)^(-1/4);
elseif (A <= 2) && (A >= 1) && (Pr<=10^5) && (Pr>=10^-3) &&
((Ra*Pr/(0.2+Pr))>=10^3)
    Nu = 0.18*(Pr/(0.2+Pr)*Ra)^0.29;
else
    Nu = 0;
end

end
```



## B.2 Additional Temperature Plots for Each Simulation Models

### B.2.1 Initial Model without Air Convection

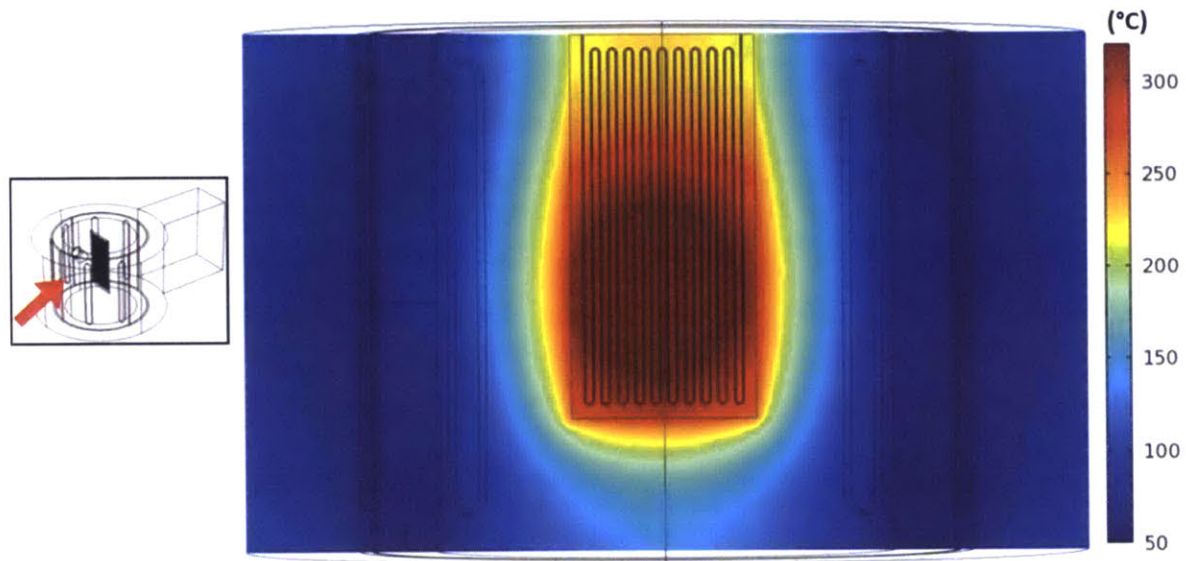


Figure B.1: Temperature of cavity center plane viewed from the front side of the unit when reactor is parallel to port at  $t=3000$  seconds under 300 W irradiation for initial model without air convection.

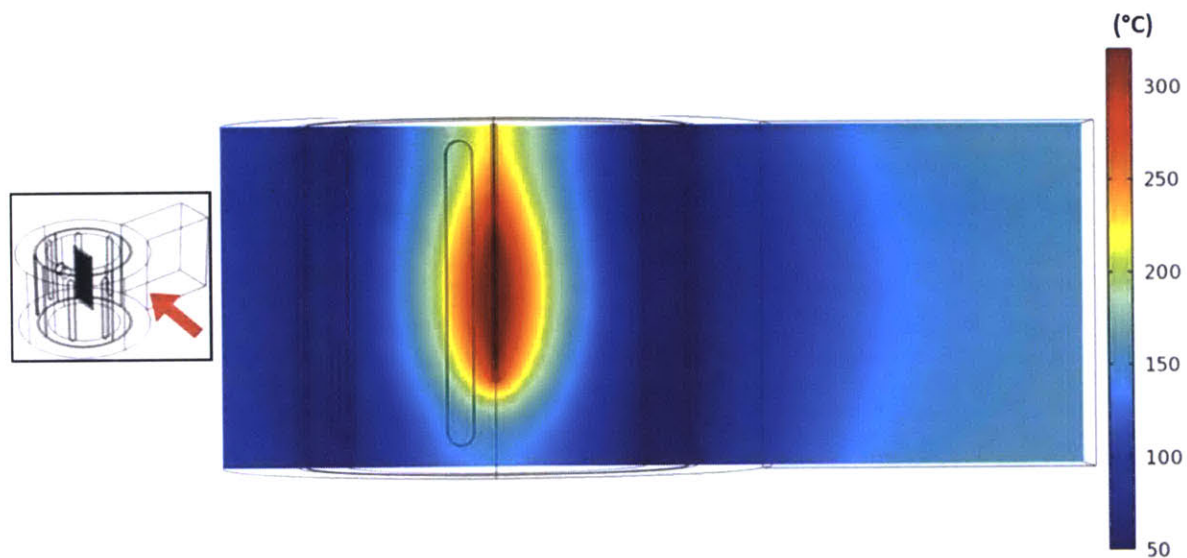
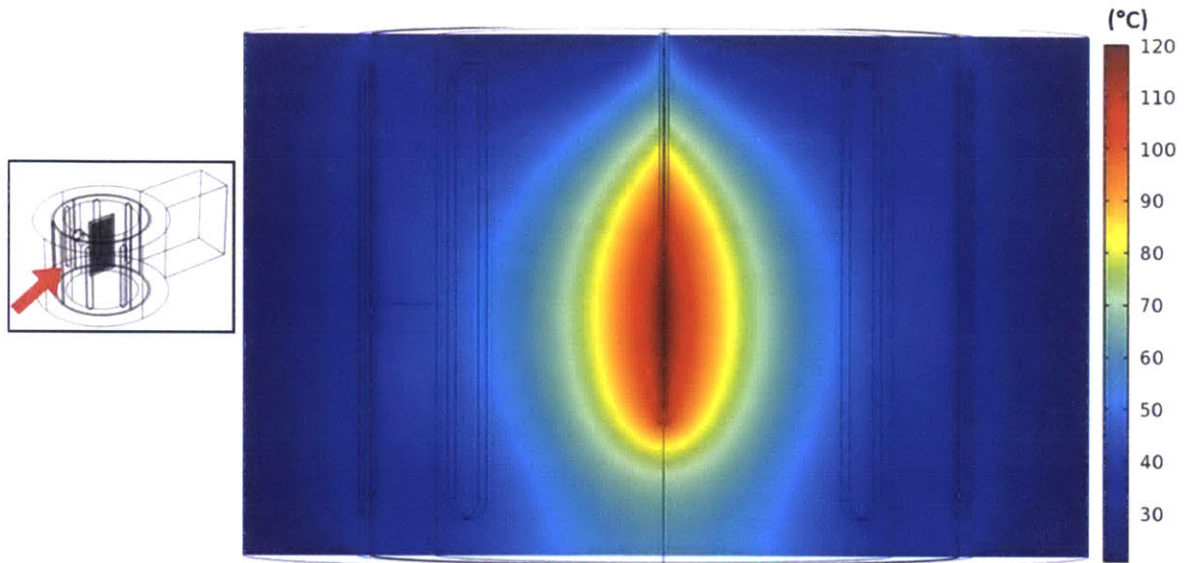
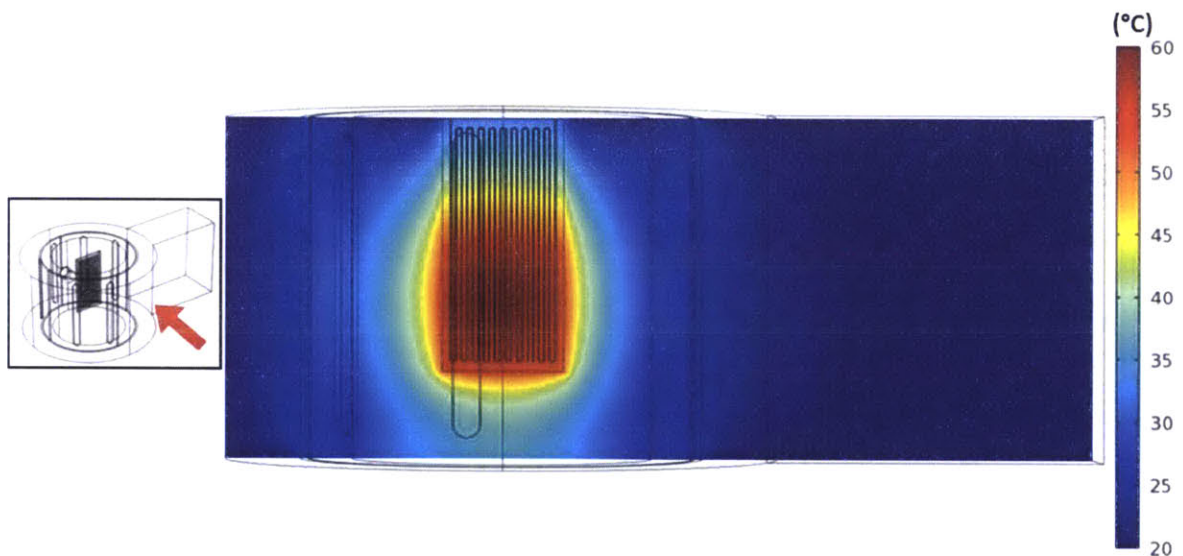


Figure B.2: Temperature of cavity and waveguide center plane viewed from the right side of the unit when reactor is parallel to port at  $t=3000$  seconds under 300 W irradiation for initial model without air convection.



**Figure B.3: Temperature of cavity center plane viewed from the front side of the unit when reactor is perpendicular to port at  $t=3000$  seconds under 300 W irradiation for initial model without air convection.**



**Figure B.4: Temperature of cavity and waveguide center plane viewed from the right side of the unit when reactor is perpendicular to port at  $t=3000$  seconds for under 300 W irradiation initial model without air convection.**

## B.2.2 Thermal Conductivity Estimation Model

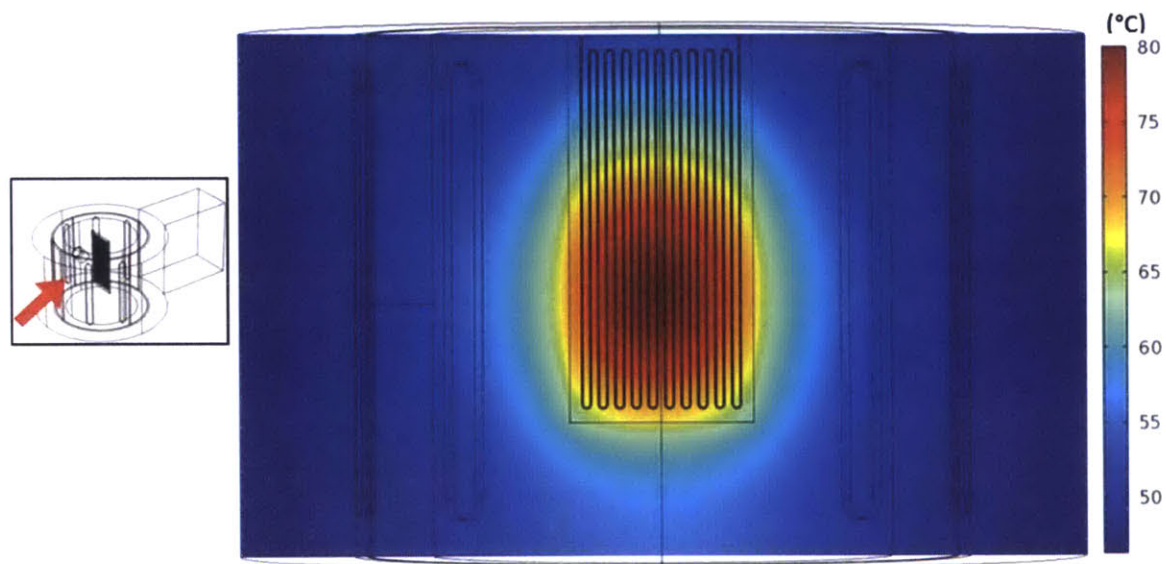


Figure B.5: Temperature of cavity center plane viewed from the front side of the unit when reactor is parallel to port at  $t=3000$  seconds under 300 W irradiation for k-estimation model.

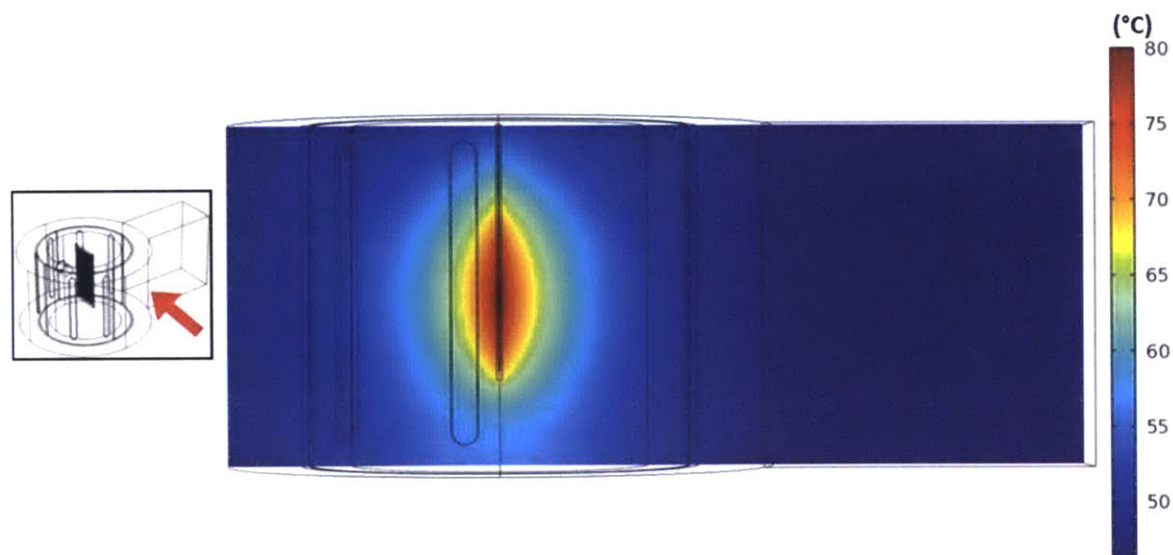
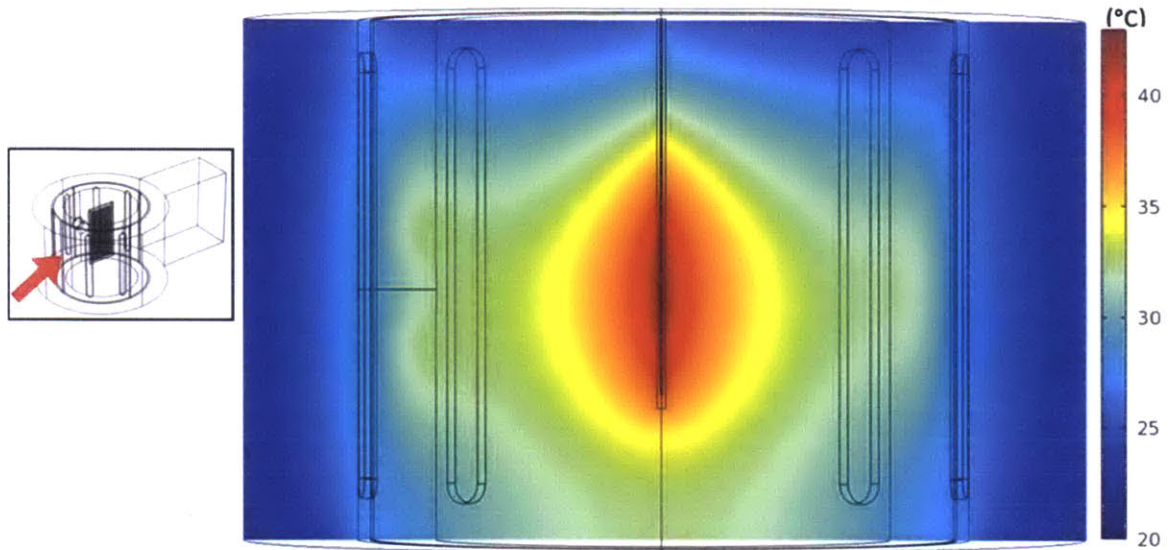
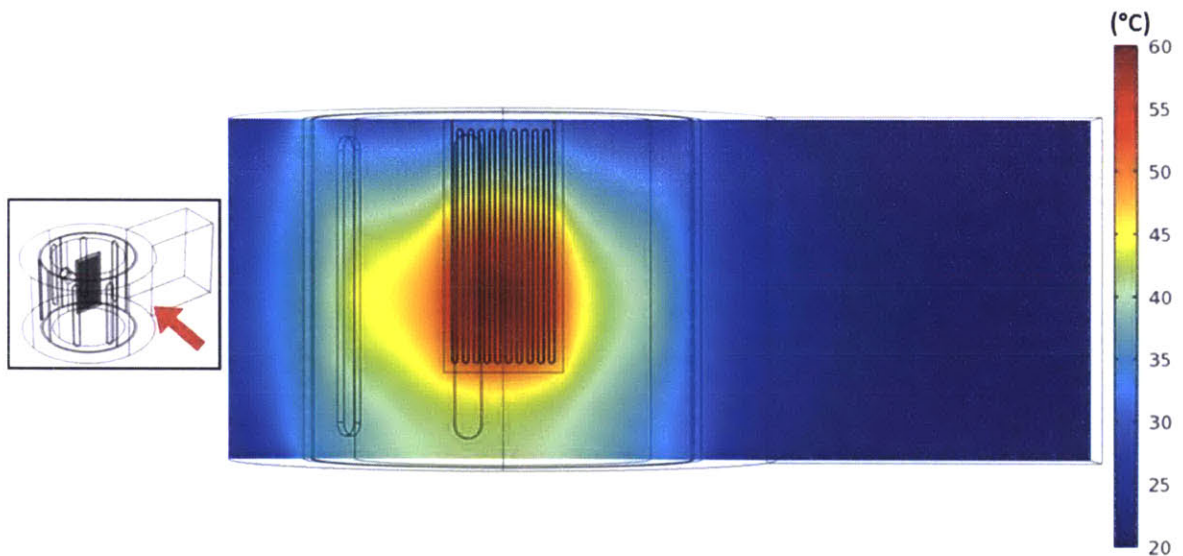


Figure B.6: Temperature of cavity and waveguide center plane viewed from the right side of the unit when reactor is parallel to port at  $t=3000$  seconds under 300 W irradiation for k-estimation model.



**Figure B.7: Temperature of cavity center plane viewed from the front side of the unit when reactor is perpendicular to port at  $t=3000$  seconds under 300 W irradiation for k-estimation model.**



**Figure B.8: Temperature of cavity and waveguide center plane viewed from the right side of the unit when reactor is perpendicular to port at  $t=3000$  seconds under 300 W irradiation for k-estimation model.**

### B.2.3 Single-Phase Flow Model

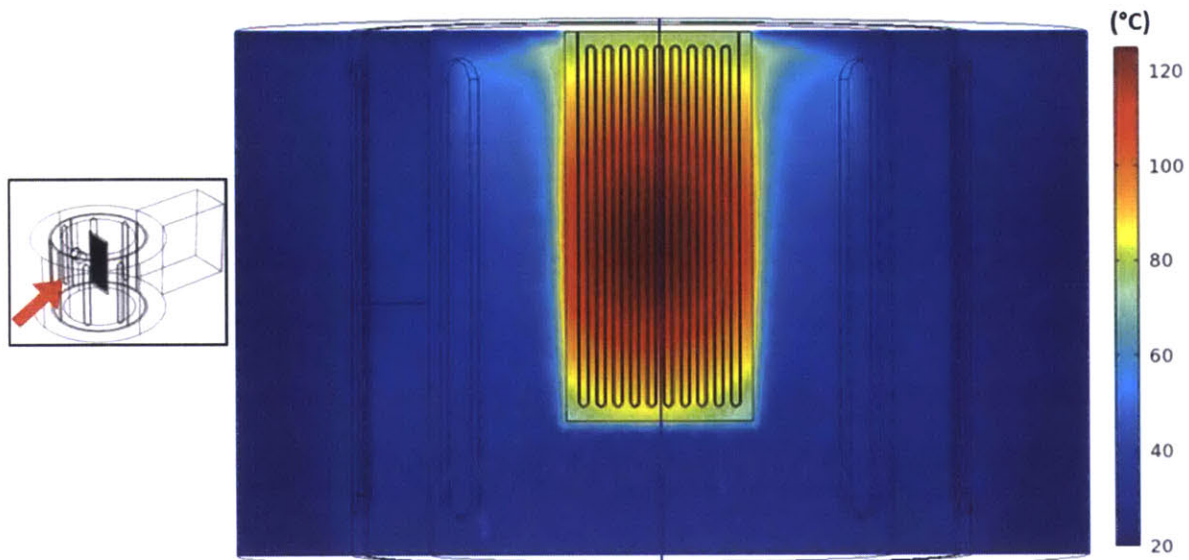


Figure B.9: Temperature of cavity center plane viewed from the front side of the unit when reactor is parallel to port at  $t=1000$  seconds under 300 W irradiation for laminar flow model.

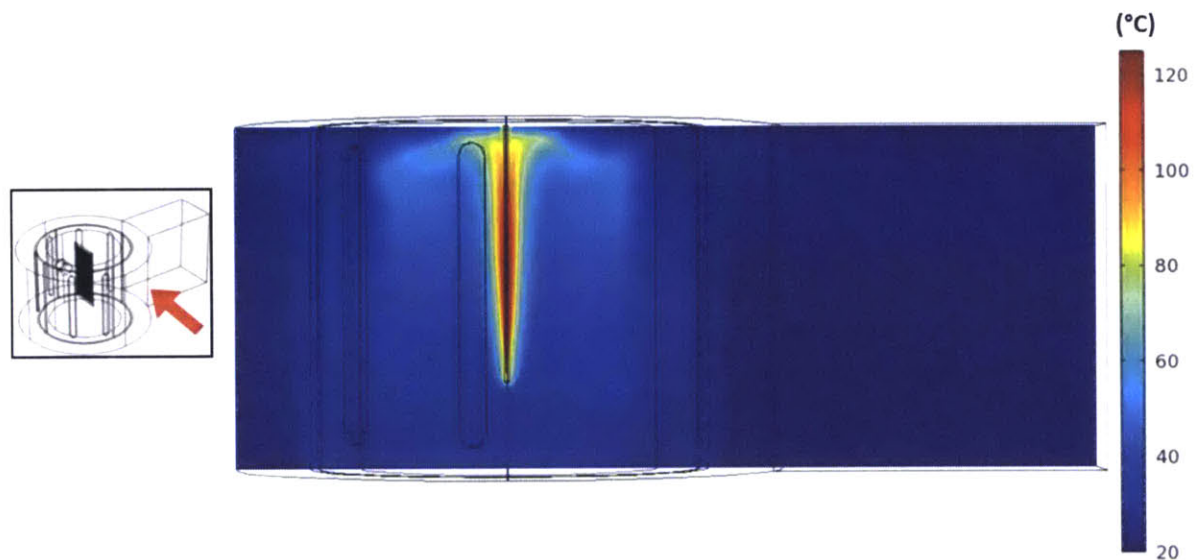
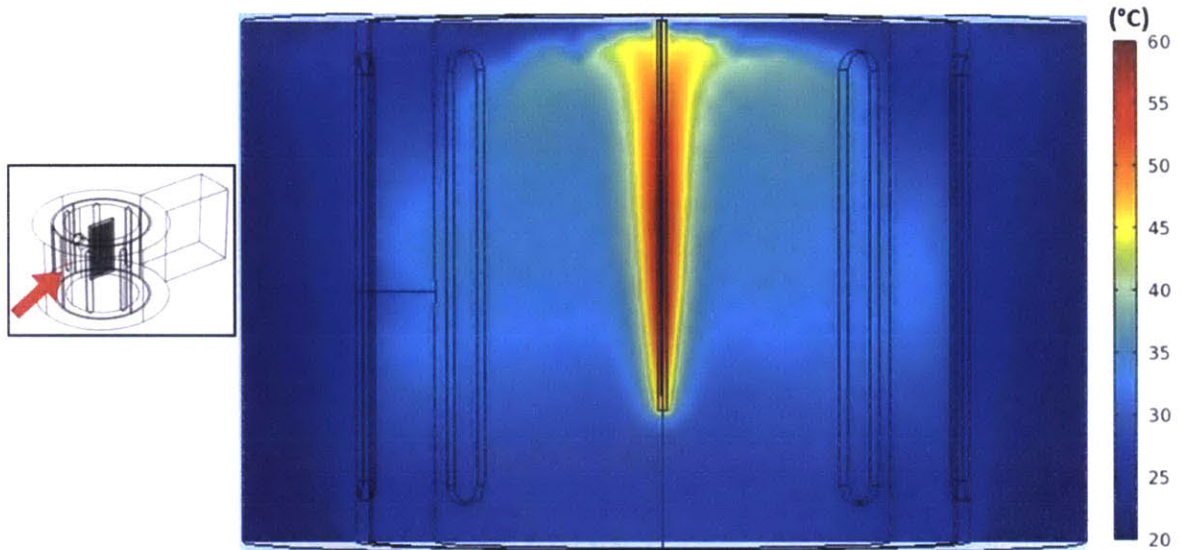
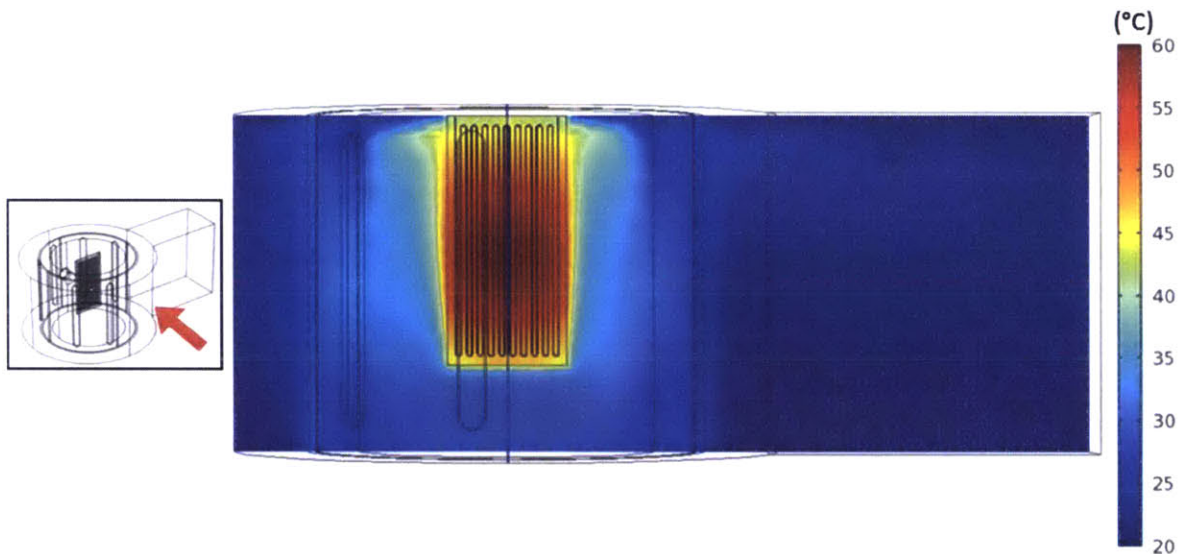


Figure B.10: Temperature of cavity and waveguide center plane viewed from the right side of the unit when reactor is parallel to port at  $t=1000$  seconds under 300 W irradiation for laminar flow model.



**Figure B.11: Temperature of cavity center plane viewed from the front side of the unit when reactor is perpendicular to port at  $t=1000$  seconds under 300 W irradiation for laminar flow model.**



**Figure B.12: Temperature of cavity and waveguide center plane viewed from the right side of the unit when reactor is perpendicular to port at  $t=1000$  seconds under 300 W irradiation for laminar flow model.**

## APPENDIX C. CHAPTER 5 SUPPORTING INFORMATION

---

### C.1 Condensation Reaction Experimental Procedure

In order to test the repeatability of the microwave microreactor setup, the reactions at each of the two positions were repeated three times, each run on different days and run through all 20 different sets of conditions (130 °C, 140 °C, 150 °C, 160 °C combined with 1 min, 2 min, 3 min, 5 min, 10 min residence times). For each of the three repeats, the *o*-phenyldiamine concentration was 0.5 M, 0.5 M, and 1 M. The concentration was varied between each run to test if the experiments fit the kinetics: the kinetics of this reaction is first order with respect to the *o*-phenyldiamine, and the concentration should not change the reaction rate. The final results were deemed repeatable since the conversion variations among the three experiment runs were all within 5 %, the error range of GC analysis (Agilent Technologies 6890).

For each temperature, the microwave was turned on at the same time the pump was started. While waiting for reaction to reach the desired temperature, the pump was set at the lowest flow rate (the longest residence time) of the desired experimental conditions. Once the temperature monitor showed that the temperature oscillation is within 3 °C of the set temperature, the flow was purged for at least two times the reactor volume, and then the first sample was collected. Each temperature and residence time condition has a collection of three samples during the same run with about a minute of purge in between each collection. We are able to assume steady-state because the results of these three samples for each condition are within 5 % of conversion, the error range of GC analysis.

For each experiment, a 0.5 M or 1 M solution of *o*-phenyldiamine (purchased from Sigma-Aldrich) was prepared with pure acetic acid, and a 0.5 equivalent of naphthalene was added as the internal standard. The conversions and yields were calculated from the GC-FID chromatography. The GC oven was set to hold at 70 °C for a minute, increase to 300 °C with a 25 °C/min ramp and hold for a minute at the final temperature. The calibration curve for the product was made with 2-methylbenzimidazole purchased from Sigma-Aldrich. The naphthalene peak is at 3.03 minute, *o*-phenyldiamine at 3.25 minute, and 2-methylbenzimidazole at 4.90 minute.

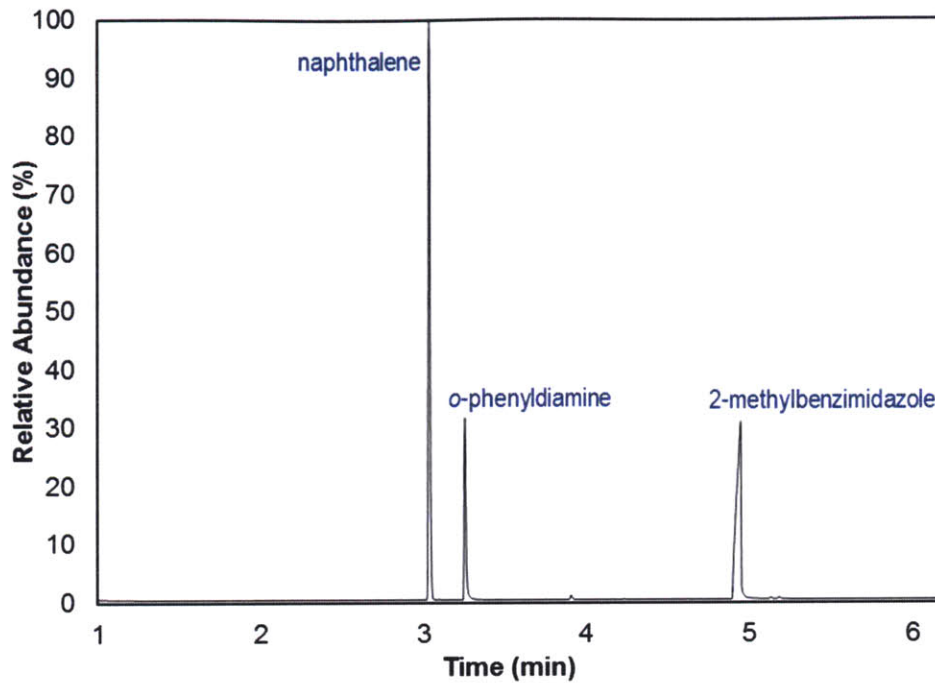


**Figure C.1: GC-FID chromatography for condensation reaction with glycerol jacket at 140 °C, 10 min residence time.**

## C.2 Matlab Code for Reactor Mean Temperature Calculation

An example of the following Matlab calculation is the quadratic function:

$$T = -2.058 \times 10^{-4}r^2 + 0.307r + 22.52$$

The mean temperature calculated by integrating the Arrhenius equation is 115 °C for all residence time, and the volume average temperature of the reactor is 95 °C for all residence time. This is an example of how the mean temperature is the same for all residence time as long as the temperature function is the same, but the mean temperature calculated from the Arrhenius equation is different than the volume average temperature.

The following Matlab code was written for the calculation:

```
%This fuction is used to calculate the average temperature from the
%microwave reactor with a temperature distribution
%The input n is the residence time in the unit of minutes
%Created on 2014/03/05 by Jen Lee

function Condensation_Temp_average(n)
syms t;      %define time
syms r;      %define space/length of reactor
```



```

r_length = 685.83; %Length of reactor [=] mm
t_res = n * 60; %Set residence time [=] sec
R = 8.3145; %Gas rate constant [=] J/mol/K
Ea = 7.67*10^4; %Activation energy [=] J/mol
T_k = 273.15; %Conversion from degC to K [=] degC

%Define Temperature distribution in the reactor:
r = r_length/t_res * t; %Define function r = r(t)
%T = 10*r/r_length + 130; %Define function T = T(r) as a linear
function
%T = 10*r^2/r_length^2 + 10*r/r_length + 130; %Define function T = T(r) as
a quadratic function
%T = -2.058 *10^(-4)*r^2+0.307*r+22.52; %Define function T = T(r) as
a quadratic function
T = -80/r_length^2 * r^2 + 80/r_length * r +130; %Concave equation with
center being hottest
%T = exp(r/r_length+4.8675);
%T = exp (t/t_res+4.8675);
hold on;
ezplot(t, T, [0, t_res]);
axis([0 600 130 150]);
figure;
ezplot(r, T, [0, r_length]);
axis([0 685.83 130 150]);
axis square;

%Start integration calculation:
T_integral = int(exp(-Ea/R/(T+T_k)),t,0,t_res); %Integrate with respect to
residence time from 0[s] to t_res[s]
T_ave = (-Ea/R)*(1/log(T_integral/t_res))-T_k; %Calculate Average
Temperature of reactor
T_ave = double(T_ave); %Transform output as a
numerical number
T_int = double(T_integral);
%Integration of T only, without rate constant fuction:
T_integral_2 = int(T,t,0,t_res); %Integrate with respect to residence time
from 0[s] to t_res[s]
T_ave_2 = T_integral_2/t_res; %Calculate Average Temperature of reactor
T_ave_2 = double(T_ave_2); %Transform output as a numerical number
T_int_2 = double(T_integral_2);

%Output result:
%disp(T_int);
disp('T_ave=');
disp(T_ave);
disp('T_ave_2=');
disp(T_ave_2);

end

```

### C.3 Fischer Indole Synthesis GC Chromatography, Mass Spectrum, and NMR

The gas chromatography flame ionization detector and mass spectrometry (GC-FID and GC/MS) was performed on an Agilent 6890 GC. Analytical thin-layer chromatography was performed on a silica gel 60 F-254 plates from EMD and visualized with UV light.  $^1\text{H}$  NMR spectra were recorded at 300.11 MHz with the chemical shifts referenced to TMS via residue solvent signals.  $\text{CDCl}_3$  was used as the solvent for all NMR samples, with the solvent peak at 7.26. For the crude product NMR spectra calculation for conversion and yield, 1,3,4-trimethoxybenzene was used as the internal standard.

For each of the GC and GC/MS samples, 100  $\mu\text{l}$  of collected solution ( $\sim 0.025$  mmol scale) was added to 0.1 ml of DCM for analysis. For the NMR sample, 100  $\mu\text{l}$  of collected solution was extracted with DCM and  $\text{NaHCO}_3$ ; the DCM phase was evaporated, and the final residue was dissolved in deuterated chloroform.

The  $\text{CDCl}_3$  and 1,3,4-trimethoxybenzene NMR spectra are included as references:

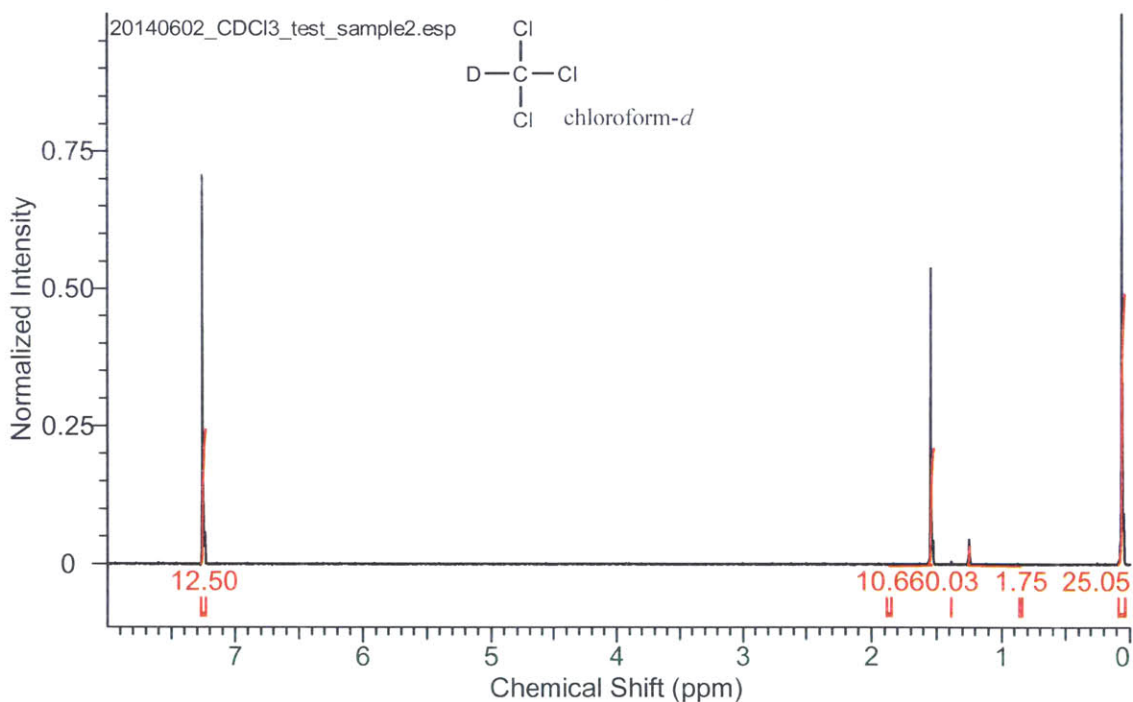


**Figure C.2: NMR spectrum of solvent deuterated chloroform.**

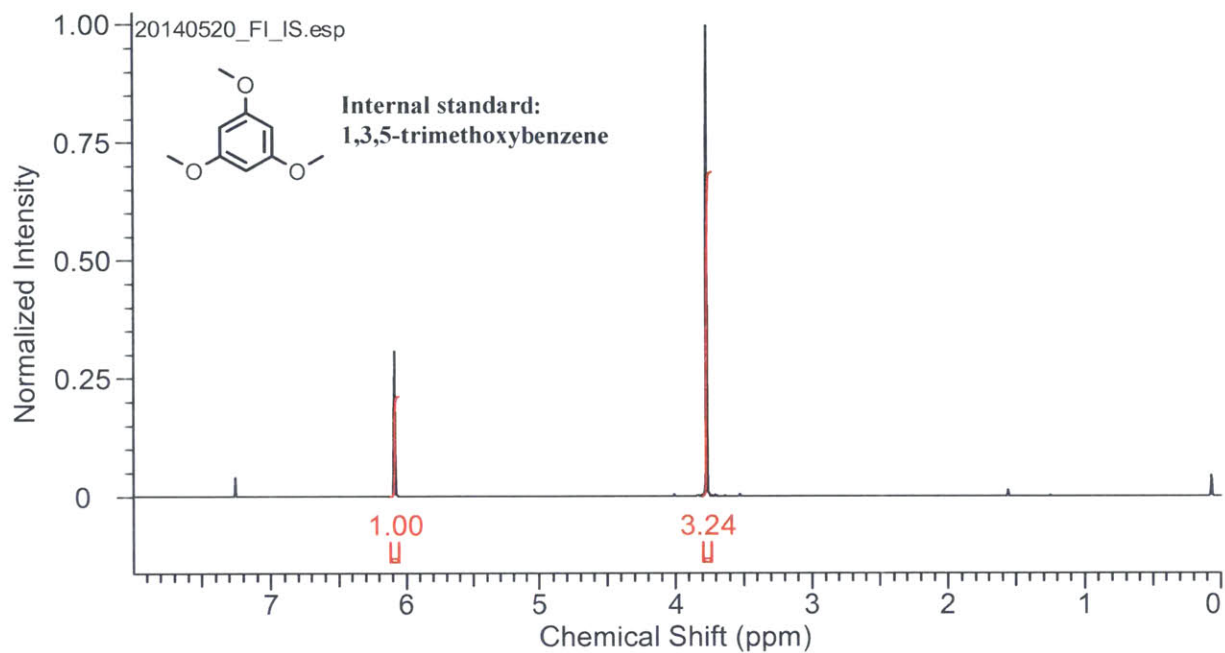


**Figure C.3: NMR spectrum of internal standard 1,3,5-trimethoxybenzene.**

### C.3.1 Product c1: 1,2,3,4-tetrahydro-1*H*-carbazole

The conversions and yields of the initial screening were calculated from GC chromatography. A product calibration curve with respect to 1,3,5-trimethoxybenzene used for the yield calculation was made with 1,2,3,4-tetrahydrocarbazole purchases from Sigma-Aldrich. The reaction product was also identified with GC/MS, and the conversion and yield were also verified by NMR.

#### GC-FID:

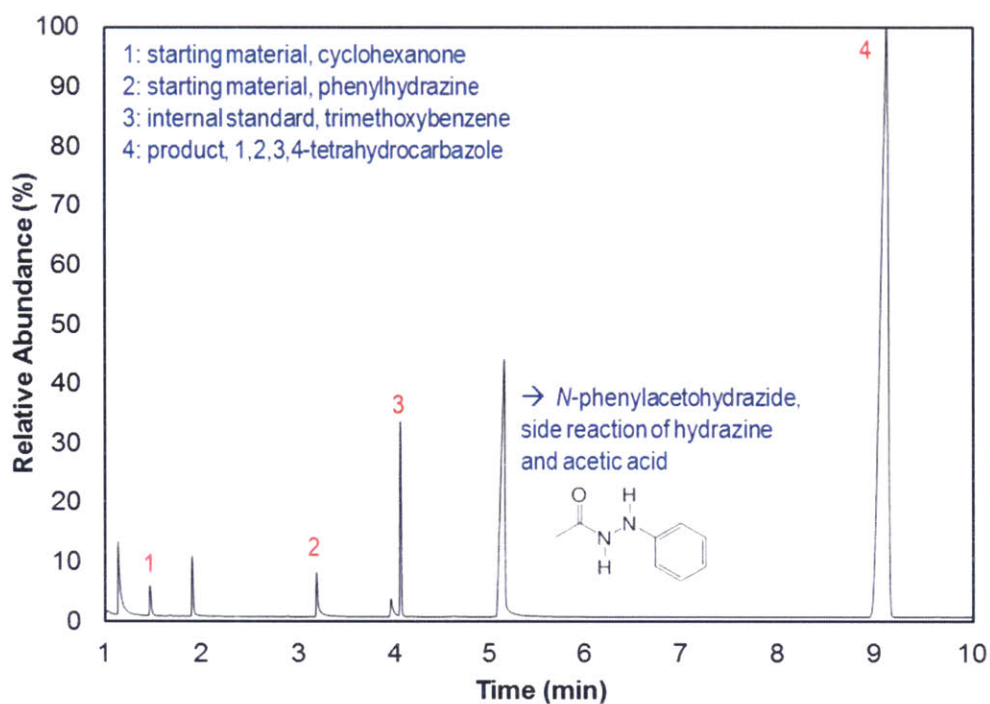


Figure C.4: GC-FID chromatography for Fischer indolization of c1 at 180 °C, 3 min residence time.

GC/MS:

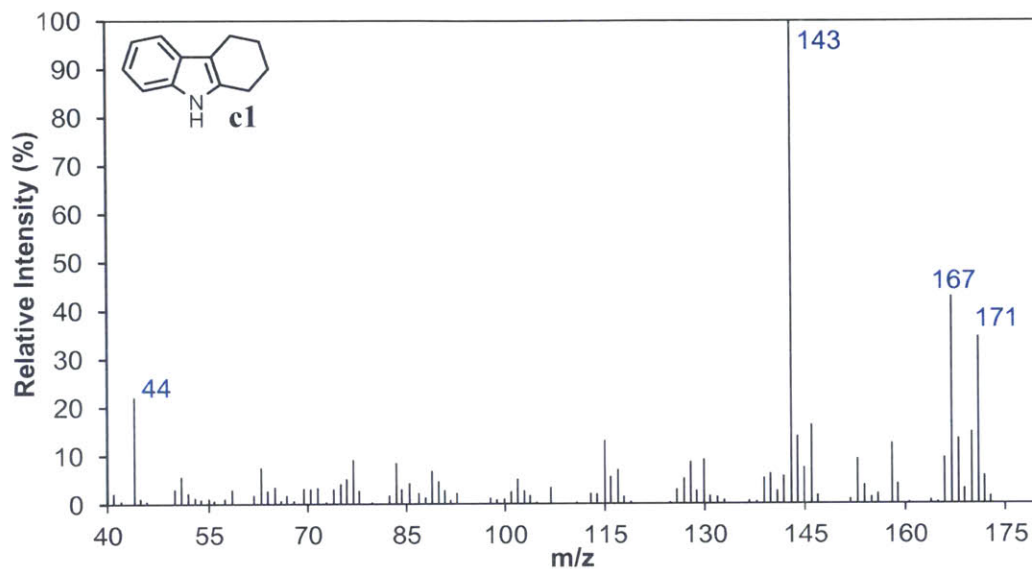


Figure C.5: GC mass spectrum for **c1**.

NMR of crude product:

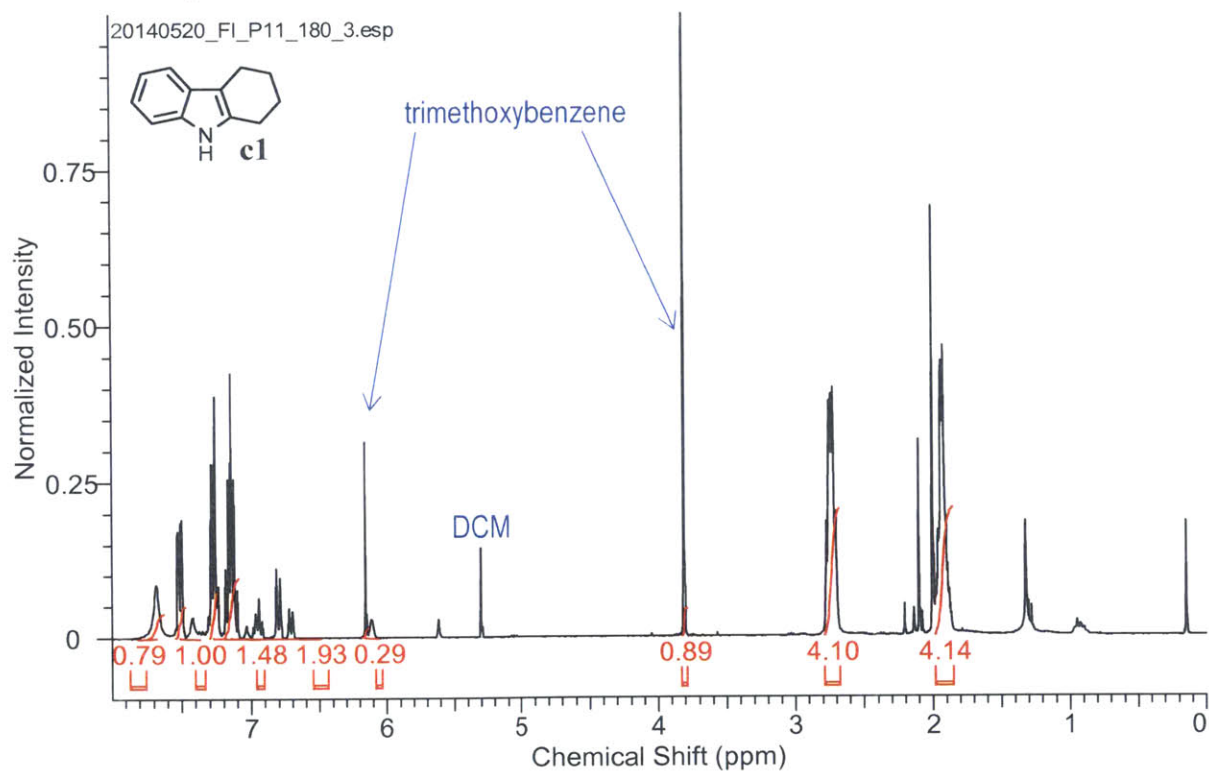


Figure C.6: NMR spectrum for crude collection of **c1** at 180 °C, 3 min residence time.

### NMR for isolated product:

The final isolated product was run with starting reagent solutions without internal standards added. 6 ml of solution was collected (1.5 mmol of expected product at full conversion). The sample was extracted with DCM and NaHCO<sub>3</sub>, and the DCM phase was evaporated. The residue was purified by running through a silica gel column chromatography with a 4:1 ratio of hexane and ethyl acetate mixture as the eluent.

The peaks at 0.6, 1.25 are silicone oil and grease, and the peaks 1.56, and 7.26 are solvent peaks. All four peaks are seen in the solvent deuterated chloroform (Figure C.7).

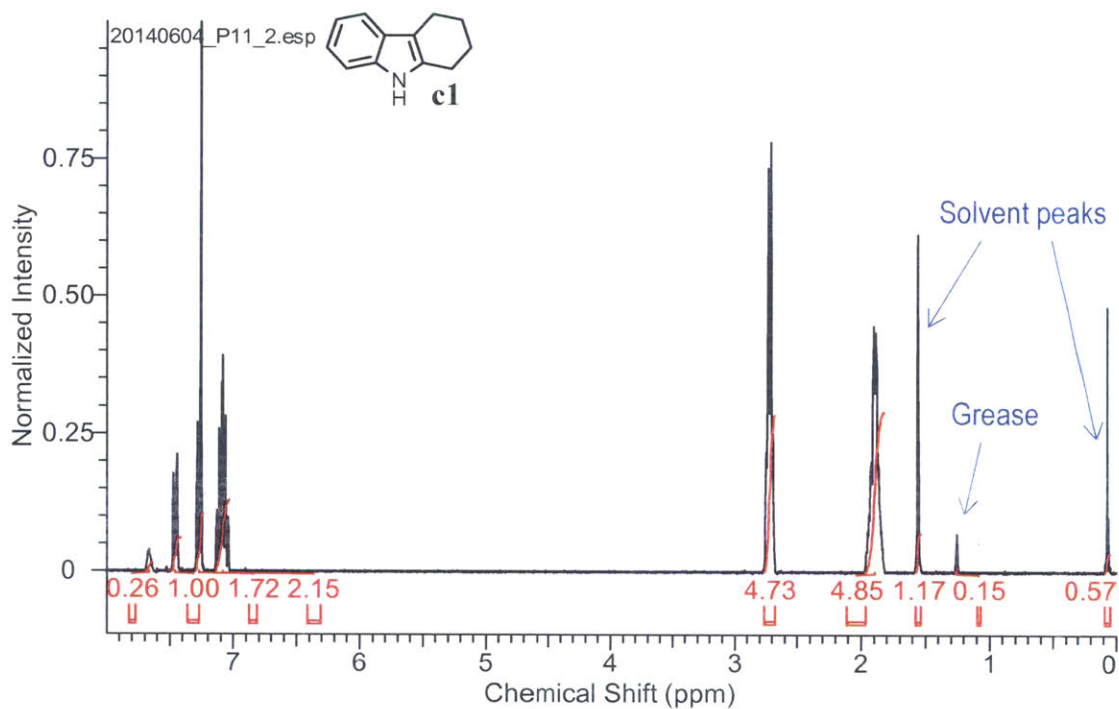


Figure C.7: NMR spectrum for purified **c1** at 180 °C, 3 min residence time.

### C.3.2 Product c2: 3-(*tert*-butyl)-2,3,4,9-tetrahydro-1*H*-carbazole

The conversions of the initial screening were calculated from GC chromatography. Since the pure product was not commercially available, the yields were only analyzed by NMR. The reaction product was identified with GC/MS.

#### GC-FID:

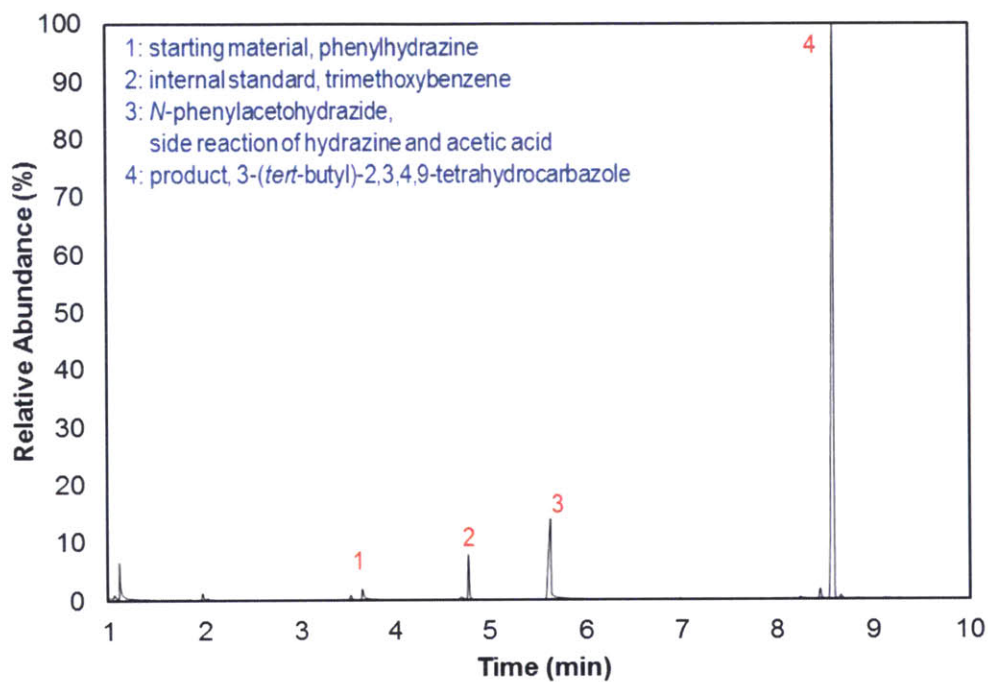
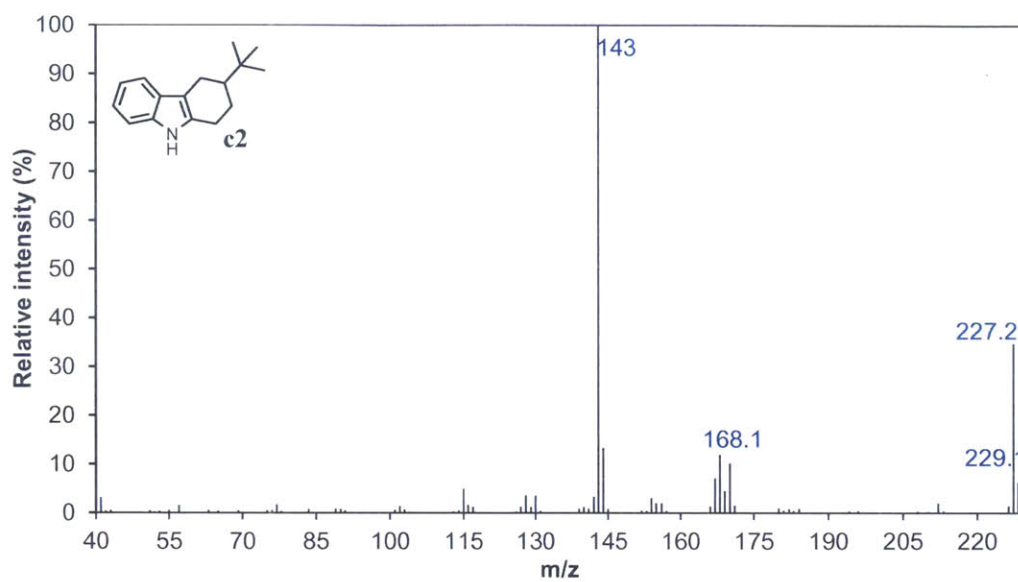


Figure C.8: GC-FID chromatography for Fischer indolization of c2 at 170 °C, 3 min residence time.

**GC/MS:**



**Figure C.9: GC mass spectrum for c2.**

**NMR of crude product:**

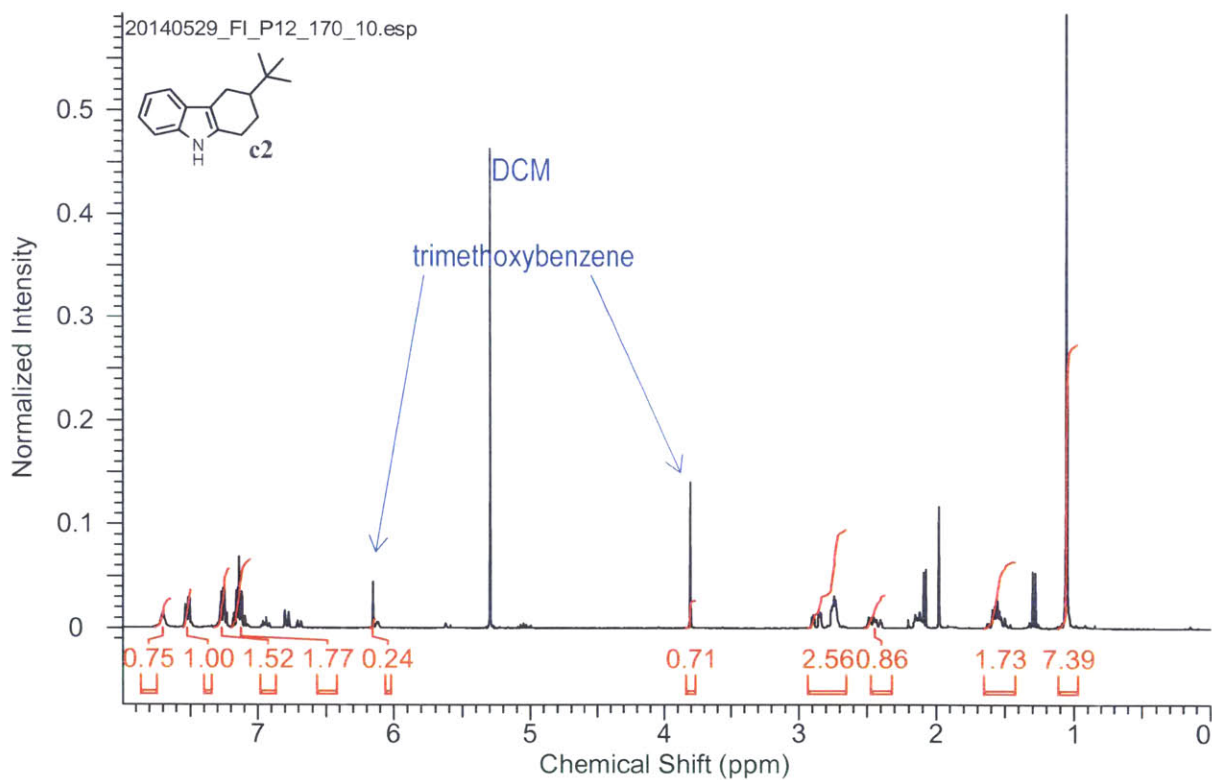


**Figure C.10: NMR spectrum for crude collection of c2 at 170 °C, 10 min residence time.**



### NMR for isolated product:

The final isolated product was run with starting reagent solutions without internal standards added. 400  $\mu\text{l}$  of solution was collected (0.1 mmol of expected product at full conversion). The sample was extracted with DCM and  $\text{NaHCO}_3$ , and the DCM phase was evaporated. The residue was purified by running through a silica gel column chromatography with a 10:1 ratio of hexane and ethyl acetate mixture as the eluent.

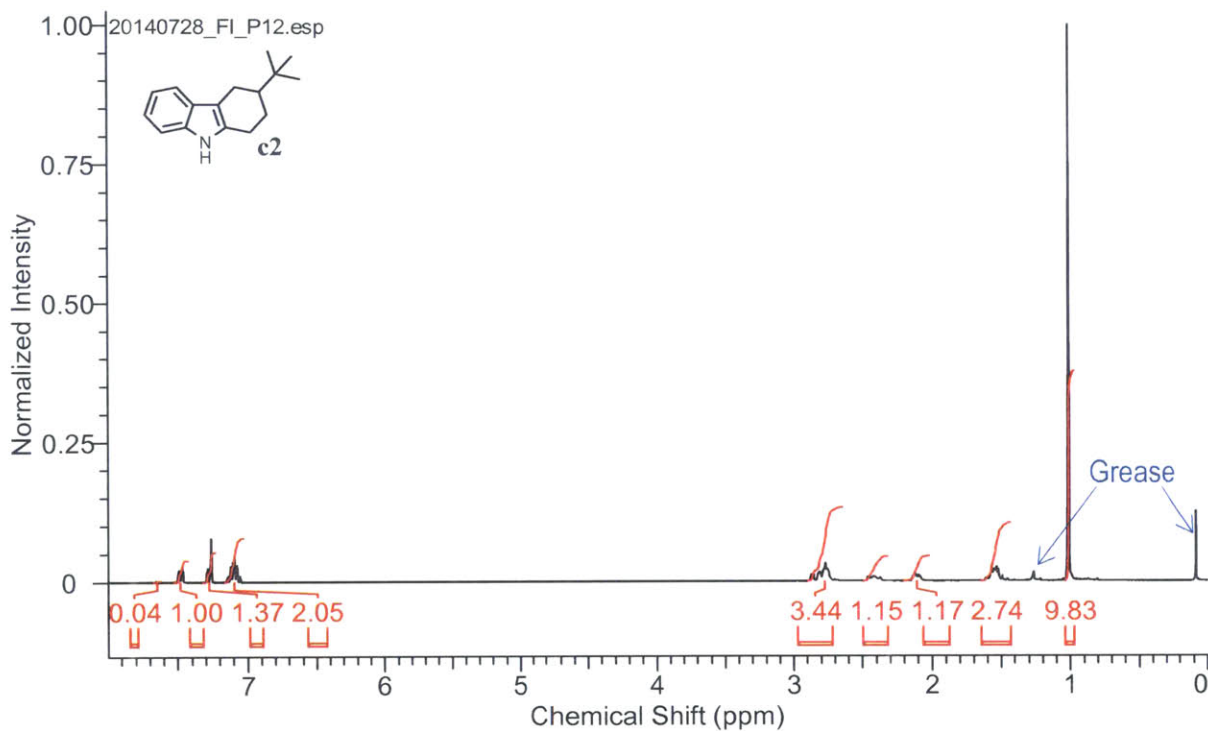


Figure C.11: NMR spectrum for purified c2 at 170 °C, 3 min residence time.

### C.3.3 Product c3: 6,11-dihydro-5H-benzo[*a*]carbazole

The conversions of the initial screening were calculated from GC chromatography. Since the pure product was not commercially available, the yields were only analyzed by NMR. The reaction product was identified with GC/MS.

#### GC-FID:

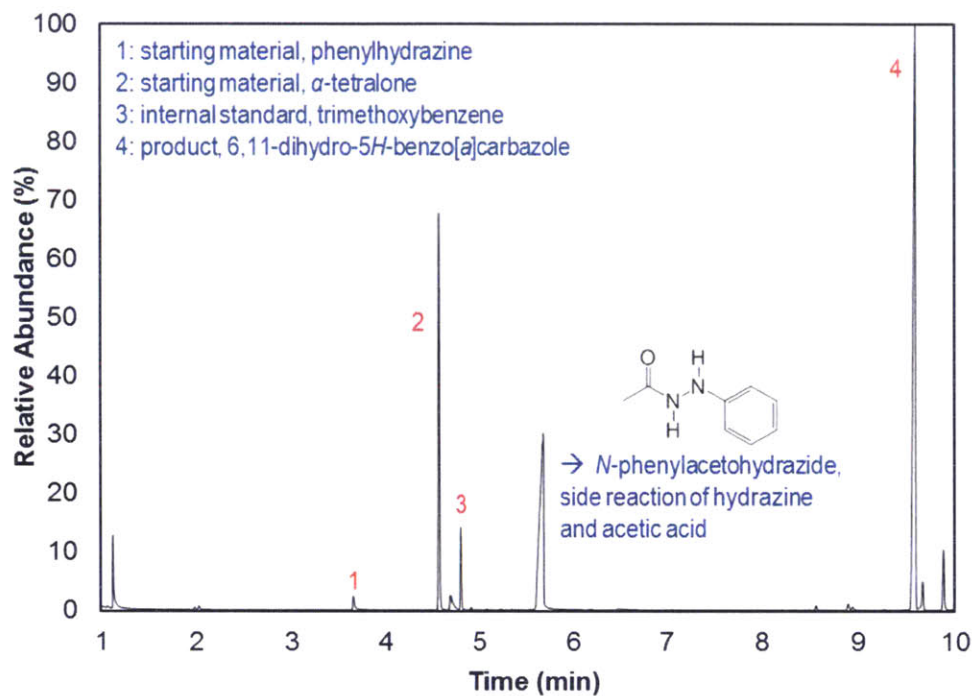
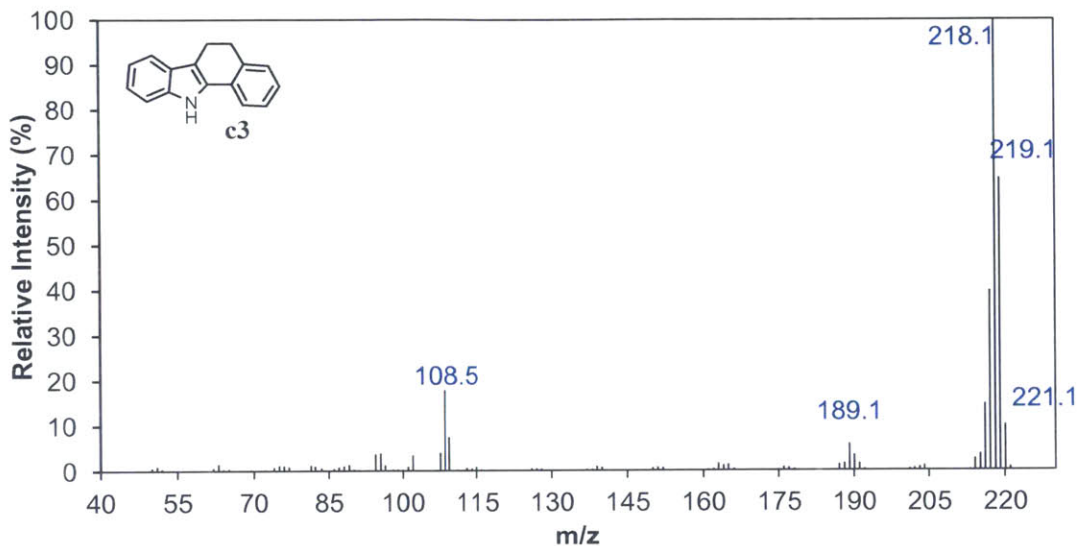


Figure C.12: GC-FID chromatography for Fischer indolization of c3 at 180 °C, 15 min residence time.

**GC/MS:**



**Figure C.13: GC mass spectrum for c3.**

**NMR of crude product:**

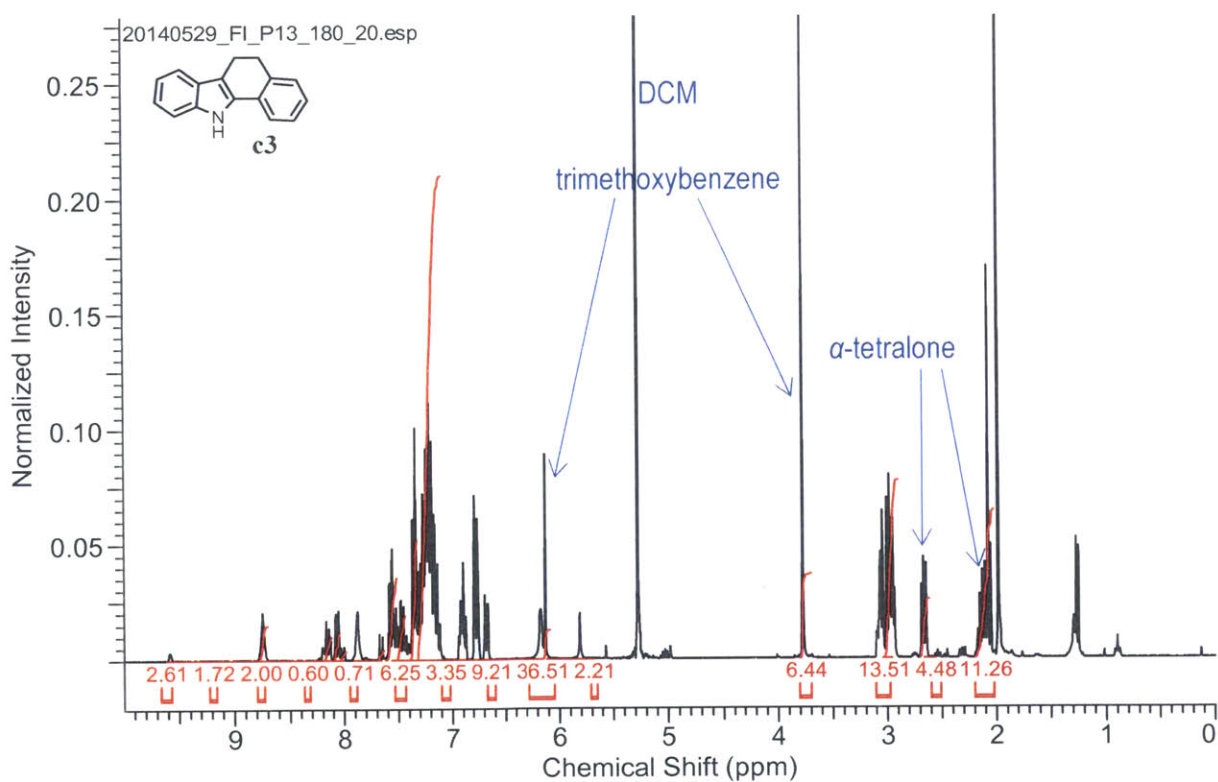


**Figure C.14: NMR spectrum for crude collection of c3 at 180 °C, 20 min residence time.**

### NMR for isolated product:

The final isolated product was run with starting reagent solutions without internal standards added. 400  $\mu\text{l}$  of solution was collected (0.1 mmol of expected product at full conversion). The sample was extracted with DCM and  $\text{NaHCO}_3$ , and the DCM phase was evaporated. The residue was purified by running through a silica gel column chromatography with a 10:1 ratio of hexane and ethyl acetate mixture as the eluent. Since the starting material,  $\alpha$ -tetralone, had the same Rf value as the product, the column collection was washed with hexane to remove the remaining  $\alpha$ -tetralone.

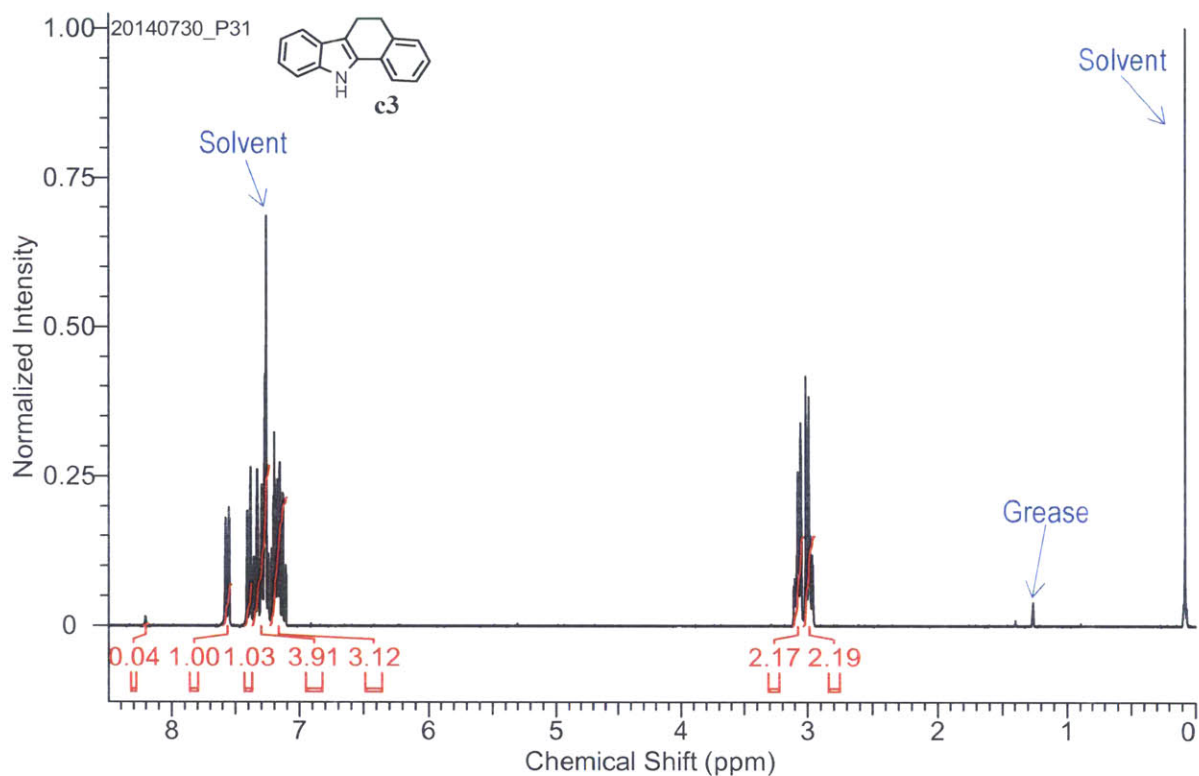


Figure C.15: NMR spectrum for purified **c3** at 180  $^{\circ}\text{C}$ , 30 min residence time.

### C.3.4 Product c4: 8-chloro-2,3,4,9-tetrahydro-1*H*-carbazole

The conversions of the initial screening were calculated from GC chromatography. Since the pure product was not commercially available, the yields were only analyzed by NMR. The reaction product was identified with GC/MS.

#### GC-FID:

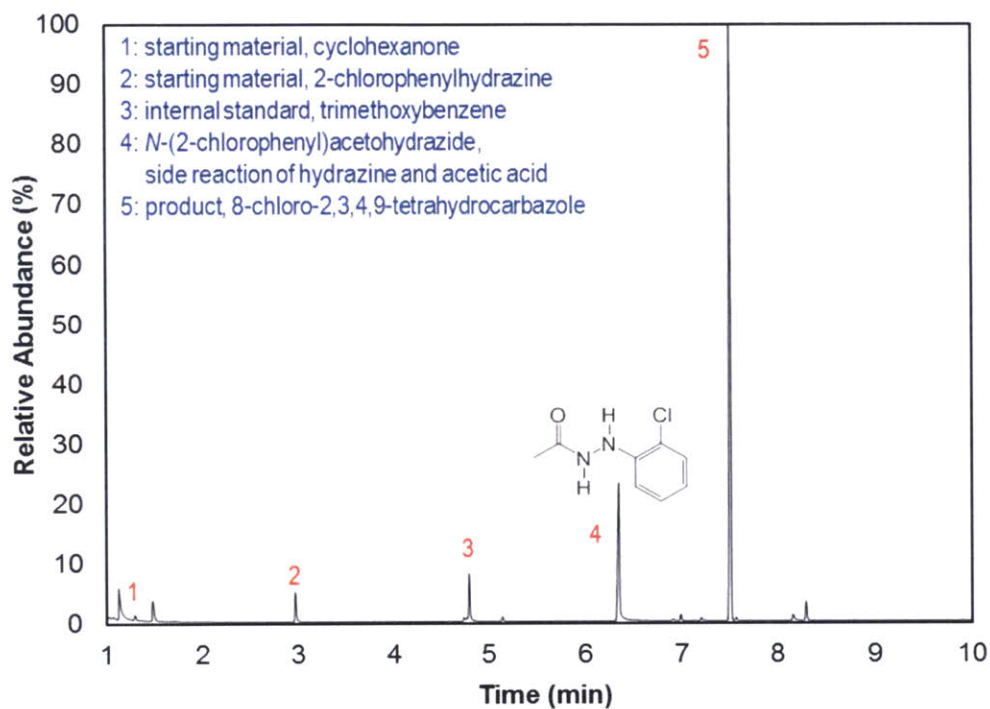


Figure C.16: GC-FID chromatography for Fischer indolization of c4 at 180 °C, 30 min residence time.

GC/MS:

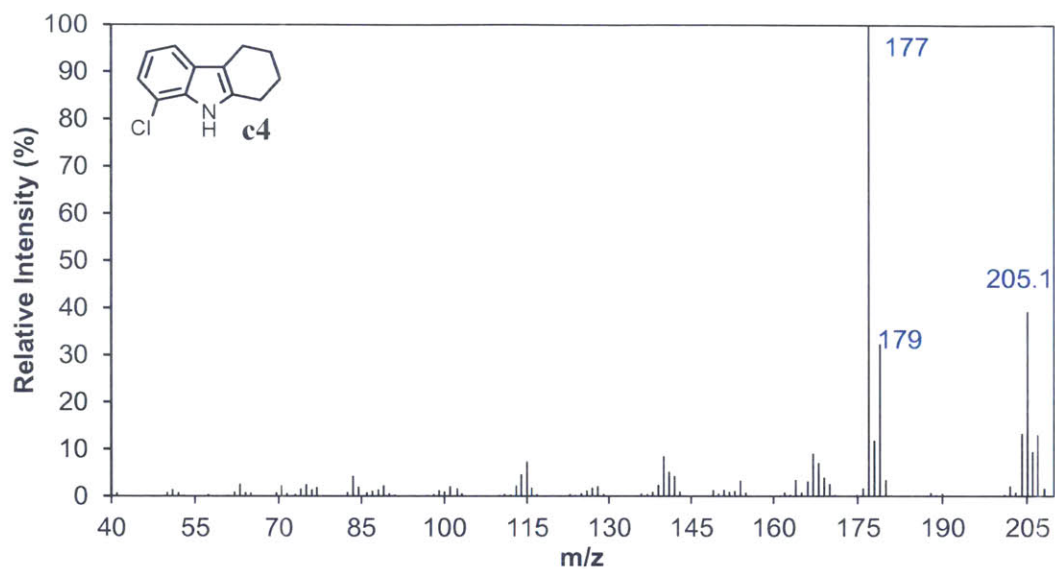


Figure C.17: GC mass spectrum for c4.

NMR of crude product:

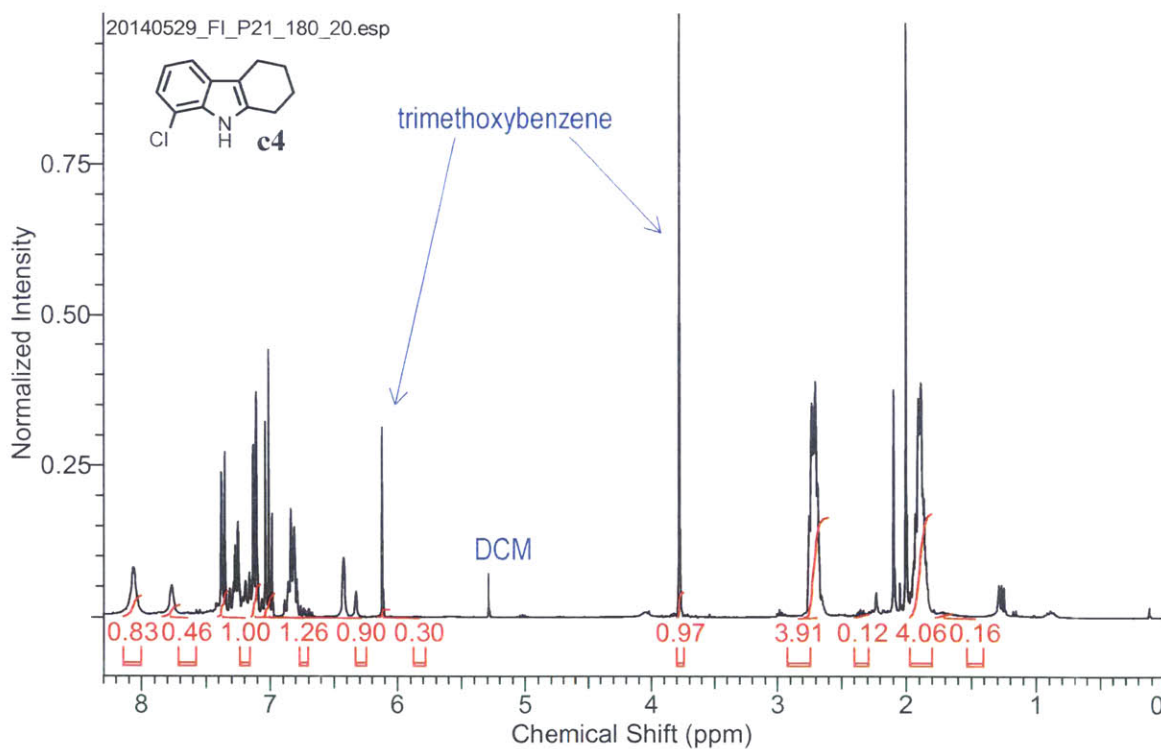


Figure C.18: NMR spectrum for crude collection of c4 at 180 °C, 20 min residence time.

### NMR for isolated product:

The final isolated product was run with starting reagent solutions without internal standards added. 400  $\mu\text{l}$  of solution was collected (0.1 mmol of expected product at full conversion). The sample was extracted with DCM and  $\text{NaHCO}_3$ , and the DCM phase was evaporated. The residue was purified by running a preparative TLC with a 20:1 ratio of hexane and ethyl acetate mixture as the eluent.

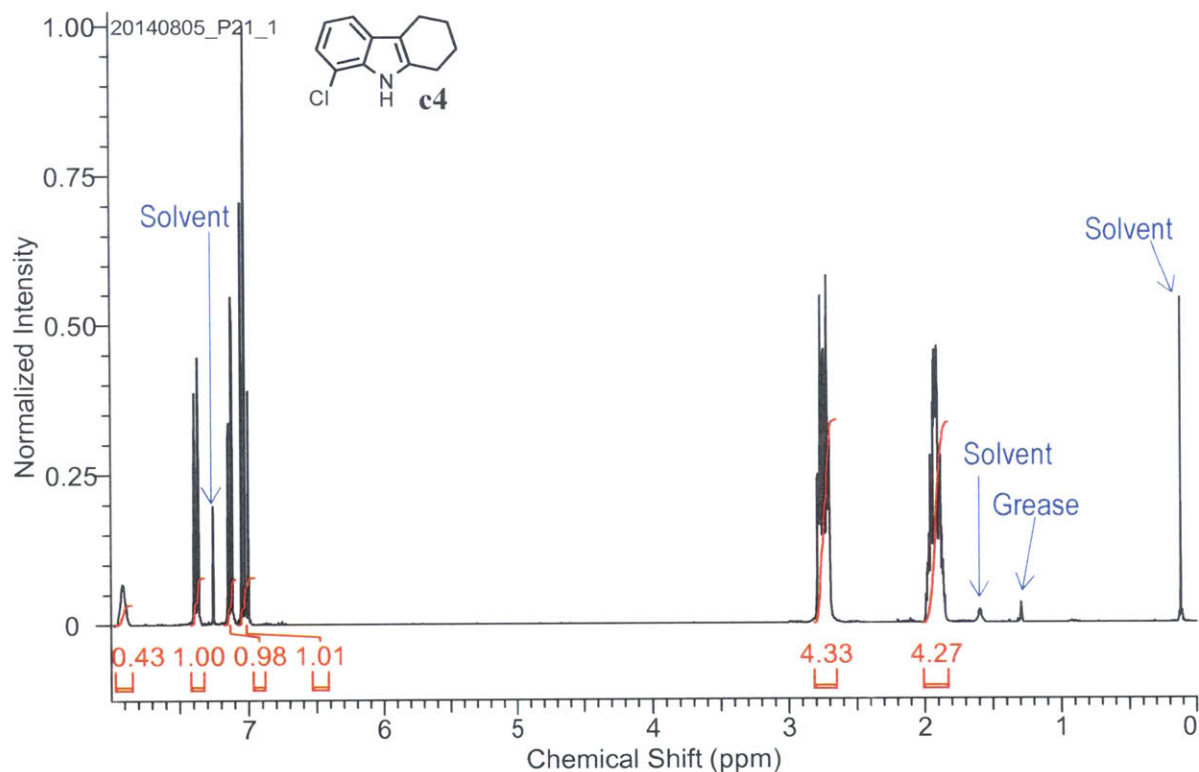


Figure C.19: NMR spectrum for purified c4 at 180 °C, 20 min residence time.

### C.3.5 Product c5: 6-methoxy-2,3,4,9-tetrahydro-1*H*-carbazole

The conversions of the initial screening were calculated from GC chromatography. Since the pure product was not commercially available, the yields were only analyzed by NMR. The reaction product was identified with GC/MS. For each of the GC and GC/MS samples, 100  $\mu$ l of collected solution ( $\sim$ 0.025 mmol scale) was added to 0.1 ml of DCM for analysis. For the NMR sample, 100  $\mu$ l of collected solution was extracted with DCM and  $\text{NaHCO}_3$ ; the DCM phase was evaporated, and the final residue was dissolved in  $\text{CDCl}_3$ .

#### GC-FID:

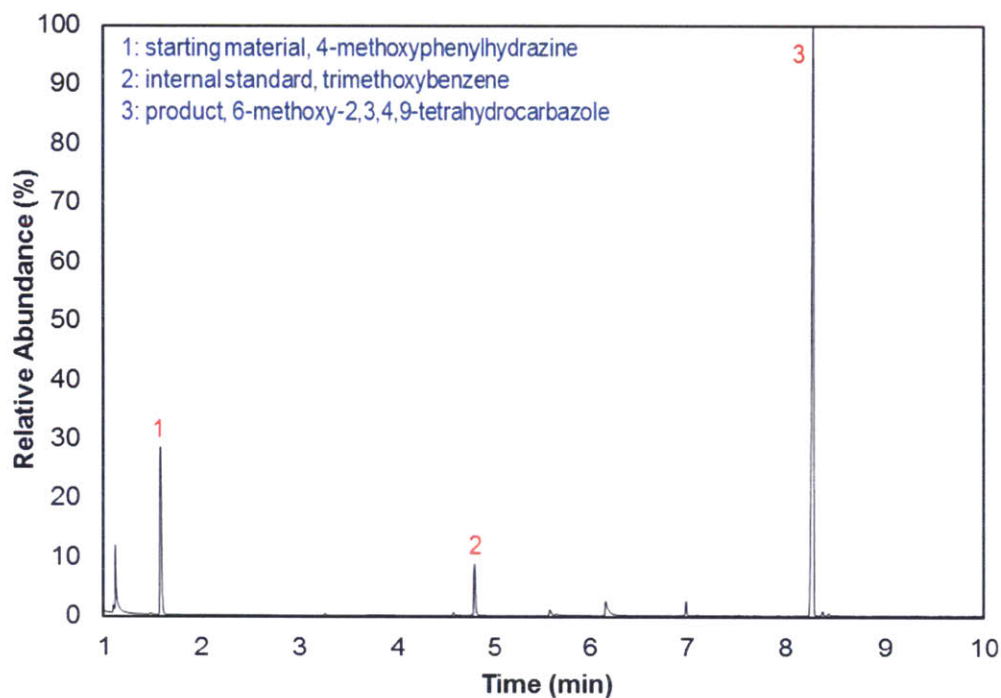


Figure C.20: GC-FID chromatography for Fischer indolization of c5 at 180 °C, 10 min residence time.



GC/MS:

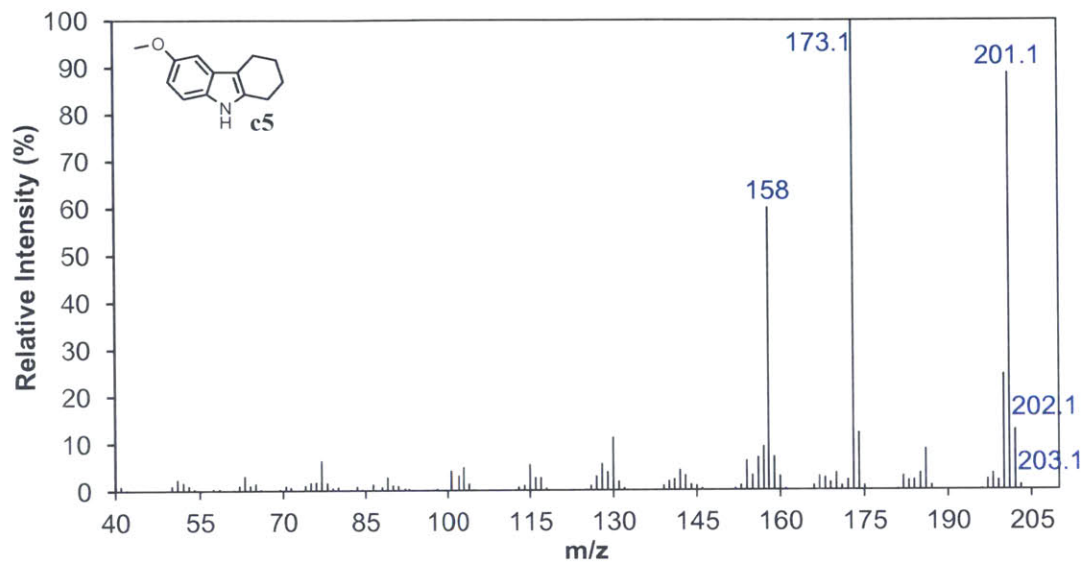


Figure C.21: GC mass spectrum for **c5**.

NMR of crude product:

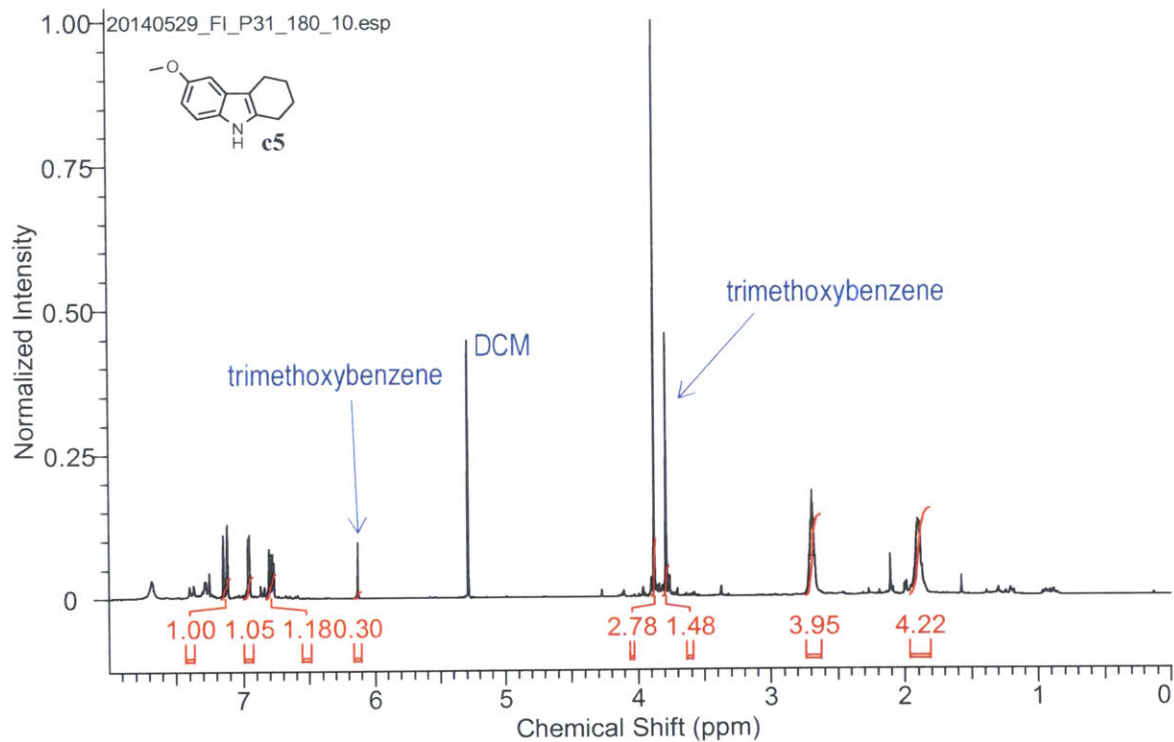


Figure C.22: NMR spectrum for crude collection of **c5** at 180 °C, 3 min residence time.

### NMR for isolated product:

The final isolated product was run with starting reagent solutions without internal standards added. 400  $\mu\text{l}$  of solution was collected (0.1 mmol of expected product at full conversion). The sample was extracted with DCM and  $\text{NaHCO}_3$ , and the DCM phase was evaporated. The residue was purified by running through a silica gel column chromatography with a 10:1 ratio of hexane and ethyl acetate mixture as the eluent.

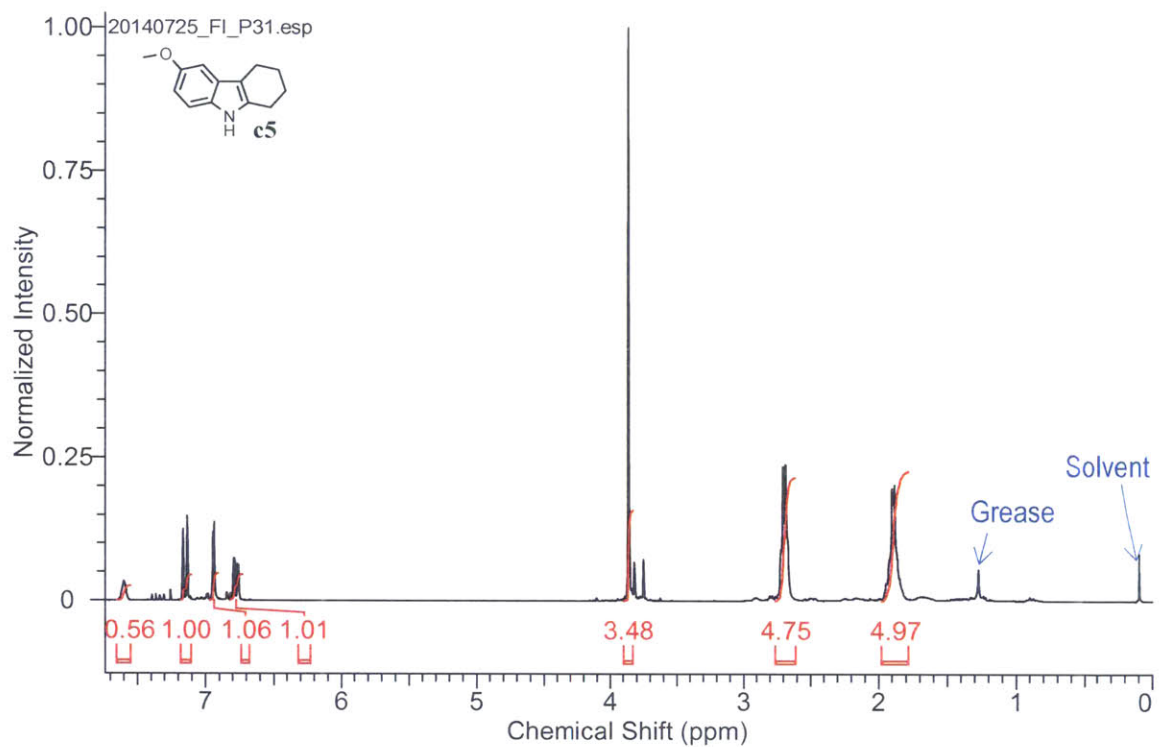


Figure C.23: NMR spectrum for purified c5 at 180 °C, 3 min residence time.